Molecular Beam Epitaxy and Characterization of Ferromagnetic Bulk and Thin (Ga,Mn)As Layers/Heterostructures

Dissertation

zur Erlangung des
naturwissenschaftlichen Doktorgrades
der Julius-Maximilians-Universität Würzburg

vorgelegt von
Lars Frederik Ebel
aus Lohne (Oldenburg), Niedersachsen

Würzburg 2013

Eingereicht am: 20.02.2013

bei der Fakultät für Physik und Astronomie

Gutachter der Dissertation:

1. Gutachter: Prof. Dr. Karl Brunner

2. Gutachter: Prof. Dr. Ralph Claessen

Prüfer im Promotionskolloquium:

1. Prüfer: Prof. Dr. Karl Brunner

2. Prüfer: Prof. Dr. Ralph Claessen

3. Prüfer: Prof. Dr. Wolfgang Kinzel

Tag des Promotionskolloquiums: 31.10.2013

Doktorurkunde ausgehändigt am: .. ..

Contents

Zusammenfassung **5**

Summary **9**

1 Introduction **11**

2 The Ferromagnetic Semiconductor (Ga,Mn)As **13**
2.1 Ferromagnetic Properties 13
2.2 Band Structure 16
2.2.1 Self-Consistent Calculations of Band Alignment and Hole Density . 18
2.3 Magnetic Anisotropy 26
2.3.1 Transport Properties 26

3 Experimental Methods **37**
3.1 The UHV-MBE Growth Chamber and in-situ Reflection High Energy Electron Diffraction 37
3.2 Epitaxial Growth 41
3.2.1 (Ga,Mn)As 41
3.2.2 (Al,Ga)As, AlAs and (Ga,In)As 47
3.2.3 Typical Growth Procedure 48
3.3 High Resolution X-Ray Diffraction 50
3.3.1 $\omega - 2\Theta$ Scans 51
3.3.2 Reciprocal Space Maps 56
3.4 Superconducting Quantum Interference Device 59
3.5 Four-Terminal Transport Measurements @ RT and LT 62

4 Bulk and Thin (Ga,Mn)As Layers **65**
4.1 Epitaxial Growth of Bulk (Ga,Mn)As at Different Growth Conditions . . . 65
4.1.1 Variation of Substrate Temperature and BEP ratio ($\frac{As_4}{Ga}$) 66
4.1.2 Magnetometry and RT-Transport Measurements 68
4.1.3 X-ray Diffraction Characterization 72
4.2 Epitaxial Growth of Thin (Ga,Mn)As Layers ($\leq 10\ nm$) 76
4.2.1 Influence of a LT-GaAs Cap Layer 76

4.2.2 5, 3.5 and 2 *nm* (Ga,Mn)As Layers with LT-GaAs Cap Layer . . . 77
4.2.3 Ferroelectrical Gating of a 7 *nm* (Ga,Mn)As Layer 78

5 Parabolically Graded Thin (Ga,Mn)As Layers 83
5.1 Realization of a Parabolically Graded Mn Distribution 83
5.1.1 Two Different Growth Techniques 84
5.1.2 Calculation of Parabolically Graded Mn Profiles 88
5.2 Variation of Mn Content at Standard Growth Conditions 92
5.2.1 Epitaxial Growth and RHEED 92
5.2.2 As-grown and Annealed Parabolic Layer Characterization 94
5.2.3 LT-Conductivity of Parabolical Graded and Homogeneous (Ga,$Mn_{0.04}$)As Layers 96
5.3 Optimization of Growth Conditions with Constant Mn Content $x = 0.025$. 100
5.3.1 Determination of Parameter Range by 70 *nm* (Ga,Mn)As Layers . . 100
5.3.2 Optimization of Growth Conditions of Thin Parabolical (Ga,Mn)As Layers 104
5.3.3 Magnetic Characterization 106
5.3.4 RT- and LT-Conductivity Measurements 107
5.3.5 Parabolically Graded Sample at Optimized Growth Conditions . . . 109
5.4 Parabolically Graded (Ga,Mn)As Layer in a Semiconductor p-n Junction . 118

6 Induced Magnetic Anisotropy in Lifted Bulk (Ga,Mn)As Layers 121
6.1 X-ray Diffraction Investigations 122
6.1.1 70 *nm* (Ga,Mn)As Layer S1 122
6.1.2 70 *nm* (Ga,Mn)As / 70 *nm* (Ga,In)As Layer S2 124
6.2 Temperature Dependent Magnetometry Results 128

7 Conclusion and Outlook 131

A Appendix 133
A.1 Determination of As_{Ga} Concentrations 133
A.2 Special Features of the UHV MBE Growth Chamber 136
A.2.1 Homogeneity of a 2" Wafer 136
A.2.2 Mirror on a Molybdenum Block 139

Bibliography 140

Acknowledgements 147

Zusammenfassung

(Ga,Mn)As ist einer der prominentesten Vertreter der ferromagnetischen Halbleiter (*ferromagnetic semiconductor*, FS). Aufgrund der hohen Dotierung des kommerziell eingesetzten GaAs Halbleiters mit magnetischen Mangan-Atomen (Mn) im Prozentbereich wird das Material ferromagnetisch. Die Kopplung von elektrischen und magnetischen Eigenschaften geschieht durch die Spin-Bahn Wechselwirkung. Seit der ersten Veröffentlichung Mitte der Neunziger Jahre durch H. Ohno [Ohn96] wurde der prototypische FS (Ga,Mn)As intensiv untersucht. Viele grundlegende Erkenntnisse wurden gewonnen, jedoch ist das Materialsystem bis heute noch nicht vollständig verstanden. Einer der Forschungsschwerpunkte liegt in der Realisierung der ferromagnetischen Eigenschaften bei Raumtemperatur (*room temperature*, RT) durch eine hohe Mn-Dotierung. Dies gilt als Voraussetzung für eine kommerzielle Nutzung dieses Materialsystems. Die bislang höchste erreichbare Temperatur, bei der ferromagnetische Eigenschaften vorherrschen, liegt bei ≈190 K [Ole08, Che09]. Andererseits gibt es den Wunsch nach relativ geringen Ladungsträgerdichten in (Ga,Mn)As durch eine niedrige Mn-Dotierung. Die elektrische Kontrolle der magnetischen Eigenschaften konnte bereits in einem Feldeffekttransistor, bestehend aus solch einer dünnen (Ga,Mn)As Schicht und einem ferroelektrischen Gate, nachgewiesen werden [Sto08].

Im Rahmen dieser Arbeit wurde das Materialsystem (Ga,Mn)As mit seinen komplexen Eigenschaften untersucht im Hinblick auf die Optimierung sehr dünner (4 nm) (Ga,Mn)As Schichten, welches mit der Technologie der Molekularstrahlepitaxie (*molecular beam epitaxie* MBE) hergestellt wurde. Der experimentelle Teil ist in drei Bereiche gegliedert: Im ersten Teil werden MBE Wachstumsparameter auf den Einfluss der Materialeigenschaften von dicken (70 nm) (Ga,Mn)As Schichten hin untersucht. Im zweiten Experimentalteil wird ein parabolisches Mn-Dotierprofil als Alternative zu einem homogenen Dotierprofil für 4 nm (Ga,Mn)As Schichten vorgestellt, welches entwickelt und epitaktisch hergestellt wurde. Eine Verbesserung der elektrischen und magnetischen Eigenschaften konnte nachgewiesen werden. Im Vergleich zu einer 70 nm (Ga,Mn)As Schicht und gleichem Mn-Gehalt $x = 0.040$ offenbarte eine dünne (Ga,Mn)As Schicht mit parabolischem Mn-Profil vergleichbare magnetische Anisotropien. Aufbauend auf diesen Ergebnissen wurden die MBE Wachstumsbedingungen für das parabolische Mn-Dotierprofil mit relativ niedrigem nominellen Mn-Gehalt $x = 0.025$ systematisch variiert und charakterisiert. Ein Wachstumsfenster konnte dabei ermittelt werden, in welchem die hergestellten Schichten verbesserte Tieftemperatur- (*low temperature*, LT) Schichteigenschaften zeigten. Im letzten Teil dieser Arbeit wird eine Anwendung der Anisotropiekontrolle von 70 nm (Ga,Mn)As

Schichten mittels eines epitaktischen lift-off (ELO) Prozesses dargestellt [Gre11].

Das epitaktische Kristallwachstum von dicken ($\geq 20\ nm$) (Ga,Mn)As Schichten mittels der MBE Technologie wurde in der Vergangenheit sehr erfolgreich eingesetzt, um reproduzierbare ferromagnetische Eigenschaften für elektrische Transportexperimente bei angelegten Magnetfeldern herzustellen. Die Anisotropiekontrolle durch lithographisch hervorgerufene Verspannungsänderung [Wen08] wurde z.B. erfolgreich als Baustein in nichtflüchtigen Speicherelementen eingesetzt [Pap07b, Mar11]. Wachstumsparameter wie Substrattemperatur T_{sub}, Mn Effusionszelltemperatur T_{Mn}, V zu III Materialflussverhältnisse (*beam equivalent pressure*, BEP ratio ($\frac{As_4}{Ga}$)) sowie die Wachstumsrate spielen für qualitativ hochwertige (Ga,Mn)As Schichten eine entscheidende Rolle. Da das Mn unter thermischen Gleichgewichtsbedingungen eine sehr geringe Löslichkeit aufweist, muss die Substrattemperatur für das Kristallwachstum unter ≈300°C gesetzt werden (im Gegensatz zu 580°C beim Hochtemperatur-GaAs Wachstum (*high temperature*, HT)). Standard-Wachstumsbedingungen von T_{sub} = 270°C und BEP ratio ($\frac{As_4}{Ga}$) = 25 wurden eingestellt. Die in-situ Wachstumsüberwachung wurde mit der Elektronenstrahlbeugung in Reflexionsgeometrie durchgeführt (*reflection high electron energy diffraction*, RHEED). Zur exsitu Charakterisierung der in dieser Arbeit hergestellten (Ga,Mn)As Schichten wurden die hochauflösende Röntgenstrahlbeugung (*high resolution x-ray diffraction*, HRXRD), Magnetometriemessungen mittels supraleitender Quanteninterferenzeinheit (*superconducting quantum interference device*, SQUID) und RT- sowie LT-Transportmessungen in 4-Punkt Hallbar-Geometrie ohne und mit angelegtem Magnetfeld eingesetzt.

Die Herstellung sehr dünner ($< 10\ nm$) (Ga,Mn)As Schichten erweist sich als Herausforderung. Neben Punktdefekten wie Arsen auf Ga-Plätzen (*Arsen-Antisites*, As_{Ga}) sowie Mn auf Zwischengitterplätzen (*Mn-Interstitials*, Mn_{Int}), welche im (Ga,Mn)As durch die tiefen Wachstumstemperaturen in hohen Konzentrationen (10^{19} bis $10^{20}\ cm^{-3}$) auftreten und als Doppeldonatoren die freie Ladungsträgerdichte signifikant kompensieren, spielen Grenzflächeninhomogenitäten zu benachbarten Halbleiterschichten und zur Oberfläche eine entscheidende Rolle. Ein stark beeinträchtigter lateraler Stromfluss in der dünnen Schicht ist die Folge. Vereinfachte Simulationen zur Bestimmung des Valenzbandkantenverlaufes mittels selbstkonsistenter Lösung von Poisson- und Schrödingergleichung bestätigten diesen Trend und zeigten einen deutlichen Einfluss dieser Defekte und Oberflächenzustände auf die Ladungsträgerdichte in sehr dünnen Schichten im Vergleich zu dicken (Ga,Mn)As Schichten bei gleichem Mn-Gehalt.

Das parabolische Mn-Dotierprofil dient dazu, eine bessere Überlappung der Ladungsträgerdichte mit magnetischen Momenten der Mn-Atome zu erreichen. Dies soll durch elektrostatische Abschirmung von mehreren Dotierspikes ober- und unterhalb einer zentralen, rund 1.4 nm dünnen (Ga,Mn)As Schicht ermöglicht werden. Aus ersten experimentellen Ergebnissen von epitaktisch hergestellten, parabolischen Schichten bei Standard-Wachstumsbedingungen mit Variation des Mn-Gehaltes ergab sich eine Verbesserung der elektrischen und magnetischen Eigenschaften gegenüber dünnen Schichten mit homogenem Mn Profil und gleichem nominellen Mn-Gehalt von $x = 0.040$. Ähnliche ferromagnetische Eigenschaften, wie sie in dicken (Ga,Mn)As Schichten vorherrschen, wurden hierbei festgestellt. In der zweiten Studie wurden die Wachstumsbedingungen für parabolische

Schichten mit geringem nominellen Mn-Gehalt $x = 0.025$ optimiert. Vereinfachte Berechnungen des Valenzbandkantenverlaufes bei RT deuteten diesen Vorteil gegenüber sehr dünnen Schichten mit homogenem Mn-Profil an. Die experimentellen Ergebnisse zeigen, dass in einem schmalen Wachstumsfenster dünne (Ga,Mn)As Schichten mit parabolischem Mn-Profil epitaktisch hergestellt werden können, die selbst bei tiefen Temperaturen (4.3 K) leitfähig sind. Somit könnten in der Zukunft diese dünnen (Ga,Mn)As Schichten zur elektrischen Kontrolle der magnetischen Anisotropien genutzt werden. Erste Messungen von (Ga,Mn)As Schichten mit parabolischem Mn-Profil in einer p-n Struktur mit Barriereschichten ergaben vergleichbare elektrische sowie magnetische Eigenschaften wie die zuvor untersuchten Einzelschichten.

Eine Anwendung der Anisotropiekontrolle in (Ga,Mn) As wird im letzten Teil dieser Arbeit vorgestellt. Dabei wurde eine 70 nm (Ga,Mn)As Schicht epitaktisch bei Standard-Wachstumsbedingungen auf einem GaAs Substrat mit darüberliegender AlAs Opferschicht abgeschieden. Mit Hilfe des epitaktischen lift-off Prozesses (ELO) wird die kompressiv verspannte (Ga,Mn)As Schicht, welche magnetische Vorzugsrichtungen in der Schichtebene entlang der [100]- und [010]-Kristallrichtungen aufweist, vom Substrat gelöst und relaxiert. Danach ist es möglich, die Schicht auf ein beliebiges Substrat abzulegen. Der Einbau einer zusätzlichen (Ga,In)As Stressorschicht zwischen AlAs und (Ga,Mn)As führt zu einer Dehnung und somit zu einer tensilen Verspannung in der Schichtebene der (Ga,Mn)As Schicht. Daraus resultiert eine Magnetisierungsvorzugsrichtung senkrecht zur Probenoberfläche entlang der [001]-Kristallrichtung, welche durch SQUID Messungen nachgewiesen wurde. Das Ablösen der Schichten auf unterschiedliche Substrate bietet die Möglichkeit anderer Untersuchungsmethoden der (Ga,Mn)As Schichten wie z.B. optische Transmissionsexperimente im sichtbaren Bereich (Saphir als Substrat) oder die Magnetisierung durch elektrostatische Kontrolle zu ändern (piezoelektrischer Kristall als Substrat).

Summary

(Ga,Mn)As is one of the prominent ferromagnetic semiconductors (FS). The commercial semiconductor GaAs becomes ferromagnetic by heavy doping with magnetic Mn atoms ($\gtrapprox$1.5%). The interaction between electrical and magnetic properties is realized by spin-orbit coupling. Since the first publication in the 90ies by H. Ohno [Ohn96], this prototypical FS has been intensively investigated. Up to now it is not completely understood. One focus of research lies in room temperature (RT) ferromagnetism of this material by heavy doping (>10%) for commercial use. Highest temperatures of ≈190 K have been achieved, which is still far from RT ferromagnetism [Ole08, Che09]. (Ga,Mn)As with a low percentage of Mn doping is useable as a model system for the electrical control of magnetic anisotropies, e.g. by a ferroelectrical gate [Sto08].

In the framework of this thesis, the (Ga,Mn)As material has been investigated in terms of optimization of very thin (4 nm) (Ga,Mn)As layers, epitaxially fabricated by the molecular beam epitaxy (MBE) technology. The experimental part is divided in three blocks: The first part presents investigations of the influence of growth parameter conditions on electrical and magnetic properties of bulk (70 nm) (Ga,Mn)As layers. The second part introduces a parabolical Mn concentration profile instead of a (4 nm) layer with a homogeneous Mn profile. Improved properties have been observed as well as comparable magnetic and electrical properties to bulk (Ga,Mn)As layers, both with a Mn content of $x = 0.040$. MBE growth parameters for the (Ga,Mn)As layers with a parabolically graded Mn profile and lowered nominal Mn content of $x = 0.025$ have been investigated. A narrow growth window has been found in which low-temperature (LT) layer properties are improved. The last part of this thesis presents an application of anisotropy control by an epitaxial lift-off (ELO) process of 70 nm (Ga,Mn)As layers [Gre11].

In the past, the epitaxial growth of bulk ($\geq$ 20 nm) layers by the MBE technology has been successfully used to fabricate reproducible ferromagnetic and electrical properties of the (Ga,Mn)As material for LT-magnetotransport experiments. The control of magnetic anisotropies has been achieved e.g. by uniaxial strain-relaxation caused by lithographical nanopatterning of stripes [Wen08], resulting in applications of non-volatile devices [Pap07b, Mar11]. Growth parameters like substrate temperature T_{sub}, Mn effusion cell temperature T_{Mn} and V to III *beam equivalent pressure* (BEP ratio ($\frac{As_4}{Ga}$)) play a crucial role of high quality (Ga,Mn)As material. Under thermal equilibrium growth conditions, Mn has a very low solubility and T_{sub} has to be decreased below ≈300°C (in contrast to 580°C for high-temperature (HT) GaAs growth). The standard growth conditions are

T_{sub} = 270°C and BEP ratio ($\frac{As_4}{Ga}$). In-situ *reflection high electron energy diffraction* (RHEED) is the chosen method to monitor the sample surface during epitaxial growth. *High resolution x-ray diffraction* (HRXRD), *superconducting quantum interference device* (SQUID) magnetometry, as well as RT- and LT-transport measurements in 4-terminal Hallbar geometry without and with an external applied magnetic field have been performed for an ex-situ characterization of the epitaxially grown (Ga,Mn)As layers.

The fabrication of very thin (< 10 nm) (Ga,Mn)As layers is challenging. Charge carriers, provided by Mn atoms on Ga sites (*substitutional Mn*, Mn_{sub}), are compensated by point defects like As atoms on Ga-sites (*As-antisites*, As_{Ga}) and Mn on interstitial lattice positions (*Mn interstitials*, Mn_{int}) with concentrations in the range of 10^{19} to 10^{20} cm^{-3}. Both point defects act as double donors. Additionally, interfaces to neighboring layers as well as the surface play a significant role in carrier compensation leading to a hindered lateral current flow in very thin layers. Simplified self-consistent solutions of Poisson- and Schrödinger-equation confirm the trend of a significant influence of these effects on carrier density in very thin (Ga,Mn)As layers compared to bulk layers.

The parabolical Mn profile of a very thin (Ga,Mn)As layer has been developed to achieve a better overlap of hole confinement and magnetic moments of Mn atoms. Therefore, a 1.4 nm (Ga,Mn)As layer has been electrostatically shielded by three doping-spikes above and underneath the center layer. Epitaxially grown layers with a parabolical grading of the Mn content at standard growth conditions reveal improved layer properties like RT-and LT-conductivity as well as a higher ferromagnetic transition temperature (*Curie temperature*, T_C) compared to (Ga,Mn)As layers with a homogeneous Mn profile. The parabolically graded sample has shown similar magnetic anisotropies like bulk (Ga,Mn)As material. In a second growth series, the growth parameter conditions have been systematically investigated for parabolically graded samples with a lowered Mn content $x = 0.025$. In a narrow growth parameter window, these layers have shown feasible LT-conductivities combined with improved T_C. Simplified self-consistent band alignment calculations have been performed and the result indicates a slight improvement of carrier density in case of a parabolically graded Mn profile compared to a homogeneous Mn profile with the same nominal Mn content $x = 0.025$. First tests of a parabolically graded (Ga,Mn)As layer, embedded in a p-n junction device, have shown comparable electrical and magnetic properties like previous grown parabolically graded layers on LT-GaAs.

In the last part of this thesis, an application of magnetic anisotropy control of bulk (Ga,Mn)As layers by the epitaxial lift-off process (*ELO*) is presented. A bulk 70 nm (Ga,Mn)As layer is deposited on a AlAs sacrificial layer with an underlying GaAs substrate. The ELO process allows the compressively strained (Ga,Mn)As layer to relax by etching of the AlAs layer. The lifted layer can be deposited on different host-substrates. The incorporation of an underlying (Ga,In)As stressor layer between AlAs and (Ga,Mn)As leads to an elongation and to a tensile strain in-plane of the (Ga,Mn)As layer. As a result, the preferred magnetic directions change from in-plane ([100] and [010] crystal directions) to out-of plane [001] crystal direction. The ELO process provides new measuring techniques e.g. optical transmission experiments (on nonabsorbing sapphire substrates) or electrostatic control of magnetic anisotropies (on piezoelectric crystal).

Chapter 1

Introduction

Moore's law, first announced in 1965 by Gordon E. Moore [Moo65] and later recalculated, says that the transistor density on a semiconductor chip doubles roughly every two years. At this rapid development, the physical limit in lithographical patterned devices will be reached soon. In order to fulfill Moore's law, the semiconductor industry arranges best efforts to improve existing technologies and to search for new materials. One of the unconventional approaches is suggested by the Spintronics. The concept is based on the fusion of *spin* and *electronics*, which combines spin and charge properties of the electron. Up to now, both properties are exploited separately in magnetic storage devices and computer chips. The implementation of this concept is embodied by a class of materials, called ferromagnetic semiconductors (FS) or diluted magnetic semiconductors (DMS). A device out of the FS material circumvents the present low spin injection at the interface between ferromagnetic metal and semiconductor where spin-scattering occurs due to the Schottky-barrier. Besides, a high spin lifetime is preferable.

(Ga,Mn)As is a prototypical FS and has been investigated since the first publication in the mid-90ies by H. Ohno [Ohn96]. The establishment of LT-MBE growth of GaAs with doping of magnetic Mn acceptors has unbosomed a multitude of transport-related phenomena [Die00]. The ferromagnetism in (Ga,Mn)As is mediated by delocalized holes provided by Mn acceptors, which couple antiferromagnetically to the magnetic moments of Mn acceptors. Relatively low ferromagnetic transition temperatures at maximum $T_C \approx$ 190K are prevalent due to strong compensation effects by high defect densities which originates from LT-growth and degrades (Ga,Mn)As material to a model system of a FS [Ole08, Wan08, Che09].

The strongly anisotropic valence band structure and its resulting magnetic anisotropies are strongly influenced by semiconductor properties like lattice strain and hole density, as well as temperature. Controlling one up to all parameters enables to change magnetic properties [She97, Abo01, Die01, Saw04]. A powerful approach to control magnetism for fundamental studies and future applications would be to locally and reversibly change magnetic properties by electrical gating of very thin (Ga,Mn)As layers with tunable hole density [Sto08]. The effect increases with a decrease of (Ga,Mn)As layer thickness and/or Mn content x. So far, however, the fabrication of such thin (Ga,Mn)As layers with a rather

low x but electrical conductance at low temperature (LT) is still a challenge.

The objective of this thesis is mainly focused on an improvement of very thin (4 nm) (Ga,Mn)As layer properties, possibly exploitable for future low-voltage control of magnetic anisotropy in a p-n junction device, comparable to [Ole08]. Thereby, a parabolical Mn profile is developed for an effective (Ga,Mn)As layer thickness of 4 nm, realized by the MBE growth technique. The aim is essentially linked to a deeper understanding of the influence of growth parameters on structural, electrical and magnetic properties, discussed for bulk (Ga,Mn)As material. The outline of this thesis is as follows:

Chapter 2 introduces the FS (Ga,Mn)As with its structural properties and concept of ferromagnetism. The band structure and influences on the hole density and resulting valence band bending for bulk and thin (Ga,Mn)As layers will be discussed in terms of simplified self-consistent band alignment calculations by $Nextnano^3$. Magnetic anisotropies and transport properties of (Ga,Mn)As will be presented at the end of this chapter.

Chapter 3 starts with an extensive description of the epitaxial growth of (Ga,Mn)As material by the MBE technique and introduces point defects like As antisites As_{Ga} and Mn interstitials Mn_{int}. It is followed by the description of the epitaxial growth of (Ga,In)As, (Al,Ga)As and AlAs compound semiconductors. In-situ RHEED, ex-situ HRXRD, SQUID magnetometry as well as RT- and LT-transport characterization methods will be presented.

Chapter 4 is divided in two parts. First, the epitaxial growth of 70 nm bulk (Ga,Mn)As material has been investigated by in-situ and ex-situ characterization methods in terms of the influence of growth parameters like substrate temperature T_{sub} and BEP ratio ($\frac{As_4}{Ga}$) on material properties. The findings have been used for very thin layers in Chapter 5. The second part introduces first efforts of epitaxial growth of very thin $\leq$10 nm (Ga,Mn)As layers at the EPIII department of the University of Würzburg. Influences of a capping layer as well as layer thickness variations have been investigated. The chapter closes with a LT-transport experiment where the magnetic properties of a thin (Ga,Mn)As layer have been electrically controlled by a ferroelectrical gate.

Chapter 5 manifests a new design for the Mn profile in a very thin layer with effective thickness of 4 nm. The MBE technique has been examined carefully to realize such Mn profile, followed by a general calculation of a parabolical Mn concentration profile in an arbitrary layer thickness. Parabolic layers, epitaxially grown at standard growth conditions and varied in nominal Mn content, have been experimentally investigated and compared to 4 nm and 70 nm (Ga,Mn)As layers with homogeneous Mn profile and nominal Mn content of $x = 0.040$. Additionally, growth conditions have been optimized for parabolical graded layers with a Mn content of $x = 0.025$. Finally, a parabolically graded layer has been embedded in a p-n structure and characterized by SQUID measurements.

Chapter 6 demonstrates an application of an induced magnetic anisotropy of a bulk (Ga,Mn)As layer by an epitaxial lift-off (ELO) process. Biaxial preferred magnetization directions in [100] and [010] crystal directions change after the lift-off process of the (Ga,Mn)As layer due to strain release. A (Ga,In)As stressor layer underneath elongates the (Ga,Mn)As layer to induce a tensile strain, resulting in a changed preferred magnetization direction along [001] crystal direction. The samples have been investigated by HRXRD and SQUID.

Chapter 2

The Ferromagnetic Semiconductor (Ga,Mn)As

This chapter will introduce the diluted magnetic semiconductor (Ga,Mn)As. First of all, the ferromagnetic properties will be discussed, followed by simplified calculations of band structure. The valence band structure is strongly anisotropic and coupled with the magnetic anisotropy. In the last section, the magnetic anisotropies and transport properties of (Ga,Mn)As material are presented, which are of importance in this thesis.

2.1 Ferromagnetic Properties

The diamagnetic III-V compound semiconductor GaAs crystallizes in a zinc blende structure, as shown in Figure 2.1(a). It consists of two face-centered cubic sublattices, shifted by $[\frac{1}{4},\frac{1}{4},\frac{1}{4}]$ with respect to each other along the body diagonal. At $T = 0\ K$, it has a direct bandgap of 1.52 eV, whereas the direct bandgap at RT is 1.42 eV.

By doping the GaAs crystal with Mn atoms, the Mn substitutes Ga on the cationic sites of the lattice, described as Mn_{sub}. If the Mn doping concentration is much below 1 %, the Mn is an isolated impurity and acts as a shallow acceptor with a binding energy of about 113 meV [Lin97]. The Mn is not isovalent to the substituted Ga and the impurity is left back in Mn^{2+} valence configuration with a localized magnetic moment of spin S = 5/2, according to its half-filled d-shell. So it provides a loosely bound hole as a charge carrier. In principle, two magnetic moments of the Mn couple antiferromagnetically. But with the fact, that this is a weak interaction in combination with a low dilution of Mn in the host material, a very small or rather no magnetic ordering takes place. The more important exchange interaction between itinerant valence band holes (*sp* states) and localized moments of the Mn atoms (*d* states) is supposed to be antiferromagnetic [Fur88].

The mechanism of hole-mediated ferromagnetism in (Ga,Mn)As with respect to the Mn concentration is illustrated in Figure 2.1(b). In the upper picture, the (Ga,Mn)As material shows isolating transport behavior with a Mn content $\ll 1$ %. Due to the weak interaction between Mn spins, the spin orientation is randomly distributed. No macroscopic

ferromagnetic ordering takes place. With increasing Mn concentration up to about 1 %, the so-called Metal-Insulator Transition (MIT) is reached, as seen in the middle picture of Figure 2.1(b). There is some overlap of the Mn impurities and delocalized hole wave functions. Insulating regions in the (Ga,Mn)As material system are chiefly present but holes hop between regions of ferromagnetic ordering. The resulting current path is very inhomogeneous. The transition between insulating regions to a long-range ferromagnetic order in the (Ga,Mn)As layer is given for an increased Mn content of $\gtrsim 2$ %. This state is illustrated in the lower picture of Figure 2.1(b). Delocalized holes and Mn spin wave functions are overlapping in long-range. As a result, the (Ga,Mn)As material behaves metallic in electrical transport.

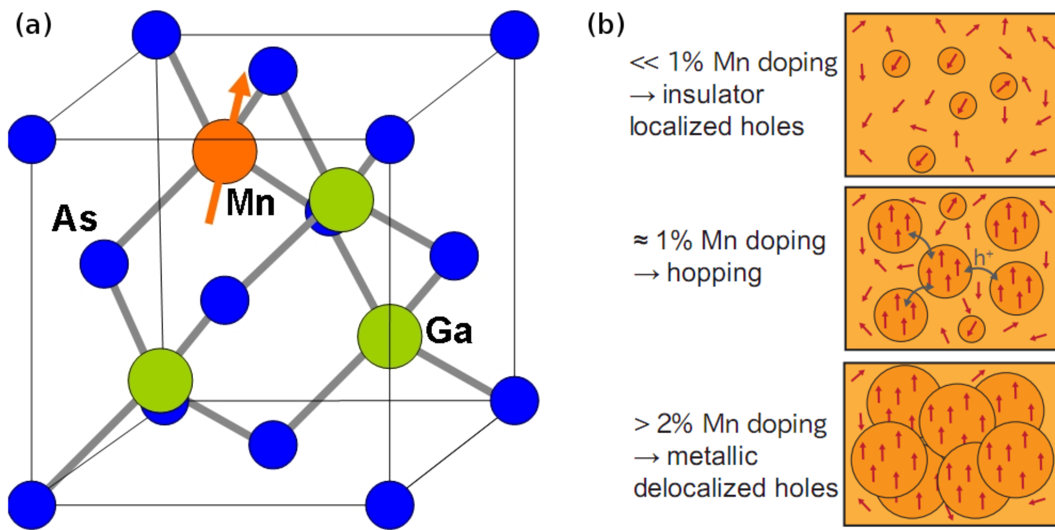

Figure 2.1: (a) GaAs unit cell in zincblende configuration with substitutional Mn on a Ga site. (b) Simplified illustration of carrier induced ferromagnetism in (Ga,Mn)As with respect to Mn concentration. The top picture shows the case with Mn concentration much lower than 1 % with localized hole at Mn impurity and insulating character of (Ga,Mn)As. The middle picture represents the metal-insulator transition at around 1 % of Mn concentration with delocalized, hopping carriers (holes h^+). At higher Mn concentrations $\gtrsim$2%, (Ga,Mn)As shows long-range ferromagnetism due to the coupling between Mn impurity and itinerant holes (from [Mar11a])

Besides the intended incorporation of Mn atoms on substitutional sites, a small fraction of the Mn is randomly incorporated on interstitial sites, so-called Mn interstitials Mn_{int}. A second type of defect caused by low temperature growth of (Ga,Mn)As is arsenic antisites As_{Ga}, where a small fraction of As atoms resides on Ga sites during the epitaxial growth. Both defects are known to have a double donor characteristic and compensate the hole density p, provided by Mn acceptors.

Due to the larger atomic radius of Mn compared to Ga as well as the incorporation of Mn_{int} and As_{Ga} into the GaAs crystal, the lattice constant of (Ga,Mn)As material $a_{(Ga,Mn)As}$ is increased with Mn content as well as Mn_{int} concentration. The epitaxial growth of (Ga,Mn)As on GaAs results in a lattice-matched (pseudomorphic) layer, i.e. the

lateral lattice constant $a_{lay} = a_{GaAs}$ is given by the GaAs substrate. According to volume conservation (Poisson effect), the (Ga,Mn)As layer is compressively strained in-plane and tensile strained out-of-plane.

The growth-induced strain in (Ga,Mn)As has in principle a strong impact on the magnetic properties. For in-plane compressively strained material, (Ga,Mn)As layers are epitaxially grown on a material with smaller lattice constant e.g. on a GaAs substrate. In case of in-plane tensile strain in (Ga,Mn)As layers, it has to be grown on a material with a higher lattice constant than (Ga,Mn)As such as on an InP substrate or on strain-relaxed InGaAs buffers. (Ga,Mn)As layers with in-plane compressive strain have an in-plane magnetic anisotropy. In-plane tensile strained (Ga,Mn)As layers have a preferential magnetic axis out-of-plane.

The most widely used and accepted theoretical description of the carrier mediated ferromagnetism in (Ga,Mn)As is the p·d mean-field Zener model, proposed by T. Dietl [Die00]. This theory correlates the Mn content and hole carrier concentration, among other things, with the Curie temperature T_C. The transition from the ferromagnetic to the paramagnetic phase in (Ga,Mn)As layers is described at

$$T_C = C \cdot N_{Mn} \cdot \sqrt[3]{p}. \tag{2.1}$$

The Curie temperature T_C depends on a parameter C which includes the coupling between localized Mn moment and delocalized hole state, the substitutional manganese concentration Mn_{sub} and the cubic root of the free hole concentration p.

In principle, high T_C values can be achieved by an increase of the Mn content and free hole concentration p. In reality, imperfections like the double donors Mn_{int} and As_{Ga} are incorporated during the epitaxial growth of the (Ga,Mn)As crystal which leads to a reduction of holes as well as a reduction of Mn concentration Mn_{sub}. In this thesis, an investigation has been performed to reduce compensating defects by optimizing growth conditions for very thin layers.

As seen in Equation 2.1, there is a direct correlation between valence band properties (holes p) and magnetic properties (Curie temperature T_C). In the following sections, the band structure as well as the magnetic properties will be introduced.

2.2 Band Structure

The starting point of the valence band structure description in (Ga,Mn)As is a GaAs host crystal which is plausible due to the p-type doping with a few percent of Mn. To follow up the qualitative explanation of hole-mediated ferromagnetism in (Ga,Mn)As as shown in Figure 2.1(b), a simplified picture of the band structure related to Mn doping is presented in Figure 2.2.

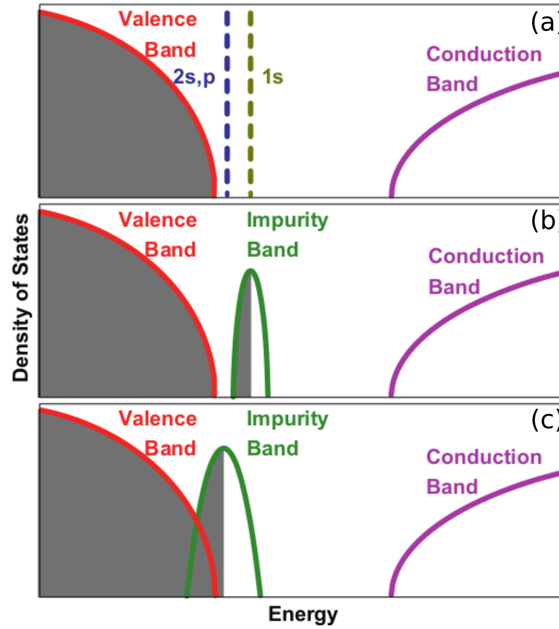

Figure 2.2: Diagram of the (Ga,Mn)As band structure with impurity band related to Mn doping: (a) Two hydrogenic states of an acceptor state in the band gap of GaAs. (b) With increasing Mn-doping density the acceptor states of the impurity band broadens. (c) The impurity band (acceptor states) merges with the valence band (hole states) for sufficiently high Mn doping concentration. The (Ga,Mn)As material is degenerated. [Bur08]

In case of a very low Mn doping $x \ll 0.01$ and in the limit of T $\rightarrow 0$, holes donated by Mn acceptors occupy hydrogenic bound states, as seen in Figure 2.2(a). The doped semiconductor (Ga,Mn)As is an isolator. The bound states overlap with increasing doping density, resulting in a broadening of states. An impurity band is formed, as shown in Figure 2.2(b). The valence band and impurity band are still seperated and the impurity band is near the s1 state of the original acceptor. The width of the impurity band is well defined by the average overlap of the hole carriers on different acceptor sites.

In the metallic doping regime $x \gtrsim 0.015$, (Ga,Mn)As behaves like a metal. It is assumed, that the Coulomb attraction of the holes to the acceptors is completely screened resulting in a shift of the impurity band into the valence band. It implies, that holes now occupy Bloch states and do not form bound states with the acceptors.

The valence band structure around the Γ-point ($k = 0$) can be described by the k·p perturbation theory and symmetry considerations. At the Γ-point, this theory is exact in the order of k^2 due to the quadratic approximation of the energy-momentum ($E - k$) relationship

$$E(k) = \frac{\hbar^2 k^2}{2m^*}, \tag{2.2}$$

where m^* is the associated effective mass [Sze07]. The influencing effects on the valence band structure can be expressed in form of Hamiltonians. In the following, the k·p perturbation theory is barely broached. More details of the band structure in (Ga,Mn)As is described in [Die01, Abo01, Sch06, Wen08]. It can be pointed out, that the sum of Hamiltonians $\mathcal{H}_{sum}$ can be written as

$$\mathcal{H}_{sum} = \mathcal{H}_{KL} + \mathcal{H}_{BS} + \mathcal{H}_{pd} \tag{2.3}$$

and diagonalization of $\mathcal{H}_{sum}$ leads to the calculated valence band structure of (Ga,Mn)As. The three different contributions of $\mathcal{H}_{sum}$ are as follows:

The valence band structure of the first six valence bands of pure GaAs is described by the 6×6 Kohn-Luttinger Hamiltonian $\mathcal{H}_{KL}$. Typical GaAs values of the phenomenological Kohn-Luttinger parameters $\gamma_1 = 6.85$, $\gamma_2 = 2.1$, $\gamma_3 = 2.9$ as well as the spin-orbit splitting $\Delta_{SO} = 0.341\ eV$ are taken into account [Vur01]. $\mathcal{H}_{KL}$ includes three two-fold degenerated valence bands, namely heavy-hole (hh), light-hole (lh) and split-off (so) bands. The direction-dependend effective masses are $m^*_{hh} = 0.5m_e$, $m^*_{lh} = 0.08m_e$ and $m^*_{SO} = 0.15m_e$, as stated in [Abo01].

The biaxial strain situation in (Ga,Mn)As layers grown on GaAs substrates which leads to an in-plane compressive strain is treated in $\mathcal{H}_{BS}$. For a detailed description of this Hamiltonian, see [Bir74].

The $p - d$ hybridization of the valence band hole and the Mn ion results in a spin-dependent coupling between holes and Mn ions. In terms of a Hamiltonian, this correlation is expressed as $\mathcal{H}_{pd} = -\beta N_0 \mathbf{s} \times \mathbf{S}$. β is the $p-d$ exchange integral, N_0 is the concentration of the cationic sites, s corresponds to the hole spin and S is the Mn spin, as mentioned in [Die01]. The expression for $\mathcal{H}_{pd}$ has a negative value due to the antiferromagnetically coupling of valence band hole p-state and Mn d-state. The exchange energy amounts to $\beta N_0 \approx -1\ eV$.

An important result of the theoretical description contains a splitting of the double degenerated valence bands SO, hh and lh, influenced by strain and $p - d$ coupling of valence band holes and Mn ions. The characteristics of every energy band $E_n(k)$ exhibit a k direction dependence which is connected to its density of states $D(E)$ within the following formalism

$$D_n(E) = \int\limits_{E_n(k)} \frac{1}{4\pi^3 \left|\bigtriangledown E_n(k)\right|} dS_E, \tag{2.4}$$

where the index n embodies the n-th energy band and dS_E is an infinitesimal element of the energy surface.

In (Ga,Mn)As material, the hole density is relatively high in the range of 10^{20} to 10^{21} cm^{-3} with Mn doping of $x > 0.02$. Thus, heavy-hole and light-hole subbands are occupied. The strongly anisotropic valence band structure in (Ga,Mn)As is coupled to its magnetic anisotropy because the hole carriers do not only participate in electrical transport but also mediate the long-range ferromagnetism, as will be presented in Chapter 2.3. The band structure is mainly influenced by lattice strain, hole density and also temperature. Controlling one up to all of these parameters enables to change the magnetic properties as shown in [She97, Abo01, Die01, Saw04]. It has been shown successfully, that e.g. uniaxial strain relaxation of nanopatterned stripes leads to a significant change in preferred axis of magnetization.[Wen07, Pap07b]. Changes in temperature for a given (Ga,Mn)As material lead also to changes in its magnetic properties [Pap07]. Additionally, tuning the hole density can change magnetic properties of (Ga,Mn)As, as shown in [Saw05].

Another powerful approach to control magnetism for fundamental studies and future applications would be to locally and reversibly change magnetic properties with tunable hole densities by electrical gating of very thin ($< 10\ nm$) (Ga,Mn)As layers. First promising results have been published by [Sto08, Rie09], where T_C in a thin (Ga,Mn)As layer has been changed about 6 to 7 K by accumulation or depletion of the hole density with help of a non-volatile, polarized ferroelectrical gate. So far, the fabrication of such thin (Ga,Mn)As layers with a rather low amount of Mn but electrical conductance at low temperature (LT) is still a challenge, as will be shown in Chapter 4.2.

The next section will give an insight into different effects which influence the valence band edge of (Ga,Mn)As material.

2.2.1 Self-Consistent Calculations of Band Alignment and Hole Density

Point defects like As_{Ga} and Mn_{int} which arise during the epitaxial growth at non-thermal equilibrium growth conditions for the ferromagnetic (Ga,Mn)As material as well as surface and interface states lead to a significant valence band bending of very thin (Ga,Mn)As layers ($< 10\ nm$) and severe compensation of hole concentration p.

In order to estimate and illustrate the band alignment in (Ga,Mn)As as well as the hole density p, the numeric semiconductor simulation software $nextnano^3$ has been used within the framework of this thesis. In the following, an overview of the basic equations and the numerical procedure of $Nextnano^3$ is presented for self-consistent band alignment and hole density calculations. Here, a 1-d device geometry along the growth direction z is considered. Details about the software can be found in [Nex11]. The physical background of the band structure calculation is the envelope function approximation [Sze07].

It is assumed, that electrons and holes of conduction and valence bands obey the 1-d Schrödinger equation

$$\left[-\frac{\hbar^2}{2m^*}\frac{\partial^2}{\partial z^2}+V(z)\right]\psi(z)=E(z)\psi(z), \tag{2.5}$$

where m^* is the effective mass for an electron or hole and $V(z)$ represents a material dependent potential which is periodic in the real lattice space and corresponds to the long-range material potential by neglecting individual impurities in the lattice. Solutions for the wave function $\psi(z)$ of Equation 2.5 represent a Bloch function

$$\psi(z)=U(z)e^{ikz}, \tag{2.6}$$

where $U(z)$ is a periodic function caused by the periodicity of the lattice. $\psi(z)$ describes an envelope function and covers only the long-range variation of the probability density. Furthermore, carriers are assumed to be in thermal-equilibrium conditions which means that holes and electrons can be described by spatially varying quasi Fermi levels $E_{F,p}$ and $E_{F,n}$. Below, both types of carriers are discussed for the sake of completeness while for the (Ga,Mn)As material only the hole carrier-related part of equations matters. The Poisson equation in one dimension is of the form of

$$-\frac{1}{e}\frac{\partial}{\partial z}\left[\epsilon_0\epsilon_r(z)\frac{\partial\psi(z)}{\partial z}\right]=p(z)-n(z)+N_A^-(z)-N_D^+(z), \tag{2.7}$$

where e is the elementary charge, ϵ_0 is the dielectric constant, ϵ_r is the material dependent dielectric constant, $p(z)$ and $n(z)$ are the hole and electron densities, $N_A^-(z)$ and $N_D^+(z)$ are the densities for ionized acceptors and donors. Both ionized impurity densities can be related to the total amount of acceptor and donor densities N_A and N_D as

$$N_A^-(z)=\frac{N_A(z)}{1+g_Ae^{\frac{E_A-E_{F,p}(z)}{kT}}} \tag{2.8}$$

and

$$N_D^+(z)=\frac{N_D(z)}{1+g_De^{\frac{E_{F,n}(z)-E_D}{kT}}}, \tag{2.9}$$

where $g_A=4$ and $g_D=2$ correspond to the degeneracy of acceptor and donor levels, $E_{F,p}$ and $E_{F,n}$ are the local Fermi energies for holes and electrons, E_A and E_D are the acceptor and donor ionization energies.

The hole current density in the one-dimensional case is given as

$$j_p(z)=q\mu_pp(z)\frac{\partial\psi(z)}{\partial z}-qD_p\frac{\partial p(z)}{\partial z}=q\mu_p\left(p(z)\frac{\partial\psi(z)}{\partial z}-\frac{kT}{q}\frac{\partial p}{\partial z}\right)=\mu_pp(z)\frac{\partial E_{F,p}}{\partial z} \tag{2.10}$$

and in similar form for the electron current density

$$j_n(z) = q\mu_n n(z)\frac{\partial\psi(z)}{\partial z} + qD_n\frac{\partial n(z)}{\partial z} = q\mu_n\left(n(z)\frac{\partial\psi(z)}{\partial z} + \frac{kT}{q}\frac{\partial n}{\partial z}\right) = \mu_n n(z)\frac{\partial E_{F,n}}{\partial z}, \quad (2.11)$$

where μ_p, μ_n, D_p and D_n are the mobilities and diffusion coefficients for holes and electrons. The right hand side of the current density Equations 2.10 and 2.11 are related to the quasi Fermi levels for holes ($E_{F,p}$) and electrons ($E_{F,n}$).

In case of steady-state conditions where carrier generation and recombination are neglected, the current densities for holes and electrons are given as

$$\frac{\partial j_p(z)}{\partial z} = 0 \quad (2.12)$$

and

$$\frac{\partial j_n(z)}{\partial z} = 0. \quad (2.13)$$

These equations relate the local carrier densities to the local Fermi levels of holes and electrons.

In principle, the *nextnano*^{3} software solves iteratively this system of equations in two steps. Poisson- and Schrödinger Equations 2.7 and 2.5 are solved first for a fixed, local quasi Fermi level to calculate the local carrier densities. The second step solves the current density Equations 2.10 and 2.11 by using the calculated carrier densities in order to calculate the new quasi Fermi level for holes and electrons. Steady-state condition and self-consistency respectively is reached when sequenced iterations lead to similar results.

The above described equations are valid for non-degenerate semiconductors. The self-consistent calculation of the band alignment in (Ga,Mn)As with p-doping in the range of 10^{20} to 10^{21} cm^{-3} by *nextnano*^{3} has been performed with the following simplifications:

- Chapter 2.2 shows, that the Mn doping in (Ga,Mn_x)As is in the range of $x \geq 10^{20}$ cm^{-3}. As a result, the impurity band is broadened and merges with the valence band edge, as illustrated in Figure 2.2. Consequently, the impurity states are no longer seperated from the valence band states and Equation 2.8 becomes invalid. *nextnano*^{3} does not treat such band mixing. The ionization energy of shallow Mn acceptor states is ≈ 0.1 eV [Sze07]. In order to bypass incomplete ionization of Mn acceptors due to a smaller thermal energy at RT of 0.025 eV, the ionization energy has been set to a value, where the acceptors are assumed to be fully ionized. An ionization energy of -1.5 eV was sufficient in these simplified calculations to achieve complete ionization.

- Magnetoresistive effects (MRs) which lead to changes of the current densities, are neglected. These effects originate from external applied magnetic fields or internal magnetic fields caused by an alignment of Mn magnetic moments in (Ga,Mn)As. Equations 2.10 and 2.11 do not include such effects in the presented simulations.

Later on, Chapter 2.3 will give an overview of important MRs in (Ga,Mn)As within the framework of this thesis.

- The inhomogeneous Mn distribution in very thin (Ga,Mn)As layers $d \leq 10\ nm$ is one of the critical factors causing a reduced conductivity compared to bulk layers. As illustrated in the middle picture of Figure 2.1 (b) in Chapter 2.1, a very thin layer has an inhomogeneous Mn distribution per area, i.e. regions with more Mn atoms compared to regions with less Mn atoms are prevalent. The first instance results in a metallic transport behavior whereas the latter case leads to hopping of hole carriers up to insulating transport behavior. As mentioned before, a 1-d device geometry with variation along the growth direction z is assumed. Thus, lateral inhomogeneities of Mn composition and impurity densities as well as interface roughnesses are neglected in the simulations.

- The p-compensation is merely simulated by the incorporation of arsenic antisites As_{Ga} with a deep donor level (impurity band) of $\sim$0.5 eV above the valence band, according to [Fee93, Gra00, Lod03]. It is assumed, that the As_{Ga} defect has a double donor character, i.e. one As_{Ga} impurity compensates two holes. The As_{Ga} concentration in LT-GaAs grown at a substrate temperature $T_{sub} = 270°\mathrm{C}$ and BEP ratio $(\frac{As_4}{Ga}) = 25$ is estimated to be $3.7 \cdot 10^{19} cm^{-3}$, according to the calibration curve at $x = 0.00$ in Figure 3.13 of Chapter 3.3. For standard bulk (Ga,$Mn_{0.04}$)As material, hole compensation is assumed to be about 70%, i.e. $[As_{Ga}] = 3.1 \cdot 10^{20} cm^{-3}$. An alternative way to estimate $[As_{Ga}]$ is described in Chapter A.1. In order to include the double donor characteristic of As_{Ga} in band alignment simulations, the implemented $[\mathrm{As}_{Ga}]$ has been multiplied by a factor of 2.

  Mn_{int} impurities also act like a double donors, as predicted in [Mac02]. Mn interstitials reduce the total magnetic moment by antiferromagnetic coupling of their spin moments with the substitutional Mn spin moments. This interaction has not been considered within the simulations. The absolute Mn_{int} density is not exactly known but lies in the order of $10^{20} cm^{-3}$. It is assumed that As_{Ga} and Mn_{int} are in balance to compensate hole carrriers provided by Mn_{Ga}, i.e. a higher As_{Ga} concentration leads to a lower Mn_{int} concentration and vice versa [Sad04].

- Surface states have been simulated by a Schottky barrier, i.e. the Fermi-level at the surface is pinned at the middle of the bandgap. It has been shown experimentally, that LT-GaAs material has a pinned surface Fermi-level at 0.7 eV above the valence band edge [Ohb93].

All of the above listed simplifications have been taken into account for band edge alignment simulations at RT. Furthermore, RT simulations have been preferred to neglect influences of hindered lateral current flows as well as magnetic Mn moments on the (Ga,Mn)As band structure. In the following, band alignment simulations of bulk 70 nm and 4 nm (Ga,$\mathrm{Mn}_{0.04}$)As layers ($[Mn_{Ga}] = 8.84 \cdot 10^{20}\ cm^{-3}$) without or alternatively with a 1 nm LT-GaAs capping layer are presented in Figure 2.3 and 2.4.

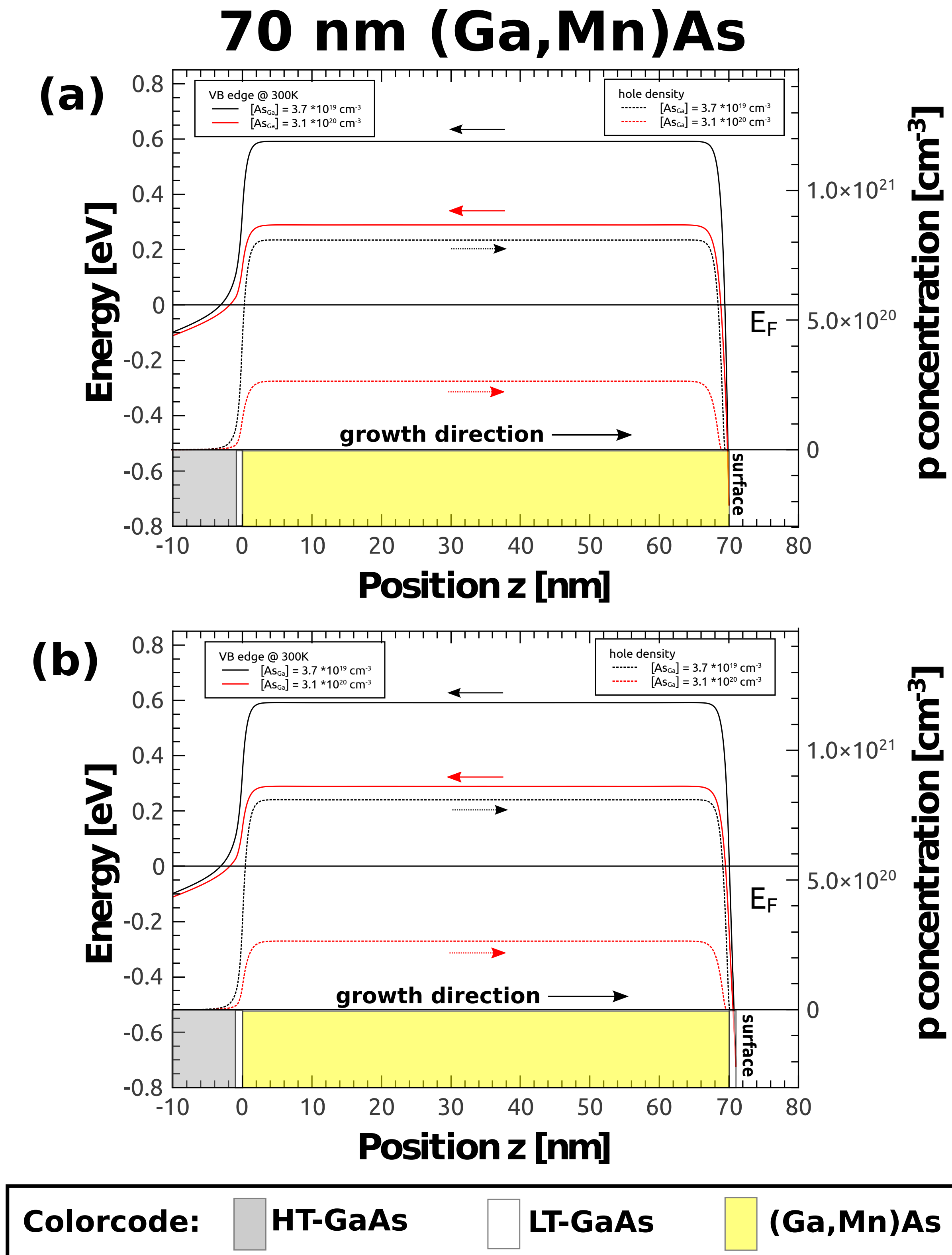

Figure 2.3: *nextnano*^{3} calculations of the valence band edges (solid lines) and free hole distributions (dotted lines) at T=300 K for a 70 *nm* (Ga,Mn$_{0.04}$)As layer without a capping layer (a) or with a 1 *nm* LT-GaAs cap layer (b). The hole carrier compensation has been simulated by [As$_{Ga}$] with concentrations according to LT-GaAs material at standard growth conditions (black color) or about 70% compensation in (Ga,Mn)As material (red color).

The hole compensation in the (Ga,Mn)As material has been modelled in two different ways: In a first simulation run, $[As_{Ga}] = 3.7 \cdot 10^{19}\ cm^{-3}$ is assumed to be the same as defined in LT-GaAs due to LT growth conditions (black lines), corresponding to a p-compensation of 8.5%. In a second simulation run, a typical compensation of 70% (red lines) is defined to be $[As_{Ga}] = 3.1 \cdot 10^{20}\ cm^{-3}$.

Figure 2.3(a) and (b) present the simulation results of the valence band bending (solid lines) as well as its calculated free hole distributions (dotted lines) for bulk 70 nm (Ga,Mn)As material.

The conduction band edge is not shown in these graphs. In principle, it lies about 1.4 eV above the valence band edge at 300 K and does not stay in the focus of interest.

The interface to LT-GaAs as well as the vicinity to the surface have an impact on the VB edge of the (Ga,Mn)As layer, as shown in Figure 2.3(a) and (b). However, the simulations reveal only a local valence band bending in bulk (Ga,Mn)As caused by a very local depletion of hole carriers at the interfaces due to a different Fermi level of LT-GaAs and a pinned Fermi level of the surface. The shape of the VB edge is the same for both degrees of compensation, whereas the 70% p-compensation leads to a shift of the Fermi level within the VB toward the VB edge from 0.592 eV (at 8.5% p-compensation) to 0.289 eV below the VB edge. As expected, the local maximal hole concentration p_{max} is reduced from $p_{max} = 8.09 \cdot 10^{20}\ cm^{-3}$ to $p_{max} = 2.65 \cdot 10^{20}\ cm^{-3}$ with an increased hole carrier compensation from 8.5% to 70%.

In Figure 2.3(b), the 70 nm (Ga,Mn)As layer is capped by a 1 nm LT-GaAs layer. The shape of the VB edge is comparable and p_{max} is the same compared to Figure 2.3(a). However, the slope of the VB edge close to the surface is now shifted 1 nm toward the LT-GaAs cap layer. As a result, the hole area density of $p_{area} = 5.52 \cdot 10^{15}\ cm^{-2}$ and $p_{area} = 1.78 \cdot 10^{15}\ cm^{-2}$ is increased by $\approx 1\%$ in both (Ga,Mn)As layers with 8.5% and 70% p-compensation.

In case of very thin (Ga,Mn)As layers without a capping layer, the VB edges are significally bent with an additional bending within the (Ga,Mn)As layer in contrast to bulk material, as seen in Figure 2.4(a).

Here, a shift of the Fermi level toward the VB edge caused by a higher degree of p-compensation has been calculated from 0.556 eV (for 8.5% compensation) to 0.231 eV (for 70% compensation) below the VB edge, which is 0.036 eV respectively 0.058 eV closer to the VB edge compared to simulated bulk material. Besides, the stronger influence of interface and surface defects is noticeable in the calculated hole densities of the simulated layers. In comparison to bulk (Ga,Mn)As layers without a cap layer and the same degrees of p-compensation (8.5% and 70%), the compensatory influence of the interface and surface defects on the free hole density in 4 nm layers results in 88.1% or 70.6% of bulk p_{max}. The hole area densities within the (Ga,Mn)As layers for a low or high degree of p-compensation are $p_{area} = 1.79 \cdot 10^{14}\ cm^{-2}$ and $p_{area} = 3.56 \cdot 10^{13}\ cm^{-2}$ respectively.

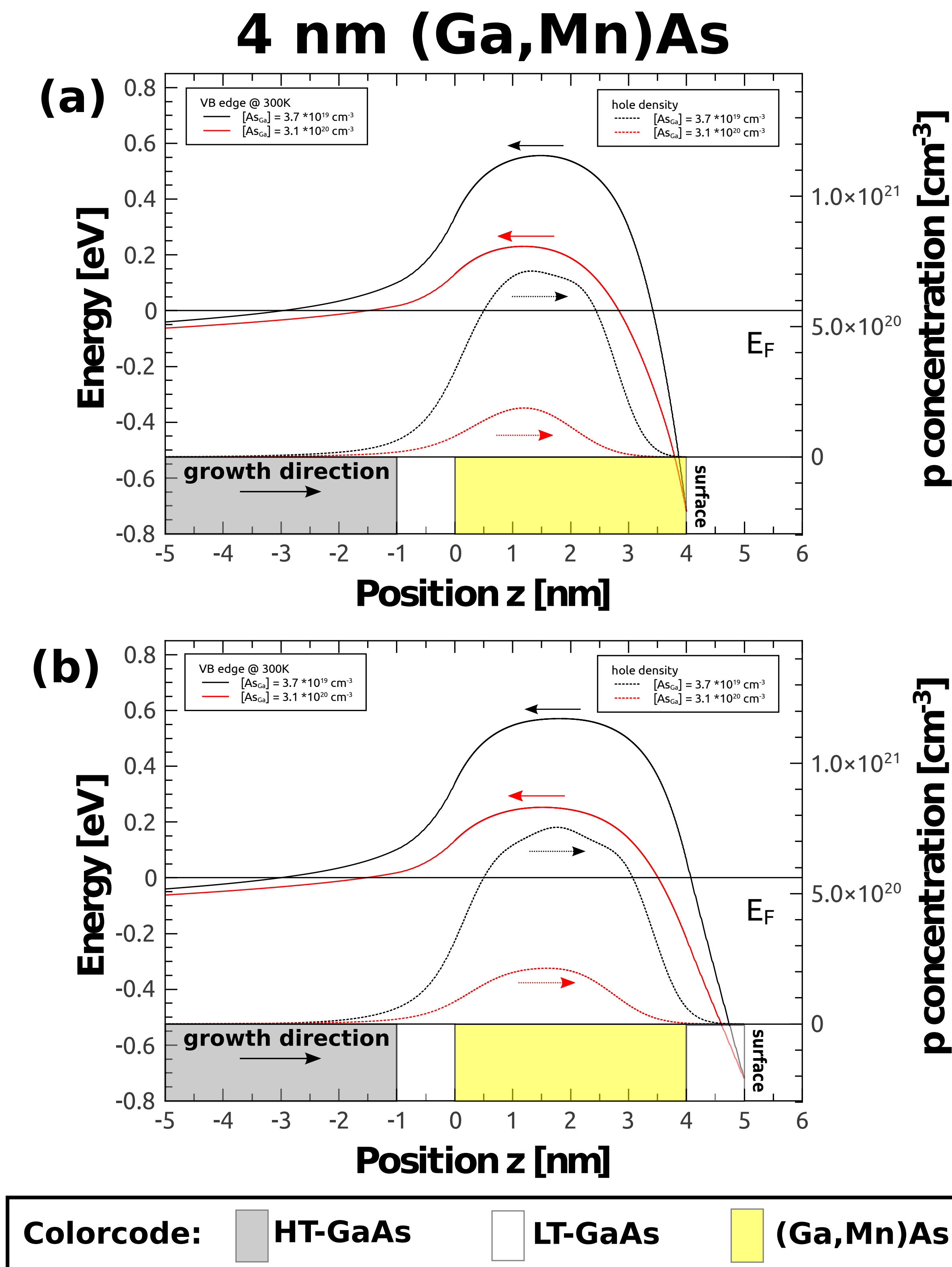

Figure 2.4: *nextnano*^{3} calculations of the valence band edges (solid lines) and hole distributions (dotted lines) at T=300 K for a 4 *nm* (Ga,$Mn_{0.04}$)As layer without a capping layer (a) or with a 1 *nm* LT-GaAs cap layer (b). The hole compensation is simulated according to bulk (Ga,Mn)As material in Figure 2.3.

In contrast to bulk (Ga,Mn)As material, the simulations show a stronger effect of a capping layer on the free hole density, as presented in Figure 2.4(b). The simulations of a 4 nm (Ga,Mn)As layer with a 1 nm LT-GaAs cap layer show higher p_{max} values, which achieve 93.2% or 88.3% of bulk p_{max} values, depending on the p-compensation. Simultaneously, the hole area densities in the (Ga,Mn)As layers are increased by 26.8% and 48.9% to $p_{area} = 2.27 \cdot 10^{14}\ cm^{-2}$ and $p_{area} = 5.30 \cdot 10^{13}\ cm^{-2}$. Additionally, the shape of the hole distribution is broadened in the simulations of the capped 4 nm (Ga,Mn)As layer.
Although the *nextnano*^{3} simulations have been calculated under particular simplifications, they illustrate qualitatively and quantitatively that bulk (Ga,Mn)As layers are in general more robust against interface defects and surface states than very thin ($< 10\ nm$) (Ga,Mn)As layers, which is plausible and later on empirically confirmed in this thesis (see Chapter 4.2). The robustness of bulk material is additionally corroborated by a minimal influence of a LT-GaAs capping layer on the hole density ($\leq +1\%$) in contrast to very thin layers. Quantitative uncertainties of the simulations arise exceedingly from the assumption of fully-ionized Mn-acceptor states. Only delocalized VB hole-states without any localized impurity states, which are present due to the band merging of VB and impurity band, have been considered as Bloch wave functions (Equation 2.6) in these simulations by *nextnano*^{3}. Such calculations without a full ionization of acceptors would result in significant lower hole concentrations compared to the presented simulations. Further, influences of an inhomogeneous Mn incorporation and/or interface roughnesses have not been taken into account in the calculations. They also might have an impact on carrier compensation.

Nevertheless, the simulations show that the compensatory impacts on carriers in a very thin (Ga,Mn)As layer increases for lower hole densities, e.g. in case of a high hole compensation caused by double donors like As_{Ga}. As a consequence of this simulation result, growth optimizations of epitaxially grown (Ga,Mn)As material are considered as an experimentally starting point to reduce compensation of free holes.

In a first step, growth conditions of bulk (Ga,Mn)As layers have been investigated, as presented in Chapter 4.1. Later on, a different non-homogeneous Mn profile has been invented for very thin (Ga,Mn)As layers to improve its magnetic and transport properties. This epitaxially grown layer structure has been investigated in dependence on the Mn content x and growth conditions for a constant x, as presented in Chapter 5. Basic information about the formation of point defects in (Ga,Mn)As and methods to reduce point defect densities are treated in Chapter 3.2.1.

2.3 Magnetic Anisotropy

In theoretical predictions, three equivalent [100] and four [111] crystal directions reflecting the coupling between preferred axes of magnetization (easy axes) and the anisotropy of the crystal via spin-orbit coupling. Easy axes along [111] have never been observed experimentally. Nevertheless, one never deals with pure bulk properties due to the epitaxial growth of (Ga,Mn)As on a substrate which has a different lattice constant resulting in a growth-induced strain within the layer. As shown in the previous Chapter, the strain has an impact on the band structure and also on the magnetic properties, as will be discussed in the following.

In this thesis, (Ga,Mn)As layers have been deposited on semi-insulating GaAs (001) substrates. Therefore, they are compressively strained. It means that the symmetry of (Ga,Mn)As is lowered to D_{2d} resulting in preferred axes of magnetization in the layer plane. A magnetic hard axis is present along the out-of-plane direction [001] at 4.2 K.

The magnetostatic energy E of a magnetic domain can be described by three anisotropy components, as shown in [Pap07], as

$$E = \frac{K_{cryst}}{4} sin(2\vartheta) + K_{uni[\bar{1}10]} sin^2(\vartheta - 135°) + K_{uni[010]} sin^2(\vartheta - 90°) - MH(\vartheta - \varphi), \quad (2.14)$$

where ϑ represents the angle between magnetization orientation and [100] crystal direction and φ corresponds to the angle between the applied magnetic field and the [100] crystal direction. The biaxial magnetic anisotropy component along [100] and [010] crystal directions is embodied by the first term of Equation 2.14. The second and third term represent the uniaxial magnetic components along a [110] or $[\bar{1}10]$ crystal direction and along a [010] crystal direction. The last term corresponds to the Zeeman splitting due to the exchange interaction between the magnetization of the sample and an external applied magnetic field H.

The source of both uniaxial anisotropy terms is still unknown up to now. Experimental determinations of the three anisotropy components offer an insight of the strength among each other, as published in [Gou08, Pap07a]. A typical ratio of the anisotropy terms is

$$K_{cryst} : K_{[\bar{1}10]} : K_{[010]} = 100 : 10 : 1. \quad (2.15)$$

It is worth to mention that the biaxial anisotropy scales with the magnetization as M^4, whereas the uniaxial anisotropy scales with M^2, as predicted theoretically in [Cal66]. Thus, with increasing temperature up to T_C and decreasing M the dominant anisotropy changes from biaxial to uniaxial.

2.3.1 Transport Properties

Ferromagnets and in particular (Ga,Mn)As as a ferromagnetic semiconductor evince an anisotropic transport behavior. In order to investigate the transport properties and anisotropy components of (Ga,Mn)As layers, Hallbar structures are the method of choice to record

the longitudinal and transverse four probe resistances as a function of an applied magnetic field.

An external magnetic field influences charge carriers of a layer resulting in changes of the conductivity. This impact is called magnetoresistive effect (MR). In this thesis, the negative magnetoresistance (NMR) and the anisotropic magnetoresistance (AMR) play a significant role in transport measurements of (Ga,Mn)As layers without and with applied magnetic field and thus are presented in the following. Additionally, the normal and anomalous Halleffect are discussed to demonstrate the difficulty of determining the free hole concentration in (Ga,Mn)As. An extensive overview of all magnetoresistive effects besides NMR and AMR, like giant magnetoresistance (GMR), tunneling magnetoresistance (TMR), colossal magnetoresistance (CMR) and extraordinary magnetoresistance (EMR), is presented in [Gro04].

Negative Magnetoresistance

Ferromagnetic transition metals like iron, nickel and cobalt show a stronger drop of resistance below the Curie temperature T_C with decreasing temperature compared to non-magnetic transition metals like palladium. A plausible explanation of such behavior has been given by Sir N. F. Mott [Mot64]. Figure 2.5 shows the splitting of d-band of a transition metal at a temperature T below T_C.

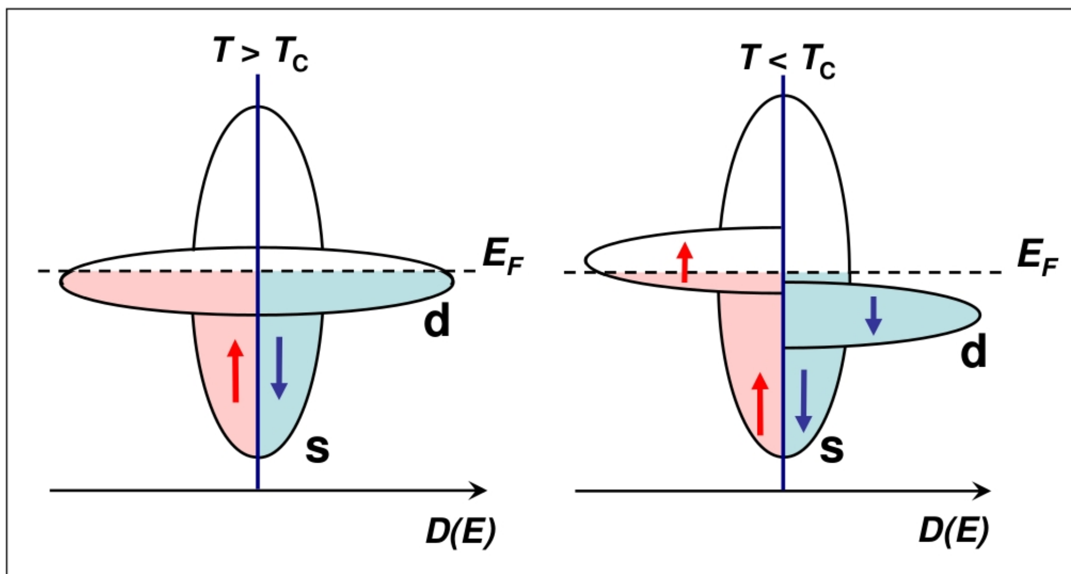

Figure 2.5: Illustration of d-band splitting in a transition metal due to finite exchange interaction. Adopted from [Gro04].

As seen in Figure 2.5(a) with $T > T_C$, the main contribution of the electric current in transition metals originates from electrons of the s-band due to its low effective mass. The resistivity results from scattering of the s-band electrons into free states of the d-band at the fermi edge E_F. A high density of d-band states leads to a high scattering

rate and therefore to a high resistivity. When the transition metal is in the ferromagnetic phase at $T < T_C$ in Figure 2.5(b), the d-subbands of minority and majority spins are split caused by finite exchange interaction and tending to a shift of the subband of the majority spin below E_F and a shift of the minority spin subband above E_F. The quantity of occupied d-states decreases with reducing temperature. Consequently, s-band electrons of the majority spin cannot be scattered into d-states. The result is a higher mobility and a lower resistivity caused by the increase of spin alignment. This effect is isotropic and therefore not sensitive to the current direction with respect to the magnetization direction. In principle, the measurement of the cooling curve in a cryostat with a temperature sensor can be used to determine T_C, as shown in Chapter 4.2.3.

Applied external magnetic fields can lead to a higher spin alignment resulting in a further reduction of resistivity at a constant temperature T. This negative magnetoresistance effect is also isotropic and thus independent of current, magnetization and applied magnetic field directions. The model of Mott can explain the change of resistivity due to spin alignment in ferromagnetic metals but neglects inelastic scattering caused by spin fluctuations. In a two-current model proposed by I. A. Campbell and A. Fert, the resistivity of a ferromagnetic metal is described by a parallel circuit of two line channels of minority and majority spin charge carriers. This model considers inelastic scattering at magnons and the exchange interaction between the two channels [Gro04].

Anisotropic Magnetoresistance

(Ga,Mn)As possesses a very strong anisotropic magnetoresistance (AMR) effect manifesting in a higher resistivity $\rho_\perp$ due to a current flow perpendicular to the magnetization compared to a lower resistivity $\rho_\parallel$ in case of a current flow parallel to the magnetization [Bax02]. It is a negative AMR in contrast to metallic ferromagnets which show positive AMR. As a consequence of the AMR, resistivity ρ is a tensor and the electric field $\mathbf{E}$ with respect to the current $\mathbf{J}$ parallel or perpendicular to the magnetization $\mathbf{M}$ can be expressed by using Ohm's law

$$\mathbf{E} = \rho_\perp \mathbf{J}_\perp + \rho_\parallel \mathbf{J}_\parallel. \tag{2.16}$$

Considering the projection onto the current flow direction, the longitudinal resistivity ρ_{xx} is [Jan57, McG75]

$$\rho_{xx} = \rho_\perp - (\rho_\perp - \rho_\parallel) cos^2(\varphi), \tag{2.17}$$

where φ is the angle between magnetization $\mathbf{M}$ and current direction $\mathbf{J}$. As can be seen by Equation 2.17, a rotation of the in-plane magnetization by applying a high magnetic field results in a sinusoidal change of longitudinal resistance ρ_{xx} with respect to φ (fixed $\mathbf{J}$ direction).

Anisotropy Fingerprint Measurements

The anisotropy fingerprint measurement technique has been developed by K. Pappert et al. to determine the anisotropy components of Equation 2.15 [Pap07a]. The process of compiling an anisotropy fingerprint includes a number of four terminal longitudinal resistance measurements (as seen in Figure 2.6(a) with applied magnetic field along different crystal directions. The magnetic field is swept from - 300 mT to + 300 mT along a direction with an angle φ referred to the current direction. Such a scan is repeated several times for different angles from $\varphi = 0°$ to $\varphi = 360°$ to compile a complete anisotropy fingerprint.

Figure 2.6 presents an example of a simulation of a magnetoresistance scan along an angle $\varphi = 70°$ for the magnetic field with respect to the current direction along [100] and the conversion to the full anisotropy fingerprint.

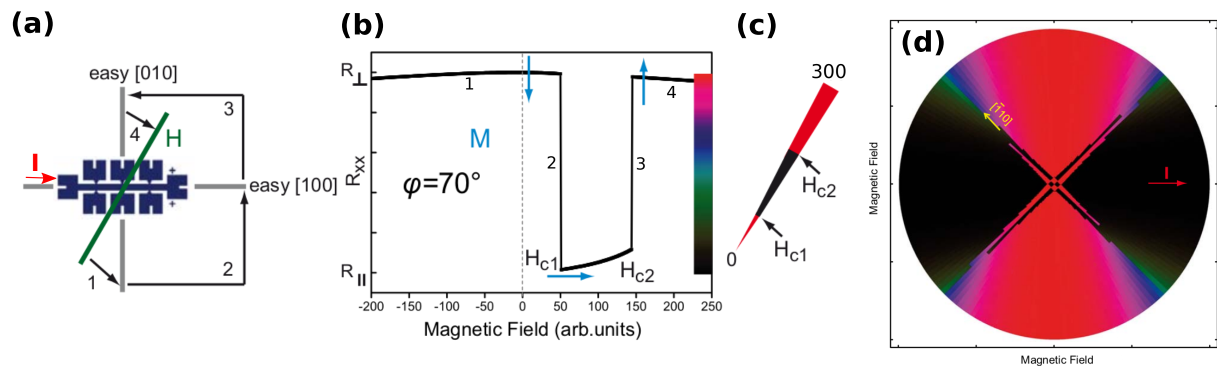

Figure 2.6: (a) Standard 4-terminal Hall-bar geometry with current direction along [100], easy axes along [100] and [010] and magnetic field direction (green line). (b) Simulated magnetoresistance scan along $\varphi = 70°$ with two switching events H_{C1} and H_{C2} corresponding to the two subsequent 90° domain wall propagation events. (c) Convertion to a sector of a resistance polar plot. (d) Full 360° simulation of the resistance polar plot composed of multiple sectors. The direction of the current flow is indicated as a red arrow. Adopted from [Gou08].

In case of high negative fields, the direction of magnetization $\mathbf{M}$ is given by the applied magnetic field. A decrease of the field leads to a relaxation of $\mathbf{M}$ by Stoner-Wohlfarth rotation until an alignment along the closest easy axis is achieved, indicated with number 1 in Figure 2.6(a). In our case, $\mathbf{M}$ is aligned along the $[0\bar{1}0]$ easy axis perpendicular to the current direction [100]. Increasing the magnetic field from negative to positive fields leads first to a direction of $\mathbf{M}$ along [100] (number 2) and at higher fields to a switching event along [010] (number 3 in Figure 2.6(a)). At high positive fields, the direction of magnetization $\mathbf{M}$ is again given by the applied magnetic field (number 4). Figure 2.6(b) shows the two switching events at positive fields, labeled as H_{c1} and H_{c2}, which correspond to the two sequential 90° domain wall nucleation/propagation events accounting for the magnetization reversal in this material [Wel02]. Now, the measurement of each scan (beginning at 0 mT to positive magnetic field values) is converted into a sector of a resistance polar plot, as seen in Figure 2.6(c). The color code for the two resistance states is given as black for low resistance and red for high resistance. The change of color is abrupt according

to the abrupt switching events of H_{c1} and H_{c2}. In case of a gradual switching, a color gradient will be present. The compilation of all sectors results in a full 360° simulation of the resistance polar plot, as seen in Figure 2.6(d).

In order to determine the three magnetic anisotropy components of Equation 2.15, the innermost region of the anisotropy fingerprint is examined. In case of a purely biaxial anisotropy behavior of (Ga,Mn)As without any uniaxial components, the inner part of the anisotropy fingerprint of Figure 2.6(d) would have a form of a perfect square with its corners along the easy axes, as simulated in Figure 2.7(a).

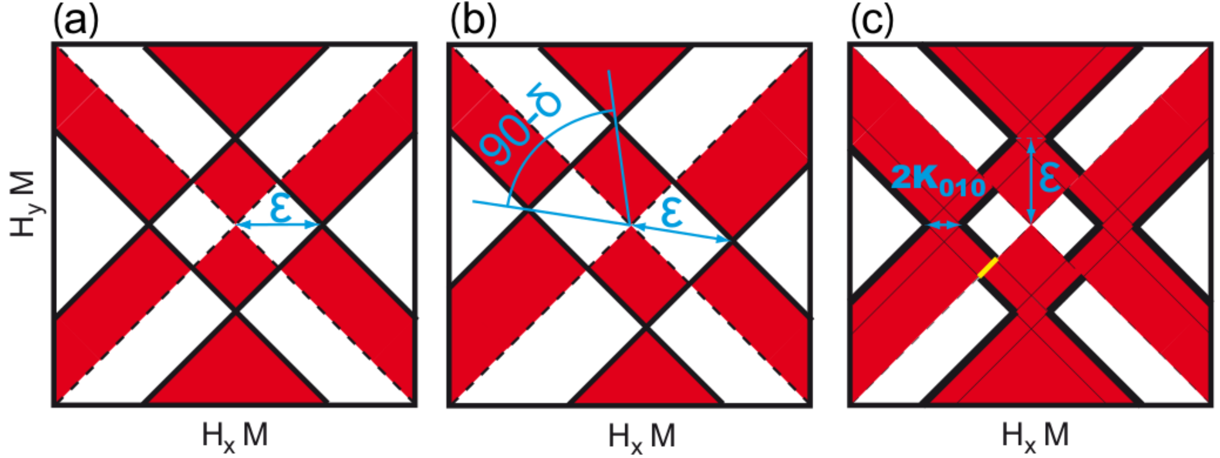

Figure 2.7: Sketches of expected shape of the inner region of an anisotropy fingerprint of a sample with (a) only a biaxial crystalline anisotropy in [100] and [010] direction (b) a biaxial anisotropy and additionally an uniaxial easy axis along [1$\bar{1}$0] (c) a biaxial anisotropy plus an uniaxial easy axis along [010]. Adopted from [Gou08].

The length of the halved diagonal of the square is given by the domain wall nucleation/propagation energy ϵ, which scales to the volume magnetization. In case of an inclusion of an additional, uniaxial anisotropy component, the two easy axes are bisected and the resulting easy axis is shifted towards the direction of the uniaxial anisotropy by an angle δ [Goe05]. Thus, the square is elongated into a rectangle, as seen in Figure 2.7(b). The strength of the uniaxial anisotropy component $K_{uni,[\bar{1}10]}$ in the [$\bar{1}$10] crystal direction relative to the biaxial anisotropy component K_{cryst} is extractable out of the angle δ due to the following relationship [Pap07] as

$$\delta = arcsin\Big(\frac{K_{uni[110]}}{K_{cryst}}\Big). \tag{2.18}$$

The mixing of the anisotropy terms $K_{uni[110]}$ and K_{cryst} leads to a rectangular shape in the anisotropy fingerprint. Therefore, it is often more favorable to use the aspect ratio of the width (W) to the lenght (L) of the rectangle, instead of the angle δ. The relationship to the anisotropy terms is given as

$$\frac{K_{uni[110]}}{K_{cryst}} = cos\Big(2arctan\Big(\frac{W}{L}\Big)\Big). \tag{2.19}$$

In case of an uniaxial anisotropy which is instead added parallel to an uniaxial easy axes, an asymmetry arises in the energy required for switching between the two biaxial easy axes. The energy required to switch towards one easy axis is lowered compared to the second easy axis. Figure 2.7(c) simulates this case, where the inner anisotropy fingerprint pattern is therefore comprised into an inner and outer square. The measure of the uniaxial anisotropy component along [010] crystal direction $K_{[010]}$ is given by the difference in the length of their half diagonal. The mixing of the anisotropy terms leads to a deformation of the pattern near the corners of the rectangle. As a result, it is often more convenient to identify $K_{[010]}$ by looking at the spacing between the sides of the squares. In case of an additionally uniaxial component $K_{uni,[\bar{1}10]}$, the spacing between the sides of the rectangle is considered. In Figure 2.7(c), the spacing is marked as a yellow line with a corresponding length of $\sqrt{2}\ K_{[010]}$.

At last, Table 2.1 compares the anisotropy components of (Ga,Mn)As layers, epitaxially grown by different research groups [Gou08].

	$\epsilon/M(mT)$	$K_{110}/K_{biax}(\%)$	$K_{010}/M(mT)$
Wü. from Fig. 4	18	18	1.0
Wü. with large [010]	8.5	7	1.4
Wü. with large [110]	12	21	0.7
IMEC	7.8	11	0.7
Nottingham	7.1	9	0.65
Tohoku	12	4	1.25
Notre-Dame	16	9	0.75

Table 2.1: Comparison of the three anisotropy components of epitaxially grown (Ga,Mn)As layers from various research groups. Adopted from [Gou08].

It can be pointed out that the biaxial anisotropy lies in the range between 7 to 18 mT. The ratio of $K_{[110]}/K_{biax}$ has a value from 4 to 21 %. The uniaxial component along the [010] crystal direction has in this comparative study a strength between 0.7 and 1.4 mT. As noted in [Gou08], the span of values for the $K_{[110]}/K_{biax}$ ratio in this table is only a reflection of the investigated set of samples. In general, this ratio is tunable over a much larger range by tuning of the hole concentration or temperature, as published in [Saw05, Pap07].

Hall Effects

In the last section only magnetoresistive effects have been discussed. The measurement of the resistivity/conductivity only offers the product of carrier concentration p and mobility

μ in (Ga,Mn)As material. As already shown in this chapter, the magnetic anisotropy is strongly coupled to the valence band of (Ga,Mn)As and therefore to the density of states as well as concentration of free holes.

In general, the most common method to measure the parameter of carrier concentration seperately uses the Hall-effect. Applying an external magnetic field B_z out of the plane and therefore perpendicular to the current path, carriers are deflected due to the Lorentz force leading to a detectable potential difference at opposing contacts, known as Hall voltage U_{xy}. In non-magnetic materials, the normal Hall effect (NHE) is measured. In ferromagnetic materials in general and in the ferromagnetic semiconductor (Ga,Mn)As in particular, the NHE is superposed by the anomalous Hall effect (AHE) due to the participation of free hole carriers in the magnetism. For both NHE and AHE, the current path, Hall voltage and applied magnetic field are aligned perpendicular to each other, $I_{xx} \perp U_{xy} \perp B_z$.

The Hall resistivity ρ_{Hall} in magnetic materials is expressed as

$$\rho_{Hall} = R_0 B + R_S M(H), \tag{2.20}$$

where $R_0 = \frac{1}{pe}$ is the ordinary (normal) Hall coefficient, R_S is the anomalous Hall coefficient and $M(H)$ is the magnetic field dependent magnetization of the sample [Ohn99]. The anomalous Hall term in Equation 2.20 is the critical contribution for a determination of free hole carrier concentration p in (Ga,Mn)As. Uncertainties of the sample magnetization M in combination with the field-dependend resistivity ρ_{xx} complicate the measurement of p.

A method for an accurate determination of hole concentrations requires measurement conditions at very low temperature in the mK region with applied magnetic fields of 22 to 27 T [Ohn99]. At very high fields, the magnetization is saturated and contributes as a constant in Equation 2.20 in ρ_{Hall}. Thus, the slope of the resistivity at high magnetic fields can be taken for direct calculation of hole concentration p in (Ga,Mn)As. Unfortunately, this measurement technique needs special cryostats to reach very low temperatures as well as high magnetic fields, both not available within the framework of this thesis.

RT-Hall measurements at low magnetic fields (± 80mT) are taken as the chosen method to estimate p of epitaxially grown (Ga,Mn)As samples with known thickness d. At 300 K and therefore much above T_C, ρ_{Hall} increases linearly just like non-magnetic materials. Thus, the behavior of magnetization M in (Ga,Mn)As is neglected and Equation 2.20 is simplified to

$$R_{Hall} d = \rho_{Hall} = R_0 B = \frac{1}{pe} B \tag{2.21}$$

$$\Leftrightarrow p = \frac{1}{\frac{\Delta R_{Hall}}{\Delta B} ed} \tag{2.22}$$

The slope of ρ_{Hall} (or R_{Hall} respectively) plays a significant role in the estimation of p. In reality, M itself is a function of temperature and magnetic field, expressed by the Brillouin-function. M saturates very fast with applied magnetic field at T $\ll T_C$ if the material is ferromagnetic. In the paramagnetic phase, M can not be forced to saturation

for T $\gg T_C$. Consequently, the magnetization M influences the Hall resistance even at RT leading to a larger slope of $\frac{R_{Hall}}{\Delta B}$. Hence, the determination of carrier concentrations by RT Hall measurements (with low applied magnetic field) contain a large error bar and is treated as a rough estimation of the lower limit of p in Chapter 4 and 5.

Additionally it is worth mentioning, that a conclusion of RT to LT free hole concentrations is quite difficult. Holes at RT are thermally activated. With decreasing temperature, holes "freeze-out" and a lower amount contributes to current flow and participate to the carrier-induced ferromagnetism in (Ga,Mn)As. An indication of a decrease in charge carriers with temperature is the measurement of conductivity, which is lowered at LT. Though, conductivity only reflects the product of carrier concentration and mobility and a residual uncertainty remains. A trend of low RT conductivity resulting in low LT conductivity is noticeable.

The origin of the anomalous Hall-effect are asymmetrical scattering effects due to the spin-orbit interaction with a non-magnetic or magnetic impurity. Both scattering mechanisms are shown in Figure 2.8 and presented in the following. A detailed description is given in [Gro04].

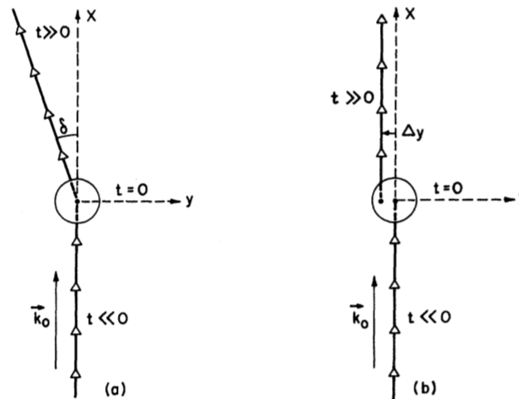

Figure 2.8: Illustration of scattering mechanisms in a ferromagnetic material. (a) Skew-scattering: A propagating spinpolarized charge carrier is scattered at the charge distribution of a non-magnetic impurity under an angle δ. (b) Side-jump scattering: The spinpolarized charge carrier is scattered at a magnetic impurity resulting in a lateral offset Δy of its trajectory. Adopted from [Ber70].

Skew Scattering

The direction-dependent scattering of a propagating spinpolarized charge carrier at a charge distribution of a nonmagnetic impurity is described by the skew scattering, as seen in Figure 2.9.

The spin-orbit interaction of the spin $\vec{s}$ and its wave vector $\vec{k}$ of the free charge carrier causes an electric dipole perpendicular to $\vec{s}$ and $\vec{k}$ which interacts with the inhomogeneous electric field of the impurity, illustrated as an electron cloud in Figure 2.9. Quantum

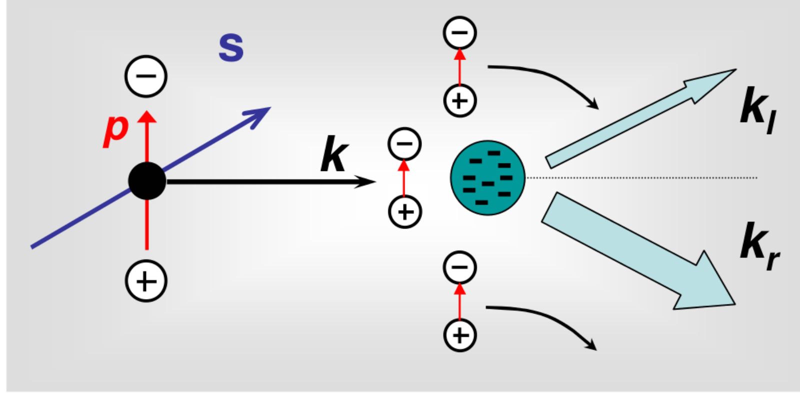

Figure 2.9: Illustration of the skew-scattering mechanism. A propagating spinpolarized charge carrier is scattered at the charge distribution of a non-magnetic impurity. The scattering probability is direction-dependent (thicker arrow in k_r direction) and therefore asymmetric with respect to the initial wave vector $\vec{k}$. Adopted from [Gro04].

mechanical calculations of transition probabilities provide direction-dependent scattering probabilities. Every scattering event effects a longitudinal and transverse contribution to the resistance. Thus, the trajectory of the free charge carrier changes with an angle δ referred to the initial trajectory direction before the scattering event, as seen in Figure 2.8(a) and 2.9. A precondition of the skew-scattering mechanism is a preferred spin direction of the charge carrier. The contribution of the skew scattering to the AHE is

$$\rho_{xy} \propto \rho_{xx} M(H). \tag{2.23}$$

Side-jump Scattering

The second scattering mechanism of a free charge carrier implies a lateral offset of its trajectory. The offset has a magnitude of 10^{-14} to 10^{-10} m, as mentioned in [Ber70]. The side-jump process is a consequence of energy conservation. The propagating free charge carrier has a kinetic energy $E_{kin} = \frac{\hbar^2 k^2}{2m^*}$ as well as a potential energy $E_{pot} = -\vec{p} \cdot \vec{E}$ of the electric dipole $\vec{p}$ in an electric field $\vec{E}$. An elastic collision with a magnetic impurity conserves the kinetic energy $\frac{\hbar^2 k'^2}{2m^*}$ but changes the direction of the electric dipole $\vec{p}$ which is always perpendicular to the wave vector $\vec{k}$. A change of $\vec{p}$ causes a change in the potential energy $-\vec{p} \cdot \vec{E}$ leading to a lateral shift Δy of the free carrier with respect to the initial trajectory in the electric potential of the scattering center, as seen in Figure 2.8(b).

The longitudinal resistivity ρ_{xx} is direct proportional to the occurrence of scattering events and the magnitude of the lateral offset. Thus, the side-jump scattering contributes to the AHE as

$$\rho_{xy} \propto \rho_{xx}^2 M(H). \tag{2.24}$$

In summary, the anomalous Hall coefficient R_S of Equation 2.20 is influenced by skew

and side-jump mechanisms as

$$R_S \propto c_1\rho_{xx} + c_2\rho_{xx}^2, \tag{2.25}$$

where ρ_{xx} is the longitudinal resistivity, c_1 and c_2 correspond to skew- and side jump scattering mechanisms. Both mechanisms seem to be important for (Ga,Mn)As material, as mentioned in [Ohn96, Ohn99, Edm03, Ruz04].

Hole Mobility μ

For semiconductors with both electrons n and holes p as carriers, the drift current $\mathbf{J}$ under an applied electric field $\mathbf{E}$ is given by

$$\mathbf{J} = \sigma\mathbf{E} = q(\mu_n n + \mu_p p)\mathbf{E} \tag{2.26}$$

where σ is the conductivity, q is the elementary electric charge, μ_n and μ_p the mobilities for electrons and holes [Sze07]. The conductivity σ is described by

$$\sigma = q(\mu_n n + \mu_p p). \tag{2.27}$$

If p $\gg$ n, as in p-type semiconductor like (Ga,Mn)As

$$\sigma = q\mu_p p. \tag{2.28}$$

The longitudinal resistivity ρ_{xx} is the inversion of σ. Thus, Equation 2.28 leads to

$$\rho_{xx} = \frac{1}{\sigma} = \frac{1}{q\mu_p p}. \tag{2.29}$$

The estimation of a hole concentration p in (Ga,Mn)As material by RT-Hall measurements and the measurement of ρ_{xx} by four-terminal longitudinal resistivity measurements (explanation later in Chapter 3.5) are taken to estimate RT-mobility μ_p. The conversion of Equation 2.29 to μ_p results in

$$\mu_p = \frac{1}{pq\rho_{xx}}. \tag{2.30}$$

RT-hole mobilities in (Ga,Mn)As have been determined by several research groups and μ_p ranges from 1 to 5 $\frac{cm^2}{Vs}$, as published in [Jun07, Alb08, Wur08]. A comparison of (Ga,Mn)As material properties has to be taken with care due to different growth chamber geometry, growth conditions, different Mn content, sample processing and measurement setups. It serves as an estimation of RT-μ_p 100 times smaller than RT-μ_p in intrinsic GaAs with $\mu_p = 400$ $\frac{cm^2}{Vs}$. As noted in [Jun07], the mean free path λ_m of holes in (Ga,Mn)As material is estimated to be ~ 1 nm.

Chapter 3

Experimental Methods

The aim of this chapter is to present the experimental methods, which are used for the epitaxial fabrication and in-situ/ex-situ characterization of (Ga,Mn)As samples within this thesis.

3.1 The UHV-MBE Growth Chamber and in-situ Reflection High Energy Electron Diffraction

Molecular beam epitaxy (MBE) is an established method to fabricate high quality semiconductor layers and systems with an accuracy of an atomic layer (monolayer ML). This method is based on the interaction between thermal activated, non-ionized molecular beams of different element sources with heated crystal substrates. The reactions on the substrate surface (like adsorption, desorption, surface migration and incorporation into the crystal lattice) proceed in non-thermal equilibrium conditions and in ultra high vacuum (UHV) with background pressures below $\sim 10^{-9}$ torr. Due to this good vacuum conditions, the mean-free path of such thermally activated molecules is much longer than the distance between effusion cell and substrate. Therefore, the molecular beams reach the substrate surface without interaction.

All samples presented in this work have been grown in a self-designed UHV MBE growth chamber, which was installed for the fabrication of (Ga,Mn)As by G.M. Schott [Sch04]. A special feature of this growth chamber is that it has only a third of the pumping volume of a standard RIBER-32 MBE chamber. The schematic design with its components can be seen in Figure 3.1. To achieve and ensure such high vacuum conditions, it has a pumping system consisting of a cryo pump, a titanium sublimator and a nitrogen shroud. The high purity material of different elements is supplied in heatable pyrolitic boron nitride (PBN) crucibles inside the effusion cells. The cell openings and therefore the molecular beams are directed towards the sample. Additionally, every cell has its mechanical cell shutter and a water cooling circuit. The nitrogen shroud has a round opening at the height of the substrate position, as seen in Figure 3.1. A main shutter is situated between shroud and sample holder which shields the sample from material fluxes of all cells. A Bayard-Alpert

pressure gauge is used to measure the fluxes (beam equivalent pressure, BEP) of each cell. It is fixed at a manipulator and can be slued into the position for BEP measurements. Further important positions of the manipulator are the transfer and growth position of the substrate holder. At last, the growth chamber has a heated viewport to have a straight look onto the sample when the main shutter is opened. A RHEED source with corresponding fluorescence screen is also part of the equipment. Its main principle is explained in the following.

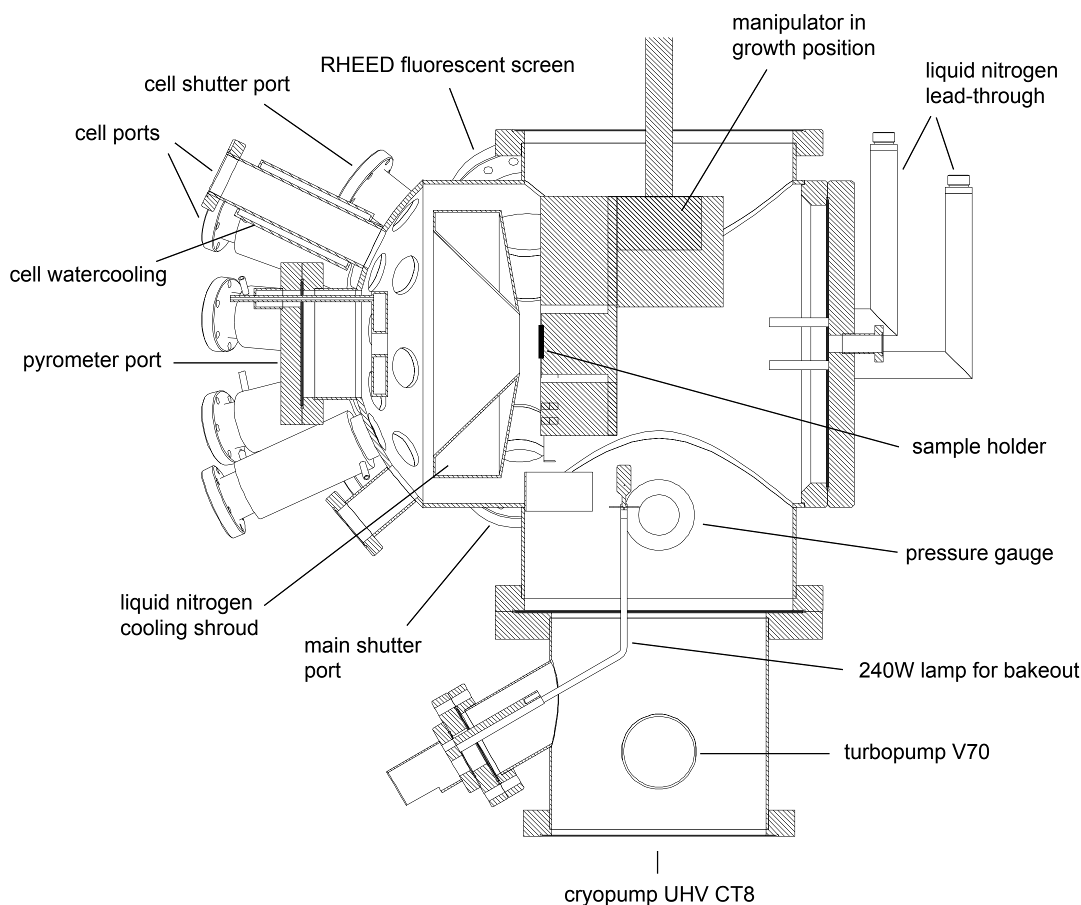

Figure 3.1: Draft of the (Ga,Mn)As MBE-chamber, in which every sample of this thesis was grown. Adopted from [Sch04].

RHEED

The most important in-situ characterization method of the epitaxial growth is reflection high energy electron diffraction (RHEED). It offers the observation of crystalline quality meaning surface roughness and surface reconstruction of the deposited layer during growth. A RHEED system consists of an electron gun which generates an electron beam with an

energy of 10 to 30 keV and which is directed onto the sample surface under a glancing incidence angle (1 to 3°). The electron beam consists of electrons which have a de-Broglie wavelength of $\lambda_{deBroglie} \sim 0.1$ $\mathring{A}$. Due to the short absorption length, the penetration depth is only a few monolayers (ML) and the electrons are mainly diffracted by the surface atoms. A phosphorous screen is mounted at the opposite side of the chamber facing the electron gun. It enables the observation of the diffraction pattern. The diffraction is not a pure reflection but rather contains a fractional, transmitted part of the electron beam, depending on the roughness of the first few atomic layers. For smooth atomic top layers, a streaky diffraction pattern is observed, whereas for a rough surface a spotty diffraction pattern is observed.

The conditions for constructive interference of the elastically diffracted electrons can be explained by the Ewald sphere construction in reciprocal space, as seen in Figure 3.2(a).

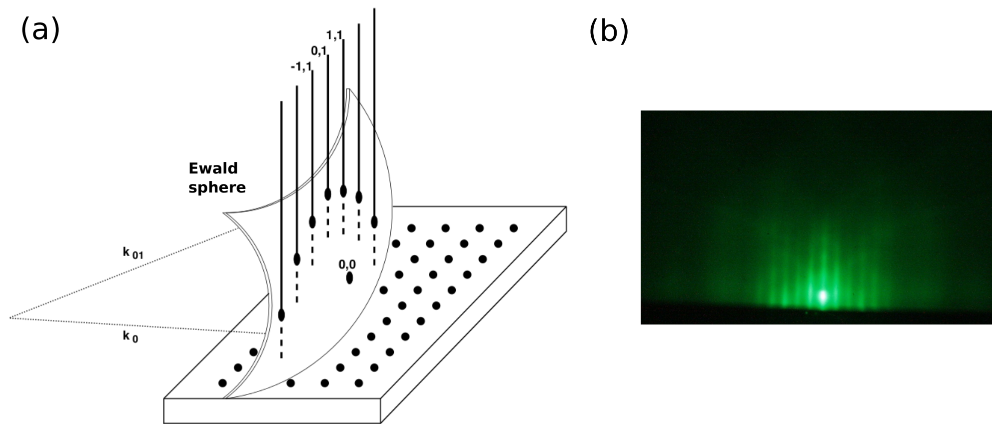

Figure 3.2: (a) Ewald sphere construction in reciprocal space for diffraction of high energy electrons at a sample surface. The reciprocal lattice of the two-dimensional crystal surface consists of vertical Ewald rods, which intersects with the Ewald sphere for constructive diffraction conditions. Adopted from [Ort01]. (b) RHEED diffraction pattern of a (2 × 4) surface reconstruction of HT-GaAs along $[1\bar{1}0]$ azimuth.

In case that the electron beam interacts with a two-dimensional crystal lattice of the first few atomic layers, a peroidically crystal surface in reciprocal space is a set of so-called Ewald-rods that are aligned vertical to the sample surface. Intersections of the Ewald-rods with the Ewald sphere result in points on a circle. Due to the fact, that the radius of the Ewald sphere is much larger ($k_0 = \frac{2\pi}{\lambda_{deBroglie}}$) than the distance between the Ewald-rods, several rods are intersected under a small angle. Broadenings of the rods and the Ewald sphere due to thermal vibrations of the crystal lattice and dispersion of the electron beam lead to typical 'streaky' diffraction patterns, extending to both sides of the reflected beam of zero order (specular spot (0,0)).

As an example of a RHEED pattern, Figure 3.2(b) shows the (2 × 4) surface reconstruction along $[1\bar{1}0]$ azimuth during growth of HT-GaAs. Kikuchi lines in a diffraction pattern originate from inelastic scattering of the electron beam. It underlines high quality of the crystal structure.

A detailed surface phase diagram of epitaxially grown GaAs on a (001) surface for different MBE growth conditions (substrate temperature and BEP ratio (As_4/Ga)) can be seen in Figure 3.3(a). The red cross indicates the growth region of HT-GaAs buffer layers grown under our standard HT-growth conditions of T_{sub} = 580°C and BEP ratio $(As_4/Ga) = 35$. with a (2 × 4) surface reconstruction.

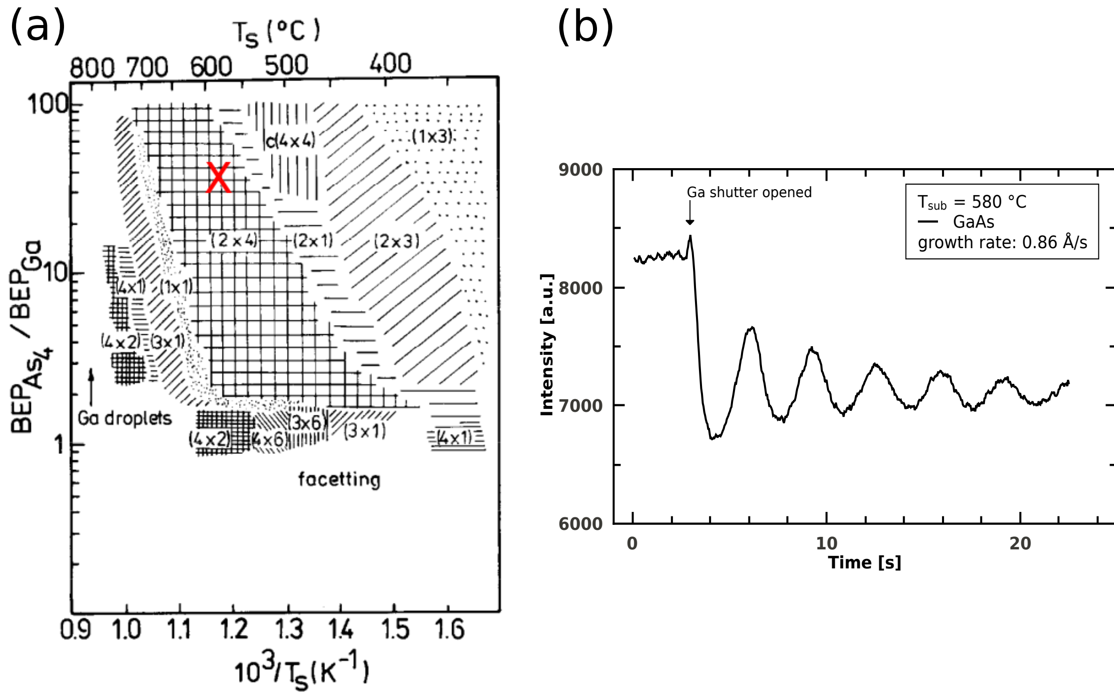

Figure 3.3: (a) Surface phase diagram for MBE growth of GaAs on a (001) surface. The surface reconstructions are plotted versus both substrate temperature and the BEP ratio ($\frac{As_4}{Ga}$). Typical HT-GaAs buffer growth is located in the (2 × 4) surface reconstruction region, indicated by the red cross. Adopted from [Dae90]. (b) RHEED oscillations during growth of HT-GaAs buffer layer at T_{sub} = 580°C and BEP ratio ($\frac{As_4}{Ga}$) = 35.

Another important application of RHEED is the determination of the growth rate by analyzing time-dependent RHEED intensity oscillations of the specular spot during layer-by-layer growth mode. In Figure 3.3(b), the growth rate of HT-GaAs is determined by the distance between two maxima of intensity of RHEED oscillations. At maximum intensity, a complete monolayer is formed. A minimum of intensity is reached for a half-deposited monolayer due to diffuse scattering and penetration of the electron beam at the rough surface. The resulting growth rate is given in ML/s. With known lattice constant of GaAs ($a_{GaAs} = 5.65325\ \AA$) and known thickness of 1 monolayer of GaAs ($1\ ML = \frac{a_{GaAs}}{2}$), the growth rate is recalculated from ML/s to $\frac{\AA}{s}$. All HT-GaAs buffer layers in this work have been grown with growth rates of $\approx 1\ \frac{\AA}{s}$.

3.2 Epitaxial Growth

In this section the epitaxial growth conditions of III-V compound semiconductors grown in this work are presented. First of all, an extensive description of (Ga,Mn)As growth is given. Later on an overview of the epitaxial growth of (Al,Ga)As, AlAs and (Ga,In)As is introduced. At last, a typical growth procedure of (Ga,Mn)As is presented.

3.2.1 (Ga,Mn)As

The transition metal Mn has a low solubility ($< 10^{18}\ cm^{-3}$) in GaAs when epitaxially grown under equilibrium growth conditions. GaAs buffer layers are typically grown at $T_{sub} = 580°C$. Ferromagnetic (Ga,Mn)As material with a relatively high Mn doping concentration ($\gtrsim$1.5%) is therefore epitaxially grown at low temperatures $T_{sub} < 300°C$, far away from equilibrium growth conditions.

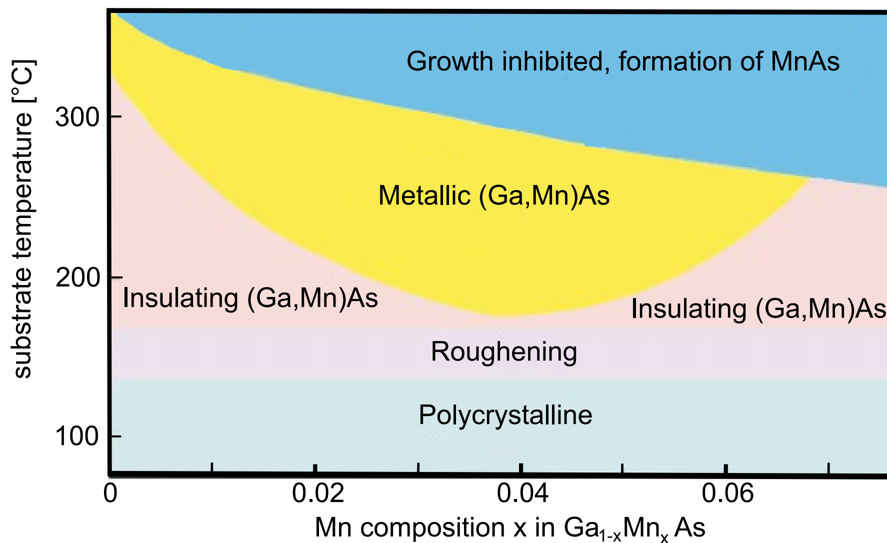

Figure 3.4: Schematic phase diagram of relation between growth parameters (substrate temperature and Mn concentration) and properties of (Ga,Mn)As layers. Adopted from [Ohn98].

Figure 3.4 illustrates the dependence of the growth conditions like substrate temperature T_{sub} and Mn content x to the (Ga,Mn)As material properties [Ohn98]. The epitaxial growth of (Ga,Mn)As at very low substrate temperatures T_{sub} leads to polycrystalline growth and a rough surface. At $T \geq 140°C$, the layer growth changes to monocrystalline growth and the rough surface smoothes out up to $\approx$ 180°C. Between 180°C $\leq T_{sub} \leq$ 310°C, an insulating or metallic behavior of (Ga,Mn)As material predominates and strongly depends on T_{sub} and Mn content x. For a very low or a very high Mn content x at a given T_{sub}, the (Ga,Mn)As material is strongly compensated by point defects like As antisites As_{Ga} due to low T_{sub} or Mn interstitials Mn_{int} in case of a high x. Therefore, the material is electrically insulating. The favorable metallic behavior is prevalent in the middle range

of x, where only 70 to 80% of the hole carriers p (provided by nominal x) are compensated. At T $\geq 310°C$, the formation of MnAs becomes prevalent and is not favored.

Campion et al. have investigated the 2D/3D growth border (metallic (Ga,Mn)As/formation of MnAs clusters border in Figure 3.4) of 50 nm (Ga,Mn)As layers as a function of Mn content and substrate temperature, as seen in Figure 3.5 [Cam03].

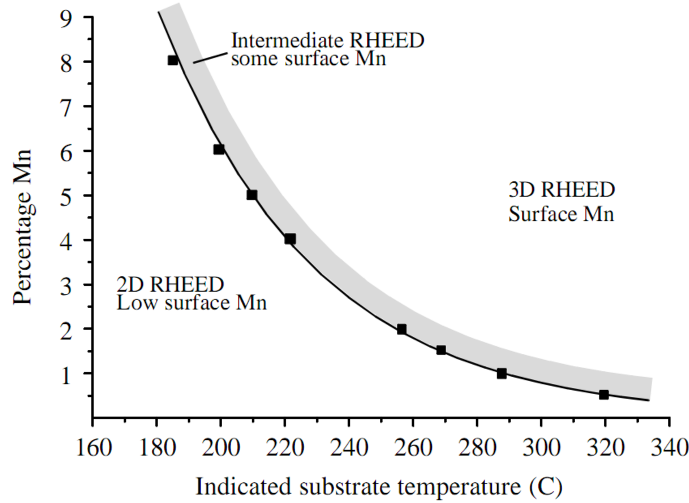

Figure 3.5: Transition of 2D to 3D growth mode of 50 nm (Ga,Mn)As layers as a function of Mn content and substrate temperature, investigated by RHEED during growth. The samples have been grown with an As_2 source. Surface Mn has been detected by Auger electron spectroscopy after growth. The growth transition shifts to higher substrate temperatures for lower Mn concentrations. Adopted from [Cam03].

A clear shift of the transition from 2D to 3D growth mode to higher substrate temperatures for lower Mn concentrations has been found. For the growth of these layers, an As cracker cell is used which provides As dimers As_2 instead of uncracked As_4 molecules. The same growth study has shown that As_2 dimere as a source material leads to a lower As antisite concentration compared to As_4 tetramer due to different incorporation kinetics [Cam03]. All (Ga,Mn)As material fabricated in this thesis has been epitaxially grown with uncracked As_4 and the 2D/3D growth border is assumed to obey the same trend.

Standard Growth Conditions

In the EP3 of the University of Würzburg, (Ga,Mn)As is grown epitaxially with a substrate temperature of 270°C and a BEP ratio $(\frac{As_4}{Ga}) = 25$. At these standard growth conditions fabricated thick (20 to 70 nm) (Ga,Mn)As layers show reproducible ferromagnetic and transport properties [Sch04, Wen08].

The amount of incorporated Mn into the GaAs lattice is controlled by the temperature of the Mn effusion cell $T_{Mn,cell}$, meaning that a higher Mn content x is achieved by increasing $T_{Mn,cell}$. The vapor pressure p_{vap} of a material can be expressed by the thermal activation of the material at a given temperature T is

$$p_{vap} = be^{-\frac{E}{k_B T}}, \tag{3.1}$$

where b is a material parameter, E is the activation energy and k_B is the Boltzmann factor.

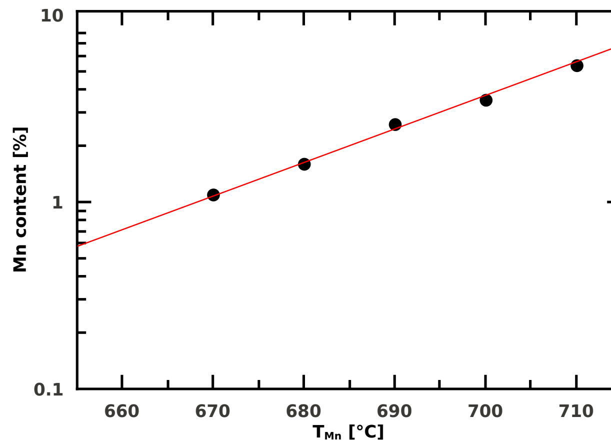

Figure 3.6: Nominal Mn content x in % for 70 nm (Ga,Mn)As layers (grown at our standard conditions) as a function of the Mn cell temperature $T_{Mn,cell}$. The red line indicates the exponential correlation between x and $T_{Mn,cell}$.

The temperature dependence of the nominal Mn content x to the Mn effusion cell temperature $T_{Mn,cell}$ is shown in Figure 3.6. The Mn content x of the 70 nm layers (grown at our standard conditions) is indirectly determined by HRXRD measurements (see Chapter 3.3). The Mn effusion cell has been operated in a small temperature range of around 40°C, resulting in $0.02 \leq x \leq 0.06$ for bulk (Ga,Mn)As material. The red line indicates the following rule of thumb [Wen08]:

An increase of $T_{Mn,cell}$ by 20°C corresponds to a doubling in Mn content x.

The fluxes of all high purity materials (Mn, Ga and As_4) have been measured with a Bayard-Alpert pressure gauge prior to epitaxial growth of (Ga,Mn)As material. Figure 3.7 shows the time-dependent change of the Mn flux at two different $T_{Mn,cell}$ 695°C and 715°C. After opening of cell and main shutter, both cell temperatures show a strong increase of the measured flux followed by a gradual decrease to a stabilized flux after $\approx$ 6 minutes at 6×10^{-9} $torr$ for 695°C and 8×10^{-9} $torr$ for 715°C. The immediate increase of the measured flux is presumably a combination of Mn flux and the residual gas of the growth chamber caused by e.g. other effusion cells. A Mn flux in the order of $\approx 10^{-9}$ $torr$ seems to be very sensitive to the background pressure $\approx 10^{-10}$ $torr$ and its value is considered with caution. The nominal Mn content x for 70 nm (Ga,Mn)As layers grown with these Mn effusion cell temperatures after flux measurements yield $x = 0.022$ (for 695°C) and $x = 0.043$ (for 715°C).

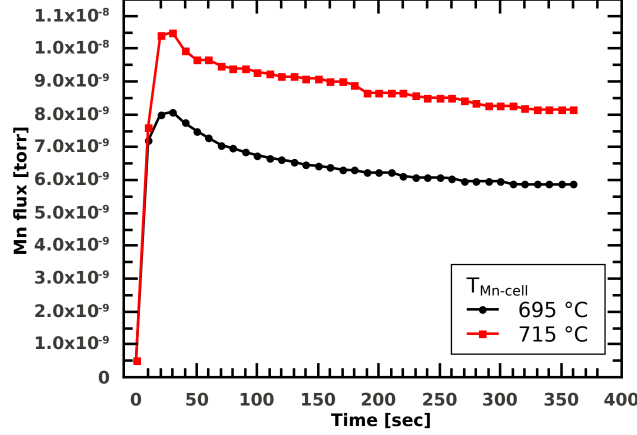

Figure 3.7: Time-dependent measurements of the Mn flux for Mn cell temperatures $T_{Mn,cell}$ =695°C and $T_{Mn,cell}$ =715°C. The fluxes stabilized after 6 minutes.

The fluxes of the Ga and As_4 effusion cells ($1{\cdot}10^{-7}torr$ and $\sim 10^{-6}torr$) complete the flux measurements to adjust the BEP ratios ($\frac{As_4}{Ga}$) for all epilayers. All (Ga,Mn)As samples in this thesis have been grown with growth rates around 0.8 to 1.0 $\frac{\AA}{s}$.

Point Defects

The described low temperature growth of (Ga,Mn)As far away from thermal equilibrium conditions results in a non-neglectable incorporation of the following point defects, which results in a partial compensation of hole carriers:

- Arsenic antisites As_{Ga}

  LT-GaAs as well as (Ga,Mn)As material is epitaxially grown under As overpressure. The incorporation of As is mainly influenced by substrate temperature T_{sub} and BEP ratio ($\frac{As_4}{Ga}$) [OHa94, Liu95, Luy97]. A part of the As atoms resides on Ga lattice sites. The As_{Ga} concentration is in the range of 10^{19} to 10^{20} cm^{-3} and leads to an increased lattice constant, as described later in Chapter 3.3.1. As_{Ga} acts as a deep double donor (0.5 eV/0.7 eV above the valence band) and compensates hole carriers p in (Ga,Mn)As material. As_{Ga} plays a critical role of electrical and magnetic properties in the low-doping regime of Mn $x < 0.015$ [Mye06], as shown in the insulating region of Figure 3.4. Under assumption of a constant BEP ratio ($\frac{As_4}{Ga}$), an increase of T_{sub} leads to a lower As_{Ga} concentration and less compensation of p leading to a metallic behavior of (Ga,Mn)As material. In case of a higher BEP ratio ($\frac{As_4}{Ga}$), there is an excess supply of As atoms which increases the formation of As_{Ga}. As a result, a stronger hole compensation and therefore an insulating behavior of the (Ga,Mn)As material is expected. It is demonstrated that (Ga,Mn)As samples grown at increased substrate temperatures (up to 250°C) and lowered BEP ratio (As_4/Ga) show higher T_C and lower longitudinal resistance R_{xx} due to less p compensation [Shi99]. High

temperature annealing at $T > 450°C$ leads to a removal of As_{Ga}. Contrariwise, the formation of MnAs clusters begins at $T > 300°C$ and the (Ga,Mn)As material degenerates, as seen in Figure 3.4.

Improved layer properties like higher Curie temperature and structural quality could be achieved by usage of an As cracker cell due to different incorporation kinetics of As_2 and As_4 which leads to lower As_{Ga} concentrations with As_2 [Cam03]. For (Ga,Mn)As material fabricated within the framework of this thesis, an As_4 source has been used.

- Manganese interstitials Mn_{int}

  Ab initio total-energy calculations have shown, that the Mn atom is able to occupy one of two metastable interstitial positions in the GaAs host-crystal [Maš04]. One position is surrounded by four Ga atoms, the other position is surrounded by four As atoms. Both positions show comparable binding energies. In agreement to experimental data, calculations of partial concentrations show that Mn_{int} increases linearly with nominal Mn content x, as shown in Figure 3.8 [Jun06]. For $x \leq 1.5\%$, Mn_{Ga} has a lower formation energy compared to Mn_{int}, as presented in the inset of Figure 3.8. Thus, Mn atoms reside on substitutional positions in the GaAs host-crystal. For $x > 1.5\%$, the formation energy of Mn_{Ga} and Mn_{int} is identical and Mn atoms resides on substitutional and interstitial Mn positions. Mn_{int} acts as a double donor like Arsenic antisite, resulting in a compensation of hole concentration p. Additionally, Mn_{int} couples antiferromagnetically to Mn_{Ga} [Edm05]. The binding energy of a $Mn_{int} - Mn_{Ga}$ pair is 26 meV [Maš04] and the total spin is much smaller compared to the local spin S $= 5/2$ of the isolated Mn_{Ga}. As a result, the ferromagnetic ordering and T_C is reduced by Mn_{int} impurities.

  Post-growth annealing of (Ga,Mn)As material at temperatures lower than growth temperatures leads to an outdiffusion of Mn_{int} impurities toward the surface [Edm04]. The energy barrier of the outdiffusion process is at 1.4 eV [Wan08]. Mn atoms are passivated by reacting to MnO in oxygen atmosphere. The passivation is stopped when a monolayer of MnO has been formed and the oxide layer has to be removed to proceed with the outdiffusion of Mn_{int}. By intense optimization of the annealing procedure, highest T_Cs of $\sim$190°C have been achieved [Ole08, Wan08, Che09].

  The following annealing procedure has been applied to bulk and very thin (Ga,Mn)As material in this work: In [Edm04], a complete outdiffusion of Mn_{int} in a 25 nm thick layer after an annealing time of 48 hrs at 185°C in air is estimated by time-dependent resistivity measurements during the annealing procedure. In case of a 70nm (Ga,Mn)As layer an annealing time of 144 hours at 185°C on a hot plate was used. Parabolically graded layers of Chapter 5 were annealed for 3 hours under the same annealing conditions.

- Vacancies

  In LT-GaAs and in (Ga,Mn)As material, Ga vacancies V_{Ga} do not play a significant role of carrier compensation due to maximum concentrations in the order of 10^{18} cm^{-3} [Luy97, Tuo04].

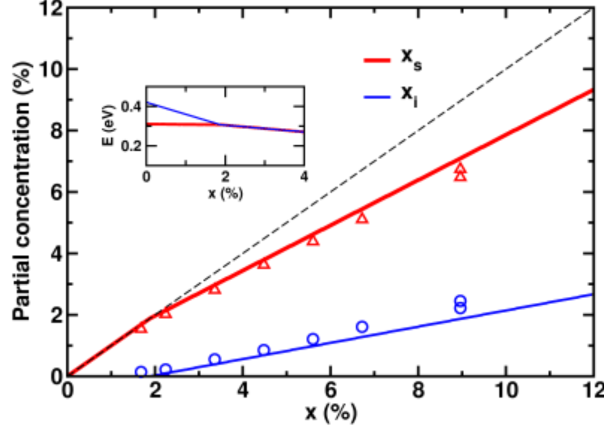

Figure 3.8: Theoretical equilibrium partial concentrations x_s and x_i of substitutional Mn_{Ga} and interstitial M_{int} impurities. The nominal Mn content $x = x_s + x_i$ is represented by the dashed line. Triangles and circles correspond to experimental Mn_{Ga} and M_{int} partial concentrations. The inset shows the formation energies of Mn_{Ga} and M_{int} as a function of nominal Mn content. Taken from [Jun06].

As_{Ga} and Mn_{int} massively compensate hole carriers. As a result, the free hole carrier density p is reduced compared to nominal x and therefore T_C decreases according to equation 2.1. The free hole carrier concentration is estimated by

$$p = x_{sub} - 2x_{int} - 2y. \tag{3.2}$$

A factor of 2 for As_{Ga} and Mn_{int} defect concentrations, noted as y and x_{int}, accounts for their double donor characters. The nominal Mn content x is the sum of substitutional and interstitial Mn content

$$x = x_{sub} + x_{int}, \tag{3.3}$$

whereas only the effective Mn content x_{eff} with

$$x_{eff} = x_{sub} - x_{int} \tag{3.4}$$

contributes to the ferromagnetism of (Ga,Mn)As material due to an antiferromagnetic coupling between Mn_{Ga} and Mn_{int}. In this work, the nominal Mn content x is stated for the epitaxially grown (Ga,Mn)As layers.

3.2.2 (Al,Ga)As, AlAs and (Ga,In)As

Besides the growth of (Ga,Mn)As on a pure HT-GaAs buffer, other III-V alloys have been epitaxially grown in this work like (Al,Ga)As, AlAs and (Ga,In)As in combination with (Ga,Mn)As heterostructures to influence the magnetic anisotropy in different applications. As presented in Chapter 6, the magnetic anisotropy has been changed by an epitaxial lift-off process of (Ga,Mn)As as well as (Ga,Mn)As/(Ga,In)As layers, using AlAs as a sacrificial layer. A fully electrical read-write device of bulk (Ga,Mn)As/(Ga,In)As has been developed by S. Mark [Mar11]. (Al,Ga)As/AlAs barriers have been used within a feasibility study of a p-n junction with a very thin (Ga,Mn)As layer, as described in Chapter 5.4.

(Al,Ga)As

In this thesis, (Al,Ga)As layers have been grown at the same epitaxial growth conditions like HT-GaAs, meaning at T$_{sub}$ = 580°C and a BEP ratio ($\frac{As_4}{Ga}$) = 35. The Al cell temperature is operated at T_{Al} = 1060°C. Figure 3.9(a) shows the time-dependend RHEED oscillations of an (Al,Ga)As layer. The distance between two maxima of intensity is used for calculation of the growth rate in ML/s, as explained in Chapter 3.1. The amount of Al is determined by the growth rate difference between (Al,Ga)As and GaAs (Figure 3.3). Here, the Al content is $x_{Al} = 0.30$. The corresponding direct bandgap of (Al,Ga)As is $E_{gap} = 1.8\ eV$, according to [Iof98]. The (Al,Ga)As layer as well as the AlAs layer, described in the next paragraph, have been used as a tunnel barrier for hole carriers, as explained in Chapter 5.4.

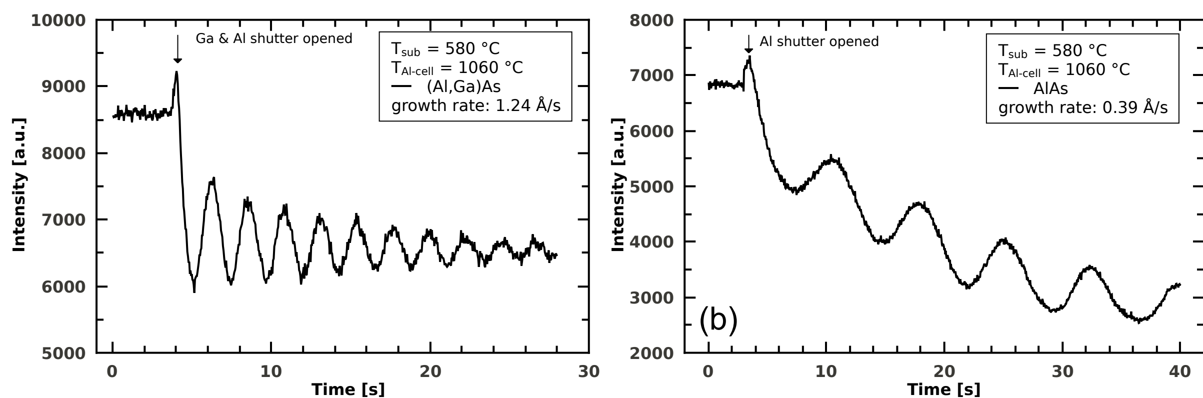

Figure 3.9: RHEED Oscillations during the growth of (a) (Al,Ga)As and (b) AlAs at T$_{sub}$ = 580 °C. Before the growth of both layers, a HT-GaAs buffer layer has been grown to ensure a smooth surface. The As-valve is opened all the time.

AlAs

The growth of AlAs in this work has been performed at different substrate temperatures, ranging from 580 to 650°C. In Figure 3.9(b), the determination of the AlAs growth rate

is analogous to the (Al,Ga)As growth rate determination by time-dependend RHEED intensity oscillations. The bulk lattice constant of AlAs is $a_{AlAs} = 5.662$ $\mathring{A}$ [Les92]. For the epitaxial growth of AlAs, the same operating Al effusion cell temperature is used compared to (Al,Ga)As growth. The resulting growth rate of 0.14 ML/s is less than half of the GaAs growth rate (0.31 ML/s) and three times smaller than the (Al,Ga)As growth rate (0.45 ML/s). In Chapter 6, AlAs sacrificial layers with thicknesses of ≈ 60 nm for lift-off processes of (Ga,Mn)As and (Ga,Mn)As/(Ga,In)As layers have been grown. In Chapter 5.4, a 10 nm AlAs layer is used as a hole carrier barrier (indirect $E_{gap} = 2.24$ eV at $T = 4$ K [Var67]) in combination with a 10 nm (Al,Ga)As layer in a p-n junction with a very thin (Ga,Mn)As layer.

(Ga,In)As

Compared to HT-GaAs, (Al,Ga)As and AlAs layer growth, the substrate temperature for epitaxially grown (Ga,In)As material is lowered to 500°C. In general, the layer thickness as well as the In content is determined by high resolution x-ray diffraction of (004) Bragg reflection under assumption of a fully strained layer without any plastic relaxation. In the example of Figure 3.10, a nominal 70 nm (Ga,In)As layer is deposited on a GaAs substrate (black curve). The simulation of this layer (red curve) has been calculated by the *Panalytical Epitaxy 4.1* software and reveals an In content of $x_{In} = 0.071$ and a layer thickness of 70 ±1 nm. The bulk lattice costant is given as [Iof98]

$$a_{(Ga_x,In_{1-x})As} = 6.0583 - 0.405 \cdot x_{Ga} \qquad \text{in } \mathring{A} \tag{3.5}$$

A detailed explanation of HRXRD diffraction patterns is described in Chapter 3.3. For layer structures with (Ga,In)As in the same layer structure with (Ga,Mn)As layers, special care has to be taken to avoid the critical layer thickness of (Ga,In)As at which plastic relaxation and therefore generation of threading misfit dislocations emerge. In [Wen08] the uniaxial elastic relaxation of nanopatterned stripes of (Ga,Mn)As/(Ga,In)As layers in relation to the magnetic anisotropy has been investigated.

3.2.3 Typical Growth Procedure

A 2" epi-ready GaAs (001) substrate is cutted into quarter wafers. A Molybdenum sample holder is placed on a hot-plate at 210°C to glue one of the quarter wafers with liquid Indium on the sample holder to ensure good thermal contact. The use of quarter wafers is based on homogeneity deviations in composition and thickness at the outer parts of a fully 2" wafer. This phenomenon is caused by a shadowing effect of the molecular beams by the N2-shroud opening, as described in Chapter A.2.1. A quarter wafer is glued almost completely inside a circle of 1", which shows homogeneous compositional and structural properties. Remaining dust is removed from the substrate surface by a Nitrogen jet. Then the sample holder is inserted into the UHV system at the load-lock. The sample is heated at around 300°C for 15 min and pumped by a scroll and turbo pump system. When the

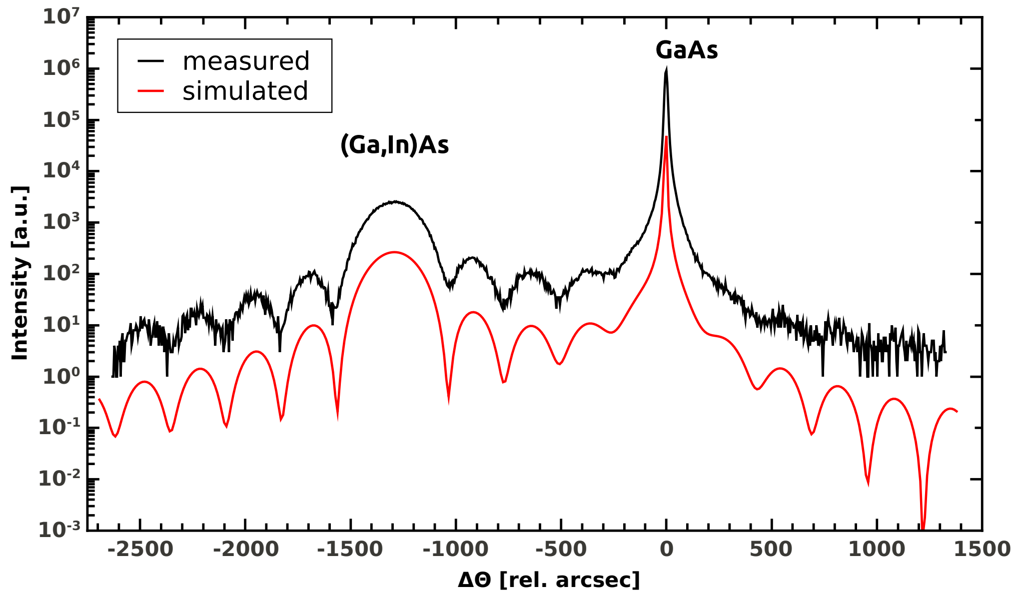

Figure 3.10: HRXRD measurement of (004) reflection of a nominal 70 nm (Ga,In)As reference layer grown on a GaAs (001) substrate (black curve). The simulation (red curve) offers an In content of $x_{In} = 0.071$ and layer thickness of $d_{(Ga,In)As} = 70 \pm 1 nm$. Thickness fringes reveal pseudomorphic growth with no plastic relaxation. The simulation has an offset for clarity.

pressure in the load-lock is low enough ($\approx 1 \times 10^{-7}$ torr) after heating, it can be transferred into the UHV MBE growth chamber.

In order to remove the remaining oxide layer on the substrate surface, the sample has been heated up to 620°C and stabilized for 15 min. While heating up the sample above the oxide desorption temperature of about 583°C [Spr87], the sample was kept under a constant As overpressure, beginning at 400°C, to prevent As desorption of the GaAs substrate. In RHEED, the phase transition was clearly visible, changing from a diffuse RHEED beam reflection of the oxide layer to the GaAs (2×4) surface reconstruction.

After the oxide desorption, the temperature was lowered and stabilized at 580°C. At this temperature, a high quality 200 nm GaAs buffer layer was grown to smoothen the substrate surface and bury defects as well as surface contaminations of the wafer. Depending on the next epitaxial grown layer, e.g. T_{sub} was lowered to 270°C for (Ga,Mn)As growth. The As-valve was closed at $T_{sub} = 570$°C to prevent the (2×4) surface reconstruction. For the growth of (Ga,In)As layers, the substrate temperature is typically lowered to 500°C.

The growth of (Al,Ga)As and AlAs was different according to the aforementioned procedures after the HT-GaAs buffer growth. T_{sub} was the same or increased after the buffer growth. Especially for the growth of the p-i-n structure of (Ga,Mn)As/AlAs/(Al,Ga)As/n-GaAs layers, (Al,Ga)As/AlAs layers have been grown at T_{sub} between 580 and 650°C.

When the epitaxial growth is completed, all fluxes are shut off simultaneously and the power output of the substrate heater is set to zero. When the sample has been cooled down to $T_{sub} \leq 200$°C, it has been transfered out of the growth chamber.

3.3 High Resolution X-Ray Diffraction

One of the most important ex-situ characterization method in this work is the high resolution x-ray diffraction (HRXRD) of thick layers. It yields lots of information for our epitaxial grown layers like crystal quality, material composition, layer thickness and strain situation. The characterization of epitaxially grown samples within the framwork of this thesis has been performed using a Philips X'Pert system with a 4-crystal Ge(220) Bartels monochromator and a 2-crystal analyzer (so-called triple-axis optics).

The diffraction geometry is given in Figure 3.11.

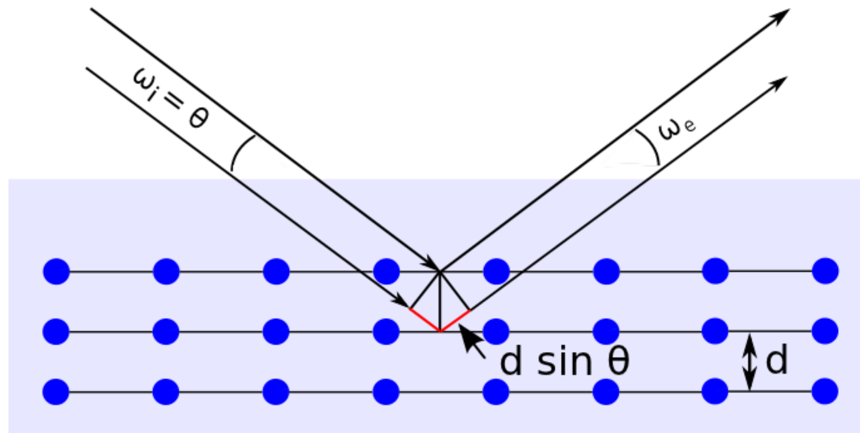

Figure 3.11: Bragg-reflection of parallel x-rays at lattice planes of a crystal to determine lattice plane spacing d. The red line indicates the path difference $2dsin(\Theta)$.

In principle, parallel x-rays with a wavelength $\lambda = 1.5405929$ $\AA$ (Cu K_α line of the x-ray source) are directed onto a sample where they enter the sample under an incident angle ω_i $(= \Theta)$ relative to the lattice planes of the sample with spacing d. Due to the law of reflection, the exit angle ω_e is equal to the incident angle ω_i. Considering the total angle between the incident x-ray beam and the detector, one gets twice the incident angle ω_i. This angle is commonly referred to as 2Θ. The condition for constructive interference of the x-rays, diffracted at atoms of neighboring lattice planes, is fulfilled if the path difference of two neighboring x-ray partial beams is an integer multiple of wavelength λ. This behavior is described by the Bragg-condition

$$n\lambda = 2d_{hkl}sin(\Theta) \qquad \text{with n} = 1,2,3,... \qquad , \tag{3.6}$$

where d_{hkl} corresponds to the spacing of diffracted lattice planes, described by Miller indices h, k, l and the diffraction angle is referred to as Θ. For a symmetric reflection, the incident angle is equal to the diffraction angle $\omega_i = \Theta$. A detailed description of the HRXRD method can be found in [Bow98].

3.3.1 $\omega-2\Theta$ Scans

A standard characterization of thick (Ga,Mn)As layers is the determination of the vertical lattice constant of the epitaxially grown layer. It provides the estimation of Mn content x and it gives also a feedback of the layer thickness as well as the crystal quality of the layers. In a cubic crystal, there are parallel lattice planes which are parallel to the sample surface. In general, the spacing d_{hkl} of two lattice planes (hkl) is defined as

$$d_{hkl} = \frac{d_{GaAs,(001)}}{\sqrt{h^2+k^2+l^2}}. \tag{3.7}$$

The separation of the (004) lattice plane is 1/4 of the bulk lattice constant $d_{GaAs,(001)}$, according to Equation 3.7 and therefore

$$d_{GaAs,(004)} = \frac{d_{GaAs,(001)}}{\sqrt{h^2+k^2+l^2}} = \frac{d_{GaAs,(001)}}{4} = 1.41\mathring{A}. \tag{3.8}$$

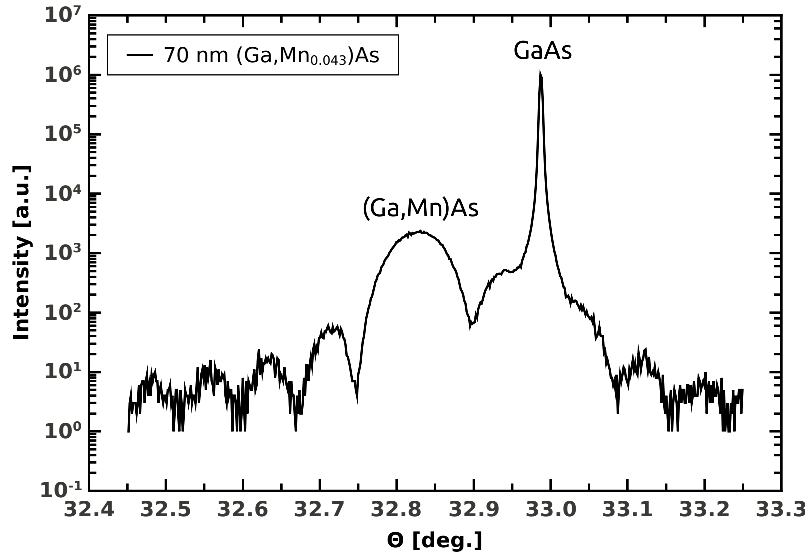

Figure 3.12: ω-2Θ scan of the (004) reflection of a 70 nm standard (Ga,Mn)As layer (nominal $x = 0.043$) grown on a GaAs substrate. The Θ deviation of the measured GaAs Bragg peak to the theoretical (004) Bragg peak at $\Theta = 33.02°$ is due to sample preparation into the X'Pert diffractometer.

Out of a symmetrical (004) diffraction pattern with (Ga,Mn)As on top of a GaAs substrate, as seen in Figure 3.12, the angle difference $\Delta\Theta$ between substrate peak Θ_{sub} and layer peak Θ_{lay} is determined by

$$\Delta\Theta = \Theta_{sub} - \Theta_{lay} = arcsin[\frac{\lambda}{2d_{sub,(004)}}] - arcsin[\frac{\lambda}{2d_{lay,(004)}}]. \tag{3.9}$$

The vertical lattice constant of the grown layer of the (001) lattice plane is calculated with the help of Equations 3.8 and 3.9 to

$$d_{lay,(001)} = 4 \cdot d_{lay,(004)} = 4 \cdot \frac{\lambda}{2sin[arcsin(\frac{\lambda}{2d_{sub,(004)}}) - \Delta\Theta]}. \qquad (3.10)$$

In case of an unstrained layer, this lattice constant $d_{lay,(001)}$ corresponds to the bulk lattice constant a_{bulk}. For pseudomorphic (Ga,Mn)As and other III-V alloys grown in this work with zincblende structure, an elastic deformation of the crystal lattice as seen in the upper part of Figure 3.14 takes place due to the pseudomorphic growth on a GaAs substrate. Up to a critical layer thickness of a grown material, $a_{\parallel} = a_{sub}$ is assumed, with $a_{\parallel}$ as the in-plane lattice constant and a_{sub} as the substrate lattice constant. The strain energy increases with increasing layer thickness. Passing the critical layer thickness, the accumulated strain energy in the layer is released by plastic relaxation, forming misfit dislocations. The bulk lattice constant a_{bulk} in a fully pseudomorphically strained layer has to be calculated out of the elastic properties of the grown material. This relation is described by the following formula [Res98]

$$a_{bulk} = \frac{1-\nu}{1+\nu}(a_{\perp} - a_{sub}) + \frac{2\nu}{1+\nu}(a_{\parallel} - a_{sub}) + a_{sub}, \qquad (3.11)$$

where ν is the Poisson ratio and $a_{\perp}$ is the vertical lattice constant of the layer material. All of the grown layers in this thesis are deposited pseudomorphically on (001) GaAs substrates without reaching the critical layer thickness to prevent high quality layers. With known vertical lattice constant $a_{\perp}$ out of a (004) ω-2Θ scan, Equation 3.11 can be expressed as

$$a_{bulk} = \frac{1-\nu}{1+\nu}(a_{\perp} - a_{sub}) + a_{sub}. \qquad (3.12)$$

The Poisson ratio ν of (Ga,Mn)As is assumed to be the same as for GaAs with $\nu = 0.310$, due to the fact that only a small percentage of Mn is incorporated in the crystal lattice of GaAs. For (Ga,In)As, the Poisson ratio with an Indium content of $x_{In} = 0.07$ is $\nu = 0.314$ while assuming a linear dependence of In content between GaAs and InAs, according to [Iof98].

ω-2Θ scans of thin layers ($< 10\ nm$) do not bear any layer informations, because the scattering volume is too low. Therefore, a statement about the estimation of defect concentrations is hence given for thick layers grown under the same nominal growth parameters. The estimation of defect densities in Chapter 4.1.3 and Appendix A.1 has been performed by analyzing the lattice parameter of bulk 70 nm (Ga,Mn)As layers.

Thickness Fringes

Besides the determination of the vertical lattice constant,an ω-2Θ scan bears information about the layer thickness. It can be calculated by the distance of neighboring interference thickness fringes of the diffraction pattern in the vicinity of the layer peak, as seen in Figure

3.12. The spacing of the fringes $\delta\Theta_f$ is related to the layer thickness d by the following formula [Bow98] as

$$\delta\Theta_f = \frac{\lambda}{2dcos(\Theta)}, \tag{3.13}$$

where λ is the used wavelength of the x-ray source and Θ is the average diffraction angle between two neighboring fringe peaks. The calculated layer thickness is used to determine the growth rate (with help of known opening times of cell shutters during growth), as well as RHEED intensity oscillations, see Chapter 3.1.

Determination of Mn Content

To determine the Mn content of a bulk layer (70 nm), ω-2Θ scans of the (004) Bragg reflection have been analyzed. As investigated and introduced by G.M. Schott, the calibration curve of Figure 3.13 is used for estimation of the Mn content x. Here, the vertical lattice constant of (Ga,Mn)As material is plotted versus the Mn content. The empirical formula of this calibration curve is given as

$$[Mn] = \frac{a_{\perp,(Ga,Mn)As} - 5.658\mathring{A}}{4.6667 \times 10^{-3}\mathring{A}} \qquad \text{in } \%. \tag{3.14}$$

The lattice constant increases with increasing Mn content and obeys Vegard's law, which describes the linear interpolation of the alloy lattice constant. The extrapolated MnAs lattice constant is given as 6.12 $\mathring{A}$. The accuracy of this method is about 1 % absolute.

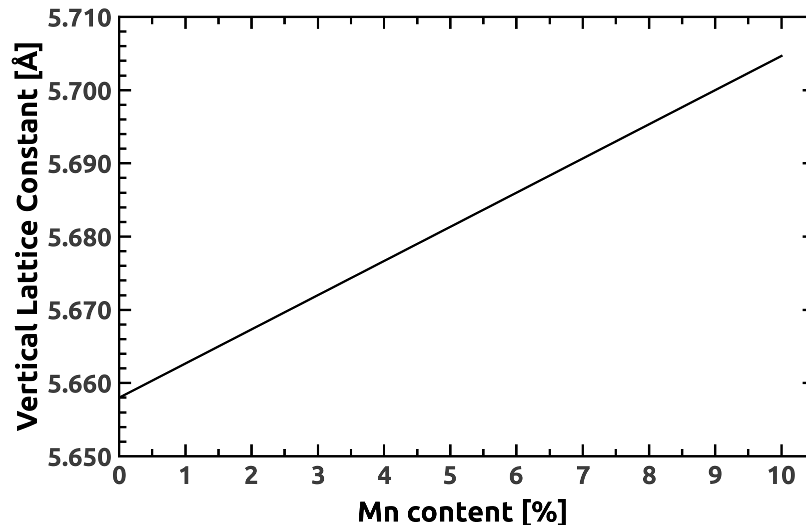

Figure 3.13: Relation between vertical lattice constant and Mn content as a calibration curve, introduced by G. M. Schott [Sch03, Sch04].

Lattice Expansion in LT-GaAs and (Ga,Mn)As

Point defects like arsenic antisites and Mn interstitials, caused by low temperature epitaxial growth far away from thermal equilibrium growth conditions, have a severe impact on the structural properties and due to its double donor character on the electric and magnetic properties of (Ga,Mn)As material.

A method to estimate As_{Ga} concentrations y in pure LT-GaAs material is published in [Liu95]. A lattice distortion associated with the substitution of Ga by As leads to a lattice expansion of LT-GaAs. The As-As bond even in a rhombohedral As crystal is slightly longer than the As-Ga bond, as noticed in [Del78]. Assuming volume conservation (Poisson effect) and taking a tetragonally strained LT-GaAs layer into account, a combination of HRXRD, near-infrared absorption (NIRA) and magnetic circular dichroism of absorption (MCDA) measurements has been used to determine the relative change of lattice parameter as a function of total As_{Ga} concentration (containing neutral $[As^0_{Ga}]$ and positively charged $[As^+_{Ga}]$) in the following equation

$$\begin{aligned} \left(\frac{\Delta a}{a_0}\right)_{rel} &= \frac{\Delta V}{V_0} = \frac{r^3 - r_0^3}{r_0^3} \cdot \frac{1}{2.2 \times 10^{22} cm^{-3}} [As_{Ga}] \\ \Leftrightarrow \qquad [As_{Ga}] &= \left(\frac{\Delta a}{a_0}\right)_{rel} \cdot \frac{r_0^3}{r^3 - r_0^3} \cdot 2.2 \times 10^{22} cm^{-3}, \end{aligned} \tag{3.15}$$

where $\left(\frac{\Delta a}{a_0}\right)_{rel}$ is the relative lattice change of the bulk lattice constant of LT-GaAs compared to the GaAs substrate ($a_{HT-GaAs} = 5.653\ \mathring{A}$), the Ga-As bond is given as $r_0 = 2.45\ \mathring{A}$, the As_{Ga}-As bond is given as $r = 2.65\ \mathring{A}$ and the factor of $2.2 \times 10^{22}\ cm^{-3}$ accounts from the amount of Ga atoms in a cubic centimeter of a pure GaAs crystal. In Figure 3.13, the LT-GaAs lattice constant (at $x = 0.000$) of $a_\perp = 5.658\ \mathring{A}$ or rather $a_{bulk} = 5.656\ \mathring{A}$, epitaxially grown at LT standard growth conditions ($T_{sub} = 270°$C and BEP ratio $(\frac{As_4}{Ga}) = 25$), corresponds to $[As_{Ga}] = 3.7 \times 10^{19}\ cm^{-3}$.

In (Ga,Mn)As material, point defect concentrations of As_{Ga} and Mn_{int} are prevalent. Density-functional theory (DFT) within the coherent potential approximation (CPA) has been applied to determine the relation between the lattice constant and concentrations of Mn on substitutional Mn_{sub} and interstitial Mn_{int} lattice sites as well as As on Ga sites As_{Ga} by minimizing the total energy of (Ga,Mn)As [Maš03]. Here, a GaAs crystal with small but finite concentrations of Mn_{sub}, Mn_{int} and As_{Ga} is assumed. The calculations reveal the following equation

$$a_{(Ga,Mn)As}(x_{sub}, y, x_{Int}) = a_{GaAs} + 0.02\mathring{A} \cdot x_{sub} + 0.69\mathring{A} \cdot y + 1.05\mathring{A} \cdot x_{Int} \qquad \text{in } \mathring{A}, \tag{3.16}$$

where $a_{HT-GaAs}$ is the well-known lattice constant of GaAs, x_{sub} is the Mn concentration on substitutional site, y is the Arsenic antisite concentration and x_{int} is the Mn concentration on interstitial site. A dependence of the lattice constant expansion due to

point defects of Mn_{int} and As_{Ga} and a neglectable increase of lattice constant by Mn on substitutional site has been pointed out. It is experimentally proven, that the incorporation of Mn interstitials increases linearly to the amount of incorporated Mn on Ga site [Kur04, Jun06]. The influence of Mn interstitials in equation 3.16 has been overestimated, as published two years later by Mašek et. al. [Maš05]. The lattice constant equation, recalculated by the full-potential linearized-augmented-plane-wave method, is given as

$$a_{(Ga,Mn)As}(x_{sub}, y, x_{int}) = a_{GaAs} - 0.05\mathring{A} \cdot x_{sub} + 0.46\mathring{A} \cdot y + 0.48\mathring{A} \cdot x_{int} \qquad \text{in } \mathring{A}. \quad (3.17)$$

Here, almost the same factors for y and x_{int} concentrations are prevalent. It is worth mentioning that, in Equation 3.17, the factor for x_{int} is about half of the factor stated in Equation 3.16 and x_{sub} slightly decreases the lattice constant of (Ga,Mn)As. The changed factors are caused by an overcoming of simplifications like atomic-sphere approximation and bulk lattice within DFT-CPA calculations. An estimation of As_{Ga} concentration by Equation 3.17 of pure LT-GaAs with $x_{sub} = 0$ and $x_{int} = 0$ ($a_{LT-GaAs,bulk} = 5.656\ \mathring{A}$) results in $[As_{Ga}] = 1.3 \times 10^{20}\ cm^{-3}$, which is a factor of three higher compared to Equation 3.15. The determination of As_{Ga} concentration out of lattice constants is therefore not as trivial as it seems, even in pure LT-GaAs material.

For (Ga,Mn)As material the bulk lattice constant $a_{bulk,ann}$ decreases after annealing and has been taken for an estimation of y. Transformation of Equation 3.17 to y (analogous with Equation 3.16) leads to

$$y = \frac{a_{bulk,ann} - a_{GaAs} + 0.05\mathring{A} \cdot x_{sub} - 0.48\mathring{A} \cdot x_{int}}{0.46\mathring{A}}. \quad (3.18)$$

It is obvious, that for a given $a_{bulk,ann}$, a higher residual Mn interstitial concentration x_{int} leads to a lower Arsenic antisite concentration y. The total amount of Mn interstitials cannot be extracted. Under assumption of a complete outdiffusion of Mn interstitials after the annealing procedure, x_{sub} as well as y stay constant and x_{int} becomes zero. Now, a maximum value of y_{max} can be estimated as

$$y_{max} = \frac{a_{bulk,ann} - a_{GaAs} + 0.05\mathring{A} \cdot x_{sub}}{0.46\mathring{A}}. \quad (3.19)$$

Furthermore, the relative change Δa of as-grown and annealed (Ga,Mn)As lattice constant ($a_{bulk,as-grown}$ and $a_{bulk,ann}$) has been used to estimate the relative change of Mn interstitial concentration Δx_{int} by Equation 3.17 (analogous with Equation 3.16) as

$$\begin{aligned} \Delta a &= a_{bulk,as-grown} - a_{bulk,ann} = 0.48\mathring{A} \cdot (x_{int,as-grown} - x_{int,ann}) \\ \Leftrightarrow \quad \Delta x_{int} &= (x_{int,as-grown} - x_{int,ann}) = \frac{a_{bulk,as-grown} - a_{bulk,ann}}{0.48\mathring{A}} = \frac{\Delta a}{0.48\mathring{A}}, \end{aligned} \quad (3.20)$$

whereas x_{sub} and y are assumed to remain unaffected by LT-annealing ($T_{ann} < 185°C$). A high value of Δx_{int} suggests a high concentration of incorporated Mn interstitials x_{int}, a

low value of Δx_{int} is interpreted as a low x_{int} in as-grown (Ga,Mn)As material. In Chapter 4.1, y and x_{int} will be determined for thick epitaxially grown (Ga,Mn)As layers at different growth parameters to provide a basis of growth conditions for a lowered As_{Ga} concentration in thin ($<10\ nm$) (Ga,Mn)As material.

3.3.2 Reciprocal Space Maps

The last section has shown, that ω-2Θ-scans of the symmetrical (004) reflection bear the measurement of the vertical lattice constant. Nevertheless, informations about the lateral lattice constants can only be obtained by a reciprocal space map (RSM) around an asymmetric reflection. A detailed description of RSM can be found in [Res98] and especially for (Ga,Mn)As layers in [Wen08] and [Ebe06].

The upper part of Figure 3.14 show the lattice constants of the unstrained (relaxed) bulk substrate (black), as well as a pseudomorphic grown layer (blue) and a relaxed grown layer (red) on a substrate. The in-plane (parallel) and vertical lattice constant for the substrate is given as a_{sub}. While growing epitaxially a layer with a larger relaxed lattice constant than the substrate, the in-plane lattice constant is lattice-matched to the substrate below the critical layer thickness and compressive strain in-the-plane is present. Due to the Poisson effect, the layer is tensile strained in growth direction meaning an extension of the vertical lattice constant is prevalent. When the critical layer thickness is exceeded, the layer relaxes plastically and its relaxed lattice constants in-plane and vertical remain larger than the substrate lattice constant. In reciprocal space, the lattice constant a corresponds to a reciprocal lattice constant, given as $\sim 1/a$. The middle part of Figure 3.14 illustrate the reciprocal lattice of all three cases, the substrate, a pseudomorphic layer and a relaxed layer. Compared to the substrate, the pseudomorphic layer has an equal in-plane lattice constant but a smaller vertical lattice constant. However, the relaxed layer has both a smaller in-plane and vertical lattice constant in reciprocal space compared to the substrate.

The combination of all three reciprocal lattices is illustrated in the lower part of Figure 3.14. Exemplary, the (115) reflection is taken to explain the behavior of relative peak positions of a pseudomorphic and relaxed layer compared to the substrate. In the zoomed region of the (115) reflection, the three peaks form a so-called relaxation triangle. The line between a pseudomorphic and a relaxed layer is called the line of relaxation. In case of a pseudomorphic layer, the peak is shifted along the surface normal. In case of a partially relaxed layer, the Bragg peak of the layer is situated on the line of relaxation. The peak of full relaxation is at the intersection of the relaxation line and the line pointing to the (000) reflection.

The degree of relaxation is defined as the ratio of the in-plane $\Delta a_{\parallel}$ and the relaxed Δa_{rel} lattice mismatch, both referred to the substrate [Wen08]:

$$\gamma = \frac{\Delta a_{\parallel}}{\Delta a_{rel}} = \frac{\frac{a_{\parallel} - a_{sub}}{a_{sub}}}{\frac{a_{rel} - a_{sub}}{a_{sub}}} = \frac{a_{\parallel} - a_{sub}}{a_{rel} - a_{sub}} \tag{3.21}$$

In case of a pseudomorphic layer, the degree of relaxation is $\gamma = 0$. The opposite case of a relaxed layer leads to a degree of relaxation of $\gamma = 1$. It is worth to mention, that all

HRXRD measurements are relative measurements related to the known lattice constant of the GaAs substrate. In the framework of this thesis, the GaAs substrate serves as a reference Bragg peak in ω-2Θ-scans and RSM.

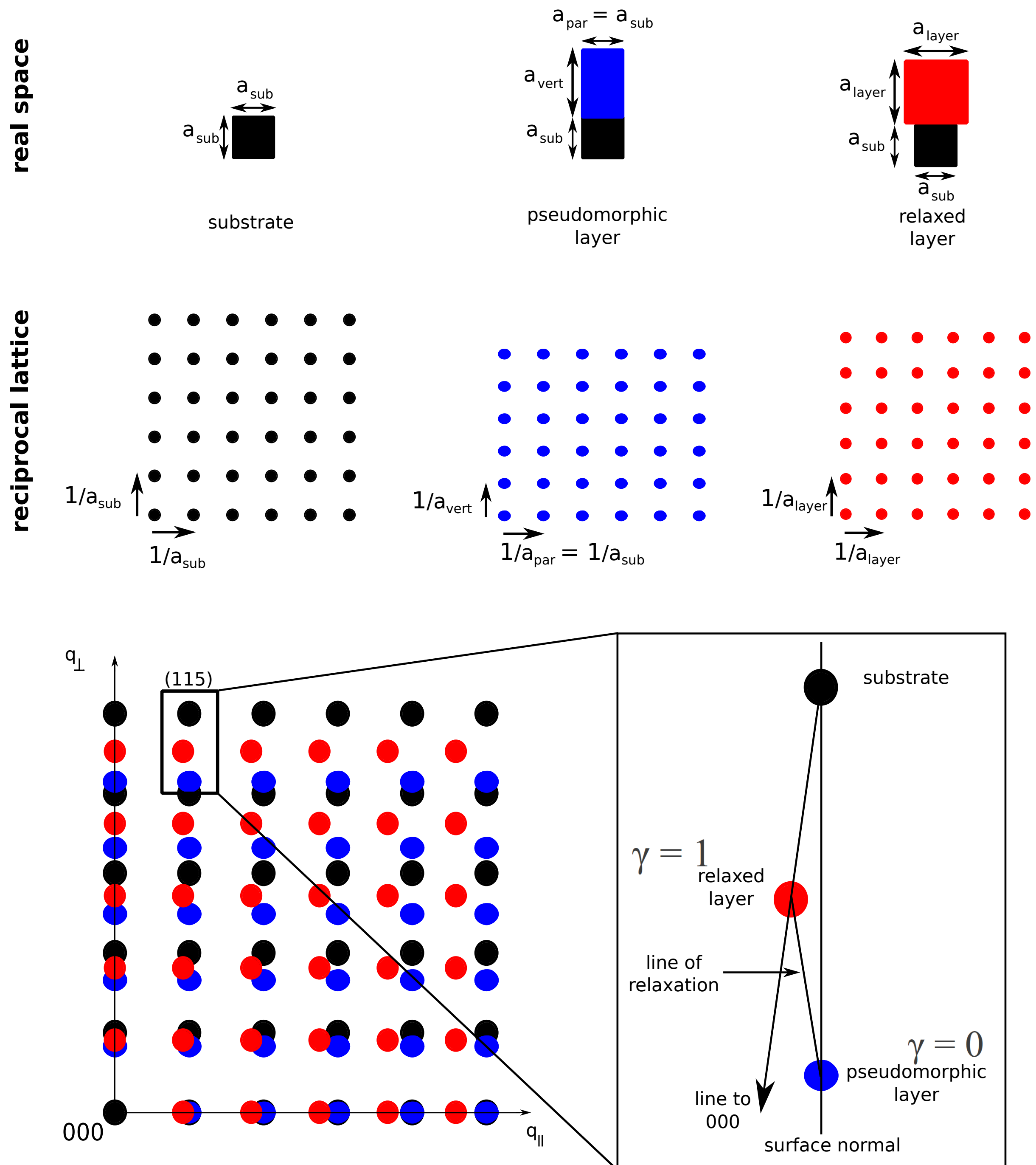

Figure 3.14: Upper part: Real space lattice constants of a substrate (black), a pseudomorphic layer (blue) and a relaxed layer (red). Middle part: corresponding reciprocal lattice for substrate, pseudomorphic layer and relayed layer. Lower part: Combination of reciprocal lattice points for the three cases with zoomed region of the asymmetrical (115) reflection and corresponding relaxation triangle.

3.4 Superconducting Quantum Interference Device

A powerful tool to quantify the magnetization of (Ga,Mn)As layers is the superconducting quantum interference device (SQUID) magnetometer. This method of characterization provides a highly accurate measurement of very small changes in magnetic flux at temperatures between 1.9 up to 400 K.
The SQUID consists of superconducting detection coils which are connected via superconducting wires to the SQUID sensor. The detection coils are mounted around the sample chamber and in the center of a superconducting external magnet. External H fields of ± 5 T can be applied. In principle, the sample is mounted in a nonmagnetic stick which moves the sample through the detection coils during a measurement. The magnetic moment of the sample is not measured directly. The magnetic field of the sample causes an electrical induction current in the detection coils which are connected to another magnetic coil. This causes a magnetic field inside the SQUID sensor, which consists of a superconducting material with two Josephson-contacts. Cooper pairs can tunnel through the Josephson-contacts up to a critical current, where no voltage drop is present. The induced current, detected by the SQUID sensor, is proportional to the magnetic flux changes. The magnetic flux must be an integer number of the magnetic flux quantum $\Phi_0 = \frac{h}{2e} = 2.0678 \cdot 10^{-15}$ Wb. Basically, the SQUID sensor is a current-voltage converter which transforms current changes in the detection coils to a periodic output voltage corresponding to a changing magnetic flux. The periodicity is equal to one magnetic flux quantum. The sensitivity of a SQUID is denoted in emu (electromagnetic unit, 1 $emu = 10^{-3}$ Am^2) and amounts $\geq 5 \times 10^{-8}$ emu.

The epitaxially grown samples have been characterized by two types of measurements: The T-dependent magnetization M(T) and the magnetic field dependence of magnetization M(H) in different crystal directions at constant temperature ($T = 4.2K$ in general).

A result of the first type of measurement is presented in Figure 3.15(a). The T-dependent magnetization M_{rem} decreases with increasing temperature T. At the Curie-temperature T_C, the long range ferromagnetic order vanishes and the Curie-Weiss paramagnetic phase takes place. The extracted value of $T_C \approx 64$ K is typical for a standard as-grown 70 nm (Ga,Mn)As layer with a Mn content of $x = 0.028$.

The second type of measurement collects the hysteresis loop at a constant temperature in different crystal directions (in most cases measured along an easy axis [100] or [010]). Exemplary, the result with applied magnetic field along an easy axis for a standard 70 nm (Ga,Mn)As layer is shown in Figure 3.15(b). In this graph, the diamagnetic signal of the GaAs substrate is subtracted after determining the slope of the hysteresis loop at high magnetic fields, where the magnetization behaves almost linear.

In order to measure the hysteresis loop of an easy axis ([100] or [010]) or hard axis ([110] or [$1\bar{1}0$]), the external applied magnetic field has to be aligned parallel to the designated crystal direction. The magnetization vector switches to the opposite direction when the applied magnetic field is switched by 180°. However, the absolute values of M_{sat} for the antiparallel magnetization directions are equal. In case of a measurement with high magnetic fields along a hard axis, the magnetization vector is directed along the hard axis

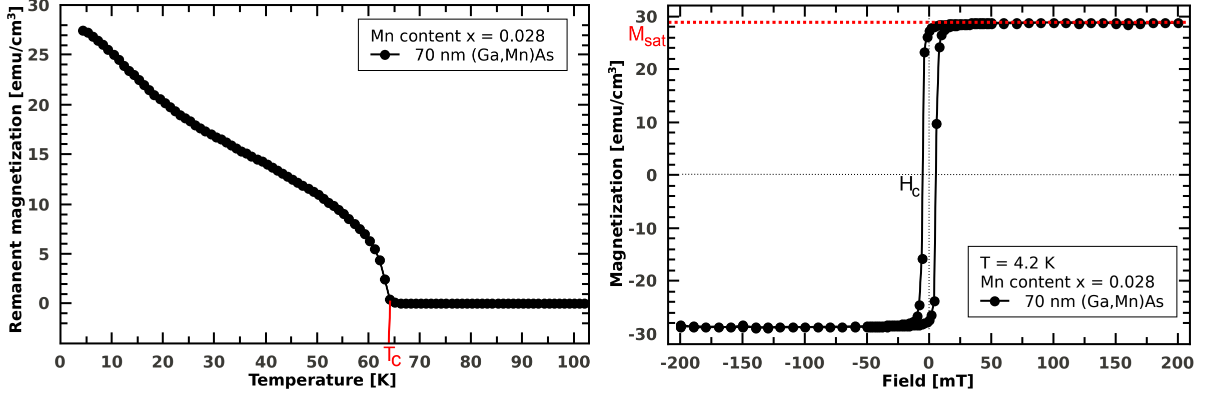

Figure 3.15: (a) T-dependent magnetization curve and (b) hysteresis curve along an easy axis direction ([100] or [010]) after subtraction of the diamagnetic signal of a 70 nm standard layer with a nominal Mn content of $x = 0.028$. The phase transition from ferromagnetic to paramagnetic phase is indicated as a red line at $T_C \approx 64\ K$. The saturation magnetization M_{sat} of a sample is taken by drawing a line of the magnetization at high fields (red dotted line). The calculated Mn content out of equation 3.24 corresponds to $x = 0.028$.

and $M_{sat,hard}$ is equal to $M_{sat,easy}$. A reduction of the applied magnetic field leads to a rotation of the magnetization direction towards the easy axis. The absolute value of the magnetization is determined by a projection onto the hard axis. In case of a zero applied magnetic field, the magnetization vector is directed along the easy axis, as illustrated in Figure 3.16.

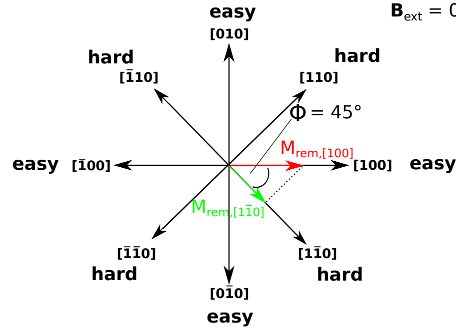

Figure 3.16: Sketch of in-plane crystal directions and magnetic easy axes and hard axes directions in (Ga,Mn)As at T = 4.2 K. The remanent magnetization $M_{rem,[100]}$ (red arrow) at zero applied magnetic field is aligned along the [100] easy axis. $M_{rem,[1\bar{1}0]}$ (green arrow) along the $[1\bar{1}0]$ hard axis is the projection of $M_{rem,[100]}$ onto the $[1\bar{1}0]$ crystal direction.

Quantitatively, the ratio of remanent magnetizations along the easy axis or hard axis (e.g. [100] and $[1\bar{1}0]$) at zero applied magnetic field is expressed as

$$\frac{M_{rem,easy}}{M_{rem,hard}} = \frac{1}{cos(\Phi)}. \tag{3.22}$$

Equation 3.22 is used to determine the angle Φ between easy and hard axis in (Ga,Mn)As material out of hysteresis loop measurements along easy and hard axis direction. In case of a mainly biaxial magnetic anisotropy, this angle is $\Phi = 45°$ and the result of Equation 3.22 is $\sqrt{2}$. The LT-saturation magnetization M_{sat} of a (Ga,Mn)As layer can be expressed by

$$M_{sat} = N_{Mn} g \mu_B S_{Mn} \qquad \text{in } [\frac{emu}{cm^3}], \tag{3.23}$$

where N_{Mn} is the nominal Mn concentration in cm^{-3}, $g = 2$ is the g-factor of Mn, $\mu_B = 9.274 \cdot 10^{-21}$ emu is the Bohr magneton and S_{Mn} is the spin of Mn. Possible values S_{Mn} are $\frac{5}{2}$ in Mn^{2+} configuration and $\frac{4}{2}$ in Mn^{3+} configuration [Ohn99]. Here, the idealized value of $S_{Mn} = \frac{5}{2}$ is used. Rearrangement of Equation 3.23 to N_{Mn} leads to

$$N_{Mn} = \frac{M_{sat}}{g \mu_B S_{Mn}} \qquad \text{in } [\frac{1}{cm^3}]. \tag{3.24}$$

Equation 3.24 can be used as an alternative method besides the HRXRD measurement to determine the Mn concentration. The measured magnetization in emu is divided by the volume of the sample V_{GaMnAs} in cm^3 (length and width of the SQUID sample is measured by a caliper, the sample thickness is known due to the growth rate and/or thickness determination by HRXRD measurements). Entering $M_{sat} = 28.8 \frac{emu}{cm^3}$ of the hysteresis curve (Figure 3.15(b)) with a known (Ga,Mn)As sample volume of $V_{GaMnAs} = 5.84 \cdot 10^{-7}$ cm^3 into Equation 3.24, the result of $N_{Mn} \approx 6.2 \cdot 10^{20}$ cm^{-3} leads to a Mn content of $x = 0.028$. The coercive field H_C of ≈ 5 mT corresponds to typical values of H_C of (Ga,Mn)As layers grown in Würzburg (up to 20 mT), as published in [Gou08].

Within the framework of this thesis, a comparison of Mn content from HRXRD and SQUID measurements did not show a clear trend. The HRXRD method is an indirect estimation of Mn content x by determination of the lattice constant expansion of (Ga,Mn)As which is strongly influenced by point defects like As_{Ga} and Mn_{int}. The determination of x by SQUID is a direct measurement of the total magnetic moment of the sample, where all free and non-compensated magnetic moments of Mn atoms participate. As will be presented in Chapter 5.3, both methods show a high accordance in determination of x of the same sample. In contrast, other samples have shown higher x determined by HRXRD. An explanation of a lower x measured by SQUID is given as follows: Substitutional Mn atoms with aligned magnetic moments participate in the longe range ferromagnetic order. A decrease of the saturation magnetization is caused by an antiferromagnetic coupling of magnetic moments between Mn interstitials and substitutional Mn. So, the calculated x is lower compared to HRXRD measurements. Annealing of (Ga,Mn)As material leads to an outdiffusion of Mn_{int}. As a consequence, the observed saturation magnetization increases (as well as T_C) and the recalculated Mn content x will be closer to the real value, as published elsewhere [Edm04]. Nevertheless the reproducibility of (Ga,Mn)As material grown under stable growth conditions is of interest for exploitation of magnetic properties by e.g. photolithographically fabricated nanostructures, more than the exact, absolute value of x.

3.5 Four-Terminal Transport Measurements @ RT and LT

An important property of (Ga,Mn)As material is the electrical conductance (even at low temperatures) due to the p-doping of the GaAs crystal with Mn impurities. For the characterization of (Ga,Mn)As layers, a standard characterization besides HRXRD and magnetometry measurements is the determination of the resistivity/conductivity at RT and LT. For that reason, a Hallbar is processed photolithographically to get a defined current path through the (Ga,Mn)As layer. The layout of a standard Hallbar is plotted in Figure 3.17(a).

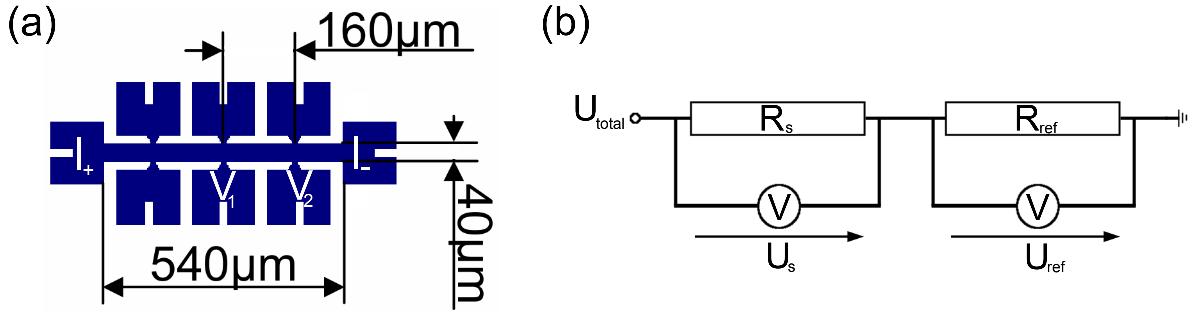

Figure 3.17: (a) Layout of a standard Hallbar, which is used for all transport measurements in this work. (b) equivalent circuit of the measuring setup, used for RT and LT transport measurements in a conventional ^{4}He can.

The current path from I_+ to I_- is along a 40 μm wide and 540 μm long stripe. The longitudinal resistance R_{xx} is measured between V_1 and V_2, which has a distance of 160 μm. The general equation for the resistivity ρ_{xx} is given as

$$\rho_{xx} = R_{xx} \cdot \frac{A}{l} = R_{xx} \cdot \frac{d_{layer} \cdot w}{l}, \tag{3.25}$$

where the cross section A of the current path, d_{layer} is the thickness of the (Ga,Mn)As layer and w is the width of the stripe. The ratio of length and width of the current path between V_1 and V_2 is 4:1. Commonly, R_{xx} is stated as resistance per square $R_\square$. So, R_{xx} is devided by 4 to get $R_\square$. In summary, the resistivity ρ_{xx} is given as follows

$$\rho_{xx} = \frac{R_{xx}}{4} \cdot d_{layer} = R_\square \cdot d_{layer} \qquad \text{in } [\Omega \cdot cm]. \tag{3.26}$$

The conductivity (in our case for hole carriers) is defined as

$$\sigma = \frac{1}{\rho_{xx}} = pe\mu \qquad \text{in } [\frac{1}{\Omega \cdot cm}], \tag{3.27}$$

where p is the hole concentration in $[cm^{-3}]$, e is the elementary charge with $1.602 \cdot 10^{-19} C$ and μ the mobility in $[\frac{cm^2}{Vs}]$. Because of the anomalous Hall effect due to high doping

concentrations (10^{20} to 10^{21} cm^{-3}), the determination of the hole concentration is very difficult in (Ga,Mn)As (see Chapter 2.3.1). In Equation 3.27, the carrier concentration as well as the mobility of holes are considered with an uncertainty. Thus, conductivity measurements at RT and LT have been sufficient in most cases for the characterization of (Ga,Mn)As layers. Nevertheless, Hall resistances under small magnetic fields ($\approx$ 80 mT) have been measured for some sample series to estimate RT hole carrier concentrations. The LT-transport measurements have been done in a conventional ^{4}He can with a so-called dipstick. The sample is mounted within a chip carrier at the tip of the dipstick. The equivalent circuit of the measuring setup in series connection is illustrated in Figure 3.17(b). In a series connection, the relation for the current is given as

$$I_{total} = I_s = I_{ref}. \tag{3.28}$$

According to Ohm's law, the longitudinal resistance of the sample $R_s = R_{xx}$ is

$$R_s = R_{xx} = \frac{U_s}{I_{ref}} = U_s \cdot \frac{R_{ref}}{U_{ref}}. \tag{3.29}$$

With known reference resistance R_{ref} (same magnitude like the sample resistance) and measured voltage drops at the sample U_s and at the reference voltage U_{ref}, the resistance of the sample $R_s = R_{xx}$ is calculated.

First of all, 2- and 4-terminal resistances are checked at RT by collecting an I-V curve from 0 to 100 mV in steps of 20 mV. The same procedure has been repeated at LT when the sample has been floated in liquid Helium and stabilized at 4.2 K. In order to collect a cooling curve in 4-terminal Hallbar geometry, 10 mV were applied during the whole cooling process while putting the dipstick slowly into the ^4He can. A cooling curve of a 70 nm (Ga,Mn)As layer grown at standard growth conditions is shown in Figure 3.18.

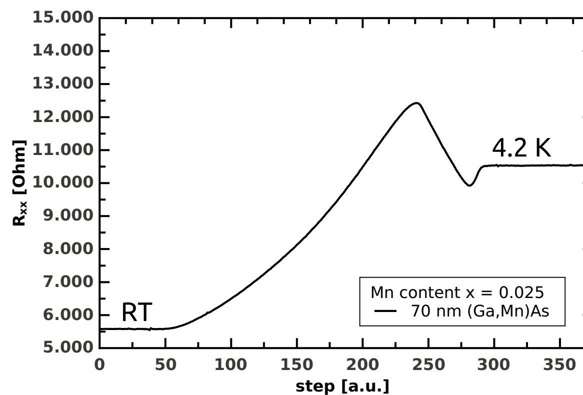

Figure 3.18: Cooling curve of a 70 nm (Ga,Mn)As layer with nominal $x = 0.025$ and mainly biaxial magnetic anisotropy. The RT- and 4K- resistances R_{xx} are marked. The LT resistance value is slightly closer to the maximum of the resistance than the RT resistance value.

A rule of thumb value for the resistance per square $R_\square$ at 4.2 K is ~ 1 $kOhm$ for a 70 nm thick layer with a Mn content of $x \approx 0.035$.

The advantage of a 4-terminal longitudinal resistance measurement is that contact resistances are neglected. The measured signal is the potential difference between the two measuring contacts. In 2-terminal resistance measurements, contact resistances lead to a stronger variation of resistance values.

Resistance measurements by measuring probes

The last paragraph has shown, that 4-terminal longitudinal layer resistance measurements in Hallbar geometry were the standard characterization method to measure reliable values of R_{xx}. Nevertheless, a quick feedback of electrical properties directly after the epitaxial growth of the sample without processing a Hallbar when needed. In this case, a multimeter Metex-M 3630 with two measuring probes and adjustable resistance ranges has been used. The resistance of the sample was checked by holding the measuring probes on the sample surface, as close as possible together ($<$1 mm). This kind of measurement is surprisingly reliable (resistance deviation around 10%) but on the other side it has disadvantages like distance and pressure variation of the measuring probes on the sample and an undefined current path through the sample. Additionally, it has been necessary to measure resistances right after removement of the epitaxial grown sample from the molybdenum block, because an oxide layer would increase the contact resistance of the layer and the comparison of different samples is less reliable. Therefore, special care was necessary and several resistance measurements at different places on a sample have been performed right after the growth.

The resistance measurement by measuring probes has been performed e.g. for measuring the resistance during the annealing procedure and directly after growth of a 70 nm layer series to get a parameter range of T_{sub} for optimizing the growth of very thin layers with a constant Mn content in Chapter 5.3. The 4-terminal longitudinal resistance measurement in Hallbar geometry and the resistance measurement by measuring probes has been compared in Chapter 4.1.2 to demonstrate reliability.

Chapter 4

Bulk and Thin (Ga,Mn)As Layers

In principle two kinds of (Ga,Mn)As layers have been grown in this work, bulk and thin layers. In Chapter 2.3, epitaxially grown bulk (Ga,Mn)As material at standard growth conditions (see Chapter 3.2.1) with its reproducible magnetic anisotropies was presented. Since many years bulk (Ga,Mn)As layers have been exploited successfully to change their magnetic properties e.g. by uniaxial strain relaxation of nanopatterned stripes or nanopatterning device structures to change magnetic properties by applied currents [Wen07, Pap07b, Mar11]. The growth of bulk material with reproducible properties is quite well under control.

One main task of this work was to get an improved comprehension of the complex behavior between the growth parameters and the resulting ferromagnetic and transport properties. Although the growth parameters of epitaxially grown (Ga,Mn)As have been investigated by several groups over many years, it was necessary to validate certain published results like stoichiometric growth border, influence of substrate temperature as well as BEP ratio ($\frac{As_4}{Ga}$) dependence on magnetic and transport properties. This step was required particularly due to a different MBE growth chamber geometry and equipment leading to slightly different growth conditions (e.g. As_4 molecules instead of As_2). Additionally, the characterization methods to determine the Mn content differ between research groups. This preliminary work provides a basis to optimize growth conditions for an improvement of magnetic and especially electric properties of very thin (Ga,Mn)As layers, as will be demonstrated in Chapter 5.

The second part of Chapter 4 reflects the very first efforts of very thin (Ga,Mn)As layers ($\leq$10 nm), which have been epitaxially grown in the EP III department at the University of Würzburg.

4.1 Epitaxial Growth of Bulk (Ga,Mn)As at Different Growth Conditions

70 *nm* (Ga,Mn)As layers, which are epitaxially grown at standard growth conditions (see Chapter 3.2.1) of $T_{sub} = 270°C$ and BEP ratio ($\frac{As_4}{Ga}$)= 25, show a mainly biaxial magnetic

anisotropy and have been successfully exploited to influence their magnetic properties. One recently published application example is described in chapter 6.

The investigation of growth conditions like substrate temperature T_{sub} and BEP ratio ($\frac{As_4}{Ga}$) with its resulting magnetic and transport properties on thick 70 nm (Ga,Mn)As layers is a principle issue in this section. The in-situ characterization has been performed by RHEED pattern observations during the epitaxial growth. Ex-situ characterizations by SQUID, HRXRD and RT-transport measurements were the choicen methods. Compared to very thin layers, it is easier to characterize bulk layers with these techniques due to a sufficiently scattering volume for x-ray diffraction and less influences of interface and surface effects.

4.1.1 Variation of Substrate Temperature and BEP ratio ($\frac{As_4}{Ga}$)

Sample series of epitaxially grown (Ga,Mn)As layers have been deposited at different substrate temperatures T_{sub} = 200°C, 220°C and 270°C with varied BEP ratios ($\frac{As_4}{Ga}$). According to calibration samples in combination with the rule of thumb for a doubling of Mn content, as presented in Chapter 3.2.1, (Ga,Mn)As layers at T_{sub} = 200°C and 220°C with nominally $x = 0.09$ and $x = 0.08$ have been epitaxially grown. In the third sample series grown at T_{sub} = 270°C, a lowered Mn content of $x = 0.05$ has been used to avoid excess of the solubility limit of Mn which would result in a segregation of Mn and/or MnAs cluster formation. The solubility limit for standard 70 nm (Ga,Mn)As layers epitaxially grown at T_{sub} = 270°C and a BEP ratio ($\frac{As_4}{Ga}$)= 25 lies between $0.06 < x < 0.07$. Table 4.1 offers an overview of the sample series.

During the epitaxial growth of all samples, the sample surface has been monitored by the in-situ RHEED technique. Different RHEED patterns of typical (1×2) surface reconstruction for 2D growth mode and spotty (1×2) RHEED patterns for 3D growth mode have been observed, as presented in Figure 4.1(a) and (b).

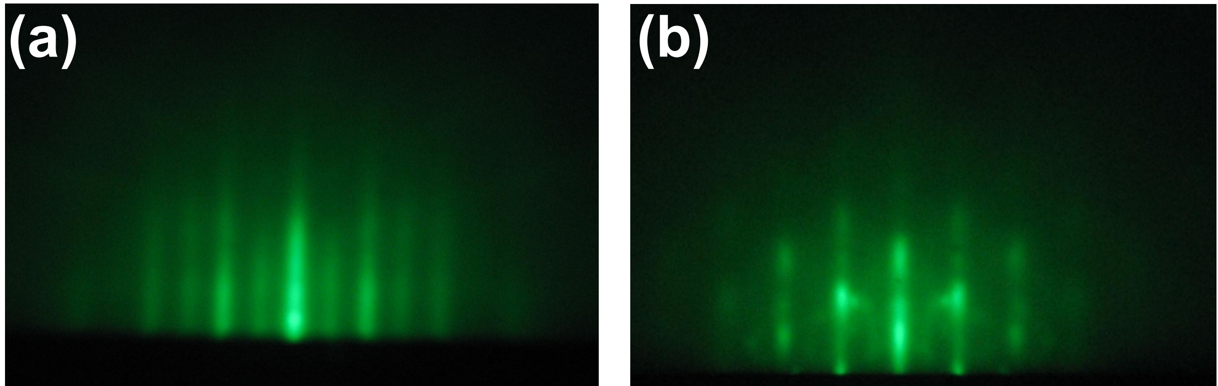

Figure 4.1: (Ga,Mn)As RHEED pattern of (a) a streaky (1 × 2) surface reconstruction presenting a 2D growth mode and (b) a spotty (1 × 2) surface reconstruction of a 3D growth mode due to a roughening of the sample surface.

Sample No.	nominal x	T$_{sub}$ [°C]	BEP ratio ($\frac{As_4}{Ga}$)	RHEED
S500	0.09	200	5.0	3D after 30 sec
S523	0.09	200	6.0	(1×2)
S496	0.09	200	7.5	(1×2)
S499	0.09	200	10.0	(1×2)
S502	0.09	200	12.5	(1×2)
S501	0.09	200	15.0	(1×2)
S563	0.08	220	5.2	3D after 30 sec
S567	0.08	220	5.8	3D after 76 sec
S568	0.08	220	6.0	3D after 180 sec
S558	0.08	220	6.1	3D after 360 sec
S559	0.08	220	6.5	(1×2)
S561	0.08	220	7.1	(1×2)
S560	0.08	220	7.5	(1×2)
S557	0.08	220	9.0	(1×2)
S605	0.05	270	14.5	3D after 20 sec
S606	0.05	270	15.1	(1×2)
S607	0.05	270	16.0	(1×2)
S604	0.05	270	19.6	(1×2)
S603	0.05	270	24.2	(1×2)

Table 4.1: Sample series of 70 nm (Ga,Mn)As layers with varied substrate temperature and varied BEP ratio ($\frac{As_4}{Ga}$). The sample series grown at T_{sub} = 270°C has a significant lower Mn content x than the other sample series.

Starting at As-rich growth conditions with an excess of As_4 overpressure for the growth of (Ga,Mn)As material in 2D growth mode, a decrease of BEP ratio ($\frac{As_4}{Ga}$) equals stoichiometric growth conditions where no excess As is incorporated as Arsenic antisite. Experimentally shown by several groups, the properties of such grown material very close to the 2D/3D growth border seems to be improved caused by a minimization of Arsenic antisite incorporation [Cam03, Mye06, Mac08]. Here, $[As_{Ga}] \approx 0$ is assumed. A further decrease of BEP ratio ($\frac{As_4}{Ga}$) leads to Ga-rich growth conditions, where extended defects are formed and a roughening of the sample surface is prevalent. As a result, a spotty RHEED pattern has been observed, as reported in [Avr05]. A second dependency of BEP ratio ($\frac{As_4}{Ga}$) is notable: The closer the epitaxial growth of (Ga,Mn)As material takes place at the 2D/3D growth border by a decrease of BEP ratio ($\frac{As_4}{Ga}$), the faster a roughening of the sample surface during growth begins. In the second growth series of Table 4.1, the BEP ratio ($\frac{As_4}{Ga}$) has been reduced in small steps close to the 2D/3D growth border. For epitaxially grown LT-GaAs material under Ga-rich growth conditions, Ga droplets are formed at the surface, as investigated by [Mye06].

There is a trend of a shift of the 2D/3D growth border to higher BEP ratio ($\frac{As_4}{Ga}$) for higher T_{sub}. For low substrate temperatures at $T_{sub} = 200°C$ with $x = 0.09$ and 220°C with $x = 0.08$, the threshold BEP ratio ($\frac{As_4}{Ga}$) increases slightly from approximately 6 to 6.5. In case of the growth series at $T_{sub} = 270°C$ with a lowered nominal $x = 0.05$ below the solubility limit of Mn, the 2D/3D growth border has been observed at a threshold BEP ratio ($\frac{As_4}{Ga}$) of about 15.

4.1.2 Magnetometry and RT-Transport Measurements

A standard characterization of an important parameter of the ferromagnetic properties of (Ga,Mn)As is the determination of the Curie temperature T_C by SQUID magnetometry measurements. T_C depends on the cubic root of the hole concentration p (Equation 2.1). Both, the resistivity ρ_{xx} and conductivity σ are connected with p by Equation 2.29.

Sample Series Grown at $T_{sub} = 200°C$

The SQUID results of the first growth series are shown in Figure 4.2 (a) where Curie temperature T_C is plotted as a function of BEP ratio ($\frac{As_4}{Ga}$). After measurements of as-grown T_Cs (black), the samples have been annealed at an annealing temperature of 185°C for 144 hrs, as described in Chapter 3.2.1. Then, T_C has been measured again (red). The gray-shaded bar corresponds to the growth region of BEP ratio ($\frac{As_4}{Ga}$), where the growth mode changes from 2D to 3D, as observed in RHEED diffraction patterns during growth. Here, T_C has the highest value very close to the growth border. Beyond this border, extended formation of defects (like Ga droplets [Mye06]) and a roughening of the surface during growth takes place, which leads to a very strong compensation of hole carriers and therefore to a suppression of a carrier-mediated ferromagnetism in this layer. The sample with BEP ratio ($\frac{As_4}{Ga}$)= 5 had no ferromagnetic response. With increasing BEP ratio ($\frac{As_4}{Ga}$) away from the growth border, T_C decreases. The sample with highest BEP ratio ($\frac{As_4}{Ga}$)= 15

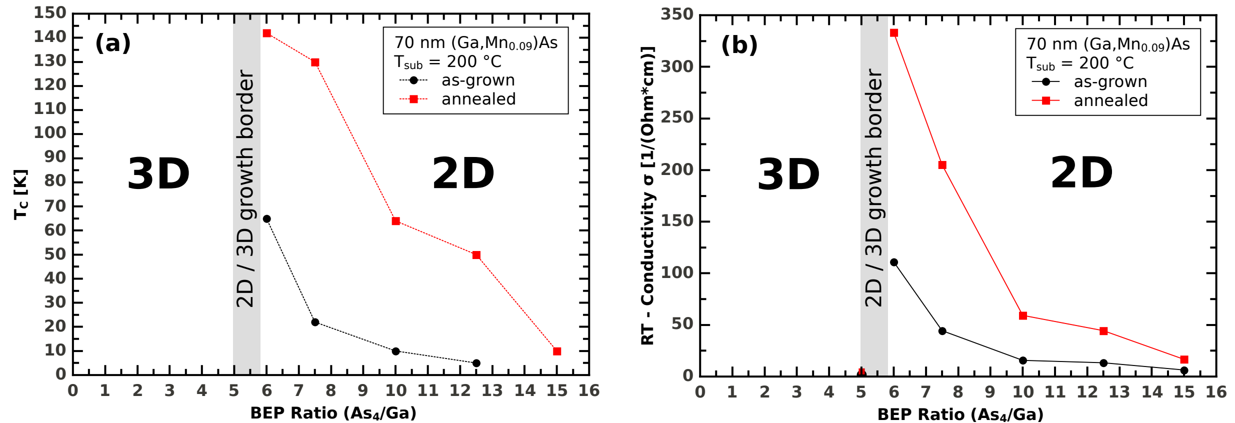

Figure 4.2: (a) Extracted Curie temperatures as well as (b) RT-conductivity σ plotted as a function of BEP ratio ($\frac{As_4}{Ga}$) for 70 nm (Ga,$Mn_{0.09}$)As layers grown at $T_{sub} = 200°C$ as-grown (black) and after annealing (red) at $T_{ann} = 185°C$ for 144 hrs. The gray bar indicates the growth border between layer-by-layer (2D) growth and a growth with roughened sample surface (3D). Highest T_C and RT-conductivity σ is achieved close to the growth border.

did not show any ferromagnetic response. This behavior can be understood as an excess incorporation of compensating defects with increasing BEP ratio ($\frac{As_4}{Ga}$), most likely As_{Ga}. The red points of Figure 4.2 correspond to the results of the annealed samples. The outdiffusion of Mn on interstitial sites leads to much higher T_C values compared to the as-grown values. For the sample with highest T_C = 142 K, the difference in T_C amounts to a factor of >2. Even the sample with highest BEP ratio ($\frac{As_4}{Ga}$)= 15 in the sample series shows a ferromagnetic response with $T_C = 10\ K$ after annealing. It demonstrates the effective reduction of the compensating defect Mn_{int} by annealing procedures.

Figure 4.2 (b) shows the RT-conductivity σ as a function of BEP ratio ($\frac{As_4}{Ga}$). The measurement results of as-grown (black) and annealed (red) samples show the same trend as for T_C. At the growth border, RT-σ reaches its maximum value then decreases with increasing BEP ratio. In this region, a RT-conductivity after annealing with a maximum value of about 333 $\frac{1}{\Omega \cdot cm}$ is mentionable. This value is ten times higher than the RT-conductivity value of a standard 70 nm (Ga,Mn)As layer with a Mn content of $x = 0.045$. An explanation of this high RT-conductivity value might be a relative high Mn content connected with the minimization of As Antisites by near-stoichiometric growth conditions.

It is known, that the determination of the carrier concentration is quite difficult due to the anomalous Hall effect, see Chapter 2.3.1. Nevertheless, the RT-hole concentrations p of the annealed samples of the sample series with $T_{sub} = 200°C$ have been determined. The result is plotted in Figure 4.3.

Again, the highest value of p is observed close to the 2D/3D growth border and the carrier concentration decreases with increasing BEP ratio ($\frac{As_4}{Ga}$). The maximum value of $p = 1.9 \times 10^{20} cm^{-3}$ corresponds to an activation fraction of about 10 %, under assumption of a nominal Mn concentration of $x = 0.09$. The doping efficiency lies in the range between 10 and 30 %, as mentioned in [Die01, Maš03, Jun05]. Compared to a standard layer with

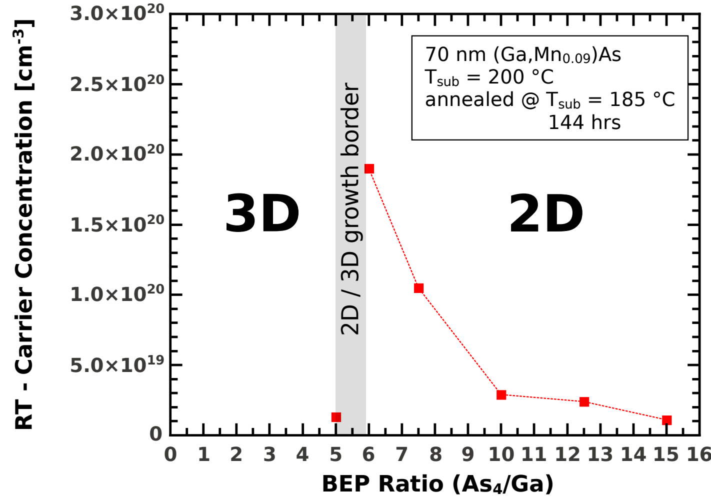

Figure 4.3: RT-carrier concentration of annealed sample series grown at $T_{sub} = 200°C$ as a function of BEP ratio ($\frac{As_4}{Ga}$). The carrier concentration has its maximum at the 2D/3D growth border, which is consistent with SQUID and RT-conductivity measurements.

nominal Mn content of $x = 0.045$ ($p = 1.1 \times 10^{20} cm^{-3}$), the RT-$p$ value is about two times higher.

In the last paragraph of Chapter 3.5, a quick and alternative method of measuring resistances of (Ga,Mn)As samples has been described. Figure 4.4 shows the RT-conductivity measurements σ in 4-terminal Hallbar geometry and the RT-resistance measurements by two measuring probes right after the growth of the as-grown sample. The reciprocal value of resistance of the multimeter method has been multiplied by the reciprocal layer thickness d for a better comparison between these two measurement techniques. In both cases, low conductivity values ($\sigma = 2 \frac{1}{\Omega \cdot cm}$ and $\frac{1}{R \cdot d} = 11 \frac{1}{\Omega \cdot cm}$) in the 3D growth region with a low BEP ratio ($\frac{As_4}{Ga}$)$= 5$ is prevalent. At the 2D/3D growth border, highest conductivity values of $\sigma = 119 \frac{1}{\Omega \cdot cm}$ and $476 \frac{1}{\Omega \cdot cm}$ have been measured. The decrease of conductivity with an increasing BEP ratio ($\frac{As_4}{Ga}$) is most likely caused by an increased incorporation of arsenic antisites. The trend is comparable for both measurement techniques. Based on this result, the multimeter measurement has been considered as a quick and reliable way to characterize the other sample series epitaxially grown at $T_{sub} = 220°C$ and $T_{sub} = 270°C$.

Sample Series Grown at $T_{sub} = 220°C$ and $T_{sub} = 270°C$

Transport measurements by the multimeter technique have been performed to characterize the sample series with increased substrate temperatures of $T_{sub} = 220°C$ and $270°C$. The results of the as-grown samples are shown in Figure 4.5 (a) and (b). Here, the reciprocal RT-resistance values multiplied by the reciprocal layer thickness d are plotted as a function of BEP ratio ($\frac{As_4}{Ga}$). In both sample series, the highest value is at the 2D/3D growth border. In Figure 4.5 (a), the border seems to be expanded but with respect to the scale of the abscissa, it is in the same range of about 1 in BEP ratio ($\frac{As_4}{Ga}$) difference. A significant

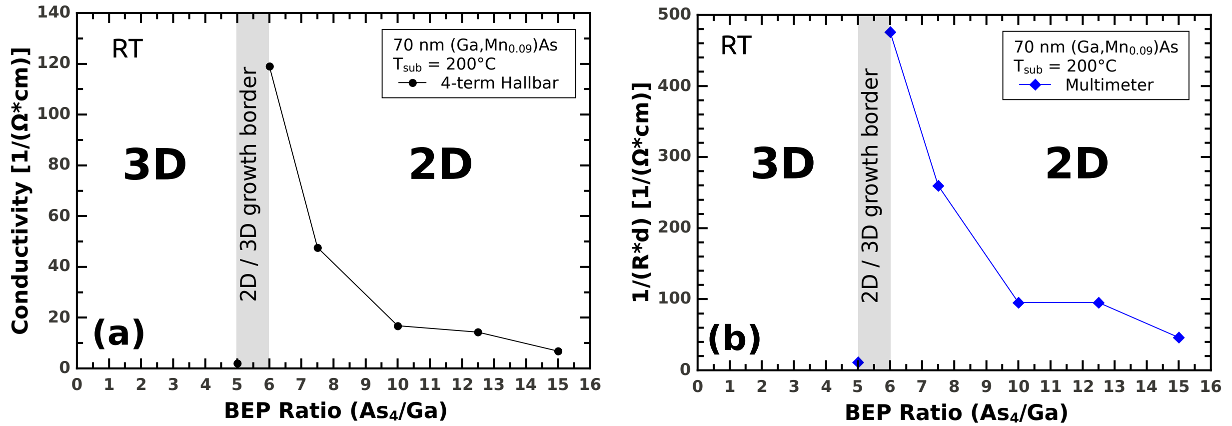

Figure 4.4: Comparison of as-grown (Ga,Mn)As RT-conductivity measurements in 4-terminal Hallbar geometry (black circles) and right after the epitaxial growth by RT-multimeter resistance measurements plotted as the inverse resistance multiplied by reciprocal layer thickness d (blue rhombi). Although the absolute resistance values differ, the trend of the conductivity curves are the same.

shift of the 2D/3D growth border to higher BEP ratios in Figure 4.5 (b) can be understood by different growth and incorporation kinetics of the compound materials, especially of a decreased sticking coefficient of As_4 due to a higher substrate temperature T_{sub} [Fox75]. In the LT-growth range of (Ga,Mn)As, the sticking coefficients of Ga and Mn are assumed to be unity. This assumptions correspond to Chapter 3.1, where the growth rate of GaAs and/or (Ga,Mn)As is mainly influenced by Ga under As overpressure growth conditions.

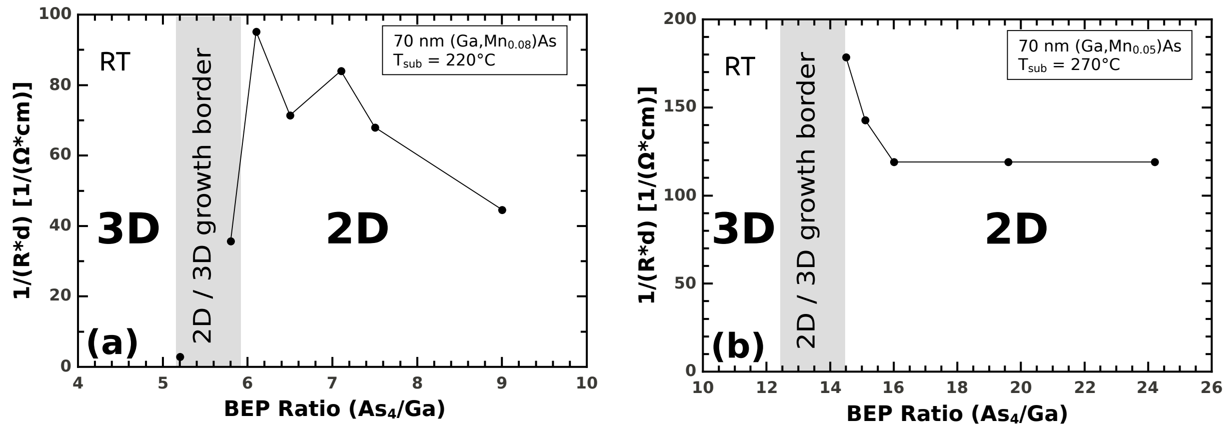

Figure 4.5: RT-conductivity $\frac{1}{Rd}$ as a function of BEP ratio $\frac{As_4}{Ga}$ for the substrate temperatures (a) $220°C$ and (b) $270°C$. Highest conductivities are measured at the border of layer-by-layer growth to polycrystalline growth.

SQUID measurements of as-grown samples close to the 2D/3D growth border reveal Curie temperatures of 67 K and 74 K (for $220°C$ and $270°C$). The higher T_C observed for higher substrate temperature of $T_{sub} = 270°C$ but with a lowered Mn content $x = 0.05$

compared to $x = 0.08$ at $T_{sub} = 220°C$ and $x = 0.09$ at $T_{sub} = 200°C$ indicates, that there is less hole carrier compensation, very likely due to a reduction of As_{Ga} incorporation by a lowered BEP ratio ($\frac{As_4}{Ga}$). At T_{sub} below $\sim 300°C$, the amount of As_{Ga} impurities in LT-GaAs increases with decreasing substrate temperature, as already observed in [Liu95]. The amount of residual As_{Ga} and Mn_{int} impurities in the given material at the 2D/3D growth border cannot be estimated out of transport measurements. (Ga,Mn)As material grown at $T_{sub} = 270°C$ has an almost constant resistance value over a large range of BEP ratio ($\frac{As_4}{Ga}$) within a standard deviation of 0,1 kΩ, determined by repeated measurements. Over time, an oxide layer is formed at the layer surface which increases the contact resistance. Therefore, the multimeter technique gives only an accurate result with a low contact resistance when measuring directly after the outward transfer of the sample. A more detailed analysis of the resistance/conductivity requires photolithographically processed structures in 4-terminal Hallbar geometry, where the current path is well defined. Here, the multimeter technique is an adequate tool to observe the principle electrical behavior of (Ga,Mn)As material, epitaxially grown at systematical changed growth conditions like BEP ratio ($\frac{As_4}{Ga}$) and T_{sub}.

The results of this Chapter have been used as a basis for an improvement of growth conditions for very thin layers in Chapter 5.3.

4.1.3 X-ray Diffraction Characterization

Chapter 3.3 has shown that the lattice constant expands with increasing Mn content, incorporated into the GaAs crystal lattice as substitutional or interstitial Mn. Additionally, Arsenic antisites which also act as compensating double donors like Mn interstitials, are incorporated due to the LT-GaAs growth. Growth parameters like BEP ratio ($\frac{As_4}{Ga}$) as well as substrate temperature T_{sub} play a significant role of the magnetic and transport properties of (Ga,Mn)As layers.

The fact, that the lattice expansion of (Ga,Mn)As material is caused by a mixture of different point defect incorporation leads to a large error of estimated defect concentrations like [As_{Ga}] and [Mn_{int}] out of HRXRD measurements, as shown in Equation 3.16 and 3.17. A separation of these defects is quite difficult, so the defect concentrations stated in this thesis have to be considered as a rough estimation.

ω-2Θ scans of the (004) reflection have been performed for all samples close to the 2D/3D growth border up to higher BEP ratios ($\frac{As_4}{Ga}$). The samples have been annealed according to the annealing procedure of Chapter 3.2.1 and the ω-2Θ scan of the (004) reflection has been repeated. The calculation of the bulk lattice constant by Equation 3.12 opens up an estimation of maximum As_{Ga} concentration y_{max} by Equation 3.19. The nominal Mn content x has been used for x_{sub} in this equation due to an unknown absolute value of Mn_{int}. Epitaxially grown samples under Ga-rich growth conditions (3D growth mode) reveal a rough surface and a degenerated crystal structure. Thus, a Bragg peak of these (Ga,Mn)As layers are not measurable. The relative change of Mn-interstitial concentration Δx_{int} has been estimated with help of Equation 3.20. It represents the difference between lattice constant of as-grown and annealed sample Δa divided by 0.48,

which is the factor for Mn interstitial concentration in Equation 3.17.

Figure 4.6 shows examplary the ω-2Θ scans of the (004) reflection of the sample grown at $T_{sub} = 200°C$ and BEP ratio ($\frac{As_4}{Ga}$)= 6. Here, the black line represents the as-grown sample with $a_\perp = 5.697$ $\mathring{A}$ ($a_{bulk} = 5.677$ $\mathring{A}$), whereas the red line corresponds to the same sample after annealing. The shift of the (Ga,Mn)As Bragg peak towards the direction of the GaAs substrate peak indicates that the vertical lattice constant decreased to $a_\perp = 5.681$ $\mathring{A}$ ($a_{bulk} = 5.668$ $\mathring{A}$). This behavior is assigned to outdiffusion of Mn interstitials to the sample surface. Values of $y_{max} = 0.0418$ and $\Delta x_{int} = 0.0187$ have been calculated.

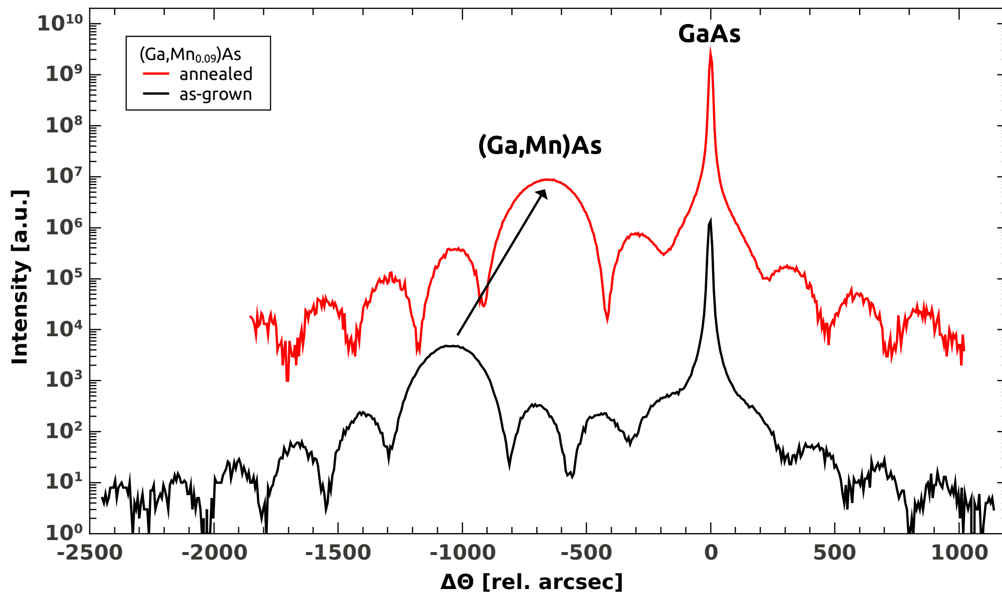

Figure 4.6: HRXRD ω-2Θ scans of the (004) reflection of a sample grown at $T_{sub} = 200°C$ and BEP ratio ($\frac{As_4}{Ga}$)= 6. After measurement of the as-grown sample (black line), it has been annealed for 144 hrs at $T_{ann} = 185$°C. The corresponding measurement after annealing (red line) reveals a shift of the (Ga,Mn)As Bragg peak towards the substrate peak of GaAs.

In Figure 4.7(a) to (c), the bulk lattice constant of the as-grown (black points) as well as annealed (red squares) samples are plotted as a function of BEP ratio ($\frac{As_4}{Ga}$) for all three sample series.

Especially in Figure 4.7(a), the trend of a decrease in as-grown bulk lattice constant above stoichiometric growth condition with a slight As-overpressure is similar to the trend of a decrease in lattice constant reported in [Mac08]. The diminishment of the as-grown bulk lattice constant is not visible at increased substrate temperatures at $T_{sub} = 220°C$ and $T_{sub} = 270°C$, as seen in Figure 4.7(b) and (c). After sample annealing, the bulk lattice constant in case of $T_{sub} = 200°C$ and $T_{sub} = 220°C$ increases significantly with BEP ratio ($\frac{As_4}{Ga}$), indicating an increase of higher As-antisite concentration and/or a higher residual Mn interstitial concentration. The annealed bulk lattice constant in the sample series grown at highest $T_{sub} = 270°C$ is roughly unchanged.

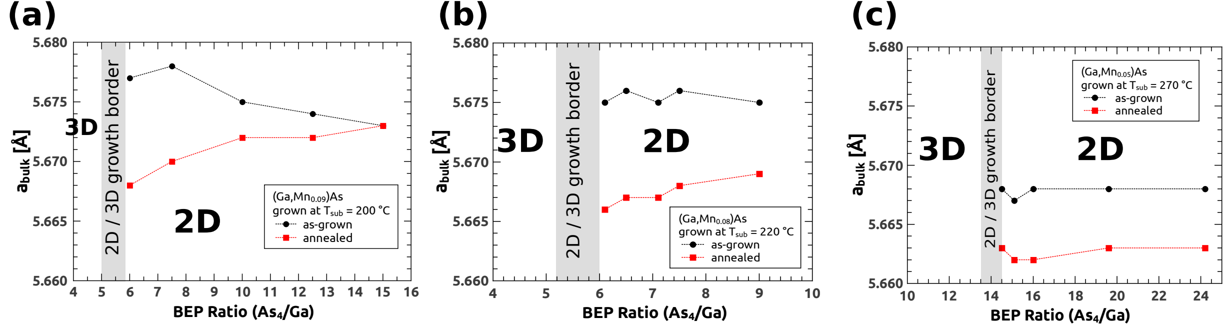

Figure 4.7: Bulk lattice constant a_{bulk} as a function of BEP ratio $(\frac{As_4}{Ga})$ in case of as-grown (black points) and annealed (red squares) samples grown at (a) $T_{sub} = 200°C$ with nominal $x = 0.09$, (b) $T_{sub} = 220°C$ with nominal $x = 0.08$ and (c) $T_{sub} = 270°C$ with nominal $x = 0.05$.

In order to correlate the influence of growth conditions on point defect densities or density changes in epitaxial grown (Ga,Mn)As material, calculated As-antisite concentrations y_{max} and relative changes of Mn-interstitial concentrations Δx_{int} as a function of BEP ratio $(\frac{As_4}{Ga})$ are plotted in Figure 4.8(a) and (b). The ratio of $\frac{\Delta x_{int}}{y_{max}}$ as a function of BEP ratio $(\frac{As_4}{Ga})$ is additionally shown in Figure 4.8(c).

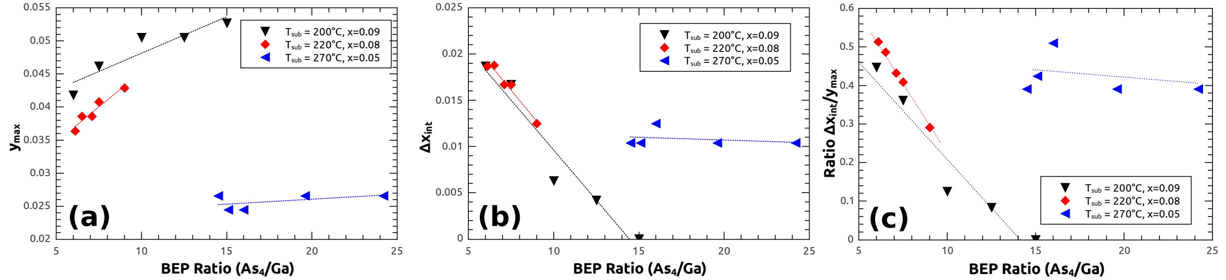

Figure 4.8: (a) Estimated maximal As-antisite concentration y_{max}, (b) relative change of Mn-interstitial concentration Δx_{int} after the annealing procedure and (c) ratio $\frac{\Delta x_{int}}{y_{max}}$ as a function of BEP ratio $(\frac{As_4}{Ga})$ for (Ga,Mn)As samples grown at $T_{sub} = 200°C$ (black triangles), $T_{sub} = 220°C$ (red rhombi) and $T_{sub} = 270°C$ (blue triangles). The dotted lines illustrate the linear trend for y_{max} and Δx_{int} with increasing BEP ratio $(\frac{As_4}{Ga})$ for all sample series.

In all growth series, y_{max} has its minimum value at stoichiometric growth conditions and increases roughly linear with increasing BEP ratio $(\frac{As_4}{Ga})$, as seen in Figure 4.8(a). The sample series grown at $T_{sub} = 200°C$ (black triangles and dotted line) and $T_{sub} = 220°C$ (red rhombi and dotted line) shows a relative similar slope in contrast to a slight slope in case of the $T_{sub} = 270°C$ sample series (blue triangle and dotted line). The reason for the lowest value for y_{max} at stoichiometric growth conditions observed for highest $T_{sub} = 270°C$ is ambiguous and might be caused by a significantly higher substrate temperature due to a lower As-antisite incorporation and/or a lower nominal Mn content $x = 0.05$. Less compensation of free holes (provided by less Mn acceptors) by point defects in case of $x =$

0.05 is assumed within the (Ga,Mn)As material. Calculating the As-antisite concentration of all three sample series at the 2D/3D growth border out of $2.2 \cdot 10^{22}\ cm^{-3}$ Ga-sites in GaAs/(Ga,Mn)As material, y_{max} is $2.2 \cdot 10^{20}\ cm^{-3}$ at $T_{sub} = 200°C$, $1.8 \cdot 10^{20}\ cm^{-3}$ at $T_{sub} = 220°C$ and $1.4 \cdot 10^{20}\ cm^{-3}$ at $T_{sub} = 270°C$.

The relative change of Mn interstitial concentration Δx_{int} after sample annealing shows a roughly linear decrease with increasing BEP ratio ($\frac{As_4}{Ga}$), as shown in Figure 4.8(b). Highest changes in Δx_{int} have been observed at the stoichiometric growth border and a lowest change at high BEP ratios. Again, the lowest Δx_{int} is observed for the sample series grown at highest substrate temperature $T_{sub} = 270°C$. This sample series shows a very low change of Δx_{int} by varying BEP ratio ($\frac{As_4}{Ga}$), comparable to the change of y_{max} in Figure 4.8(a).

The correlation of y_{max} and Δx_{int} is shown in Figure 4.8(c), where the ratio of $\frac{\Delta x_{int}}{y_{max}}$ is plotted as a function of BEP ratio ($\frac{As_4}{Ga}$). A high ratio of Δx_{int} over y_{max} corresponds to a high concentration of Mn interstitials, and a low ratio represents low Mn interstitial concentration in as-grown (Ga,Mn)As material. The graph shows in principle the same behavior as presented in 4.8(b). In contrast to the consideration of a pure relative change of Mn interstitial concentration Δx_{int}, the ratio $\frac{\Delta x_{int}}{y_{max}}$ offers a qualitative insight to the fraction of compensating defects relating to As_{Ga} and Mn_{int}. Within a series of samples epitaxially grown at low substrate temperatures, $\frac{\Delta x_{int}}{y_{max}}$ decreases with an increase of BEP ratio ($\frac{As_4}{Ga}$). This finding can be interpreted as a low As_{Ga} concentration and high Mn_{int} concentration at stoichiometric growth conditions. A higher BEP ratio ($\frac{As_4}{Ga}$) increases the incorporation of As_{Ga} and simultaneously lowers the Mn_{int} concentration. In other words, there is a balance between the two types of point defects which are mainly responsible for the hole compensation in (Ga,Mn)As material, as mentioned in [Sad04]. This interpretation is supported by transport and SQUID measurements in Chapter 4.1.1 and 4.1.2, which show improved material properties at stoichiometric growth conditions with a reduced As_{Ga} concentration. Again, a substrate temperature of $T_{sub} = 270°C$ reveals a relative constant ratio $\frac{\Delta x_{int}}{y_{max}}$. It demonstrates that these (Ga,Mn)As material properties are robust against small deviation of growth conditions and show comparable defect densities. The handling of reproducible bulk layer properties seems to be easier at $T_{sub} = 270°C$ compared to growth at lower substrate temperatures, where the (Ga,Mn)As material is more sensitive to growth conditions.

In summary, the investigation of growth conditions related to structural, electrical and magnetic properties of bulk (Ga,Mn)As material shows, that it is possible to influence As-antisite concentration by an increase of substrate temperature T_{sub} as well as an adjusted BEP ratio ($\frac{As_4}{Ga}$) with minimal excess of As overpressure leading to stoichiometric growth conditions. Mn_{int} concentrations increase with increasing nominal Mn content x and can be effectively reduced by sample annealing or an increasing BEP ratio ($\frac{As_4}{Ga}$). The latter case results in bad magnetic and transport properties of (Ga,Mn)As material due to an increased As_{Ga} concentration. These findings have been taken into account for spanning a growth parameter space for optimized growth conditions of very thin (Ga,Mn)As layers with a different layer design, as will be presented in Chapter 5.3.

4.2 Epitaxial Growth of Thin (Ga,Mn)As Layers ($\leq$ 10 nm)

As already described in Chapter 2.2, the influence of the magnetic properties can be realized by an electrical control of a thin (Ga,Mn)As layer, e.g. by low-voltage control in a p-n junction or by a ferroelectric gate [Owe09, Sto08]. Such devices require thin (Ga,Mn)As layers with simultaneously ferromagnetic properties and sufficient electrical conductivity at LT. The following sections present first studies of thin (Ga,Mn)As layers, epitaxially grown under standard growth conditions.

4.2.1 Influence of a LT-GaAs Cap Layer

The first epitaxial thin (Ga,Mn)As layers at the Würzburg MBE group have been fabricated by J. Wenisch. These samples have been characterized within the framework of the diploma thesis of M. Zimmermann [Zim07]. Two 10 nm layers with nominal Mn content of $x = 0.043$ have been grown at standard growth conditions (see Chapter 3.2.1), one layer without and the other layer with a 2 nm LT-GaAs cap. In order to measure a clear signal of the remanent magnetization without the perturbing sample-dependent remanent magnetic fields of H_{rem} $\approx$ -5 Oe, the measuring procedure was as follows: After applying a saturation field of +3000 Oe at 4.2 K to saturate the magnetization of the sample, the T-dependent magnetization M(T), as seen in Figure 4.9(a) and (b), has been measured with a negative or positive auxiliary field of -15 $Oe < H < 0$ Oe (blue line) and 0 $Oe < H <$ 15 Oe (red line).

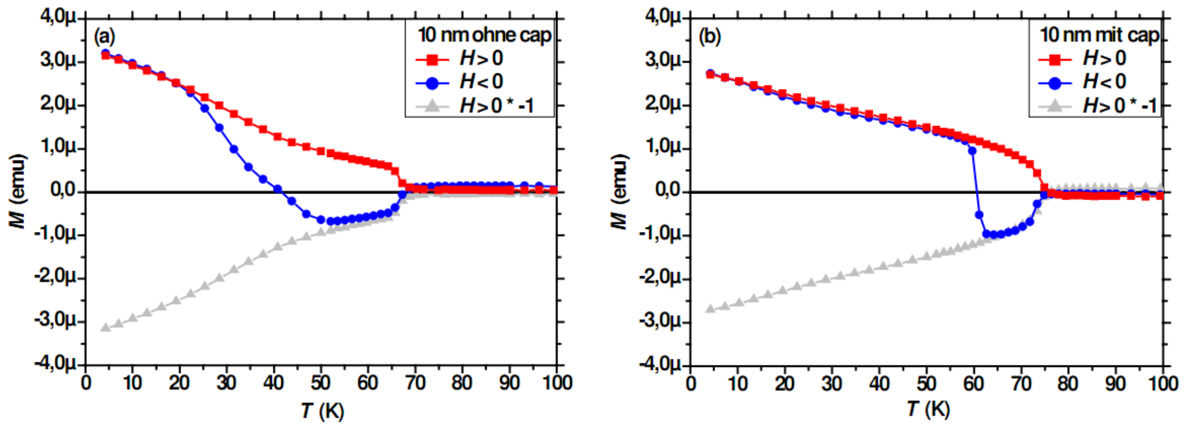

Figure 4.9: T-dependent measurements of the remanent magnetization for a 10 nm (Ga,Mn)As layer (a) without and (b) with a 2 nm LT-GaAs cap layer. Both layers have the same nominal Mn content of $x = 0.043$. A clear improvement of T_C from 67 K (a) to 75 K (b) can be achieved by capping the (Ga,Mn)As layer with a 2 nm LT-GaAs cap layer. Taken from [Zim07].

In Figure 4.9(a), the shape of the measured curve with $H > 0$ Oe (red line) is typical for a T-dependent magnetization curve, as seen in Chapter 3.4. The measurement with a negative applied auxiliary field $H < 0$ Oe (blue line) is quite different. It is expected to

show a clear switching event of the magnetization before reaching T_C, where the coercive field H_c of the sample is smaller than the applied magnetic auxiliary field H. Nevertheless there is a gradual change of the T-dependend magnetization between 20 K and 50 K compared to an abrupt switching. It has been concluded that the 10 nm (Ga,Mn)As layer is not homogeneous in its magnetic properties. Rather, inhomogeneities are presumably caused by magnetic domains with different properties. It can be speculated, that a random incorporation of Mn within the (Ga,Mn)As material, surface defects due to oxidation of the first MLs and/or point defects like As_{Ga} and Mn_{int} might be responsible for the inhomogeneous magnetic behavior of the (Ga,Mn)As layer. These factors lead to a locally strong compensation of the p-doping of the layer, as described in Chapter 2.2. As a result, a local variation of the ferromagnetic properties is present in the (Ga,Mn)As material.

The T-dependent magnetization measurements of the 10 nm (Ga,Mn)As layer with a 2 nm LT-GaAs cap layer is presented in Figure 4.9(b). For $H > 0$ Oe (red line), the shape of the remanent magnetization curve is similar to Figure 4.9(a). In contrast to the 10 nm (Ga,Mn)As layer without a cap layer, the remanent magnetization curve for the negative auxiliary field H (blue line) shows a clear switching event for $H_c < H$. The LT-GaAs cap layer protects the 10 nm (Ga,Mn)As layer from severe compensation of holes by surface states, which confirms the self-consistent band alignment calculations of 4 nm (Ga,Mn)As layers in Chapter 2.2.1. An increase of T_C from 67 K to 75 K also demonstrates the beneficial influence of the LT-GaAs cap.

As a conclusion, surface states play a crucial role for the ferromagnetic properties in thin (Ga,Mn)As layers.

4.2.2 5, 3.5 and 2 nm (Ga,Mn)As Layers with LT-GaAs Cap Layer

Using the result of the last section as a starting point, three (Ga,Mn)As layers with thicknesses of 5, 3.5 and 2 nm have been grown with a 2 nm LT-GaAs cap layer at standard growth conditions, as seen in Figure 4.10.

All layers have the same nominal Mn content of $x = 0.043$. In comparison to the 10 nm layer, the 5 nm and the 3.5 nm (Ga,Mn)As layer show relatively high T_Cs of 65 K. Even a 2 nm thin layer shows a ferromagnetic response at 4.2 K and a Curie temperature of $T_C = 35K$. Within the framework of the diploma thesis of M. Zimmermann [Zim07] it has been shown, that the presented layers did not show any reproducible electrical conductance at LT which is essential for gating experiments with a ferroelectric gate. Only 1 out of 18 samples has shown a finite but unreproducible electrical LT-conductivity. All other samples did not show any feasible LT-conductivity.

In summary, in thin layers (d $\leq$ 10 nm), surface defects and point defects like Mn interstitials Mn_{int} and/or As antisites As_{Ga} caused by LT-GaAs/(Ga,Mn)As epitaxy lead to severe compensation of p-doping and valence band bending. Thus, defects play a crucial role for the ferromagnetic properties. Additionally, local inhomogeneities in Mn incorporation and defect distribution seem to cause drastic variations in conductivity of very thin (Ga,Mn)As layers at LT.

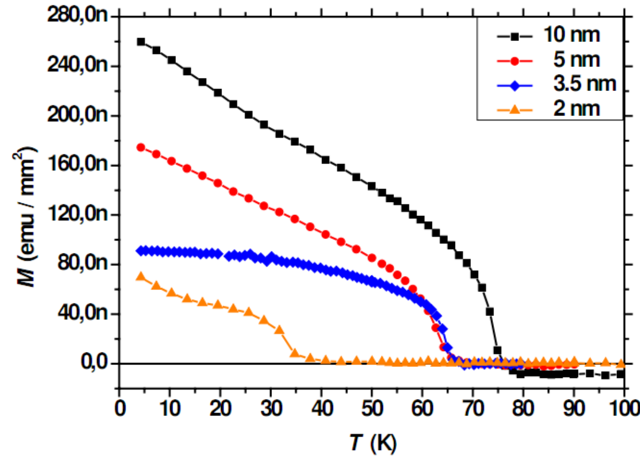

Figure 4.10: T-dependent measurement of the magnetization with (Ga,Mn)As layer thicknesses of 10, 5, 3.5 and 2 nm, all layers capped with a 2 nm LT-GaAs layer. All layers have a nominal Mn content of $x = 0.043$. Taken from [Zim07].

4.2.3 Ferroelectrical Gating of a 7 nm (Ga,Mn)As Layer

The very thin (Ga,Mn)As layers presented in the last sections have been epitaxially grown at standard growth conditions, according to the epitaxial growth of bulk (Ga,Mn)As material in Chapter 3.2.1. In order to fabricate a first functional layer for the electrical control of magnetic properties, a series of 7 nm layers without a LT-GaAs capping layer but with equal/higher nominal Mn content ($x = 0.042$, 0.052 and 0.057) has been epitaxially grown at standard growth condition. The compromise of layer thickness and an increased hole carrier concentration through a higher Mn content has been chosen to gain a beneficial electrical conductivity at LT. Magnetometry characterization of a 7 nm layer compared to a 3.5 nm layer, both with nominal Mn content of $x = 0.057$, is shown in Figure 4.11.

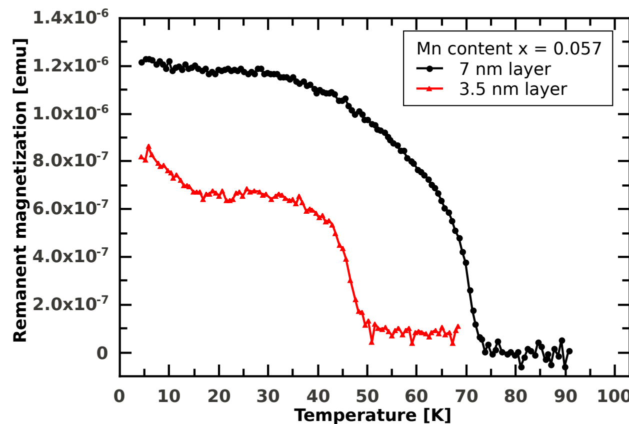

Figure 4.11: Comparison of the T-dependent magnetization of a 7 nm thin layer (black) and a 3.5 nm thin layer (red). Both layers have a nominal Mn content of $x = 0.057$.

A clear increase in T_C of 74 K for the 7 nm layer compared to 50 K for the 3.5 nm layer is visible. The result is consistent with the first growth series of thin layers in Figure 4.10. The offset of the magnetization curve for the 3.5 nm layer arises from an internal offset of the SQUID magnet, but the Curie temperature is not affected by this offset. The influence of inhomogeneities and surface/point defects on the magnetic properties is obviously much lower for the 7 nm layer compared to the 3.5 nm layer.

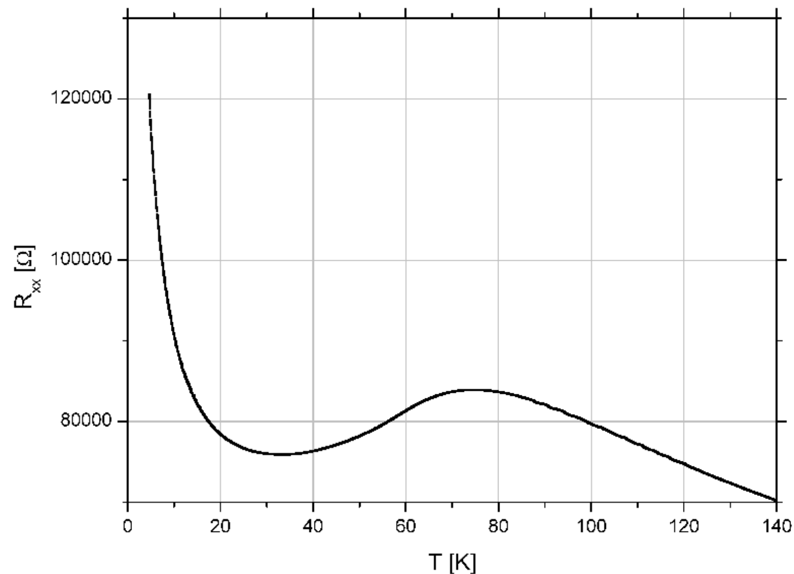

Figure 4.12: Cooling curve of a 7 nm (Ga,Mn)As layer in Hall bar geometry while gated in depletion mode. First, the resistance value increases with decreasing temperature up to T_C. Then, the ferromagnetic ordering of the sample takes place which leads to a decrease in resistance for a further temperature decrease. At least, the resistance increases again and reaches the highest value at 4.2 K. Taken from [Fre09].

In the diploma thesis of M. Freitag [Fre09], the 7 nm layer with high Mn content ($x = 0.057$) and a 660 nm thick ferroelectric gate (P-VDF) on top shows promising transport results in 4-terminal hall-bar geometry, comparable to results of [Sto08]. The longitudinal resistance R_{xx} of the (Ga,Mn)As layer has been measured according to Chapter 3.5 with a reference resistance of 100 $k\Omega$. In Figure 4.12, the cooling curve of the layer is plotted. Before the cooling process of the sample, the ferroelectric gate has been polarized with $+70$ V, which corresponds to the depleted state of the (Ga,Mn)As layer. During the cooling process in a cryostat, R_{xx} increases with decreasing temperature, which is a typical behavior for a doped semiconductor. When the temperature reaches the Curie temperature, the ferromagnetic ordering takes place inside the sample and R_{xx} decreases with T due to the NMR effect, as explained in Chapter 2.3.1. The maximum of longitudinal resistance R_{xx} is around 76 K. In contrast to a cooling curve for a standard thick layer, as seen in Figure 3.18, R_{xx} increases again up to a much higher value at 4.2 K compared to R_{xx} around T_C.

Figures 4.13(a) to (c) show the result of the gating experiment. After collection of

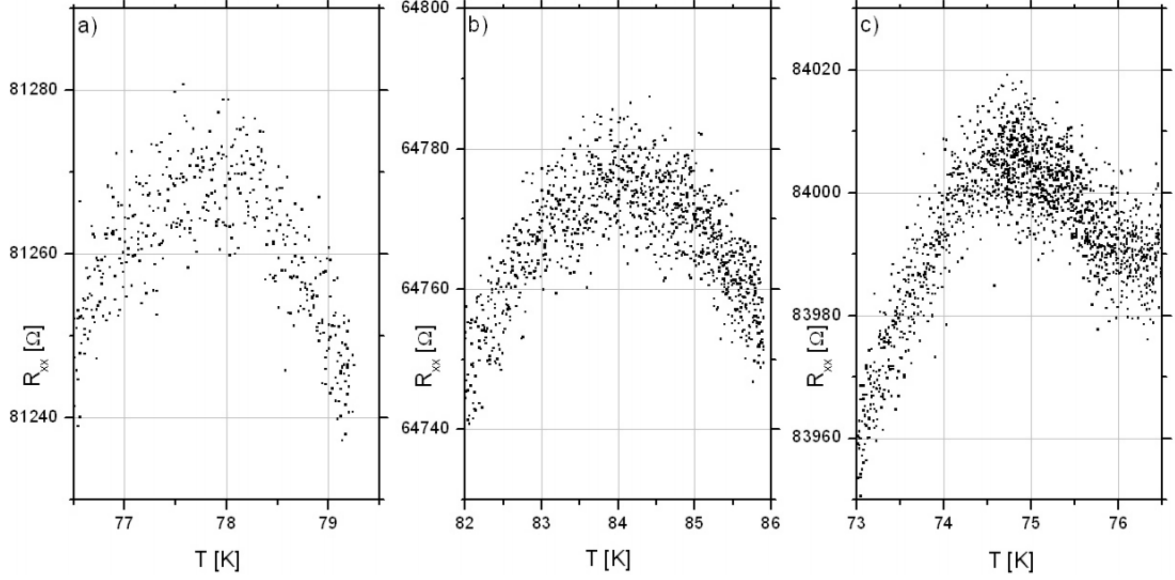

Figure 4.13: Longitudinal resistance R_{xx} of a gated (Ga,Mn)As layer in (a) depletion mode, (b) accumulation mode and (c) a second depletion mode by inversion of polarization of the ferroelectric P-VDF gate. A change in T_C of 7 ± 2 K has been achieved. Taken from [Fre09].

the cooling curve, e.g. in depletion mode as seen before, the maximum of R_{xx} has been identified. To confirm the exact value for T_C it was necessary to sweep the temperature around the maximum of R_{xx} very slowly (about 1 K / 30 min) several times (Figure 4.13(a)). After T_C has been determined, the sample was heated up to RT again and the accumulation mode has been applied by inversion of the polarization of the P-VDF (-70 V). A cooling curve is collected again with the same procedure of T_C determination, as described above (Figure 4.13(b)). At last, the measurement has been repeated in depletion mode to confirm the switching effect of T_C, as seen in Figure 4.13(c).

In case of the depletion modes in Figure 4.13(a) and (c), the longitudinal resistance R_{xx} referring to a Curie temperature T_C changed from 81.270 $k\Omega$ at 78 K in the first measurement to 84,050 $k\Omega$ at 75 K in the second measurement. According to the mean-field Zener model description of (Ga,Mn)As, there is a correlation between T_C and resistance R. Assuming a reciprocal dependence between longitudinal resistance R_{xx} and hole carrier concetration p

$$R_{xx} \propto \frac{1}{p} \tag{4.1}$$

Equation 2.1 of Chapter 2.1 leads to

$$T_C \cdot \sqrt[3]{R_{xx}} = const.. \tag{4.2}$$

For the first depletion state in Figure 4.13(c), the result is 338 $K\sqrt[3]{k\Omega}$. In accumulation mode the value is 337 $K\sqrt[3]{k\Omega}$ and for the second depletion mode, the resulting value

of 328 $K\sqrt[3]{k\Omega}$ is slightly lower. The analysis of these switching modes shows an aging process presumably by heating and cooling processes of the sample. On the other hand, the feasibility of thin layers for a voltage control of the magnetic properties has been demonstrated successfully.

For the 7 nm layer with nominal $x = 0.042$ as well as for the 3.5 nm layer with nominal $x = 0.057$ it was not possible to get either a cooling curve with a maximum at T_C or electrically conductible layers at low temperatures. Severe compensation and inhomogeneities in Mn content are too strong to fabricate usable and electrically conductible devices for LT-gating experiments. Even a macroscopic magnetization of these samples is measureable by SQUID.

To summarize the aforementioned experiments in this chapter it is a challenge to get proper thin (Ga,Mn)As layers ($< 10\ nm$) with reproducibility in magnetic and transport properties with a LT-GaAs cap or with a higher Mn content. Problems like inhomogeneities due to Mn incorporation and local depletion of holes due to surface and point defects can not be suppressed sufficiently by conventional growth conditions which are used for thick standard layers. In order to get a stronger voltage control of T_C by electrical gating it is essential to have a very thin layer and a low Mn content.

These layer properties might be achieved by a change of growth conditions in order to decrease point defects, especially As antisites As_{Ga}. A higher substrate temperature and an adjusted BEP ratio ($\frac{As_4}{Ga}$) in the stoichiometric growth regime are possible parameters to reduce As_{Ga} concentration, as investigated in Chapter 4.1. A new non-homogeneous layer thickness distribution in a very thin (Ga,Mn)As layer and therefore a non-homogeneous Mn profile along the growth direction has been invented to reduce the impact of interface and surface defects on the hole density, as will be presented in the following Chapter.

Chapter 5

Parabolically Graded Thin (Ga,Mn)As Layers

Chapter 4.2 has shown, that it is challenging to fabricate very thin (Ga,Mn)As layers which are useful for gating experiments. The preconditions of a thin layer and additionally a low Mn content demands a reduction of compensating effects (see Chapter 4.1.3) and simultaneously a confinement of the charge carriers. For AlGaAs/GaAs superlattices with a total layer thickness of 130 $\AA$ a parabolical grading was successfully grown with improved electrical properties compared to a non-parabolical grading of a AlGaAs/GaAs superlattice [Wan92]. In the following it will be described how a structural design of thin (Ga,Mn)As layers with parabolical grading of the Mn content has been developed, epitaxially grown and investigated, in contrast to earlier grown, homogeneous layer structures and GaAs/(Ga,Mn)As superlattices.

5.1 Realization of a Parabolically Graded Mn Distribution

The challenge in the epitaxial growth of very thin (Ga,Mn)As layers contains of ferromagnetic properties and usable electrical LT-conductivity at once. This objective is achieved by the principle idea of a different Mn distribution in a very thin layer. A center (Ga,Mn)As region in a very thin layer (6 nm), which has highest nominal Mn content, is shielded electrostatically by outer regions of a decreasing amount of Mn impurities from compensating surface states and point defects. It is obvious, that inhomogeneities of the Mn incorporation cannot be neglected. But with having this kind of Mn profile, a better confinement of holes is assumed, at which more charge carriers might couple to the Mn magnetic moments and lead to improved magnetic and transport properties.

Two feasibility studies have been performed to realize a parabolical Mn distribution with highest Mn content in the middle of the very thin (Ga,Mn)As layer by MBE growth: An analog alloy growth technique by ramping the Mn effusion cell temperature during growth of thin layers and a digital alloy growth technique by using Mn cell shutter sequences to

insert LT-GaAs spacers between (Ga,Mn)As layers.

5.1.1 Two Different Growth Techniques

Analog Alloy Growth Technique for a Parabolical Mn Distribution

A characterization of ramping the Mn effusion cell temperature has been implemented to estimate a discrepancy of actual and nominal Mn cell temperature during the growth of a very thin (Ga,Mn)As layer.

For this feasibility test the reference sample of Chapter 3.3 has been used to state the Mn content at the center of a layer, as seen in Figure 3.12. Here the reference (Ga,Mn)As layer with a Mn content of $x = 0.043$ has been grown epitaxially with a Mn cell temperature $T_{Mn} = 715°C$ and a Mn flux of 8×10^{-9} $torr$ (measured right before the growth). To ramp the temperature of the Mn cell a starting value of $T_{Mn} = 695°C$ has been used, which corresponds to a Mn content of $x = 0.022$ with a measured Mn flux of 6×10^{-9} $torr$. The Mn content of the lower Mn cell temperature is estimated by using the $20°C$ rule of Figure 3.6 and both Mn fluxes are determined by Mn flux measurements, as seen in Figure 3.7. The behavior of the Mn cell is investigated for a total ramping time of 60 s, which would correspond to an epitaxial growth of 6 nm, under assumption of a growth rate of 1 $\frac{Å}{s}$. During the first 30 s, the power supply of the Mn cell has an output power of around 100 W (10,2 V and 10,2 A) for an increasing temperature ramp of almost $20°C$. After 30 s, the output power is set to zero voltage/current to cool down the Mn cell immediately. The temperature has been noted every 5 s. This procedure was repeated a second time to guarantee reproducibility of temperature behavior of the Mn cell.

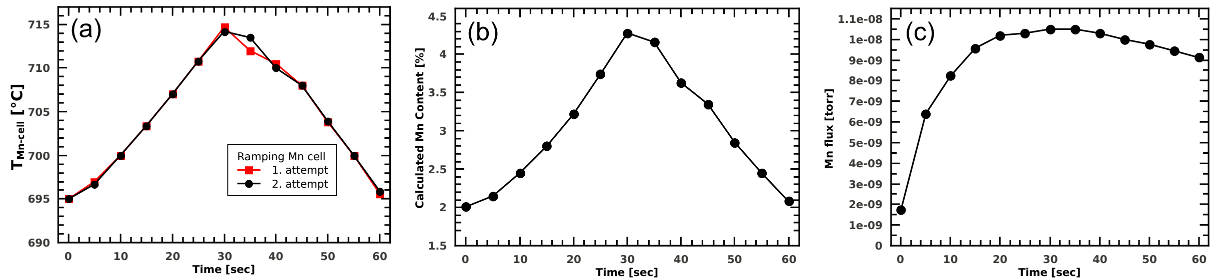

Figure 5.1: (a) Ramping of the Mn cell temperature, (b) calculated Mn content x out of calibration curve and (c) BEP of Mn during ramping.

In Figure 5.1(a), the second curve of the ramping procedure behaves almost completely congruent with the first measurement. The only deviation within $2°C$ arises around the maximum after the beginning of the cooling process. It also shows, that after 60 s the cell temperature reaches almost the initial temperature. Using these temperatures and the $20°C$ rule of Chapter 3.2.1, the Mn content x is calculated in Figure 5.1(b). After 30 s, a doubling in Mn content ($\approx$ 4.3 %) has been calculated compared to the outer parts ($\approx$ 2.1 %). The calculation of x seems promising, but a comparison of the cell temperature

with the Mn flux during the ramping procedure (Figure 5.1(c)) shows, that a reliable value of x right after $t > 0$ s cannot be stated. The flux measurement is always superposed by the background pressure ($\sim 10^{-10}$ $torr$) of the growth chamber. Thus, small material fluxes like the Mn flux ($\sim 10^{-9}$ $torr$) is always stronger influenced in comparison to higher material fluxes for e.g. Ga ($\sim 10^{-7}$ $torr$) or As_4 ($\sim 10^{-6}$ $torr$), as discussed in Chapter 3.2.1. It is not sure that the BEP of Mn changes instantaneously with an increased or decreased temperature ramp. The shape of BEP measurement in Figure 5.1(c) behaves like typical BEP measurements of the Mn within the first 60 s when the Mn cell is still in an unstable state, as shown in Figure 3.7.

It is an essential problem, that the BEP of the Mn effusion cell has a large error bar during the ramping procedure. Thermal lags and non-steady state temperature distributions within the Mn cell lead consequently to difficulties in determining of incorporated Mn content which hinder reproducible growth of very thin (Ga,Mn)As layers.

Considering this feasibility study of the Mn cell, the analog growth technique does not seem to be very suitable and reliable for our requirements for a reproducible, epitaxial growth of very thin (Ga,Mn)As layers.

Digital Alloy Growth Technique for a Parabolical Graded Mn Distribution

The second method to realize a parabolical grading of a Mn profile is based on a digital alloy growth technique with Mn shutter opening sequences. The objective is to get a complete interruption of the Mn flux in a minimal time interval. Hereby the Mn effusion cell is operated with a constant effusion cell temperature T_{Mn} and therefore with a known Mn content, according to the calibration curve of Figure 3.6. The limiting factor of this technique is the time delay of the Mn shutter movement from closed to opened position and reverse. A comparison of the analog and digital alloy growth technique for AlGaAs/GaAs quantum wells in a parabolical shape has shown, that the digital growth technique is more reliable than the analog growth technique while having improved electrical and optical properties, as published in [Che93, Gei99, Mil84].

The feasibility study of the digital alloy growth technique has been performed as follows: A fixed concave mirror on a molybdenum block (see Appendix A.2.2) is inserted into the UHV system, transferred into the MBE growth chamber on the manipulator and then slued into growth position, facing the mirror to the effusion cells. The pyrometer port which is a heated viewport at the backside of the chamber offers a glance at the mirror. When the main shutter is opened, it is possible to see the cell openings with its shutters. The overview of the growth chamber geometry has been illustrated in Figure 3.1. At the viewport, the RHEED camera is mounted to detect the intensity of heat radiation of the Mn cell. The time resolution of this camera is 0.040 s. The Mn cell temperature is set to $T_{Mn} = 715\ ^{\circ}C$. Every measurement of heat radiation has been started at closed Mn shutter position. Four different time intervals $t_{inter} = 1.0$, 0.5, 0.2 and 0.1 s for Mn shutter movement sequences in opened and closed position have been tested, each with three repetitions. Time intervals < 0.1 s are not accepted by the software control of the MBE growth chamber. The result is presented in Figure 5.2(a) to (d).

The intensity of heat radiation is around 0 in arbitrary units (a.u.) for the closed Mn shutter position and around 800 a.u. for the opened Mn shutter position, as can be seen in Figure 5.2(a) to (c). For $t_{inter} = 1.0$, 0.5 and 0.2 s, increased or decreased Δt_{open} and/or Δt_{close} within the Mn shutter sequences cannot be detected. The mean values for opened time interval $\overline{\Delta t_{open}}$ and closed time interval $\overline{\Delta t_{close}}$ have been determined at half of the maximum intensity at 400 a.u.. In Figure 5.2(a), $\overline{\Delta t_{open}} = 0.996$ s and $\overline{\Delta t_{close}} = 1.007$ s correspond to $t_{inter} = 1.0$ s within the time resolution of 0.040 s. The same correspondence occurs for Figure 5.2(b), where $\overline{\Delta t_{open}} = 0.503$ s and $\overline{\Delta t_{close}} = 0.497$ s agree to $t_{inter} = 0.5$ s. For both time intervals of $t_{inter} = 1.0$ s and $t_{inter} = 0.5$ s, the ratio is $\frac{\overline{\Delta t_{open}}}{\overline{\Delta t_{close}}} \approx 1$. In case of a Mn shutter time interval of $t_{inter} = 0.2$ s for opening and closing time, $\overline{\Delta t_{open}} = 0.193$ s and $\overline{\Delta t_{close}} = 0.208$ s still fit quite well, as seen in Figure 5.2(c). The ratio of $\frac{\overline{\Delta t_{open}}}{\overline{\Delta t_{close}}}$ is lowered to 0.9, which means, that the time delay starts to influence the shutter movements within 0.2 s intervals. On the other side, the time resolution of the camera (0.040 s) plays a significant role for a time interval sequence of $t_{inter} = 0.2$ s to determine a delay of the Mn shutter movement. A maximum number of five data points can be detected within an opened or closed Mn shutter position. In Figure 5.2(d), the opening and closing time of the Mn shutter cannot be determined correctly within the time resolution. The measurement shows, that the time interval of $t_{inter} = 0.100$ s is represented by only one data point in opened Mn shutter position. In principle, a maximum number of two data points would represent such time interval. For every subsequent opened Mn shutter position, the intensity increases, but never reaches the maximum intensity of 800 a.u. compared to $t_{inter} = 1.0$, 0.5 and 0.2 s shutter sequences. The time distance $t = 0.200$ s for two neighboring intensity peaks corresponds to a complete sequence of two subsequent opened Mn shutter positions, interrupted by one closed Mn shutter position. The time interval for opened Mn shutter position is estimated to be 0.047 s whereas the closed time interval is around 0.151 s which lead to a ratio $\frac{\overline{\Delta t_{open}}}{\overline{\Delta t_{close}}} \approx \frac{1}{3}$. As a conclusion out of these measurements, a time interval of at least 0.5 s is definitively save for the epitaxial growth of very thin (Ga,Mn)As layers with no influence of delayed Mn shutter movements.

As a conclusion of the presented growth techniques, the digital alloy growth technique is the method of choice to fabricate very thin (Ga,Mn)As layers with a parabolical grading of Mn composition. Uncertainties as discussed for the analog alloy growth technique are mainly reduced to Mn shutter movements. The Mn cell temperature is operated at a constant value T_{Mn} which offers a previous calibration of Mn content x. Additionally, Mn shutter time intervals of $t_{inter} \geq 0.5$ s should be used to assure that there is no influence of a time delay on the shutter movement for a completely continuous or interrupted Mn flux.

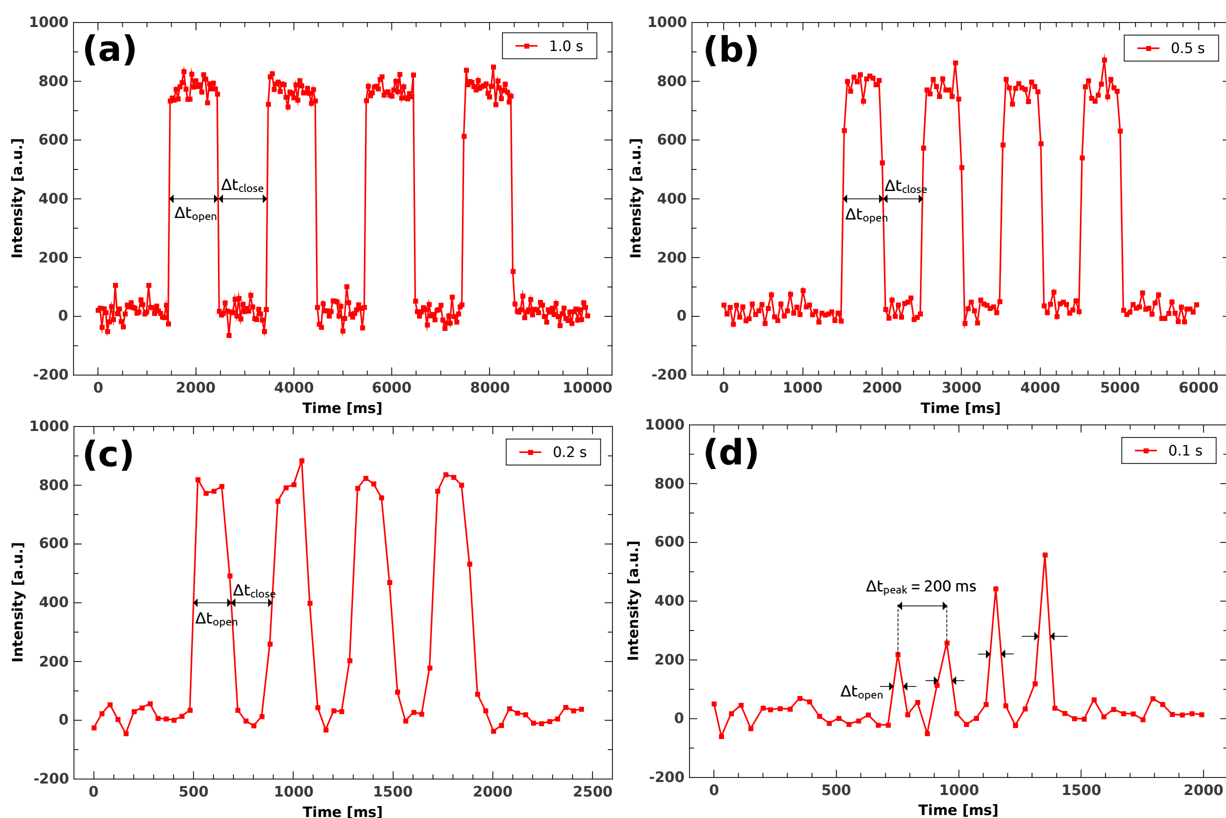

Figure 5.2: Feasibility study of Mn cell shutter sequences with opening time intervals (a) 1.0 s, (b) 0.5 s, (c) 0.2 s and (d) 0.1 s. The time resolution is 0.04 s. An opening time of the shutter < 0.2 s leads to an uncompleted opening of the cell shutter.

5.1.2 Calculation of Parabolically Graded Mn Profiles

A comparison of the analog and digital alloy growth technique in the last subsections has shown, that a parabolical grading of the Mn distribution in a very thin (Ga,Mn)As layer is easier to fabricate by using the digital alloy growth technique. This method operates with a constant Mn cell temperature during the whole epitaxial growth. Previous calibrations of the Mn content x at certain cell temperatures can be achieved by growing standard 70 nm layers and subsequent determination of x by HRXRD. The Mn flux is controllable by the opening and closing of the Mn shutter during growth of LT-GaAs. Measurements of the different time intervals between opened and closed Mn shutter positions have shown that a time interval of at least 0.5 s is long enough for the Mn shutter to be completely in opened or closed position and time delay of the shutter movement plays no crucial role. It results in a hypothetical layer thickness of only 0.5 $\AA$ with respect to a growth rate of 1.0 $\frac{\AA}{s}$.
At first, general equations for calculating a parabolical grading of Mn distribution within an arbitrary layer thickness d_{lay} will be introduced. The location-dependent Mn content $x(z)$ in a parabolical profile along the local variable z can be described as

$$x(z) = x \cdot f(z) \tag{5.1}$$

where x is the nominal Mn content and $f(z)$ is a parabolical function. The boundary conditions of function $f(z)$ have been chosen to be $f(z) = 0$ for $z = \pm\, d_{lay}/2$ and $f(z) = 1$ for $z = 0$. It corresponds to the nominal Mn content x in the middle and zero Mn content at the border of the layer with layer thickness d_{lay}. Therefore, the normalized function $f(z)$ is given as

$$f(z) = 1 - \left(\frac{z}{d_{lay}/2}\right)^2 \tag{5.2}$$

In principle, Equation 5.1 together with 5.2 can be used to calculate any parabolical Mn profile in an arbitrary layer thickness. For our purpose, a total (Ga,Mn)As layer thickness of 4 nm in a parabolical grading embedded in LT-GaAs has been chosen, which is between the layer thickness of 3.5 and 7 nm of Chapter 4.2. A 4 nm reference layer with a homogeneous Mn profile is assumed to get rather a measurable LT electrical conductance compared to an even smaller thickness.

The parabolical grading is realized by dividing d_{lay} into a number of $2n$ different (Ga,Mn)As layer thicknesses, starting with the thickest layer thickness at the center and the thinnest layer thickness at the border of the layer $z = \pm\frac{d_{lay}}{2}$. The layer thickness of a section d_s is defined as

$$d_s = \frac{d_{lay}}{2 \cdot n} \qquad \text{in } [\AA] \tag{5.3}$$

The normalized Mn content $x(z)$ in a parabolical profile within a layer thickness of $d_{lay} = 60$ $\AA$ has been calculated. The result is illustrated as a black line in Figure 5.3. At $z = 0$ $\AA$, the Mn content x reaches its maximum value $x(z) = 1$, whereas at $z = \pm 30$ $\AA$, the

Mn content x is reduced to zero $x(z) = 0$. In order to implement the parabolical grading, the (Ga,Mn)As layer has been devided into 8 sections of constant witdh. According to Equation 5.3, the layer thickness of a section d_s is defined as

$$d_s = \frac{d_{lay}}{2 \cdot n} = \frac{60\mathring{A}}{2 \cdot 4} = 7.5\mathring{A}. \tag{5.4}$$

In order to comprehend the design of the parabolical Mn profile, the calculation of (Ga,Mn)As layer thicknesses $d_{s_n,(Ga,Mn)As}$ and LT-GaAs spacers $d_{s_n,LT-GaAs}$ is presented for positive z from $z = 0$ $\mathring{A}$ to $z = 30$ $\mathring{A}$. The calculation of $d_{s_n,(Ga,Mn)As}$ and $d_{s_n,LT-GaAs}$ with negative z is done in analogy to the symmetry of the parabola.

The integration of $x(z)$ within a section corresponds to the layer thickness of (Ga,Mn)As $d_{s_n,(Ga,Mn)As}$. Simultaneously, the division of $d_{s_n,(Ga,Mn)As}$ by the growth rate (e.g. 1 $\frac{\mathring{A}}{s}$) corresponds to the time interval of the opened Mn shutter. For all sections $s_{n=1,2,3,4}$, the integrals have the following forms

$$d_{s_n,(Ga,Mn)As} = \int_{d_{s_n}} x(z)dz \tag{5.5}$$

The difference in layer thickness between d_{s_n} and $d_{s_n,(Ga,Mn)As}$ is the layer thickness of the LT-GaAs spacer $d_{s_n,LT-GaAs}$. Furthermore, $d_{s_n,LT-GaAs}$ is divided by 2 to place equal fragments of LT-GaAs on both sides next to the (Ga,Mn)As layer within a section.

$$d_{s_n,LT-GaAs} = d_{s_n} - d_{s_n,(Ga,Mn)As} \tag{5.6}$$

$$d_{s_n,LT-GaAs/2} = \frac{d_{s_n,LT-GaAs}}{2} \tag{5.7}$$

In Figure 5.3, the parabolical grading of (Ga,Mn)As layer thicknesses is plotted as yellow bars. Sampling nodes (red points) of the $x(z)$ curve lie in the center of sections $s_{1,2,3,4}$ and are used to center the calculated (Ga,Mn)As layers within these sections.

The integrated thickness of (Ga,Mn)As layers is $d_{eff,(Ga,Mn)As)} = 40$ $\mathring{A}$. A clear decrease of (Ga,Mn)As layer thicknesses to the outer region of the total layer with $d_{lay} = 60$ $\mathring{A}$ is mentionable. The inset of Figure 5.3 shows, that the LT-GaAs spacer thickness of $d_{LT-GaAs} = 0.16$ $\mathring{A}$ at the center ($z = 0$) is within a critical layer thickness and a simultaneously critical time interval considering a growth rate of 1 $\frac{\mathring{A}}{s}$. In such a short time interval of 0.16 s, an influence of a time delay of the Mn shutter movement cannot be excluded, as discussed in Chapter 5.1.1.

Three arrangements have been made for the final layer structure. Primarily, the LT-GaAs spacer layer right before the first (Ga,Mn)As layer is added to the LT-GaAs growth start. Secondly, the LT-GaAs spacer layer at the center ($z = 0$) is skipped due to the delayed movement of Mn shutter and to have a relatively "thick" (Ga,Mn)As layer in the center part of the whole layer structure. Ideally, the center is shielded electrostatically by adjacent (Ga,Mn)As layers. At last, the LT-GaAs spacer layer right after the last

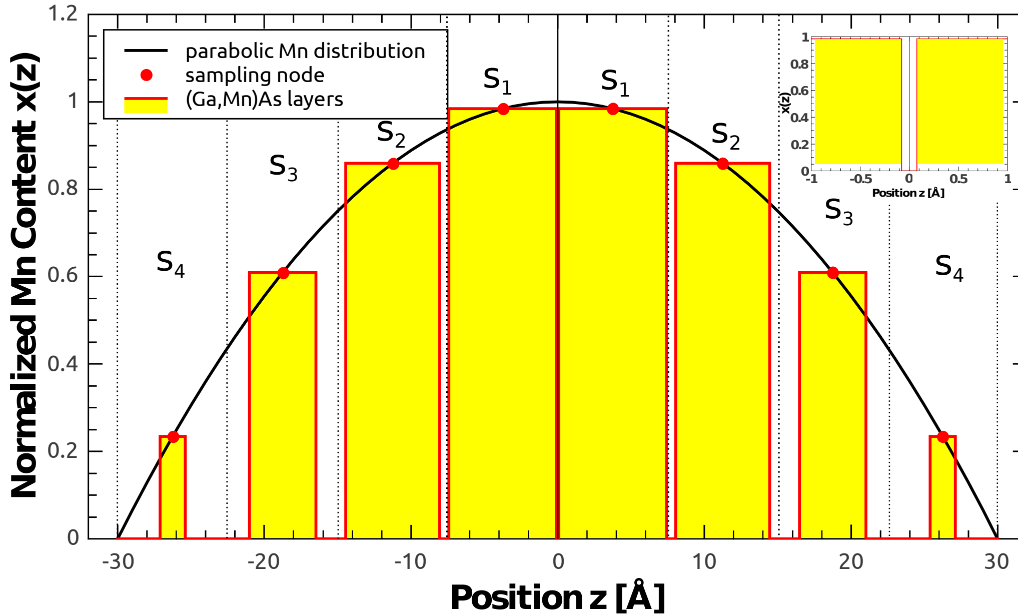

Figure 5.3: Parabolical shape of Mn distribution (black curve) and parabolical grading of (Ga,Mn)As layer thicknesses (yellow bars). Sampling nodes are used to center the (Ga,Mn)As layers within sections $s_{1,2,3,4}$. The inset shows the region around $z = 0$, where $d_{LT-GaAs} = 0.16$ $\AA$.

(Ga,Mn)As layer is added to the LT-GaAs capping layer. Therefore taking the LT-GaAs spacer layers between the (Ga,Mn)As layers into account, the total layer thickness is 52 $\AA$.

Table 5.1 gives an overview of the layer structure of a parabolically graded Mn distribution with $n = 4$, meaning four different (Ga,Mn)As layer thicknesses. Here, layer thicknesses of ≥ 0.6 $\AA$ are used and correspond to time intervals of ≥ 0.6 s, assuming a growth rate of 1 $\frac{\AA}{s}$. These Mn shutter opening times are above the critical time interval. Hence, it is assumed that time delays of the Mn shutter movements are uniform and are not critical for the epitaxial growth of the final parabolic layer structure.

Based on Table 5.1, the Mn shutter sequence of the parabolically grading for a growth rate of 1 $\frac{\AA}{s}$ is additionally shown in Figure 5.4. At $t = 0$ the epitaxial growth of the parabolical grading begins with an opening of the Mn shutter. The graph shows that the total Mn shutter sequence up to the end of the last opened position lasts 52 s which corresponds to the calculated layer thickness of 52 $\AA$ of (Ga,Mn)As and LT-GaAs spacer layers.

Type of Layer	calc. thickness [$\mathring{A}$]
LT-GaAs cap	10.0
(Ga,Mn)As	2.0
LT-GaAs	3.9
(Ga,Mn)As	4.7
LT-GaAs	1.7
(Ga,Mn)As	6.3
LT-GaAs	0.6
(Ga,Mn)As	14.0
LT-GaAs	0.6
(Ga,Mn)As	6.3
LT-GaAs	1.7
(Ga,Mn)As	4.7
LT-GaAs	3.9
(Ga,Mn)As	2.0
LT-GaAs start	10.0
HT-GaAs buffer	2000
GaAs semi-insulating	substrate (001)

Table 5.1: Final layer structure with parabolically graded Mn distribution used in this thesis. The LT-GaAs spacer between the center sections s_1 ($d = 0.16\mathring{A}$) has been removed to reveal a thick layer in the center and to avoid an influencing time delay of Mn shutter movements.

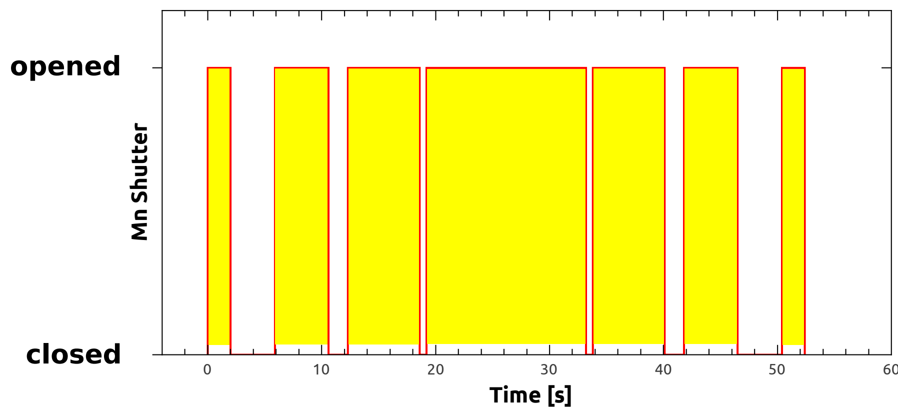

Figure 5.4: Mn shutter sequences for a parabolically grading of Mn content with effective thickness of (Ga,Mn)As layers $d_{eff,(Ga,Mn)As} = 4\ nm$. The yellow regions are the time intervals in which the Mn shutter is opened. The growth rate is 1 $\frac{\mathring{A}}{s}$.

5.2 Variation of Mn Content at Standard Growth Conditions

This section presents the fabrication of a parabolical layer structure by epitaxial MBE growth and subsequent sample characterization. In a first sample series standard growth conditions (see Chapter 3.2.1) have been used while varying the Mn content.

5.2.1 Epitaxial Growth and RHEED

The total layer structure of the parabolical graded Mn profile sample is grown epitaxially as follows: First of all, a 200 nm HT-GaAs buffer has been deposited at $T_{sub} = 580°C$ and at a BEP ratio of ($\frac{As_4}{Ga}$)= 40 on a GaAs (001) semi-insulating substrate. The LT-growth of the parabolically graded layer structure has been started at our standard growth conditions of $T_{sub} = 270°C$ and a BEP ratio of ($\frac{As_4}{Ga}$)= 25 with a 1 nm layer of LT-GaAs, according to Table 5.1. Finally the parabolically graded layer has been capped with a 1 nm LT-GaAs layer.

An overview of the sample series is given in Table 5.2. The sample series contains parabolically graded (Ga,Mn)As layers with a nominal Mn content ranging from $x = 0.005$ to 0.10. Additionally, a parabolic layer without a 1 nm LT-GaAs cap layer as well as a 70 nm layer and a 4 nm reference layer with homogeneous Mn profile and a 1 nm LT-GaAs cap layer have been grown at the same growth conditions and the same Mn content of $x = 0.04$. The Mn content calibration has been accomplished by HRXRD measurement of the 70 nm layer. This layer is the starting point for all other samples within this series to nominally state the Mn content referred to the rule of thumb for Mn content in Chapter 3.3. According to the opening time of the Mn cell, the 4 nm reference layer has nominally the same amount of Mn atoms like the parabolically graded layer with nominal $x = 0.04$ and a nominally total effective (Ga,Mn)As layer thickness of 4 nm. The difference between these two layers is a different distribution of Mn along the growth direction, resulting in a slightly larger total layer thickness of 5.2 nm due to the LT-GaAs spacers. As mentioned before, interface roughnesses and interdiffusion of Mn atoms at monolayer scale during deposition might result in a smoothening of the Mn distribution. Mn diffusion into LT-GaAs has already been observed in (Ga,Mn)As / GaAs superlattices by cross-sectional scanning tunneling microscopy [Mik04]. The parabolical layer structure is considered as a single ferromagnetic layer which seems to be plausible due to former neutron scattering experiments on (Ga,Mn)As / GaAs superlattices, where (Ga,Mn)As layers (10 ML) are ferromagnetically coupled even for GaAs spacer thicknesses of 6 to 8 ML (17.0 to 22.6 $Å$) [Sad02].

Sample No.	nominal x	Mn profile	RHEED	Remarks
S651	0.005	parabolic	(1x2)	
S652	0.01	parabolic	(1x2)	
S590	0.02	parabolic	(1x2)	
S589	0.03	parabolic	(1x2)	
S576	0.04	parabolic	(1x2)	
S593	0.04	parabolic	(1x2)	without LT-GaAs cap
S577	0.06	parabolic	(1x2)	
S592	0.08	parabolic	(1x2)+spotty	roughening after t > 7 sec
S591	0.10	parabolic	(1x2)+spotty	roughening after t > 7 sec
S577	0.04	homogeneous	(1x2)	70 nm reference layer
S575	0.04	homogeneous	(1x2)	4 nm reference layer

Table 5.2: First growth series of parabolically graded (Ga,Mn)As layers and reference samples. All layers have been grown at $T_{sub} = 270°$C and BEP ratio $(\frac{As_4}{Ga}) = 25$. Samples with a Mn content $x > 0.06$ show a gradual surface roughening. The solubility limit is presumably reached at $T_{sub} = 270°$C for such high Mn concentrations.

During MBE deposition, the maximum intensity of the streaky (1×2) RHEED pattern is reached in the middle of the parabolical layer. Additionally, for samples with very high Mn content $x \geq 0.08$, a gradual surface roughening during growth has been observed by a spotty (1×2) RHEED pattern. A crossing of the solubility limit of Mn at a substrate temperature of $T_{sub} = 270°C$ is assumed for this observation. After growth, samples with a Mn content up to $x = 0.06$ showed a slightly weaker but still streaky (1×2) RHEED pattern, presumably due to the LT-GaAs capping layer. A (1×1) surface reconstruction has been observed for epitaxially grown LT-GaAs material by A.Shen [She97].

5.2.2 As-grown and Annealed Parabolic Layer Characterization

Extracted Curie temperatures T_C out of SQUID measurements of the as-grown parabolically graded (Ga,Mn)As layers with varied Mn content are shown in Figure 5.5(a) (black dots).

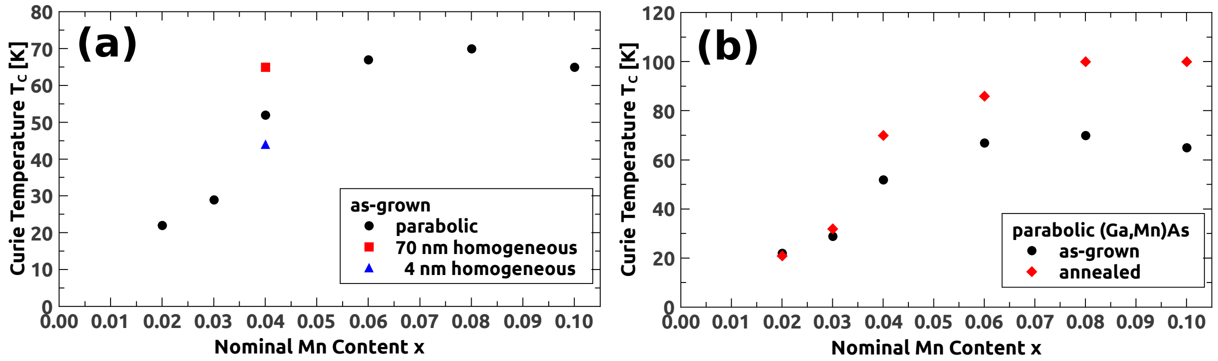

Figure 5.5: (a) Curie temperature T_C vs. nominal Mn content x for as-grown layers with parabolical graded (black dots) as well as 70 nm homogeneous (red square) and 4 nm homogeneous (blue triangle) Mn profile with $x = 0.04$. (b) Comparison of T_C vs. x before (black dots) and after annealing (red rhombi).

Samples with $x \geq 0.02$ reveal ferromagnetic response at $T = 4.2K$ and Curie temperatures up to $T_C = 70K$ for a Mn content $x = 0.08$. At such high Mn content x, the layer-by-layer growth has changed to a gradual surface roughening which has been explained in the last section by the excess of the solubility limit of Mn at prevalent growth conditions. The minimum Mn content of $x > 1$, necessary for ferromagnetism in bulk (Ga,Mn)As layers [Sad00], is in agreement with the result of thin, parabolical graded layers. The reference samples with a homogeneous Mn profile and a nominal Mn content of $x = 0.04$ with 70 nm (red square) and 4 nm (blue triangle) are also shown in Figure 5.5(a). The Curie temperature of the parabolical graded layer with $x = 0.04$ is located between the two T_C values of the thin and thick reference layers. A detailed comparison of these layers is discussed later on in this section.

In Figure 5.5(b) T_Cs of the as-grown samples (black dots) are compared to T_Cs of the annealed samples (red rhombi). The as-grown samples have been annealed for 3 hrs at $T_{ann} = 185°C$ on a hot plate after the first SQUID measurement, as described in Chapter 3.2.1. The annealing procedure leads to an increase of Curie temperature up to 100 K for a nominal Mn content of $x = 0.08$ which corresponds to an increase of 30 K. Although having a 1 nm LT-GaAs cap layer it is still possible for Mn interstitials to diffuse to the surface. A LT-GaAs cap layer of at least 8 to 10 MLs ($\sim$ 22.6 to 28.3 $\AA$) forms an electrostatic barrier for outdiffusion of Mn interstitials, as published in [Sto03, Ade11]. It is worth mentioning, that such increase of T_C after the annealing procedure has not been measured for samples with a moderate Mn content of $x = 0.02$ and $x = 0.03$. Only a maximum increase of $T_C = 3$ K after annealing has been determined. Hence, it can be

assumed that incorporated arsenic antisites with concentrations of $\sim 10^{19}$ to 10^{20} cm^{-3} are mostly responsible for the compensation of hole carrier concentration in case of low-doped (Ga,Mn)As samples. Mn interstitials obviously play a minor role, according to the results of the magnetometry measurements before and after annealing.

RT-conductivity values have been performed by the method described in Chapter 3.5. Additionally, the estimation of RT-hole concentration by Hall-measurements with low applied magnetic fields up to about 80 mT is additionally explained in this Chapter. The multiplication of the measured carrier concentration and the total effective layer thickness of parabolically graded (Ga,Mn)As ($d_{eff,(Ga,Mn)As} = 4 \cdot 10^{-7}$ cm) results in a calculated sheet carrier concentration. As already mentioned, these values have to be taken with special care and serve as a rough estimation of hole concentration in the sample. The results are presented in Figure 5.6(a) and (b).

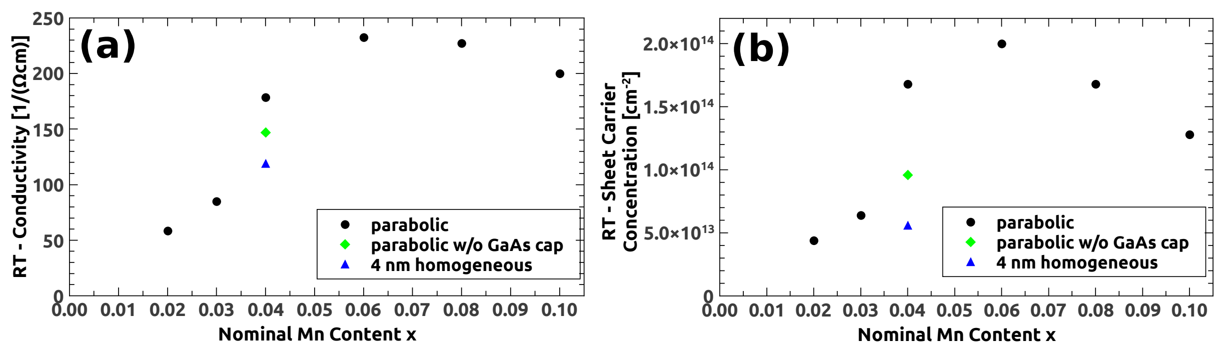

Figure 5.6: RT measurement results in 4-terminal Hallbar geometry of (a) conductivity and (b) sheet carrier concentration vs. nominal Mn content x for parabolic layers (black dots) as well as parabolic layer without a GaAs cap (green rhomb) and 4 nm reference layer (blue triangle), both with $x = 0.04$). A consistent behavior of both graphs is visible with highest RT-conductivity and RT-sheet carrier concentration values at $x = 0.06$.

The measured RT-conductivity values and RT-sheet carrier concentrations versus the nominal Mn content x of parabolically graded samples which show ferromagnetic response ($x \geq 0.02$, black dots), a parabolic layer without a LT-GaAs cap layer (green rhombi) and a 4 nm reference layer (blue triangle), both with the same Mn content $x = 0.04$, are plotted. The trend in both graphs is the same with maximum values of conductivity (RT-$\sigma = 233$ $\frac{1}{\Omega cm}$) and sheet carrier concentrations (RT-$p_{sheet} = 2.0 \cdot 10^{14}$ cm^{-2}) at a nominal Mn content of $x = 0.06$. Compared to the assumption of a free hole carrier concentration of $p = 1.3 \cdot 10^{21}$ cm^{-3} for $x = 0.06$ without any compensation, the sheet carrier concentration is calculated to be $p = 5.3 \cdot 10^{14}$ cm^{-2}. Therefore, the RT-activation fraction amounts 38 %, which is roughly a factor of 2 higher compared to a 70 nm (Ga,Mn)As layer epitaxially grown at standard growth conditions with a Mn content of $x = 0.04$ and measured $p = 1.9 \cdot 10^{20}$ cm^{-3}, as mentioned in Chapter 4.1.2. This result supports the presented SQUID results, where the parabolically graded layer with $x = 0.06$, which is close to the solubility limit of Mn at standard growth conditions, shows highest T_C, as seen in Figure 5.5(a).

Influence of LT-GaAs Cap and Comparison to 4 nm Homogeneous Layer with $x = 0.04$

Besides the variation of Mn content x for parabolically graded layers, one parabolically graded sample without a LT-GaAs capping layer and a 4 nm reference layer with a LT-GaAs cap have been grown under standard growth conditions with nominally the same Mn content $x = 0.04$. Both layer results (marked as green rhomb and blue triangle) are shown in Figure 5.6(a) and (b).

First a decrease of RT-σ and RT-sheet carrier concentration p_{sheet} is measured in case of the parabolic layer without a LT-GaAs cap layer (RT-$\sigma = 147 \frac{1}{\Omega cm}$ and RT-$p_{sheet} = 9.6 \cdot 10^{13}$ cm^{-2}) compared to the parabolically graded layer with a LT-GaAs cap (RT-$\sigma = 184 \frac{1}{\Omega cm}$ and RT-$p_{sheet} = 1.68 \cdot 10^{14}$ cm^{-2}). Such influence of the capping layer can be interpreted as a shielding of surface defects from the (Ga,Mn)As layer, as already discussed in Chapter 2.2.1 and 4.2. Without a LT-GaAs cap layer the depletion of holes is higher and RT-σ as well as RT-p_{sheet} is consequently lowered.

The RT-conductivity σ value of the 4 nm reference layer with a LT-GaAs cap amounts only 65 % (RT-$\sigma = 119 \frac{1}{\Omega cm}$) of the RT-conductivity σ for the parabolic layer with a 1 nm LT-GaAs cap layer. Even the parabolic layer without the capping layer and the same Mn content x has still higher values, as can be seen in Figure 5.6(a). In Figure 5.6(b), the RT-sheet carrier concentration is only a third of the value for the parabolic layer with a LT-GaAs capping layer.

A conclusion out of these RT-measurements is that a parabolic distribution of Mn atoms along the growth direction in a very thin layer is helpful for a reduction of compensating effects like surface and point defects. It seems that the parabolical grading of Mn profile in a very thin layer reduces the randomness of Mn incorporation resulting in a decreased inhomogeneity of the potential landscape. Thus, a higher RT-conductivity as well as a higher sheet concentration of mobile holes have been achieved compared to a layer with a homogeneous Mn profile and its normal randomized Mn distribution.

At this point it is obvious, that RT-measurements alone are not sufficient to characterize these layers, especially its ferromagnetic and electrical properties. Therefore, LT-measurements at 4.2 K have been performed in the following section to characterize the ferromagnetic properties of such thin graded layers.

5.2.3 LT-Conductivity of Parabolical Graded and Homogeneous (Ga,$Mn_{0.04}$)As Layers

The last section showed results of RT-conductivity measurements. Besides these characterizations, cooling curves as well as magnetic anisotropy fingerprints have been performed to compare LT-properties of a parabolically graded layer with a Mn content of $x = 0.04$ and 0.06 and a 4 nm reference layer with $x = 0.04$. The ferromagnetic properties are only present in (Ga,Mn)As layers below T_C.

Temperature-dependent resistance measurements have been done in 4-terminal Hallbar geometry in a cryostat. The longitudinal resistance R_{xx} has been measured according to

Chapter 3.5 with a reference resistance of 100 $k\Omega$. R_{xx} is a function of time during the cooling process. The measurement begins at RT and ends at a stable state at $T = 4.2\ K$. The results of all three samples are presented in Figure 5.7(a) to (c).

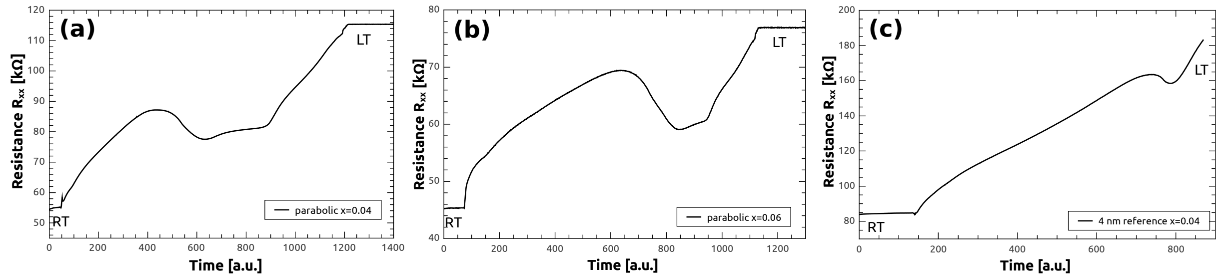

Figure 5.7: Cooling curves in 4-terminal Hallbar geometry for (a) parabolic graded layer with $x = 0.04$, (b) parabolic graded layer with $x = 0.06$ and (c) 4 nm reference layer with $x = 0.04$.

In principle, all three measurements show lowest R_{xx} at RT, the local maximum during the cooling process which corresponds to the incipient ferromagnetic ordering at T_C within the layer and at last a R_{xx} value at $T = 4.2\ K$, which is higher compared to the R_{xx} value at the local maximum. The same behavior of temperature-dependent resistance measurements has already been observed for the 7 nm (Ga,Mn)As layer of Chapter 4.2.3. A higher value of R_{xx} for all thin layers after the local maximum is in contrast to our standard bulk (Ga,Mn)As cooling curves, where R_{xx} at $T = 4.2\ K$ lies below the local maximum. A higher compensation of hole carriers and/or inhomogeneous lateral current flow through the thin (Ga,Mn)As layer might be responsible for higher R_{xx} at low temperatures.

Table 5.3 gives an overview of RT- and LT-resistance and conductivity values of these layers.

	parab. $x = 0.04$	parab. $x = 0.06$	homog. $x = 0.04$
RT-R_{xx} $[k\Omega]$	54.5	45.3	84.0
LT-R_{xx} $[k\Omega]$	115.4	76.9	183.0
RT-σ $[\frac{1}{\Omega \cdot cm}]$	183.5	220.8	119.0
LT-σ $[\frac{1}{\Omega \cdot cm}]$	86.7	130.0	54.6

Table 5.3: RT- and LT-resistance R_{xx} and conductivity σ values of parabolically graded (Ga,Mn)As layers with Mn content of $x = 0.04$ and $x = 0.06$ and of a 4 nm reference layer with $x = 0.04$.

First of all, RT- and LT-values of the parabolic layer with a Mn content of $x = 0.06$ in Figure 5.7(b) is highest, compared to a homogeneous or parabolically graded layer with $x = 0.04$. The higher Mn content results in a higher conductivity. LT-σ of all layers are about half of their RT-σ values.

At RT and LT, the parabolic layer with a Mn content of $x = 0.04$ in Figure 5.7(a) has a lower resistance and therefore a higher conductivity value compared to the reference layer

with homogeneous Mn profile in Figure 5.7(c), although having the same amount of Mn, according to the total Mn shutter opening times during epitaxial growth. In turn, this result confirms magnetometry and Hall-measurements which show higher T_C and higher RT-sheet hole carrier concentration in case of the parabolically graded Mn profile.

4-terminal longitudinal magnetoresistance measurements with applied in-plane magnetic fields up to ± 300 mT at different angles Φ relative to the current direction in a [100] crystal direction at 4.2 K have been performed. The domain wall nucleation/propagation energy per volume magnetization ϵ/M and the strength of the uniaxial anisotropy constant along a [110] direction K_{110} relative to the biaxial anisotropy constant K_{biax} have been extracted, according to Chapter 2.3.1.

Figure 5.8 shows the inner region of an anisotropy fingerprint from 0 to 30 mT of the parabolic layer with $x = 0.04$. A value of 18 mT for ϵ/M lies in the range of published values and corresponds to values presented in Chapter 2.3.1, [Gou08]. A doubling in K_{110}/K_{biax} ratio of 39% for the parabolic layer compared to the ratio of 17 % for the bulk layer might be caused by a higher doping efficiency. A comparison of RT charge carrier activation fraction of the parabolically graded layer and bulk reference layer (both with $x = 0.04$) in Chapter 5.2.2 confirms qualitatively this assumption by a higher RT activation fraction of 38 % for the thin layer compared to bulk material. As mentioned before, the determination of LT-hole carrier concentrations needs special cryostats equipped with magnets for very high magnetic fields ($H > 20$ T) due to the superposed signal of the anomalous Hall-effect (Chapter 2.3.1). This kind of measurement has not been performed within the framework of this thesis. Therefore, the conclusion of RT to LT carrier concentration has to be regarded with suspicion. In general, the ratio of K_{110}/K_{biax} can be tuned for example as a function of hole concentration and temperature, as proofed in [Saw05] and [Pap07].

Aside from stronger rotation of magnetization switching events, shown in Figure 5.8 as a color gradient from black (low resistance) to red (high resistance), it is not possible to estimate a uniaxial anisotropy component K_{010} along a [010] crystal direction for the parabolic layer.

In total, this section has shown, that epitaxial growth of a very thin (Ga,Mn)As layer with a parabolically graded Mn distribution shows ferromagnetic response at Mn content of $x \geq 0.02$. A comparison of a parabolically graded Mn distribution compared to a homogeneous Mn distribution for the same Mn content $x = 0.04$ and an effective layer thickness of 4 nm shows, that the parabolical grading improves magnetic and electrical properties. Additionally, anisotropy fingerprint measurements show that the magnetic properties of such thin layers have a similar magnetic anisotropy behavior like standard bulk material for the same Mn content ($x = 0.04$) with a more pronounced uniaxial component.

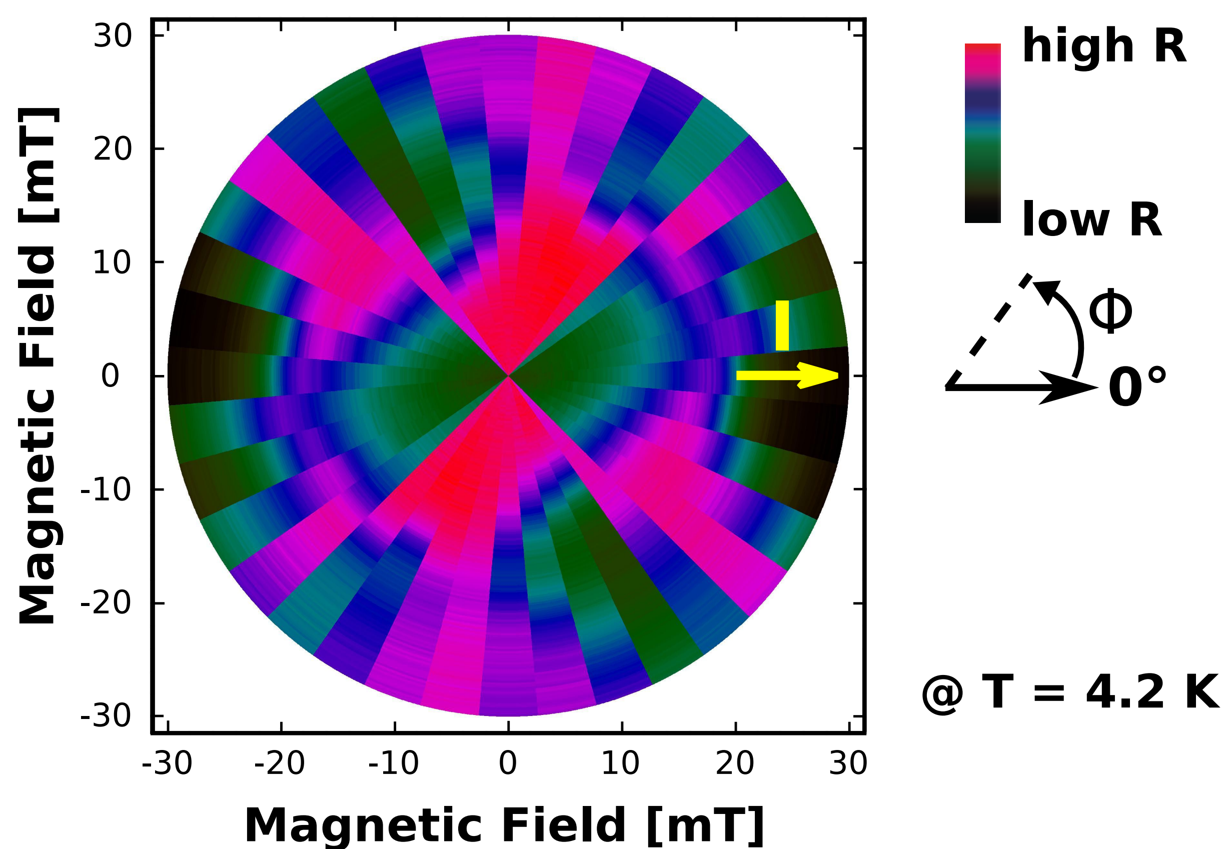

Figure 5.8: Anisotropy fingerprint of a parabolic layer with $x = 0.04$ and 1 nm LT-GaAs cap layer. The rectangular shape indicates a biaxial anisotropy and additionally an uniaxial anisotropy component along a [110] direction.

5.3 Optimization of Growth Conditions with Constant Mn Content $x = 0.025$

The last section has shown that the parabolic grading of the Mn distribution is suitable to have a very thin ferromagnetic layer with a feasible electrical LT-conductivity. These properties are improved compared to previous epitaxial growth of thin (Ga,Mn)As layers, where "freezed-out" regions are responsible for hindered current paths and led to contacting problems of thin layers, as described earlier in Chapter 4.2.

As discussed in the motivation for very thin layers, electrical gating is a possible application of these layers. As described in the diploma thesis of M. Freitag [Fre09], ferroelectrical gating has been achieved for a 7 nm layer with a Mn content of at least $x = 0.049$ by a change of 20 % in resistance and a change of Curie temperature T_C of about 7 K. It is obvious, that a higher gating effect is possible with a lowered Mn content x.

Out of the first growth series of parabolically graded (Ga,Mn)As layers samples with $x = 0.02$ and 0.03 have shown a ferromagnetic response. Using this result as a starting point, the epitaxial growth of parabolically graded layers with a moderate Mn content of $x = 0.025$ have been optimized. This Mn content has been chosen to be in a save region where the (Ga,Mn)As layer shows ferromagnetic behavior at low temperatures.

5.3.1 Determination of Parameter Range by 70 nm (Ga,Mn)As Layers

In Chapter 4.1 the crucial role of point defects like As_{Ga} and Mn_{int} on the properties of (Ga,Mn)As have been discussed. Especially for As_{Ga} a trend to lower antisite defect concentrations by an increased substrate temperature T_{sub} and/or lowered BEP ratio ($\frac{As_4}{Ga}$) down to the 2D/3D growth border is noticeable. Additionally, the substrate temperature dependent Mn content x at the 2D/3D growth border of Figure 3.5 in Chapter 3.2.1 confirms a shift of the growth border to higher substrate temperatures for lower x. For a systematical investigation of growth conditions for samples with parabolically graded Mn distribution and a moderate Mn content of $x = 0.025$, it is favorable to restrict the parameter range of substrate temperature and BEP ratio ($\frac{As_4}{Ga}$).

In this context a preseries of 70 nm thick (Ga,Mn)As layers have been epitaxially grown with constant BEP ratio ($\frac{As_4}{Ga}$) = 25 while varying T_{sub} to determine the 2D/3D growth border of a distinct Mn content of $x = 0.024$. In total, 7 samples with substrate temperatures ranging from 270 to 330°C in steps of 10°C have been fabricated. Surface reconstruction observations during growth by RHEED, HRXRD measurements, SQUID measurements as well as 2 terminal RT resistance measurements (see Chapter 3.5) served as a first overview of the feasible parameter range.

Table 5.4 lists the growth parameters of the sample preseries.

RHEED patterns of samples with T_{sub} up to 310°C showed streaky (1×2) surface reconstructions during and after the epitaxial growth due to layer-by-layer growth mode, as seen in Figure 5.9(a). At the beginning of the epitaxial growth with higher T_{sub} ≥320°C,

Sample No.	$\mathbf{T}_{sub}$ °C	BEP ratio $(\frac{As_4}{Ga})$	RHEED-Reconstruction
S632	270	25	streaky (1×2)
S635	280	25	streaky (1×2)
S630	290	25	streaky (1×2)
S636	300	25	streaky (1×2)
S631	310	25	streaky (1×2)
S634	320	25	spotty (1×2) & hexagonal after 120 sec
S633	330	25	spotty (1×2) & hexagonal after 65 sec

Table 5.4: Preseries of 70 nm thick (Ga,Mn)As layers with nominal Mn content of $x = 0.024$ and constant BEP ratio $(\frac{As_4}{Ga}) = 25$ while varying T_{sub}.

a spotty (1×2) RHEED pattern and later on a pure hexagonal RHEED pattern has been observed. For T_{sub} =320°C the change has been monitored after 120 s, for T_{sub} =330°C the change has taken place already 65 s after growth start. The hexagonal RHEED pattern is presented in Figure 5.9(b).

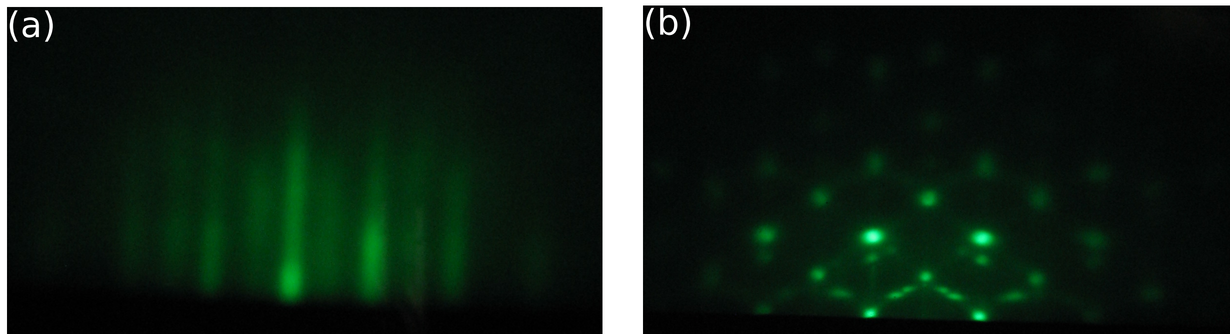

Figure 5.9: RHEED diffraction patterns after growth of 70 nm (Ga,Mn)As layers (with nominal Mn content $x = 0.024$ and BEP ratio $(\frac{As_4}{Ga} = 25)$ for (a) layer-by-layer growth up to T_{sub} =310°C along $[1\bar{1}0]$ azimuth and (b) RHEED pattern for T_{sub} ≥320°C.

The hexagonal structure can be explained by the phase transition diagram of Ohno et al., as seen in Figure 3.4 of Chapter 3.2.1. At higher substrate temperatures above ≈310 °C, segregation of Mn and/or MnAs cluster formation is prevalent and lead to extended defect concentrations. This behavior is in contrast to the typical layer-by-layer growth mode. Nevertheless, the exact surface temperature of the grown samples cannot be determined by measuring the substrate temperature with a thermocouple in thermal contact to the backside of a molybdenum block. Other methods like band-edge absorption spectroscopy (used by e.g. *kBandiT* of RTA Instruments Ltd.) might be a helpful tool for a more accurate substrate temperature measurement.

2-terminal measurements by multimeter probes have been used right after the growth to get a first electrical characterization of the samples. Later on, magnetometry measurements have been implemented. Both results are shown in Figure 5.10(a) and (b).

T_C as well as the inverse resistance $1/R$ in dependence of substrate temperature T_{sub} show highest values at T_{sub} =280°C and 290 to 300°C respectively. Compared to the growth at standard growth conditions at T_{sub} =270°C with BEP ratio $(\frac{As_4}{Ga}) = 25$, an increase of inverse resistance and T_C up to a substrate temperature of T_{sub} ≈290°C can be interpreted as a reduction of Arsenic antisite concentration due to a higher T_{sub}, which leads to less hole carrier compensation in the (Ga,Mn)As layer. A further increase of T_{sub} leads to a decline of electrical and magnetic properties caused by roughening of the surface as seen in RHEED during growth for $T_{sub} = 320$ and 330°C due to Mn segregation and/or MnAs clusters which strongly compensate hole carriers.

As a conclusion of this preseries, substrate temperatures ranging from 270 to 310°C in steps of 20°C with BEP ratios $(\frac{As_4}{Ga})$ of 15, 20 and 25 (according to minimum BEP ratio at 270°C in Chapter 4.1.1) have been chosen to span the parameter space of the growth conditions for optimization of parabolically graded (Ga,Mn)As layers with a Mn content of $x = 0.025$.

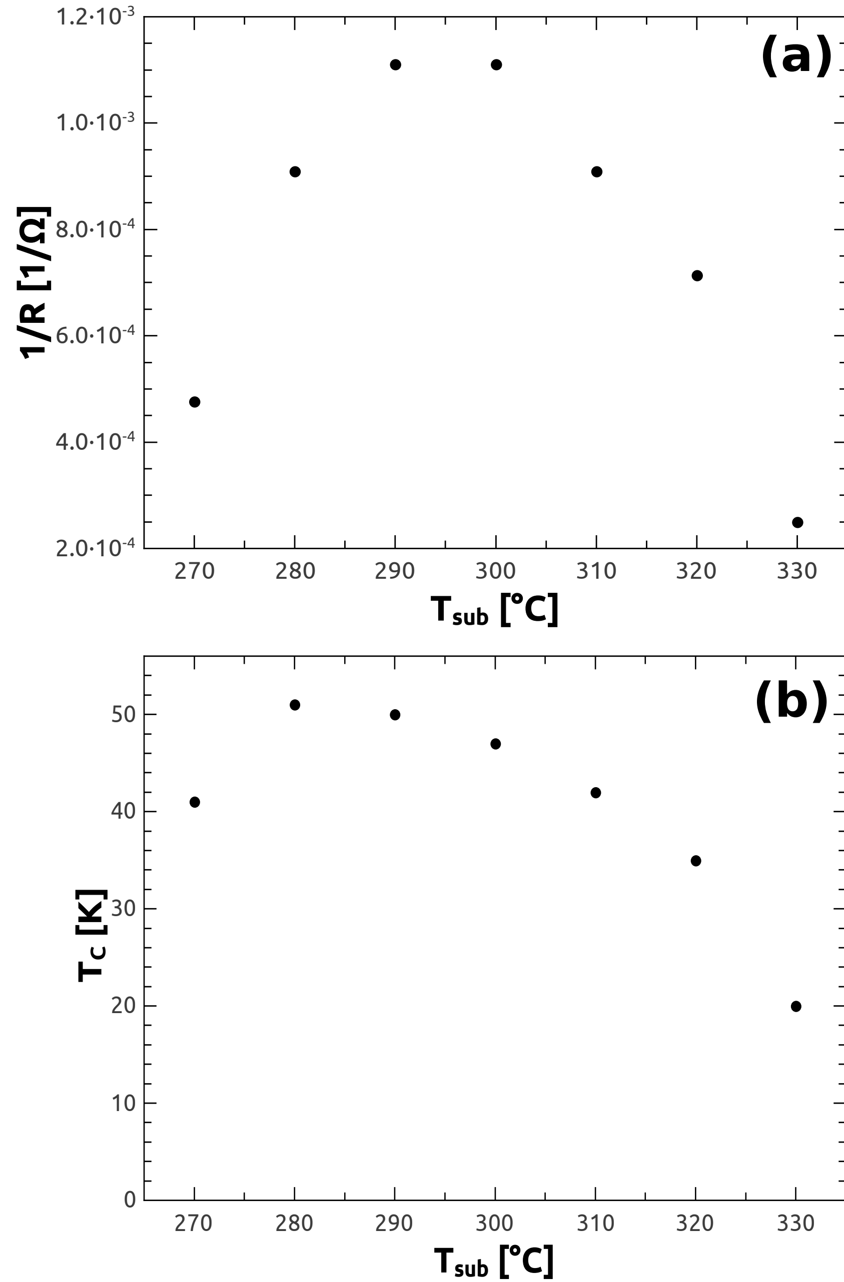

Figure 5.10: Inverse resistance $1/R$ (a) and Curie temperature T_C (b) as a function of substrate temperature T_{sub} of 70 nm (Ga,$\mathrm{Mn}_{0.024}$)As layers. Highest values for $1/R = 1.1 \cdot 10^{-3}\ \frac{1}{\Omega}$ and $T_C \approx 50\ K$ are achieved around T_{sub} =290°C.

5.3.2 Optimization of Growth Conditions of Thin Parabolical (Ga,Mn)As Layers

In the last Section 5.3.1 a reasonable parameter range for thick layers has been determined, which will be used in the following for epitaxial growth optimization of parabolically graded (Ga,Mn)As layers with a moderate Mn content of $x = 0.025$. Substrate temperatures of 270, 290 and 310°C with BEP ratios ($\frac{As_4}{Ga}$) of 15, 20 and 25 have been used. The growth parameters of the complete sample series is listed in Table 5.5.

Sample No.	$\mathbf{T}_{sub}$ °C	BEP ratio ($\frac{As_4}{Ga}$)	RHEED	Remarks
S710		15	streaky (1×2)	
S711	270	20	streaky (1×2)	
S712		25	streaky (1×2)	
S713		15	streaky (1×2)	
S714	290	20	streaky (1×2)	
S715		25	streaky (1×2)	
S722		15	streaky (1×2)	
S721	310	20	streaky (1×2)	
S716		25	streaky (1×2)	
S723	290	20	streaky (1×2)	reproduction of S714
S725	295	20	streaky (1×2)	T_{sub} 5°C higher than S714/S723
S724	290	20	streaky (1×2)	like S714/S723 with $x = 0.016$
S709	260	25	streaky (1×2)	70 nm reference $x = 0.025$
S787	290	20	streaky (1×2)	70 nm optimized growth & $x = 0.022$

Table 5.5: List of parabolically graded (Ga,Mn)As layers with nominally $x = 0.025$ grown at $T_{sub} = 270$, 290 and 310°C and BEP ratios ($\frac{As_4}{Ga}$) = 15, 20 25. Thick reference layers at standard growth conditions, $T_{sub} = 290$°C and BEP ratio ($\frac{As_4}{Ga}$) = 20 have been grown as well. S724 with $x = 0.016$ deviates from the other samples in the chosen Mn content.

Besides the (Ga,Mn)As layers grown under systematical changed growth conditions, a reproduction of S714 at $T_{sub} = 290$°C and BEP ratio ($\frac{As_4}{Ga}$) = 20 has been grown (S723), as well as a parabolically graded layer under the same growth conditions with lowered Mn content $x = 0.016$ (S724). One sample with a small intended deviation of 5°C at $T_{sub} = 295$°C and BEP ratio ($\frac{As_4}{Ga}$) = 20 has been grown additionally (S725). The Mn content has been determined by HRXRD of a 70 nm bulk (Ga,Mn)As layer (S709). A second 70 nm bulk layer (S787) with comparable Mn content of $x = 0.022$ has been grown at $T_{sub} = 290$°C and BEP ratio ($\frac{As_4}{Ga}$) = 20, which turned out to be optimal for parabolic layers like S714, S723 and S724.

During and after the growth of all parabolically graded (Ga,Mn)As layers and bulk reference layers, all RHEED patterns showed a typical streaky (1×2) surface reconstruction,

as seen in Figure 5.11(a). Mn segregation and/or MnAs clusters would lead to pronounced surface roughening, which can be excluded by RHEED observations. A convenient way to investigate the surface of a sample is the Nomarski interference microscopy. Its vertical resolution achieves a few *nm*. Examplarily, a Nomarski image shows typical cross-hatch structures along [110] and [$\bar{1}$10] directions, as seen in Figure 5.11(a). The origin of the cross-hatches is threading dislocations which arise out of small precipitates in the substrate and intersect the substrate surface along [110]. For a more detailed description of this defect type and an overview of defect types in (Ga,Mn)As layers, see [Cun86] and [Wen08]. In general, all epitaxially grown (Ga,Mn)As layers on a semi-insulating GaAs (001) substrate in this thesis have shown a cross-hatch pattern.

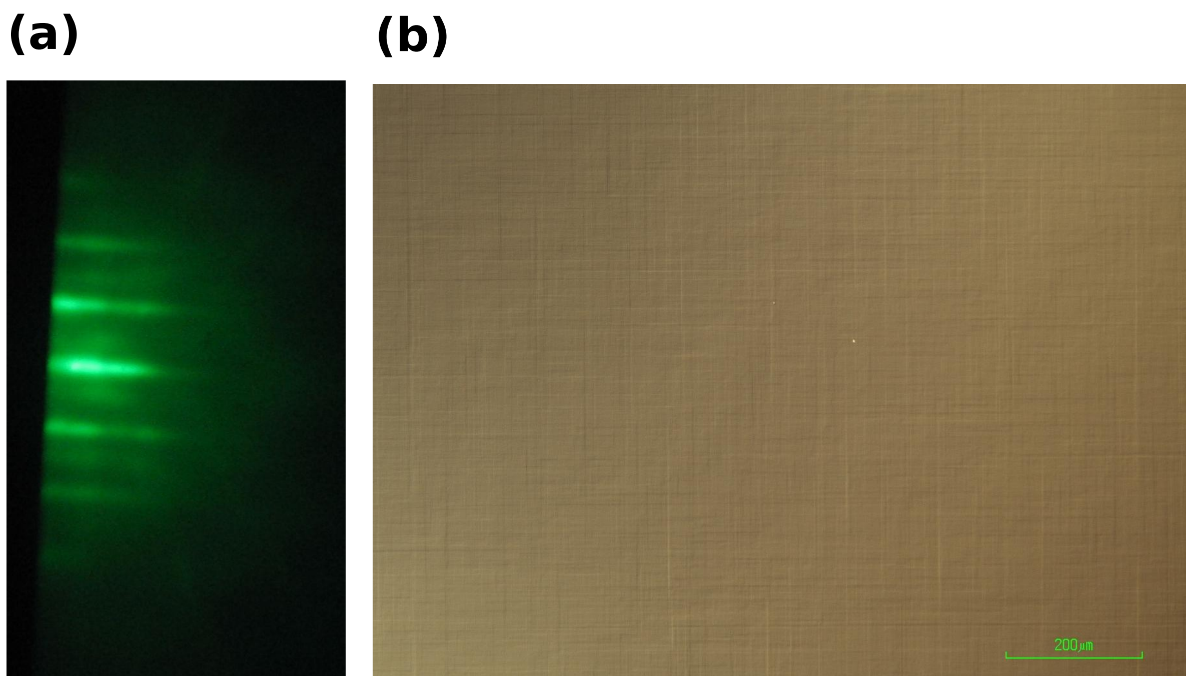

Figure 5.11: (a) Streaky (1×2) RHEED pattern and (b) Nomarski interference microscope image with cross-hatches of a parabolically graded layer. All grown layers of the sample series have shown such structural property.

The samples have been investigated by SQUID measurements, RT- and LT-transport measurements and anisotropy fingerprint measurements. The thick reference layers have been additionally analyzed by HRXRD. In the following, the results will be presented and discussed.

5.3.3 Magnetic Characterization

SQUID magnetometry measurements of parabolically graded as-grown samples at T_{sub} = 270, 290 and 310°C and BEP ratios ($\frac{As_4}{Ga}$) = 15, 20 and 25 have been performed to determine the Curie temperature T_C. Figure 5.12 shows a plot of extracted T_C as a function of growth parameters in the given range.

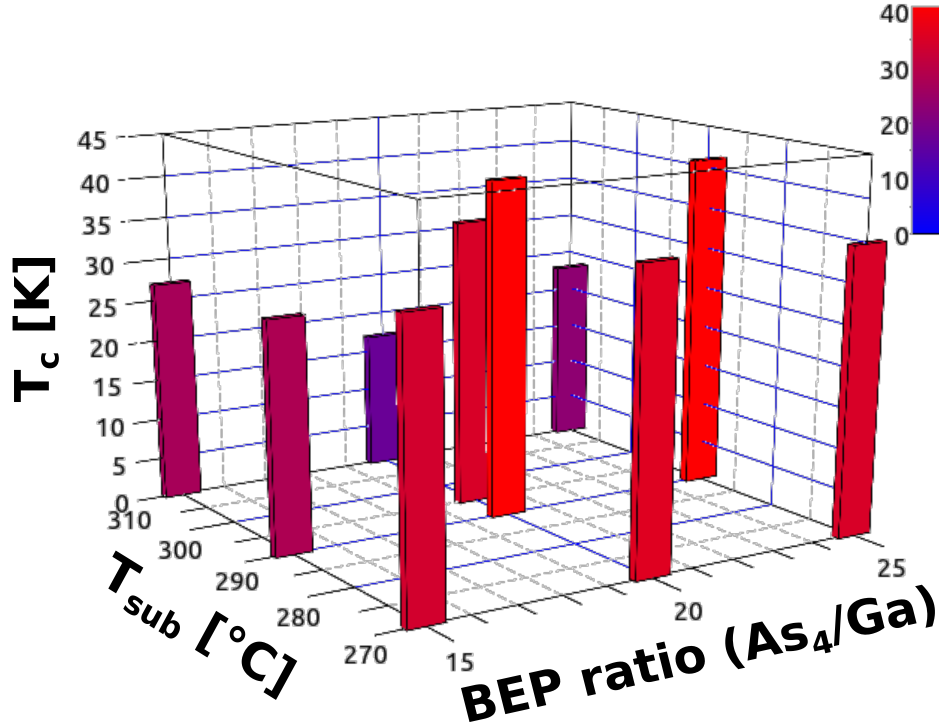

Figure 5.12: Plot of extracted T_C of parabolically graded (Ga,Mn)As layers with a Mn content of $x = 0.025$ as a function of T_{sub} and BEP ratio ($\frac{As_4}{Ga}$). The sample at T_{sub} =295°C and a BEP ratio ($\frac{As_4}{Ga}$) = 20 shows, that small deviations of growth conditions lead to a decreased T_C.

It is worth mentioning, that all epitaxial grown (Ga,Mn)As layers in a parabolically graded Mn profile show ferromagnetic response with T_Cs ranging from 17 to 41 K. Samples grown at T_{sub} =270°C have a T_C around 35 K whereas for T_{sub} =310°C, T_C is lowest down to 17 K. At T_{sub} =290°C and a BEP ratio ($\frac{As_4}{Ga}$) of 20 and 25, highest T_C of 41 K has been achieved. Compared to the preseries of Section 5.3.1 at 70 nm (Ga,$Mn_{0.024}$)As layers with a maximum T_C = 51 K, the maximum Curie temperature around T_{sub} =290°C of the parabolically graded layer is reduced.

Additionally, a parabolically graded (Ga,Mn)As layer with an intended slightly higher substrate temperature of 295°C and BEP ratio ($\frac{As_4}{Ga}$) = 20 has been grown. A T_C of 35 K shows, that even small deviations in growth conditions of substrate temperature and/or BEP ratio ($\frac{As_4}{Ga}$) lead to deteriorated ferromagnetic properties.

5.3.4 RT- and LT-Conductivity Measurements

In the following, transport measurements of the sample series presented in the last section with systematical change of growth conditions have been performed at RT as well as at $T = 4.2\ K$. Hallbars have been processed out of a sample piece of the different layers to measure RT- and LT-longitudinal resistances along a defined current path, as described in Chapter 3.5. By exploiting Equations 3.26 and 3.27 with consideration of an effective layer thickness of (Ga,Mn)As $d_{eff,(Ga,Mn)As} = 4\ nm$, the resistivities and conductivities have been determined. The results of RT-conductivity and LT-conductivity are shown in Figure 5.13(a) and (b).

As seen in Figure 5.13(a), RT-σ values ranges from 89 to a maximum value of 187 $\frac{1}{\Omega cm}$ at $T_{sub} = 295$°C with BEP ratio $(\frac{As_4}{Ga}) = 20$. The plot shows a slight trend to higher σ values which might be a result of a lowered hole carrier compensation presumably by a lowered As_{Ga} concentration with higher T_{sub}. The parabolically graded (Ga,Mn)As layer with a higher Mn content of $x = 0.04$ of the first growth series shows a comparable value of RT-$\sigma \approx 184\ \frac{1}{\Omega cm}$ which indicates, that an increased substrate temperature T_{sub} and/or reduced BEP ratio $(\frac{As_4}{Ga})$ leads to an improvement of RT-conductivity.

Conductivity measurements at $T = 4.2\ K$ have been performed to characterize the electrical properties of the parabolically graded (Ga,Mn)As layers for different growth conditions. LT-σ of the layer grown at $T_{sub} = 290$°C and a BEP ratio $(\frac{As_4}{Ga}) = 20$ reveals a value of 58 $\frac{1}{\Omega cm}$. As Figure 5.13(b) illustrates, even the small intended changes in growth parameters cause a drastic drop of LT-σ. An increase of substrate temperature by only 5°C leads to a lower LT-σ of 52 $\frac{1}{\Omega cm}$, as mentioned before in Section 5.3.3.

The reproduction (S723) of sample S714 which has been grown under optimized growth conditions reveals LT-$\sigma = 43\ \frac{1}{\Omega cm}$ and bares the difficulty of growing very thin (Ga,Mn)As layers with reproducible layer properties. A difference of 20 % in LT-σ is maintainable for very thin layers which are still electrical conductant at 4.2 K. Out of Figure 5.13(b) it can be assumed, that carrier compensation by defects and sample inhomogeneities result in lateral localisation and tunneling/hopping transport of holes and dominates the LT-σ of very thin (Ga,Mn)As layers. Local carrier depletion in regions with increased defect density is suspected to cause hindered and inhomogeneous current flow between remaining microscopic regions with metal-like conductance and ferromagnetic order within such thin (Ga,Mn)As layers.

Looking at the results of the second growth series, the fabrication of very thin (Ga,Mn)As layers with graded Mn doping profile in a narrow growth parameter window show improved magnetical and electrical properties. As already mentioned, these layers are probably usable for gateable devices. A comparison of the sample ($x = 0.025$) grown at optimized growth conditions (T_{sub} =290°C and BEP ratio $(\frac{As_4}{Ga}) = 20$) with low doped samples of the first series ($x = 0.020$ and $x = 0.030$) in Section 5.2 shows that T_C has been increased by at least 12 K due to adjustment of growth conditions for low doped thin (Ga,Mn)As layers. Simultaneously, the RT-conductivity σ has been improved by at least a factor of 2 for the sample grown at optimized growth conditions (RT-$\sigma \approx 160\ \frac{1}{\Omega cm}$) compared to samples of the first growth series (RT-$\sigma \approx 58\ \frac{1}{\Omega cm}$ for $x = 0.020$ and RT-$\sigma =\approx 85\ \frac{1}{\Omega cm}$ for $x = 0.030$).

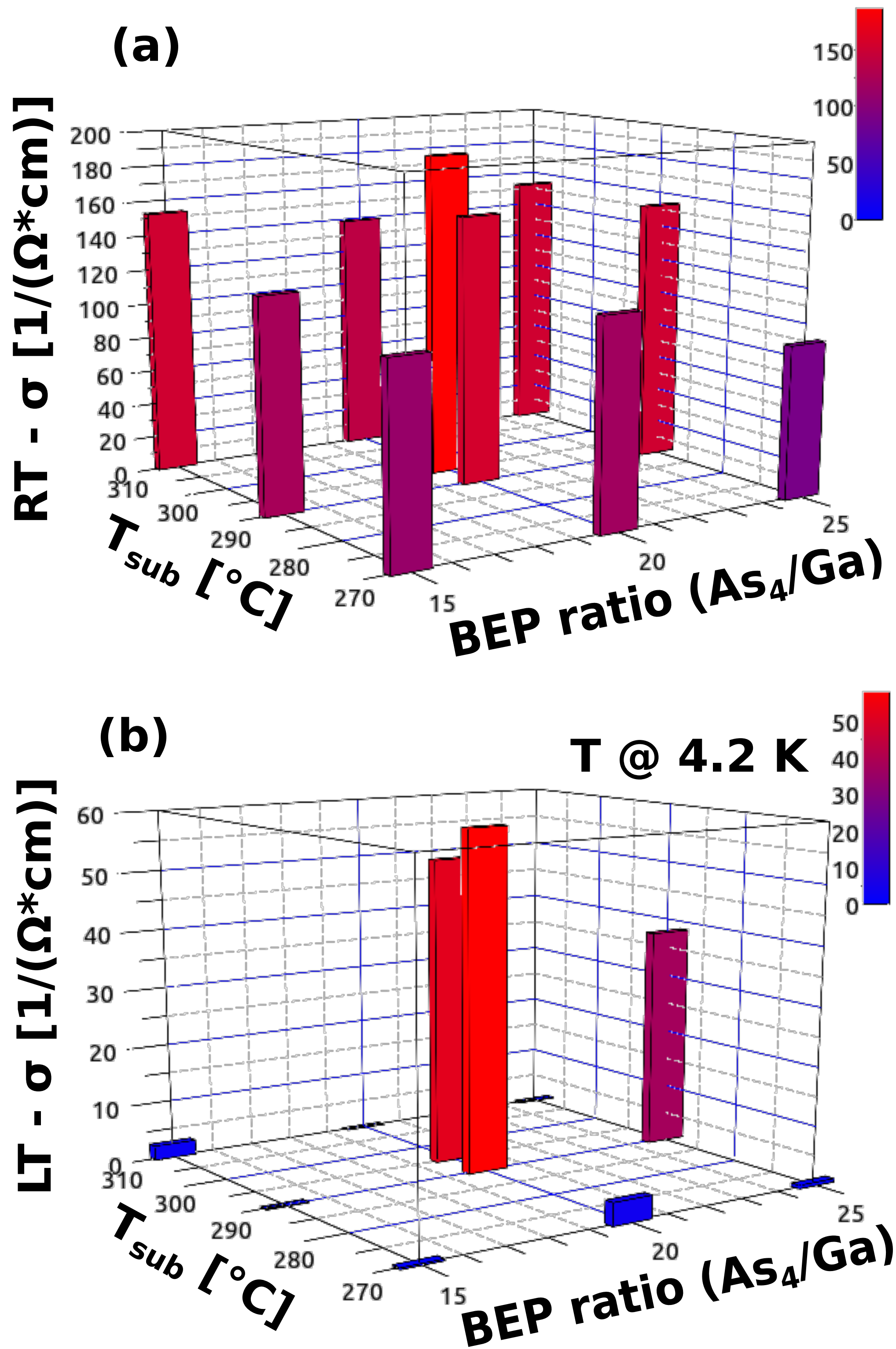

Figure 5.13: 4-terminal transport measurements in Hallbar geometry of parabolically graded (Ga,Mn)As layers with a Mn content of $x = 0.025$ as a function of T_{sub} and BEP ratio ($\frac{As_4}{Ga}$) at (a) RT and (b) $T = 4.2\ K$.

5.3.5 Parabolically Graded Sample at Optimized Growth Conditions

The last two sections have shown, that for a parabolically graded sample with a Mn content of $x = 0.025$, improved T_C and LT-σ have been achieved by optimized growth conditions around T_{sub} =290°C and BEP ratio $(\frac{As_4}{Ga}) = 20$. A comparison with known properties of bulk material with the same Mn content has been performed in the following to classify the properties of a parabolically graded layer. Additionally, a bulk layer grown at optimized growth conditions for parabolically layers has been fabricated with a comparable Mn content of $x = 0.022$.

Comparison of Hysteresis Loop with Bulk Material

The magnetic properties of parabolically graded (Ga,Mn)As layers have been investigated by determination of T_C out of T-dependent remanent magnetization measurements at zero-applied magnetic field. Furthermore, a typical magnetic property of a ferromagnet reveals a hysteresis loop, as seen in Chapter 3.4. In Figure 5.14 hysteresis loops of a 70 nm layer (Ga,Mn)As (black curve) grown under standard growth conditions (S709) and of a very thin layer with parabolically graded Mn profile (S723) are plotted. The Mn content in both samples is $x = 0.025$. T_C of bulk and thin layer is 51 K and 41 K respectively.

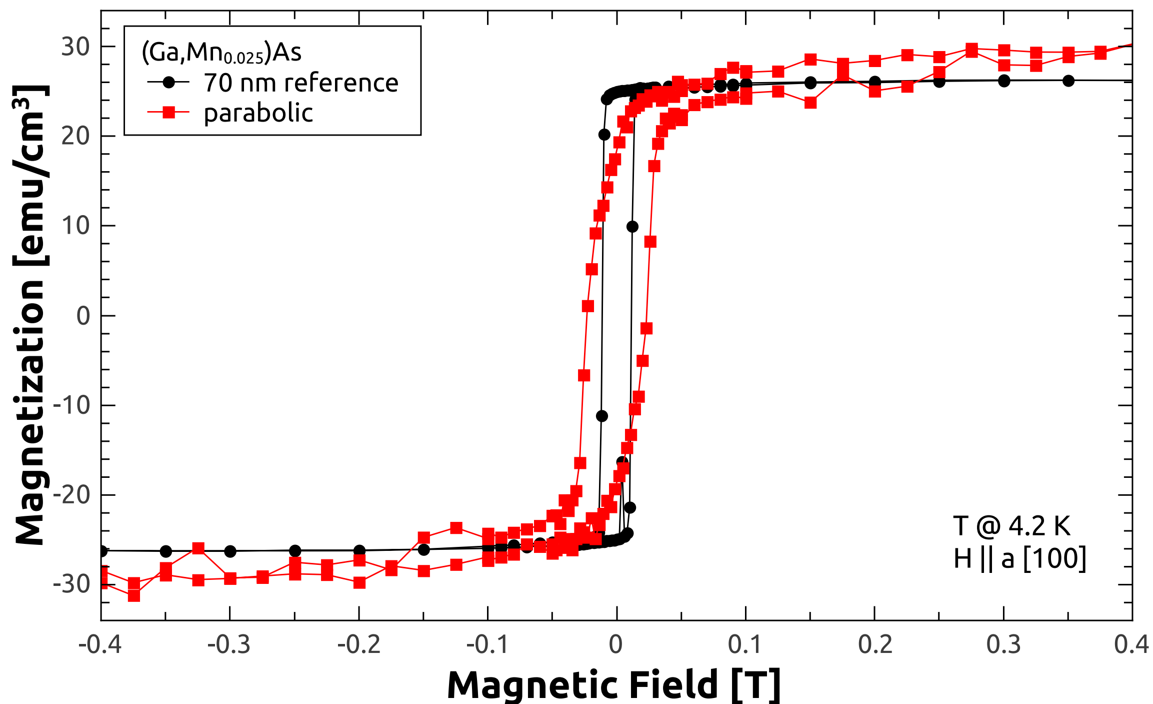

Figure 5.14: Magnetization measurements along a [100] direction at $T = 4.2$ K of a 70 nm bulk reference layer (black) and optimized parabolically graded layer (red), both with nominally $x = 0.025$.

The bulk layer shows a typical hysteresis loop at $T = 4.2\ K$ with saturation magnetization $M_{sat} = 26\ \frac{emu}{cm^3}$ and corresponding Mn concentration of $5.6 \cdot 10^{20}\ cm^{-3}$, according to Equation 3.24. The resulting Mn content of $x = 0.025$ is identical to the HRXRD calibration measurement. The coercive field $H_C = 11\ mT$ lies in the typical range of (Ga,Mn)As layers.

The magnetization curve along a [100] direction of the parabolically graded layer has apparently a hysteretic feature. To quote the magnetization referred to the volume, an effective (Ga,Mn)As layer thickness of 4 nm has been used. The saturation magnetization $M_{sat} = 30\ \frac{emu}{cm^3}$ is slightly higher compared to M_{sat} of bulk material. The coercive field $H_C = 23\ mT$ is a factor of 2 higher compared to bulk material but H_C is roughly in the experimentally confirmed range of (Ga,Mn)As material, as mentioned in Chapter 3.4. In contrast to the hysteresis loop of bulk material around zero-applied magnetic field H, the remanent magnetization M_{rem} is lower than the saturation magnetization M_{sat}. The measured strength of magnetization at $H = 0\ T$ is a projection onto the measured crystal direction. A lowered M_{rem} at zero-applied magnetic field H has been seen in all thin (Ga,Mn)As layers with parabolically graded or homogeneously distributed Mn profile. A gradual alignment or rotation of the macroscopic magnetization direction along the applied and increasing magnetic field H is suspected to cause such hysteretic feature. It indicates, that the magnetization at zero-applied field points to a different crystal direction, presumably to $[\bar{1}10]$ direction, which suggests a stronger uniaxial component $K_{[\bar{1}10]}$. The origin of a slightly higher M_{sat} for the parabolically graded layer compared to bulk material with the same Mn content (here $x = 0.025$) is multifaceted and cannot be clearly determined. The amount of Mn in samples with a parabolical grading of Mn profile is assumed to correspond to an effective layer thickness of 4 nm with a homogeneous Mn profile. It is in agreement to the Mn shutter opening time (see Chapter 5.1). Therefore, differences in M_{sat} might be related to the inaccuracy in the nominal Mn content x and/or the measurement of magnetization. Besides, non-ferromagnetic regions and/or Mn interstitials Mn_{int} might also explain a lowered M_{sat} in the 70 nm bulk (Ga,Mn)As layer.

T-dependent magnetization measurements along [100] (black curve) and $[\bar{1}10]$ direction (red curve) are shown in Figure 5.15(a) for a 70 nm (Ga,Mn)As layer and in Figure 5.15(b) for a parabolically graded (Ga,Mn)As layer. Both layers have been grown under optimized growth conditions, i.e. T_{sub} =290°C and BEP ratio ($\frac{As_4}{Ga}$) = 20, with comparable Mn content $x = 0.025$ (parabolic layer) and $x = 0.022$ (70 nm layer) respectively.

In case of the bulk layer with $x = 0.022$ grown at optimized growth conditions an improved $T_C = 56\ K$ in Figure 5.12(b) is mentionable compared to the aforementioned bulk layer with $T_C = 51\ K$ grown at standard growth conditions and slightly higher Mn content $x = 0.025$. Furthermore, the LT-conductivity at $T = 4.2\ K$ with LT-$\sigma = 212\ \frac{1}{\Omega \cdot cm}$ is a factor of 4 higher for the bulk layer grown at optimized growth conditions compared to the bulk layer grown at standard growth conditions with LT-$\sigma = 56\ \frac{1}{\Omega \cdot cm}$. This result is in good agreement to the preseries of Section 5.3.1, where an increase of T_{sub} up to about 290°C leads to higher T_C and LT-σ. The layer with parabolically graded Mn content in Figure 5.15(c) has $T_C = 36\ K$. Compared to the sample piece with $T_C = 41\ K$ of Figure 5.12), at which the measurement has been performed six months earlier, slight layer inhomogeneities

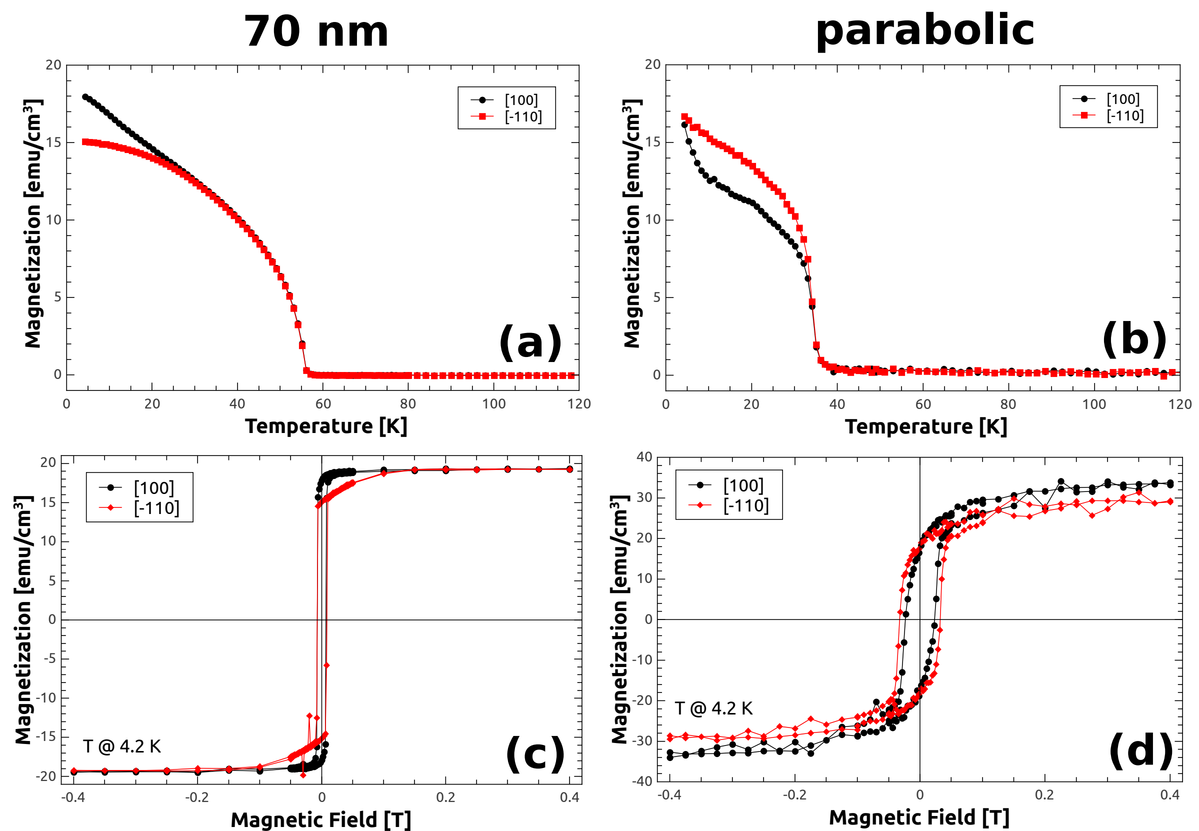

Figure 5.15: T-dependent magnetization measurements along [100] (black) and [$\bar{1}$10] direction at zero-applied magnetic field after saturation of magnetization of (a) a 70 nm (Ga,Mn)As reference layer $x = 0.022$ and (b) a parabolically graded (Ga,Mn)As layer $x = 0.025$. Both layers have been grown at optimized growth conditions. Hysteresis loops of (c) 70 nm and (d) parabolical layer are measured at $T = 4.2$ K.

of the wafer are suspected to cause the decrease in T_C by thermal instability of the substrate temperature during epitaxial growth. A remarkable aging effect of the sample by e.g. a random outdiffusion of substitutional Mn atoms has not been observed. Hysteresis loops measured at $T = 4.2\ K$ along in-plane [100] and $[\bar{1}10]$ directions show a different behavior of remanent magnetization M_{rem} in case of bulk material compared to a parabolically graded layer, as seen in Figure 5.15(c) and (d). The bulk layer has a slightly higher remanent magnetization at $H = 0\ T$ in [100] direction $M_{rem,[100]} = 18\ \frac{emu}{cm^3}$ compared to $M_{rem,[\bar{1}10]} = 15\ \frac{emu}{cm^3}$ in $[\bar{1}10]$ direction. According to Equation 3.22, the ratio of the remanent magnetizations is 1.19 and therefore $< \sqrt{2}$. The corresponding angle θ between [100] and $[\bar{1}10]$ is calculated to be 33.5° which deviates from $\theta = 45°$ for (Ga,Mn)As material with mainly biaxial magnetic anisotropy, as seen in Figure 3.16 of Chapter 3.4. The uniaxial magnetic anisotropy component is suspected to be stronger in magnitude compared to standard bulk material. The coercive field $H_C = 6.9\ mT$ lies within the range of up to 20 mT, as presented in Chapter 2.3.

The parabolically graded layer has equal remanent magnetization of $M_{rem} = 18.5\ \frac{emu}{cm^3}$ along [100] and $[\bar{1}10]$ direction. The ratio $\frac{M_{rem,[100]}}{M_{rem[\bar{1}10]}}$ is equal to 1 which results in $\theta = 0°$. This result could be interpreted as a reduction of magnetic anisotropy, where the magnitude of the uniaxial magnetic anisotropy component is equal to the biaxial magnetic anisotropy component. In the thin layer, the coercive fields of $H_{C,[100]} = 23\ mT$ and $H_{C,[\bar{1}10]} = 32\ mT$ are slightly higher compared to the typical range of standard (Ga,Mn)As bulk layers.

Anisotropy Fingerprint

4-terminal longitudinal magnetoresistance measurements with applied in-plane magnetic fields up to $\pm 300\ mT$ at different angles Φ relative to the current direction in [100] crystal direction at 4.2 K have been done for the bulk layer and parabolically graded layer. The anisotropy fingerprints of the inner region of these measurements are presented in Figure 5.16(a) and (b).

The anisotropy fingerprint of bulk material grown at $T_{sub} = 290$°C and BEP ratio $(\frac{As_4}{Ga})$ $= 20$ shows a pronounced rectangular shape of the fingerprint pattern with the longest side of the rectangle along $[\bar{1}10]$ crystal direction. As described in Chapter 2.3.1, such fingerprint shape shows a biaxial easy axis anisotropy component and additionally a $[\bar{1}10]$ easy axis anisotropy component. The extraction of the domain wall nucleation/propagation energy out of the fingerprint reveals $\epsilon/M \sim 9\ mT$. Compared to earlier measurements of ϵ/M of various (Ga,Mn)As samples grown at different growth conditions, ϵ/M is in the region of published values, see [Gou08]. The calculation of the aspect ratio of the width to the length of the rectangle by Equation 2.19 results in $K_{[\bar{1}10]}/K_{biax} \sim 0.54$, which is larger compared to published values and even larger compared to the parabolically graded layer with $x = 0.04$ of the first parabolical growth series. A strong gradual switching of magnetization events is visible as a color gradient from low (black) to high (red) resistance states R compared to bulk material grown under standard growth conditions.

The result of the 4-terminal longitudinal magnetoresistance measurement of the parabol-

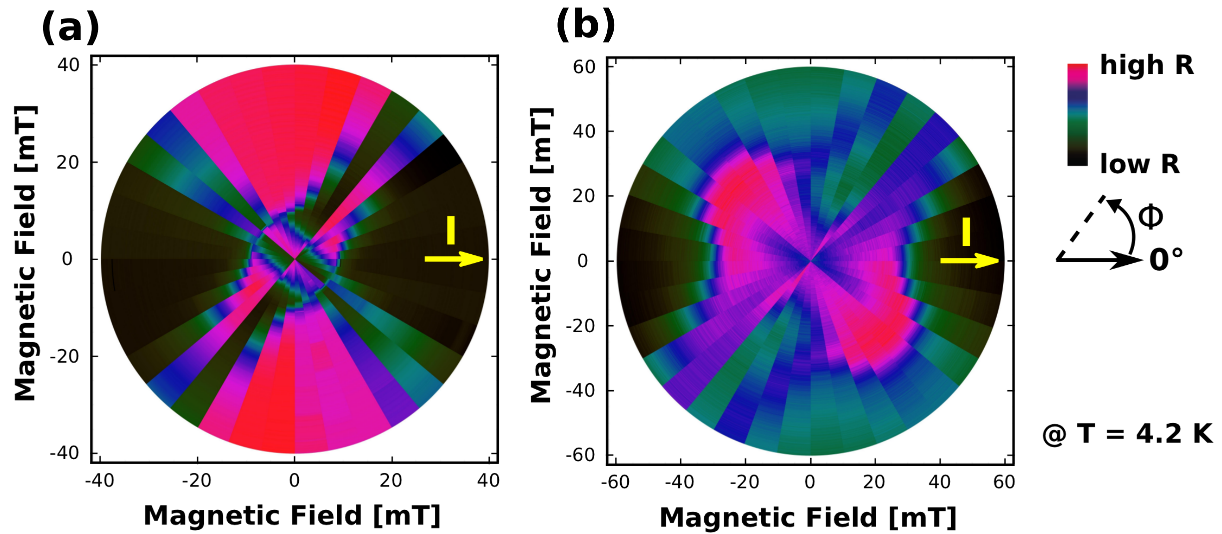

Figure 5.16: Anisotropy fingerprints measured at $T = 4.2\ K$ of (a) a 70 nm (Ga,Mn)As layer with $x = 0.022$ and (b) a parabolically graded (Ga,Mn)As layer with $x = 0.025$. Both layers are grown at $T_{sub} = 290$°C and BEP ratio $(\frac{As_4}{Ga}) = 20$.

ically graded layer is presented in Figure 5.16(b). Along the $[\bar{1}10]$ direction there might be an uniaxial anisotropy component. But neither a square-like nor a rectangular feature of the anisotropy fingerprint can be used to determine ϵ/M as well as $K_{[\bar{1}10]}/K_{biax}$. The anisotropy fingerprint shows that the magnetic anisotropy has changed dramatically in the parabolically graded layer compared to standard epitaxial grown bulk layers as well as in the bulk layer grown under optimized growth conditions for the thin layer. At this point of investigation, it is not possible to state the exact values of anisotropy components. An indication of a stronger uniaxial component seems to be present in this layer which is supported by the remanent magnetization M_{rem} of SQUID measurements at zero-applied magnetic field H. Moreover, the transport properties of epitaxially grown parabolically graded layer within the ascertained growth parameter window facilitate further magnetoresistance measurements. The question arises whether it is possible to change the magnetic anisotropies of such layers as seen in Figure 5.16(b) and/or whether the metal-insulator transition can be reached by tuning of the hole density.

Simulation of Valence Band Bending and Estimation of p

From the experimental point of view a very thin (Ga,Mn)As layer with a parabolical grading of Mn distribution grown within a narrow growth parameter window yields to magnetic and electrical properties, which might be exploited for gated magnetotransport devices. The optimization of growth conditions has been accomplished to reduce compensating defects like the arsenic antisite defect density.

The bending of the VB edge of thick and thin (Ga,Mn)As layers caused by the influence of interface defects and surface states has already been calculated within the Poisson-

and Schrödinger-equation simulation software *nextnano*^{3}, as presented in Chapter 2.2.1. Simplifications like e.g. the negligence of layer inhomogeneities have been discussed in this Chapter.

In order to simulate a very thin (Ga,Mn$_{0.025}$)As ($[Mn_{Ga}] = 5.525 \cdot 10^{20}\ cm^{-3}$) layer with a parabolically graded Mn profile presented in Table 5.1, the following assumptions and experimentally determined concentrations of the arsenic antisites [As$_{Ga}$] have been used:

- $[\mathrm{As}_{Ga}] = 1.1 \cdot 10^{19}\ cm^{-3}$ for LT-GaAs, determined from HRXRD measurement of a 500 nm LT-GaAs layer which has been epitaxially grown at $T_{sub} = 290°C$ and BEP ratio ($\frac{As_4}{Ga}$) = 20 (see Appendix A.1).
- $[\mathrm{As}_{Ga}] = 1.75 \cdot 10^{20}\ cm^{-3}$ for (Ga,Mn$_{0.025}$)As, determined from HRXRD measurement of a 70 nm (Ga,Mn$_{0.025}$)As layer which has been epitaxially grown at $T_{sub} = 290°C$ and BEP ratio ($\frac{As_4}{Ga}$) = 20 (see Appendix A.1).
- A digital switching of the donor density with Mn content is assumed. For a linear relation of donor density and Mn content, a smearing of [Mn] by diffusion and surface roughness results also in a smearing of donor density profile. No significant influence on the results is assumed.
- A possible beneficial reduction of [Mn$_{int}$] by LT-GaAs spikes is not considered here.

For a thick (Ga,Mn)As layer, a p-compensation of 63.3% results from these [As$_{Ga}$] which appears reasonable and is about that observed by [Die01, Mašo03, Jun05]. For comparative purposes with p_{max} of very thin layers, the maximum local hole density of bulk (Ga,Mn)As $p_{max} = 2.03 \cdot 10^{20}\ cm^{-3} = p_{nom}$ is defined as the nominal hole density p_{nom}. Its nominal hole area density $p_{area,nom}$ for a 4 nm (Ga,Mn)As layer is calculated by

$$p_{area,nom} = p_{nom} \times 4 \cdot 10^{-7} cm^{-1} = 8.12 \cdot 10^{13} cm^{-2} \qquad (5.8)$$

Further parameters of the simulations are taken from Chapter 2.2.1.

The results of band alignment simulations and hole distributions at RT of a 4 nm reference layer with homogeneous Mn distribution and a layer with a parabolically graded Mn distribution, both without or with a 1 nm LT-GaAs cap layer, are shown in Figure 5.17.

The shape of the VB edges of the layers with a homogeneous Mn profile without (black line) and with (red line) a LT-GaAs cap layer in Figure 5.17(a) are congruent with each other up to the interface to the LT-GaAs growth start layer. The influence of surface states leads to a very strong VB edge bending within the very thin (Ga,Mn)As layer. Nevertheless, a capping layer causes less hole depletion in a 4 nm (Ga,Mn)As layer in the vicinity of the surface. In this case, the part of the VB edge (red line) which lies above the Fermi energy is broadened, providing a higher amount of unoccupied Mn acceptor states compared to an uncapped (Ga,Mn)As layer.

The hole distributions of a 4 nm (Ga,Mn)As layer without or with a 1 nm LT-GaAs cap layer are presented in Figure 5.17(b). The maximum local hole density p_{max} increases

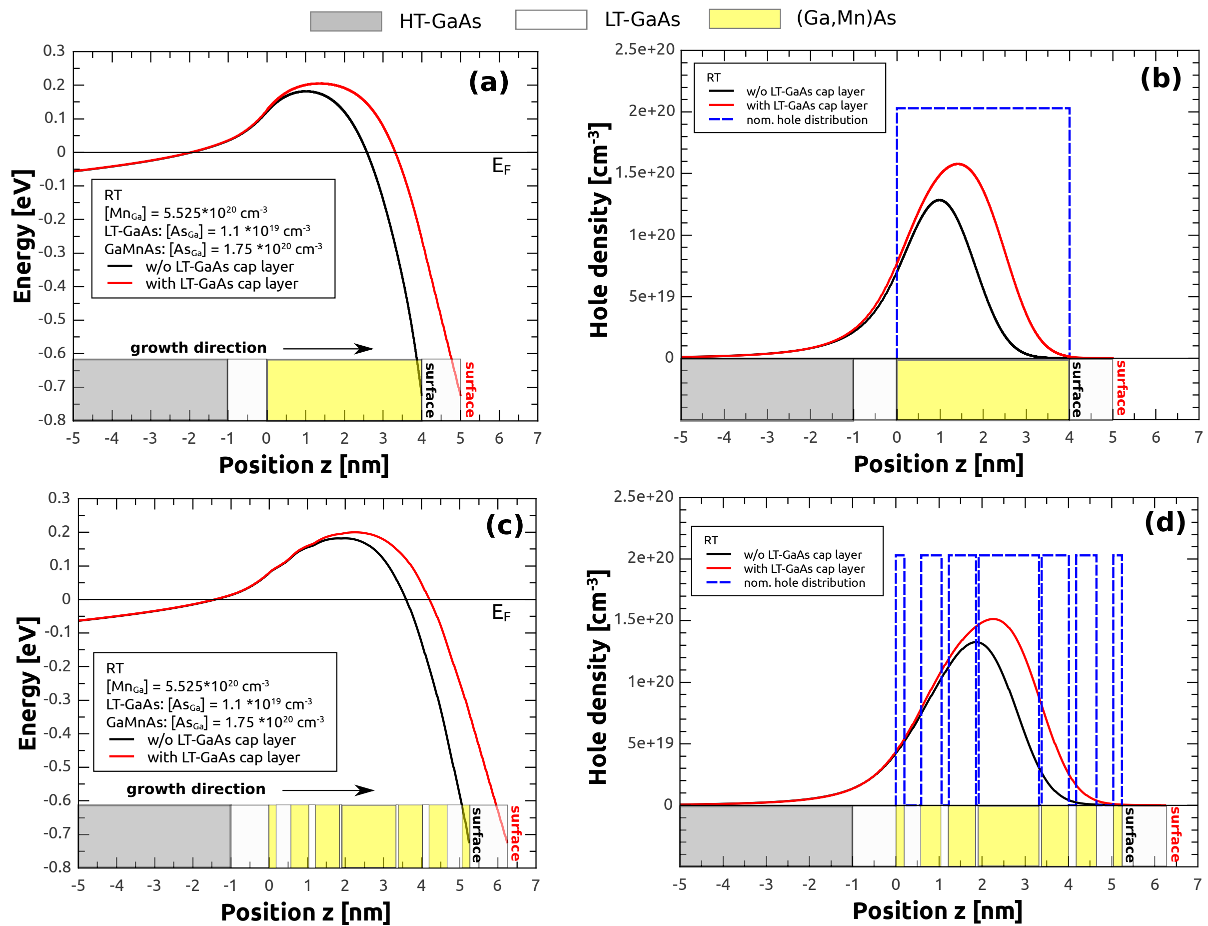

Figure 5.17: (a) Self-consistent solution of the VB edge profiles and hole distributions of two different layer structures with a Mn acceptor density of $5.525 \cdot 10^{20}$ cm^{-3} and without (black lines) or with (red lines) a 1 nm LT-GaAs cap layer. (a) and (b) correspond to a homogeneous Mn distribution and (c) and (d) belong to a parabolically graded Mn distribution. Both layer structures have a total (Ga,Mn)As thickness of $d_{eff} = 4$ nm and the nominal hole density value of a thick (Ga,Mn)As reference layer is represented by the blue broken line.

from $1.28 \cdot 10^{20}$ cm^{-3} to $1.58 \cdot 10^{20}$ cm^{-3} which corresponds to an improvement of 23.4% with a capping layer. The hole area density p_{area} in the (Ga,Mn)As layer is increased from $p_{area,-cap} = 2.30 \cdot 10^{13}$ cm^{-2} to $p_{area,+cap} = 3.67 \cdot 10^{13}$ cm^{-2} and corresponds to 28% and 45% of $p_{area,nom}$ in Equation 5.8. The results confirm the simulations in Chapter 2.2.1, which show a significant increase of the hole density in very thin layers by a cap layer.

Self-consistent band alignment calculations of a very thin layer with parabolically graded Mn profile without or with a 1 nm LT-GaAs cap layer are presented in Figure 5.17(c) and (d). The parabolic-like shape of the VB edges in Figure 5.17(c) are qualitatively comparable to the above presented 4 nm (Ga,$Mn_{0.025}$)As layer VB edges with homogeneous Mn profile in Figure 5.17(a). A cap layer (red line) also leads to less hole depletion within the parabolic (Ga,Mn)As layer compared to the uncapped parabolic layer (black line). Shallow undulations of the VB edges, in particular visible at the first nanometer of the parabolically graded layer, arises from digital doping by Mn and As_{Ga}.

The maximum local hole density of $p_{max} = 1.33 \cdot 10^{20}$ cm^{-3} is 3.9% higher for the uncapped parabolically graded layer compared to the homogeneous Mn profile. A broadening of the hole density distribution leads to a higher hole area density. Regarding the effective (Ga,Mn)As layer thickness of $d_{eff} = 4.0$ nm, $p_{area,eff} = 2.62 \cdot 10^{13}$ cm^{-2} amounts 32% of $p_{area,nom}$. The inclusion of LT-GaAs layer interruptions leads to the total (Ga,Mn)As layer thickness of $d_{tot} = 5.2$ nm, resulting in $p_{area,tot} = 3.18 \cdot 10^{13}$ cm^{-2}, which is 39% of $p_{area,nom}$. d_{eff} of the parabolically graded Mn profile is equal to the 4 nm layer with a homogeneous Mn profile and therefore the total amount of Mn acceptors is the same. Thus, the simulations for an uncapped layer suggest an improvement of p_{area} of at least 4% with respect to $p_{area,nom}$ by an implementation of a parabolical grading of Mn profile with Mn spikes below and above a 1.4 nm thin center (Ga,Mn)As layer.

The simulation of a parabolically graded layer with a 1 nm LT-GaAs cap layer shows a similar trend like the uncapped version. But, $p_{max} = 1.51 \cdot 10^{20}$ cm^{-3} is 4.4% lower compared to p_{max} for the (Ga,Mn)As layer with homogeneous Mn profile and a capping layer. Considering the hole area density with respect to the effective or total thickness of the (Ga,Mn)As layer, $p_{area,eff} = 3.62 \cdot 10^{13}$ cm^{-2} and $p_{area,tot} = 4.27 \cdot 10^{13}$ cm^{-2} amount 44.6% up to 52.6% of $p_{area,nom}$. In comparison to p_{area} of the homogeneous Mn profile in a 4 nm (Ga,Mn)As layer with a cap layer, $p_{area,eff}$ is 0.6% lower and $p_{area,tot}$ is 7.4% higher with respect to $p_{area,nom}$. Due to inhomogeneities in lateral Mn concentrations and defect donor densities which exceed the limit of $nextnano^3$ simulations, the difference in (local) hole density of parabolic and homogeneous thin (Ga,Mn)As layers may increase. Here, the result is not as clear as for the uncapped layer structure designs.

However, the improved robustness of hole density against surface effects in a parabolically graded Mn profile can be corroborated by the percental change of p_{area} between uncapped and capped layer with respect to $p_{area,nom}$. In case of the homogeneous Mn profile, the change of p_{area} amounts +59.6%. For the parabolically graded Mn profile, $p_{area,eff}$ and $p_{area,tot}$ increase by +38.2% and +34.3%. A lower increase of hole area density in case of the parabolic layer indicates, that the influence of interface and especially surface defects is reduced. According to the linear increase of Mn interstitials x_{int} with the nominal Mn content x presented in Figure 3.8, it can be assumed, that the compensation of holes at

the outer parts of the parabolically graded layer is reduced due to a lower Mn content x with negligible $[x_{int}]$.

As a conclusion interface as well as surface defects in (Ga,Mn)As can be reduced/shielded by the design of the Mn profile in a sample to improve the amount of free carriers, as successfully demonstrated in these simulations. Although the input of the simulations originates from antisite concentrations grown under non-standard growth conditions, the trend of higher free hole densities in the parabolically graded Mn profile compared to a homogeneous Mn profile is in agreement with experimental results of Chapter 5.2. A higher hole density combined with a better overlap to the Mn magnetic moments should lead to higher Curie temperatures T_C, as proofed in SQUID measurements.

In summary the choice of growth parameters and the Mn distribution within a very thin (Ga,Mn)As layer have a crucial influence of the magnetic and electrical properties. It has been shown, that similar magnetic anisotropy properties compared to standard bulk (Ga,Mn)As material have been achieved for very thin (Ga,Mn)As layers with a parabolically graded Mn profile epitaxially grown under standard growth conditions at $T_{sub} = 270°$C and BEP ratio $(\frac{As_4}{Ga}) = 25$ with $x = 0.04$. Additionally, it has been shown in the first growth series, that a parabolical grading of Mn profile leads to improved properties compared to a homogeneous Mn profile with the same amount of Mn, considering the same total opening time of the Mn shutter.

In order to reduce the arsenic antisite defect concentration $[As_{Ga}]$, a systematic variation of growth parameters has been performed to find optimized growth conditions for parabolically graded layers with a moderate Mn content of $x = 0.025$. Magnetometry measurements as well as electrical transport measurements reveal improved Curie temperatures T_C and LT-conductivities σ. Within a narrow growth parameter window around $T_{sub} = 290°$C and BEP ratio $(\frac{As_4}{Ga}) = 20$, the magnetic properties seem to have a strong uniaxial anisotropy component $K_{uni,[\bar{1}10]}$ with similar magnitude as the biaxial anisotropy component K_{biax}. Up to now, the driving mechanism of improved properties is not well understood. *nextnano*^{3} RT band alignment simulations give a first insight of the overlap between hole density and Mn profile. Moreover, a deeper understanding of the interplaying influences of confinement of holes and their coupling to Mn magnetic moments on the (anisotropic) magnetic and bandstructure properties will require a detailed theoretical model as well as further structural, magnetic and LT-transport studies of very thin (Ga,Mn)As layers with graded Mn profile. As shown in experiments, parabolically graded layers show applicable electrical conductance at 4.2 K and seem promising for exploitation of the magnetic properties e.g. by a low-voltage control of a p-n semiconductor device. Feasibility tests of such a device with first measurements are presented in the following.

5.4 Parabolically Graded (Ga,Mn)As Layer in a Semiconductor p-n Junction

Epitaxial growth optimization of very thin (Ga,Mn)As layers with a parabolically graded Mn profile has been investigated in detail in the last Section 5.3. As a result, a narrow growth parameter window has been found, where such samples show improved electric and magnetic properties at 4.2 K. In principle, such thin (Ga,Mn)As layers with parabolically graded Mn profile could be used for a low-voltage control of its ferromagnetic properties, e.g. as an embedded ferromagnetic (Ga,Mn)As layer in an all-semiconductor epitaxial p-n junction, presented in [Owe09]. At 4.2 K, the lateral resistivity has been increased in a 5 nm (Ga,Mn)As layer by 100% with a gate-voltage between -1 and 3 V.

Similar to a semiconductor p-n junction in [Owe09], our sample device structure with an embedded parabolically graded Mn profile (sample number: S731) is as follows: First of all, the highly n-doped part of the p-n junction is realized by the epitaxial growth of a HT-GaAs:Si layer (n $\approx 1 \cdot 10^{19}$ cm^{-3}) on a n-doped GaAs (001) substrate. Electrostatic barriers for electrons and holes of the n-GaAs and (Ga,Mn)As p-n junction layers have been implemented by a 10 nm $Al_{0.3}Ga_{0.7}As$ and a 10 nm AlAs spacer layer to enlarge the conduction and valence band offset. The (Ga,Mn)As layer with $x \approx 0.02$ has a hole density of p $\sim 10^{20}$ cm^{-3}. Growth details of the spacer layers are described in Chapter 3.2.2. In principle, an influence of (Ga,Mn)As layers is easier for low-doped material at low-voltage experiments due to a stronger depletion/accumulation of the present hole density compared to a higher Mn content with correspondingly higher hole density. Besides, a lower Mn content reduces the probability of Mn interstitial incorporation. As explained in Chapter 3.2.1, highly mobile Mn interstitials can diffuse into the depletion region during epitaxial growth which would lead to unintended leakage currents for the p-n junction.

The magnetic characterizations of the parabolically graded Mn profile epitaxially grown on a semi-insulating GaAs (001) substrate (sample S723 of Chapter 5.3) and a (Ga,Mn)As layer with $x = 0.020$ with parabolical grading embedded in a p-n junction on a n-GaAs (001) substrate have been perfomed by SQUID measurements, as shown in Figure 5.18.

The hysteresis loop (without subtraction of the diamagnetic signal) of the parabolically graded Mn profile embedded in a p-n junction (red curve) is similar to the hysteresis loop of the reference layer on i-GaAs. The slopes of the hysteresis loops deviate from each other which is caused by a different diamagnetic signal of different sample pieces. Such behavior is in empirical agreement within this work. Both layers reveal a Curie temperature T_C of 41 K (not-shown), although the nominal Mn content of the (Ga,Mn)As layer on n-GaAs is half a percent lower compared to the reference sample. The measured LT-conductivity in 4-terminal Hallbar geometry amounts to $\sigma_{xx} = 35.7 \, \frac{1}{\Omega \cdot cm}$, which is about 30 % lower compared to the reference layer with $\sigma_{xx} = 52 \, \frac{1}{\Omega \cdot cm}$. In relation to the different Mn content in both layers ($x = 0.020$ in n-p junction and $x = 0.025$ in reference), the LT-conductivity measurement reflects quite well the difference in hole density of 20 % provided by Mn acceptors and additional uncertainty of hole compensation.

These preliminary investigations demonstrate that the quality of parabolically graded

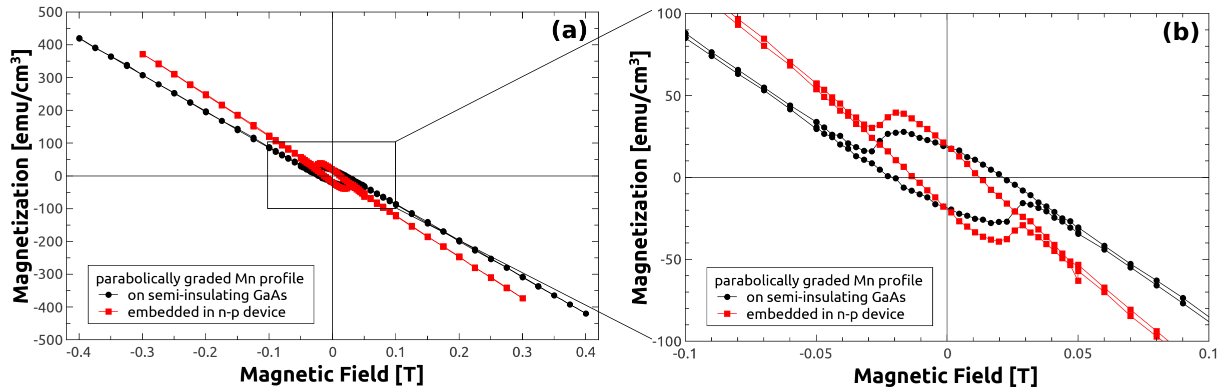

Figure 5.18: SQUID measurements of the parabolically graded Mn profile epitaxially grown on a semi-insulating GaAs substrate (black) and embedded in a p-n device (red). Figure (a) gives as an overview of the measurement and Figure (b) is the zoom-in of the hysteresis loops.

(Ga,Mn)As layer is high and the implemented layers of AlGaAs/AlAs serve as a well-defined barrier against an outdiffusion of holes from the (Ga,Mn)As layer. The same Curie temperature as the reference layer without any barrier structure underneath the parabolical grading of the Mn profile serves as an indicator for equal material quality.

In a first attempt to change the longitudinal resistance of a parabolic layer, a LT low-voltage gating experiment in 4-terminal longitudinal Hallbar geometry of the above described layer structure design has been performed. Here, the longitudinal resistance has been increased by up to 20% with applied gate voltages between 0 and 2 V. The experiment has shown, that there is a leakage current through the barrier at high voltages around 2 V, but in principle the ferromagnetism in such a thin (Ga,Mn)As layer can be tuned. For future studies, it seems possible to reduce the Mn content in order to reach the metal-insulator-transition, which might open the possibility to switch-on and switch-off the ferromagnetism in (Ga,Mn)As material by applying a low gate voltage.

Finally, the reproducibility of (Ga,Mn)As layers with a parabolical grading of the Mn profile and comparable magnetic as well as electric properties in different structure designs has been demonstrated. As a conclusion, such kind of Mn profile seems promising for a low-voltage control of ferromagnetism in a very thin (Ga,Mn)As layer.

Chapter 6

Induced Magnetic Anisotropy in Lifted Bulk (Ga,Mn)As Layers

As described in Chapter 2.3, the magnetic anisotropy of epitaxially grown (Ga,Mn)As material depends on the hole concentration, the strain of the layer and the temperature. (Ga,Mn)As films deposited on (001) GaAs substrates are compressively strained in-plane ($a_{(Ga,Mn)As} > a_{GaAs}$), resulting in a mainly biaxial magnetic easy axes in [100] and [010] crystal direction and a magnetic hard axis along [001] crystal direction.

In cooperation with F. Greullet a method to control the magnetic anisotropy in (Ga,Mn)As layers by an epitaxial lift-off (ELO) process has been established [Gre11]. It allows to induce an out-of-plane magnetic easy axis by depositing the (Ga,Mn)As layer on top of a different host substrate after the ELO process.

The sample structure of the prepared and investigated layers are as follows: After the growth of the 200 nm HT-GaAs buffer layer on the (001) GaAs substrate, a 60 nm AlAs sacrificial layer grown at conditions presented in Chapter 3.2.2 has been deposited. The first investigated layer structure (S1) has a single 70 nm (Ga,Mn)As layer with a Mn content of nominal $x = 0.035$, grown at standard conditions. The second layer structure (S2) has a 70 nm (Ga,In)As layer with an In content of nominal $x_{In} = 0.07$ followed by a 70 nm (Ga,Mn)As layer, again grown at standard growth conditions and the same Mn content like S1 of nominal $x = 0.035$. Both samples have been epitaxially grown one after another to guarantee the same Mn content. The details of the lift-off procedure is described in [Gre11]. After lift-off, the layers have been deposited on different host-substrates like [Si/SiO_2] and sapphire. Van der Waals bonds adhere the layer on the substrate.

Figure 6.1 shows optical microscopy and secondary electron microscopy (SEM) pictures of a 70 nm lifted (Ga,Mn)As layer (S1) on a [Si/SiO_2] substrate. These images demonstrate, that milimeter-sized areas of the (Ga,Mn)As film still have good surface morphology after the lift-off. However, some cracks are visible due to tension induced by the ELO process and/or pollution at the surface of the substrate.

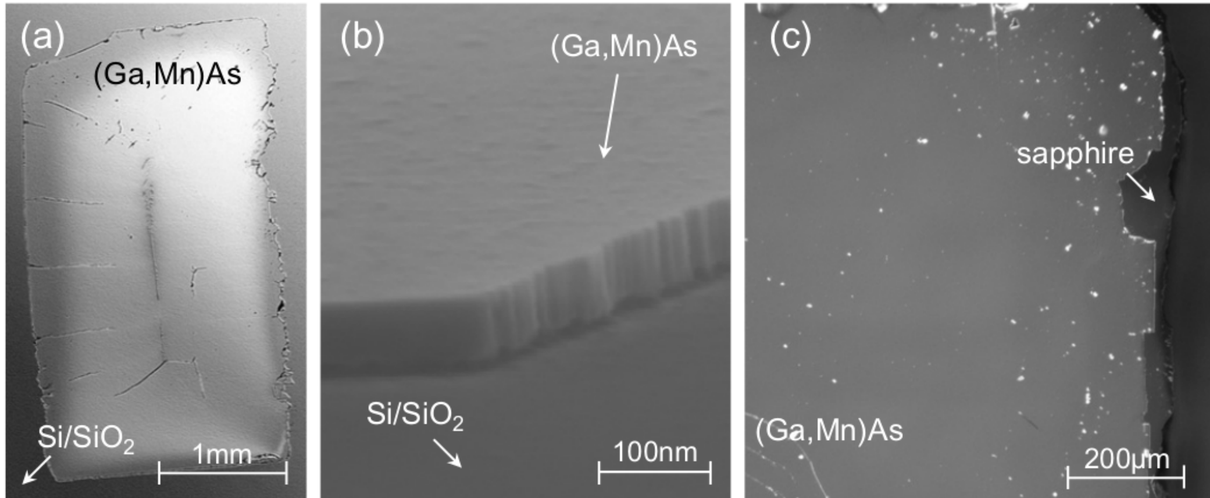

Figure 6.1: (a) Optical microscope image of a 70 nm lifted (Ga,Mn)As layer on a [Si/SiO_2] substrate and (b) SEM side view image. (c) Optical microscope image of a 70 nm lifted (Ga,Mn)As layer on a sapphire substrate. Taken from [Gre11].

6.1 X-ray Diffraction Investigations

The strain situation in as-grown as well as lifted layers S1 and S2 has been investigated by HRXRD measurements.

6.1.1 70 nm (Ga,Mn)As Layer S1

Figure 6.2 shows an $\omega-2\Theta$ scan of the (004) reflection of the as-grown sample AG S1 (black curve) with its simulation (red curve). Here, the (Ga,Mn)As peak position is overlaid with the AlAs Bragg peak. Both layers have similar bulk lattice constants with $a_{(Ga,Mn)As,bulk} = 5.665\mathring{A}$ and $a_{AlAs,bulk} = 5.662\mathring{A}$. A simulation of a single 70 nm (Ga,Mn)As layer, using the same fitting values from the (Ga,Mn)As layer in S1, reveals $a_{\perp} = 5.673 \pm 0.002$ ($a_{bulk} = 5.664 \pm 0.003$). The layer thicknesses of (Ga,Mn)As and AlAs have been determined by the fit of the diffraction pattern to 70$\pm$1 nm and 60 $\pm$1 nm. The variation of layer thickness in the fitting procedure has shown, that thickness fringes on the left side of the GaAs peak are mainly influenced by the (Ga,Mn)As layer thickness, the right side is mainly influenced by the layer thickness of AlAs. A comparison of the measured curve with the fitting curve indicates high quality of the layer structure.

After the epitaxial lift-off process, the 70 nm (Ga,Mn)As layer has been deposited on a [Si/SiO_2] substrate and two $\omega - 2\Theta$-scans of the (004) reflection have been accomplished, as seen in Figure 6.3. After the first measurement (black curve, named as 0°), the sample is rotated about 180° in Φ direction (red curve). A small shift $\sim 0.01°$ of the two (Ga,Mn)As Bragg peaks is visible, as seen in the inset of Figure 6.3. The shift can be interpreted as a tilt of the (Ga,Mn)As layer with respect to the Si lattice due to the lift-off-process where the layer is only fixed onto the host-substrate by van-der-Waals bonding.

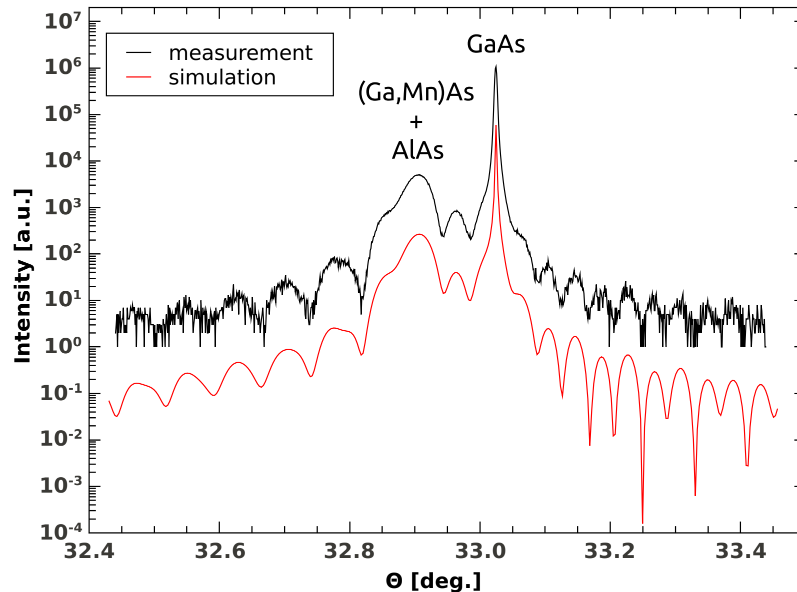

Figure 6.2: HRXRD $\omega - 2\Theta$ scan of as-grown 70 nm (Ga,$Mn_{0.035}$)As / 60 nm AlAs on GaAs substrate (black curve) with simulation (red curve). The thickness fringes reveal high quality of the epitaxially grown layers.

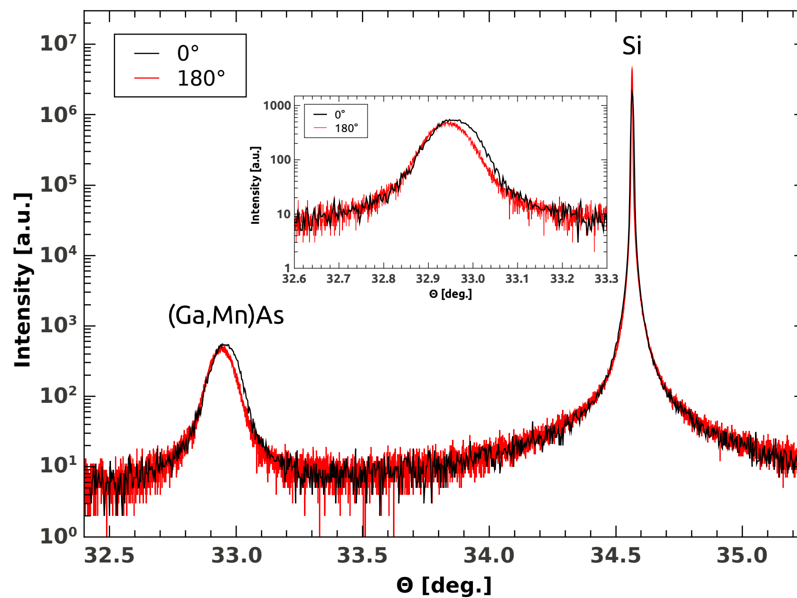

Figure 6.3: HRXRD (004) reflection $\omega - 2\Theta$ scans of lifted 70 nm (Ga,$Mn_{0.035}$)As on [Si/SiO_2] substrate, measured at $\Phi = 0°$ (black curve) and then sample rotated at $\Phi = 180°$ (red curve). The inset shows the zoomed region of the (Ga,Mn)As Bragg peak position for $\Phi = 0°$ and $\Phi = 180°$. A corresponding tilt of $\sim 0.01°$ of the layer on a different host-substrate after the lift-off process can be estimated.

Using Bragg's law (Equation 3.6) and a nominal GaAs peak position of $\omega = 33.023°$, the vertical lattice constant of the lift-off (Ga,Mn)As layer is $a_\perp = 5.665 \pm 0.003$. The estimated error bar implies the tilt of the layer. This vertical lattice constant $a_\perp$ corresponds quite well to the bulk lattice constant $a_{bulk} = 5.664 \pm 0.003$ of the as-grown layer. So, elastic relaxation has been taken place but a quantitative analysis can not be given due to the lack of information about the in-plane lattice parameters. A reciprocal space map will not bear these informations, because the lifted layer is adhered by van-der-Waals bonding with a tilt onto the host-substrate (Si substrate) and a reference point of the substrate peak is not given.

6.1.2 70 *nm* (Ga,Mn)As / 70 *nm* (Ga,In)As Layer S2

In sample S2 a stressor layer of (Ga,In)As has been added between the (Ga,Mn)As and AlAs layer to enforce the strain release of the (Ga,Mn)As layer after the ELO process. (Ga,In)As material with nominal $x_{In} = 0.07$ has a larger bulk lattice constant than (Ga,Mn)As material with nominal $x = 0.035$. Thus, $a_{(Ga,In)As,bulk} > a_{(Ga,Mn)As,bulk}$ and the (Ga,In)As layer should induce a tensile strain to the (Ga,Mn)As layer after elastic relaxation. Figure 6.4 shows the as-grown sample S2 with 70 *nm* (Ga,Mn)As / 70 *nm* (Ga,In)As on 60 *nm* AlAs and a GaAs (001) substrate.

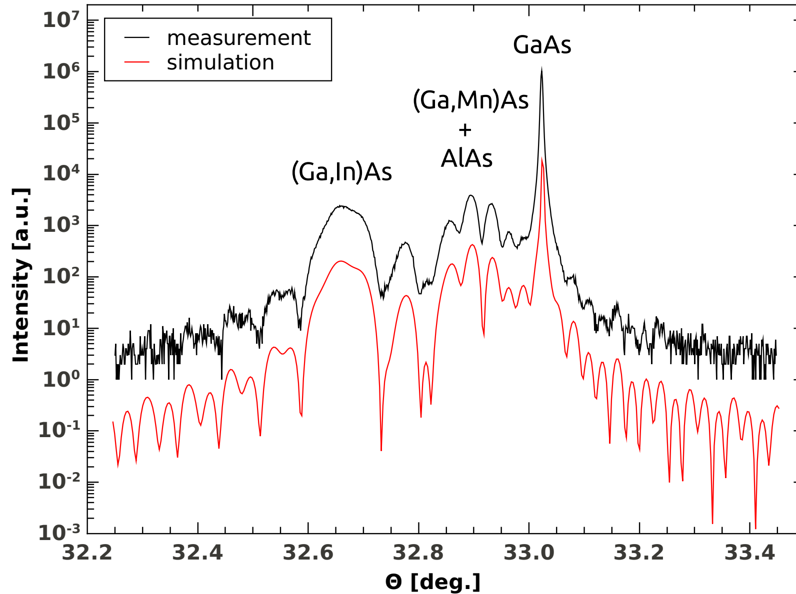

Figure 6.4: $\omega - 2\Theta$ scan and simulation of the (004) reflection of as-grown 70 *nm* (Ga,$Mn_{0.035}$)As / 70 *nm* (Ga,$In_{0.07}$)As on GaAs (001) substrate. The good agreement with the simulation as well as the appearance of thickness fringes reveals a pseudomorphical growth on the GaAs substrate without any plastic relaxation.

The $\omega - 2\Theta$ scan reveals pronounced thickness fringes which indicates, that the thickness of all layers is below the critical thickness for plastic relaxation and therefore fully strained

on GaAs leading to an in-plane lattice constant of GaAs substrate $a_{\parallel} = 5.653\AA$. Besides the clear (Ga,In)As Bragg peak, the position of the (Ga,Mn)As Bragg peak is uncertain due to interferences, very likely by the AlAs layer and/or (Ga,In)As layer (compare e.g. Figure 6.2).

Figure 6.5 presents the $\omega - 2\Theta$ scans of the (004) reflection of sample S2 after the lift-off process and deposition on a [Si/SiO_2] substrate. The sample was measured at $\Phi = 0°$ (black curve) and at $\Phi = 180°$ (red curve). The layer peaks are shifted towards larger angles compared to the as-grown sample in Figure 6.4. Furthermore, no thickness fringes occur presumably due to slight undulations of the layers on the [Si/SiO_2] substrate. Additionally, a very slight deviation of the layer peak positions is observable, as seen in the inset of Figure 6.5. This deviation is estimated to be $\sim 0.01°$ and is very likely caused by a tilt of the layer with respect to the host-substrate. The Bragg condition, represented by Equation 3.6, has been taken to determine the vertical lattice constant of both layers out of the $\omega - 2\Theta$ scan. For the (Ga,In)As layer, it yields to $a_{\perp} = 5.692 \pm 0.003\AA$, for the (Ga,Mn)As layer it accounts to $a_{\perp} = 5.658 \pm 0.003\AA$.

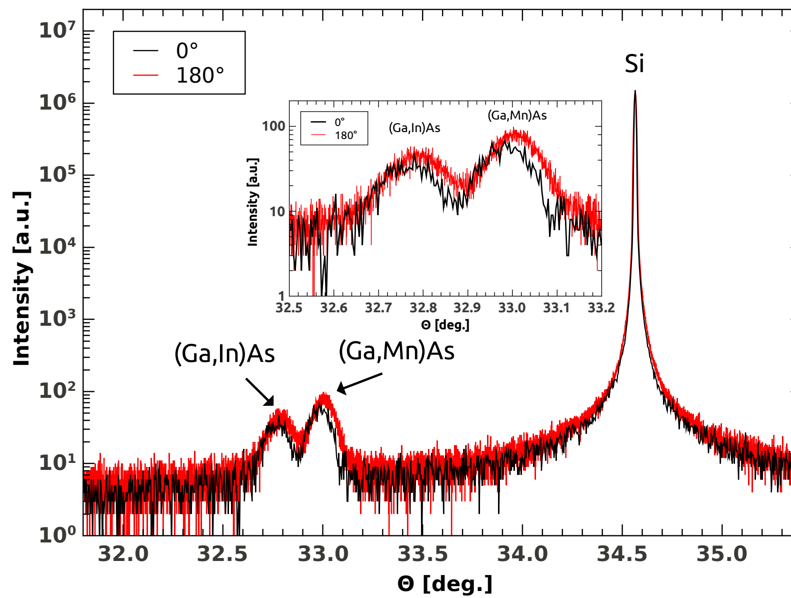

Figure 6.5: $\omega - 2\Theta$ scans of the (004) reflection of lifted 70 nm (Ga,$Mn_{0.035}$)As / 70 nm (Ga,$In_{0.07}$)As on [Si/SiO_2] substrate, measured at $\Phi = 0°$ (black curve) and $\Phi = 180°$ (red curve). The inset shows the zoomed region of the (Ga,Mn)As / (Ga,In)As layer peak positions for $\Phi = 0°$ and $\Phi = 180°$. Again, a tilt of $\sim 0.01°$ like sample S1 is estimated by the shift of the Bragg peaks.

Reciprocal space maps before and after the lift-off process of sample S2 are shown in Figure 6.6(a) and (b). As explained in Chapter 3.3, the layer and substrate Bragg peaks of pseudomorphically grown material are aligned along the [001] direction (surface normal). The degree of relaxation is therefore $\gamma = 0$, according to Equation 3.21. In Figure 6.6(a), all layer peaks are aligned along the [001] direction indicating that no plastic relaxation

has been taken place and the layers are compressively strained, as expected for (Ga,Mn)As layers epitaxially grown on a GaAs (001) substrate. Such strain breaks the cubic symmetry of a zinc-blende structure, as presented in Chapter 2.3 and leads to a magnetic hard axis along the perpendicular to plane direction ([001] direction).

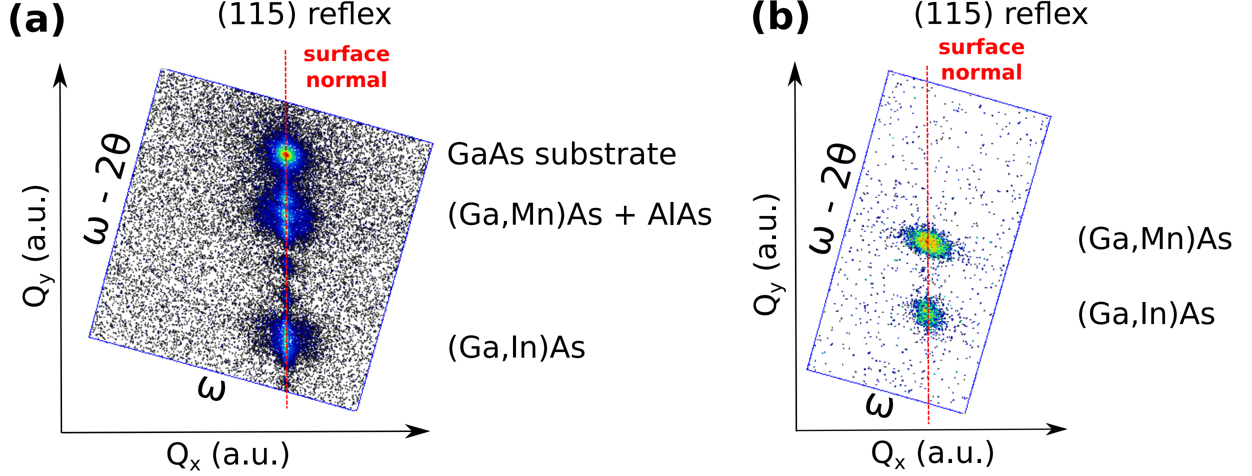

Figure 6.6: RSM of (115) reflex of (a) as-grown 70 *nm* (Ga,Mn)As / 70 *nm* (Ga,In)As / 60 *nm* AlAs on GaAs substrate and (b) lifted 70 *nm* (Ga,Mn)As / 70 *nm* (Ga,In)As on [Si/SiO_2]. (a) All layers are pseudomorphically grown on the substrate, indicated by the peak positions on the surface normal. A separation of (Ga,Mn)As and AlAs layer peaks is not possible due to interference features. (b) (Ga,Mn)As and (Ga,In)As layers seem to have same in-plane lattice constants referred to the surface normal implying elastic relaxation.

Figure 6.6(b) shows the case after the lift-off process where both layers of (Ga,In)As and (Ga,Mn)As are again aligned along the surface normal ([001] direction). This measurement suggests that both layers have the same in-plane lattice constants $a_{\parallel}$ and are still epitaxially connected after the elastic relaxation. The broadening of the peaks in ω direction is explainable most likely due to a change of strain situation within the layers (introduced by the ELO process) leading to defects and additionally undulations of the layers on the host-substrate.

In the reciprocal space map of Figure 6.6(b), there is no substrate per se to refer to. Hence, the in-plane lattice constants have to be estimated by using the macroscopic linear elasticity theory in form of Equation 3.11 in Chapter 3.3.1 as follows

$$a_{\parallel,ELO} = a_{bulk} - \frac{1-\nu}{2\nu}(a_{\perp} - a_{bulk}) \tag{6.1}$$

where $a_{bulk} = 5.682 \pm 0.002\mathring{A}$ is the calculated bulk lattice constant by Equation 3.5, $a_{\perp} = 5.692 \pm 0.003\mathring{A}$ is the measured vertical lattice constant and $\nu = 0.314$ is the Poisson ratio of (Ga,$In_{0.07}$)As. The result of Equation 6.1 for the in-plane lattice constant is $a_{\parallel,ELO} = 5.673 \pm 0.006\mathring{A}$. Compared to the as-grown sample S2 with $a_{\parallel} = 5.653\mathring{A}$, $a_{\parallel}$ increases after the ELO process meaning, that the (Ga,In)As stressor layer is relaxed but it

is still compressively strained due to $a_{\|,ELO} < a_{bulk}$. However, the reduction of compressive strain in the (Ga,In)As layer after the ELO process is observable in a shift of the Bragg peak to higher angles i.e. $a_{\perp}$ decreases according to the Poisson effect, as seen in Figure 6.5 compared to Figure 6.4.

The RSM of sample S2 after ELO process shows, that (Ga,In)As as well as (Ga,Mn)As are still epitaxially connected. Equation 6.1 is not applied to (Ga,Mn)As because the Poisson ratio as well as the bulk lattice constant are not reliably established. This correlation is strongly influenced by growth parameter conditions and point defect concentrations as mentioned in Chapter 3.2.1. The layer peaks of the (Ga,In)As and (Ga,Mn)As layer in Figure 6.6 are aligned along the surface normal in [001] direction, leading to the same Q_x values. As a conclusion, the (Ga,Mn)As in-plane lattice parameters are assumed to be the same as for the (Ga,In)As layer after elastic relaxation and the (Ga,Mn)As layer is therefore under tensile strain.

6.2 Temperature Dependent Magnetometry Results

The magnetic properties of layers S1 and S2 before (AS) and after the lift-off process (ELO) have been investigated by magnetometry measurements with a SQUID. Curie temperatures of $\sim 60\ K$ have been measured for all samples.

In Figure 6.7 magnetization curves with applied magnetic field along the perpendicular-to-plane direction [001] have been measured at $T = 4.3\ K$ and $30\ K$.

Both as-grown samples AG S1 and AG S2 in Figure 6.7(a) and (c) reveal a hard axis of magnetization, detected as elongated magnetization curves without any remanent magnetization at $H = 0$. The necessary applied magnetic field to force the magnetization along [001], defined as H_s, is about $H_s = 0.18\ T$ at $T = 4.3\ K$ and $H_s = 0.20\ T$ at $T = 30\ K$. After the lift-off process and deposition on a [Si/SiO_2] substrate the sample ELO S1 shows a reduced $H_s = 0.14\ T$, as seen in Figure 6.7(b). ELO S2 has a different shape of the magnetization curve (Figure 6.7(d)). At 4.3 K, there is a hysteretic feature with remanent magnetization along [001] in the magnetization curve and H_s is reduced to 0.05 T. This feature is more pronounced at 30 K with a square hysteresis loop around zero magnetic field. Compared to the as-grown case of S2, the magnetic easy axis changed from in-plane to out-of-plane [001]. An explanation of the sudden reorientations of magnetization along the [001] direction at finite field values, referred to as H_s, originate from the competition between several anisotropy terms. The dominant term at 4.3 K is the cubic anisotropy term which is softened at higher temperatures (30 K). The value of H_s is connected to the present strain situation within the layer, so the reduction of H_s can be explained by the elastic relaxation of the (Ga,Mn)As layer due to the lift-off procedure.

Furthermore, local measurements by using the spatially resolved polar magneto-optical Kerr effect (P-MOKE) have shown, that perpendicular-to-plane domains expand over the whole sample while increasing the temperature from 20 K to 40 K [Gre11].

In summary, the epitaxial lift-off process is a technique to change the magnetic anisotropy of (Ga,Mn)As by release of the growth-induced compressive strain. Depositing the lifted layer on top of different host-substrates offers the opportunity to investigate the samples e.g. by optical transmission experiments in the visible range (sapphire as non-absorbing host-material) or electrostatic control of the magnetization by varied strain (piezo-electrical ceramic substrates) which is not possible for as-grown layers.

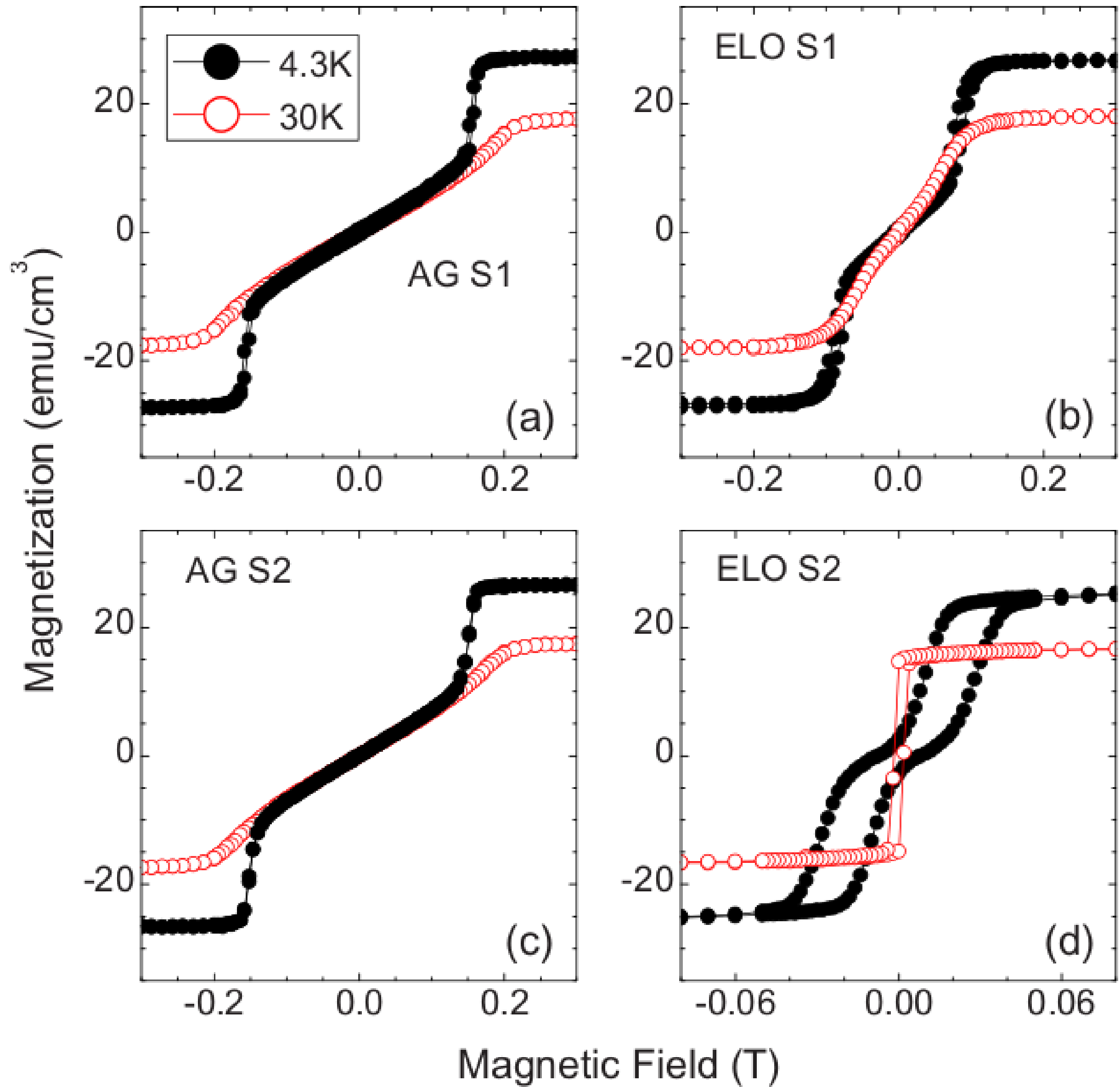

Figure 6.7: Magnetization curves with magnetic field along perpendicular-to-plane direction [001] at 4.3 K (solid circles) and 30 K (open circles). 70 nm (Ga,Mn)As layer (a) before (AS S1) and (b) after lift-off process (ELO S1). 70 nm (Ga,Mn)As / 70 nm (Ga,In)As layer (c) before (AS S2) and (d) after lift-off process (ELO S2). The abscissa in (d) is different compared with (a) to (c). Taken from [Gre11].

Chapter 7

Conclusion and Outlook

The diluted magnetic semiconductor (Ga,Mn)As is considered as a model system for future spintronic devices. The knowledge of its ferromagnetic properties and complex magnetic anisotropies has been acquired during the last two decades. (Ga,Mn)As material is fabricated by the MBE technique and structural, magnetic and electrical characterization has been performed by a wide range of methods, as presented in Chapter 2 and 3. The EP III department at the University of Würzburg has extensive experience in epitaxial growth of bulk (Ga,Mn)As material with layer thicknesses of 20 to 70 nm and photolithographic nanopatterning.

The main emphasis is placed on the control of magnetic anisotropies by e.g. uniaxial strain-relaxation of nanopatterned stripes causing a change of preferred magnetization direction [Wen07] or low-current control of magnetic anisotropies by a fully-electrical read-write device [Mar11]. In this thesis the control of magnetic anisotropy in (Ga,Mn)As layers has been realized by an epitaxial lift-off (ELO) process [Gre11], which is based on strain-induction and presented in Chapter 6. It allows to induce an out-of-plane magnetic easy axis by deposition of the (Ga,Mn)As layer on top of a different host substrate after the ELO process.

The fabrication of very thin ($<$10 nm) (Ga,Mn)As layers bares challenges compared to bulk material due to strong influences of surface defects and point defects leading to severe compensation of p-doping. Very thin (Ga,Mn)As layers grown at standard growth conditions, which are well-established for bulk material, reveal a drastic variation of conductivity and therefore infeasible electrical properties for LT-transport experiments. A new design has been developed to distribute the homogeneous Mn profile of a 4 nm (Ga,Mn)As layer into a parabolical Mn profile with a relatively "thick" centered layer of 14 $\mathring{A}$, as presented in Chapter 5. The center layer is surrounded by three thin (Ga,Mn)As/LT-GaAs layer sequences above and underneath that are ideally used for electrostatical shielding the center from surface and point defects. In a first growth series at standard growth conditions, it has been shown that the new layer design with the same nominal Mn content ($x = 0.040$) improves layer properties and the magnetic properties are comparable to bulk (Ga,Mn)As material with mainly biaxial anisotropy and an additional uniaxial component. Furthermore, simplified self-consistent band alignment calculations suggest a slightly higher hole

density and a stronger robustness against interface defects and surface effects compared to very thin layers with a homogeneous Mn profile. In order to get a deeper understanding of the interplaying influences of confinement of holes and their coupling to Mn magnetic moments on the (anisotropic) magnetic and bandstructure properties, a detailed theoretical model as well as further structural, magnetic and LT-transport studies of very thin (Ga,Mn)As layers with graded Mn profile are required for the future.

In a second growth series, growth parameters for thin, parabolically graded (Ga,Mn)As layers with lowered Mn content of $x = 0.025$ have been systematically investigated. As a result, a narrow growth parameter window has been observed, where this kind of layer is conductible at LT and shows ferromagnetic behavior.

Finally, a first parabolically graded layer built-in a p-n junction device seems promising for future low-voltage gating experiments at LT. Further developments of the Mn profile, a lowered Mn content closer to the metal-insulator-transition and/or thinner layers ($\leq$3.5 nm) might be possible continuations of the actual status of parabolically graded (Ga,Mn)As layers.

Appendix A

Appendix

A.1 Determination of As_{Ga} Concentrations

Arsenic antisites As_{Ga} are one of the main point defects responsible for hole carrier compensation in (Ga,Mn)As, as presented in Chapter 3.2.1. A 500 nm LT-GaAs layer and a 70 nm (Ga,Mn)As layer have been grown at optimized growth conditions for (Ga,Mn)As layers with a parabolical grading of Mn profile (T_{sub} = 290°C and BEP ratio ($\frac{As_4}{Ga}$)=25) in order to estimate [As_{Ga}] for band alignment simulations, presented in Chapter 5.3.5. Both layers have been characterized by HRXRD measurements to determine the vertical lattice constant of these samples. The conversion from $a_\perp$ to a_{bulk} has been implemented by Equation 3.12. The arsenic antisite concentrations have been estimated by Equation 3.15 for the LT-GaAs layer and Equations 3.16 and 3.17 for the (Ga,Mn)As layer after annealing under assumption of a complete outdiffusion of Mn interstitials Mn_{int}.

Figure A.1(a) and (b) present the HRXRD ω-2Θ-scan of the symmetrical (004) reflection of a 500 nm LT-GaAs layer (black line) as well as the simulation of the sample (red line).

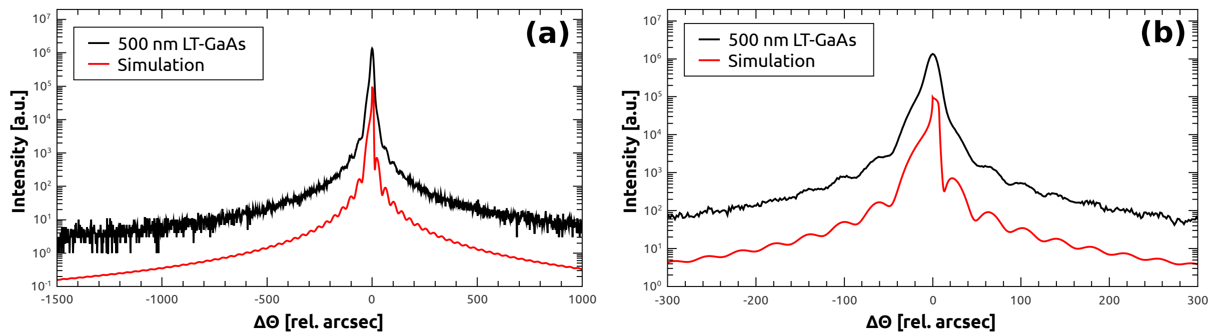

Figure A.1: HRXRD ω-2Θ-scan of the symmetrical (004) reflection of (a) a 500 nm LT-GaAs layer (black line) with its simulation (red line) and (b) the zoomed region around the GaAs substrate peak of the same measurement. The offset of the two measurements arises out of clarity.

The distance between interference fringe peaks around the GaAs substrate peak in Figure A.1(a) and (b) corresponds to a LT-GaAs layer thickness of $d = 500\ nm$. The LT-GaAs Bragg peak is in the flank of the GaAs substrate peak and complicates the determination of the vertical lattice constant. On that score, the sample has been simulated by *Epitaxy* with (Ga,In)As material. The In content for the simulation is very low (x_{In} < 0.001) and Vegard's law (Equation 3.5) can be applied due to the linear dependence of lattice constant expansion with In content. Thus, the bulk lattice constant of LT-GaAs $a_{LT-GaAs,bulk}$ is given as

$$a_{LT-GaAs,bulk} = a_{(Ga_x,In)As,bulk} = 6.0583 - 0.405 \cdot x_{Ga} \qquad \text{in } \mathring{A} \tag{A.1}$$

where $a_{(Ga_x,In)As}$ is the calculated bulk lattice constant of (Ga$_x$,In)As, according to Equation 3.5. The fit of the HRXRD measurement offers a Ga content of $x_{Ga} = 0.9993$ and an In content of $x_{In} = 0.0007$ respectively. By Equation A.1, the bulk lattice constant of $a_{LT-GaAs,bulk} = 5.654\ \mathring{A}$ yields to an arsenic antisite concentration of $[As_{Ga}] = 1.1 \cdot 10^{19} cm^{-3}$. Compared to the vertical lattice constant of LT-GaAs of the calibration curve in Chapter 3.2.1, $a_\perp = 5.658\ \mathring{A}$ and therefore $a_{LT-GaAs,bulk} = 5.656\ \mathring{A}$ shows $[As_{Ga}] = 4 \cdot 10^{19} cm^{-3}$. In case of optimized growth conditions for parabolically graded layers, [As$_{Ga}$] in LT-GaAs is lowered by a factor of 4 due to an increase of 20°C in substrate temperature and a reduction of BEP ratio ($\frac{As_4}{Ga}$) from 25 to 20. An arsenic antisite concentration of $[As_{Ga}] = 1.1 \cdot 10^{19} cm^{-3}$ has been taken for LT-GaAs in band alignment simulations of Chapter 5.3.5.

Additionally, the arsenic antisite concentration [As$_{Ga}$] has been estimated in case of an epitaxially grown (Ga,Mn)As material at optimized growth conditions (S787 of Table 5.5 in Chapter 5.3). Thereby, the vertical lattice constant has been measured by HRXRD for the as-grown and annealed sample. The annealing procedure leads to an outdiffusion of Mn interstitials. A total outdiffusion of Mn interstitials $x_{int} = 0$ is assumed, as described in Chapter 3.2.1. This assumption corresponds to an upper limit of [Mn$_{int}$].

Figure A.2 shows the HRXRD ω-2Θ-scans in relative arcsec of the symmetrical (004) reflection of the 70 nm (Ga,Mn)As layer (S787) with Mn content $x = 0.022$ (a) before (black line) and (b) after annealing (red line).

Although the Mn content of $x = 0.022$ is moderate, the annealing procedure leads to a smaller vertical lattice constant caused by a Mn interstitial outdiffusion. In case of the as-grown (Ga,Mn)As sample, $a_\perp = 5.668\ \mathring{A}$ corresponds to $a_{(Ga,Mn)As,bulk} = 5.661\ \mathring{A}$. After annealing of the sample, the vertical lattice constant of $a_\perp = 5.663\ \mathring{A}$ corresponds to a bulk lattice constant of $a_{(Ga,Mn)As,bulk} = 5.658\ \mathring{A}$. Depending on the factor for the arsenic antisite concentration y of $0.69\mathring{A}$ and $0.46\mathring{A}$ in Equations 3.16 and 3.17, these equations have been gathered to estimate the arsenic antisite concentration [As$_{Ga}$] in a (Ga,Mn)As layer. Assuming a total outdiffusion of Mn interstitials $x_{int} = 0$ and a Mn content of $x_{sub} = 0.022$, the transformation of Equations 3.16 and 3.17 to y leads to

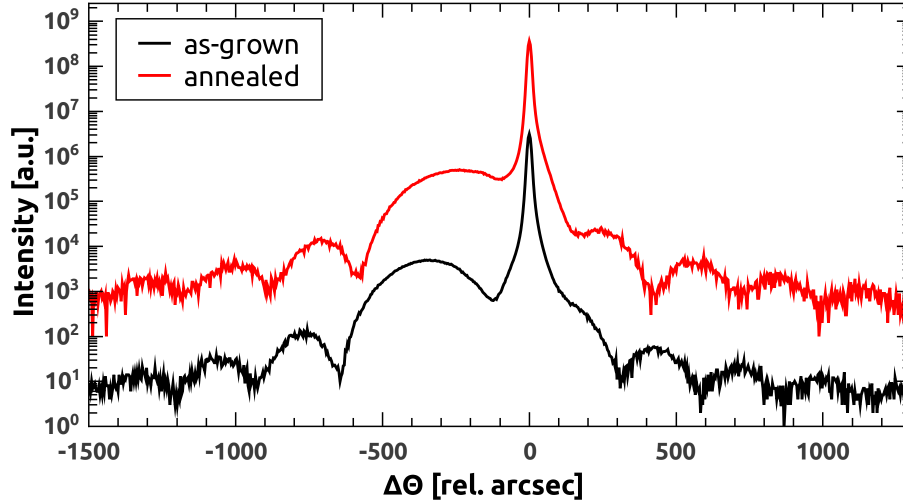

Figure A.2: HRXRD ω-2Θ-scan of the symmetrical (004) reflection of a 70 nm (Ga,Mn)As layer with $x = 0.022$ (a) as-grown (black line) and (b) after annealing (red line). The offset of the two measurements arises out of clarity.

$$[As_{Ga}] = y = \frac{a_{(Ga,Mn)As,bulk} - a_{GaAs} - 0.02\mathring{A} \cdot x_{Sub}}{0.69\mathring{A}} \times 2.2 \cdot 10^{22} cm^{-3} \tag{A.2}$$

$$[As_{Ga}] = y = \frac{a_{(Ga,Mn)As,bulk} - a_{GaAs} + 0.05\mathring{A} \cdot x_{Sub}}{0.46\mathring{A}} \times 2.2 \cdot 10^{22} cm^{-3} \tag{A.3}$$

$a_{GaAs,bulk} = 5.653$ $\mathring{A}$, $a_{(Ga,Mn)As,bulk} = 5.658$ $\mathring{A}$ and $x_{Sub} = 0.022$ have been used in these equations to calculate the range of arsenic antisite concentration [As$_{Ga}$]. The result gives a range from $1.4 \cdot 10^{20} cm^{-3}$ to $2.8 \cdot 10^{20} cm^{-3}$. It is worth mentioning, that [As$_{Ga}$] of (Ga,Mn)As layer is roughly one order higher compared to pure LT-GaAs.

In principle, the determination of [As$_{Ga}$] by HRXRD measurements has to be taken with special care. In case of Equation 3.15 used for pure LT-GaAs without the incorporation of substitutional and/or interstitial Mn, the bulk (Ga,Mn)As layer constant would lead to $[As_{Ga}] = 7.0 \cdot 10^{19} cm^{-3}$. It shows, that the determination of arsenic antisite concentration from HRXRD measurements should be regarded as an estimation and [As$_{Ga}$] should lie in the range of 10^{19} to $10^{20} cm^{-3}$, as stated elsewhere [Gra00].

As a conclusion of these estimations, a mean value of $[As_{Ga}] = 1.75 \cdot 10^{20} cm^{-3}$ for (Ga,Mn)As material grown at optimized growth conditions has been taken for band alignment calculations in Chapter 5.3.5.

A.2 Special Features of the UHV MBE Growth Chamber

A.2.1 Homogeneity of a 2" Wafer

As presented in Chapter 3.1, the design of the MBE growth chamber offers a pumping volume of one-third compared to a RIBER 32 growth chamber. The compact layout with a N2-shroud in front of the sample has an impact on the homogeneity of the epitaxially grown heterostructures on a full 2" wafer.

At the beginning of this work, 70 *nm* GaMnAs/60 *nm* AlAs on GaAs heterostructures on complete 2" epi-ready GaAs (001) substrates for lift-off processes have been grown, as presented in Chapter 6.

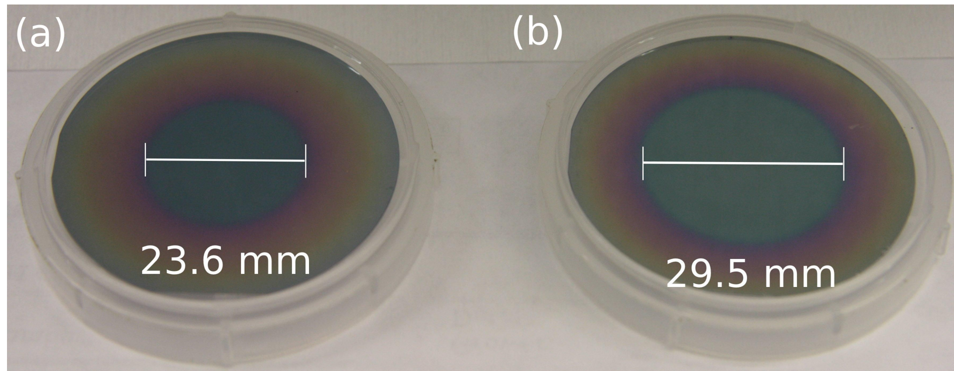

Figure A.3: 2" GaAs (001) wafer with epitaxial grown 70 *nm* GaMnAs/60 *nm* AlAs layer structure. Different growth position of the wafer: (a) 2 *cm* and (b) 1.5 *cm* behind the N2-shroud opening.

The wafer of Figure A.3(a) shows a center part of 23.6 *mm* in diameter which is homogeneous in color. Concentrical rings in different colors are visible at the outer regions of the 2" wafer. The position of the substrate during growth is adjusted about 2 *cm* behind the N2-shroud opening. This position corresponds to the flux gauge position during flux measurements of the effusion cells.

The same layer structure has been grown on another 2" GaAs (001)wafer, as seen in Figure A.3(b). For this growth procedure, the wafer is positioned as close as possible behind the N2-shroud (about 1.5 *cm*). The distance is limited by the position of the main shutter, which can be moved between N2-shroud opening and substrate. For the epitaxially grown layer, the center part with homogeneous color has a greater diameter of about 29.5 *mm*. Concentrical rings with different colors are still present.

The inhomogeneity of the layers has been investigated by HRXRD measurements of the (004) reflection of two different samples. Two sample pieces from different positions of the wafer from a sample of Figure A.3 (70 *nm* GaMnAs/ 60 *nm* AlAs) have been measured. One of the samples is cleaved out of the center part with homogeneous color part and a

second piece is cleaved out of the color ring part. The dimension of both samples are 5×10 mm with the short edge parallel to the radius of the wafer.

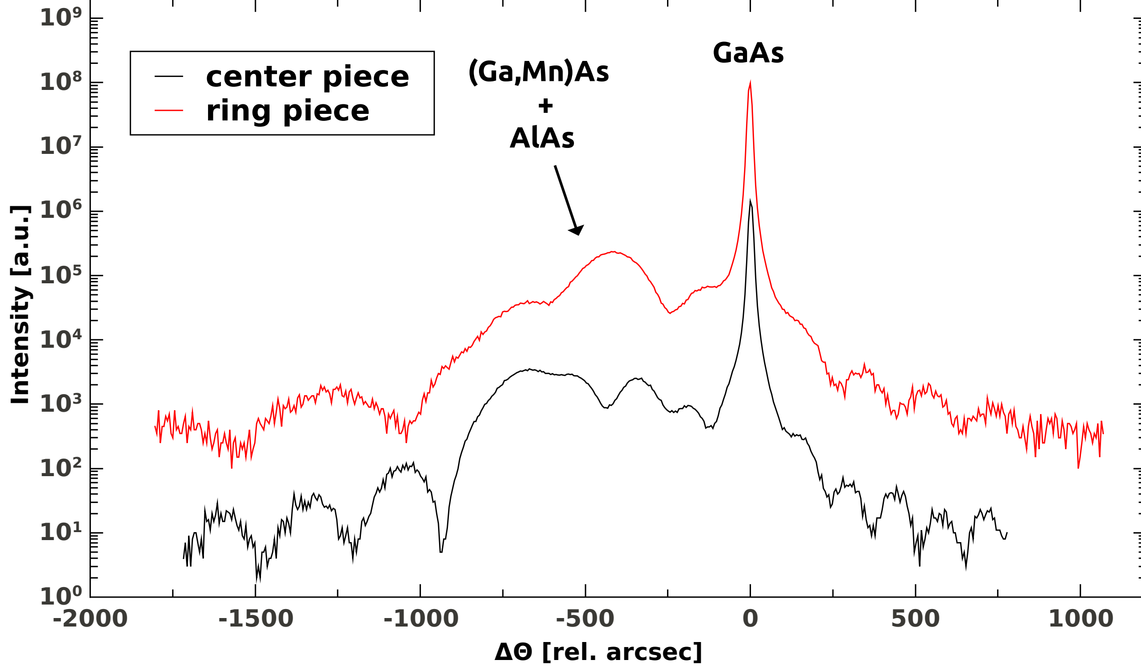

Figure A.4: ω-2Θ scan of the (004) reflection of center piece (black curve) and ring piece (red curve) taken from a 2" GaAs wafer with epitaxially grown GaMnAs/AlAs layer structure. A significant decrease of GaMnAs film thickness of about 47 % is measurable. A decrease in Mn content (about 17 %) has to be considered with a large error bar due to the interference with the underlying AlAs film.

Figure A.4 shows ω-2Θ scans of the center piece (black curve) and the ring piece (red curve). The comparison of both diffraction patterns exhibit a significant decrease in the (Ga,Mn)As film thickness of the the ring piece which is visible by a greater distance of fringe peaks at the left side of the GaAs peak. The film thickness changes from 71.0 nm to 38.0 nm which corresponds to a decrease of $\approx$ 47 %. The fringe peaks on the right side of the GaAs peak are dominated mostly by the AlAs film thickness. Again, a decrease is measurable in film thickness. Here, the decrease amounts 12 %. Out of the given layer structure, an exact statement of the Mn content due to the interference of the AlAs and (Ga,Mn)As peak in (004) reflection cannot be issued due to a similar vertical lattice constants $a_{AlAs} = 5.661$ $\mathring{A}$ of AlAs and (Ga,Mn)As (see calibration curve in Figure 3.13). A Mn content of $x = 0.049$ (center) and $x = 0.041$ (ring) has been estimated by simulation of the given HRXRD measurements, which results in a decrease of about 17 %.

The second sample is a 70 nm GaMnAs layer epitaxially grown (with nominally $x = 0.036$ (S682)) on a GaAs substrate for a systematical analysis with HRXRD measurements. This layer did not show any color ring features due to the lack of an underlying AlAs layer. Four sample pieces at different positions on the wafer are cleaved for HRXRD

measurements. Compared to the sample of Figure A.3(b), two of the cutted pieces are situated inside the center part of homogeneous color (center of wafer 0 mm to 6.5 mm, [S1]; 6.5 to 12.0 mm, [S2]), one inside the color rings (16.0 mm to 21.0 mm, [S3]) and the fourth sample at the edge of the wafer (width 4 mm, [S4]). The height of every sample piece is 10 mm. Figure A.5(a) presents the results of the ω-2Θ scans of the (004) reflection and Figure A.5(a) connects the results to the position on the wafer.

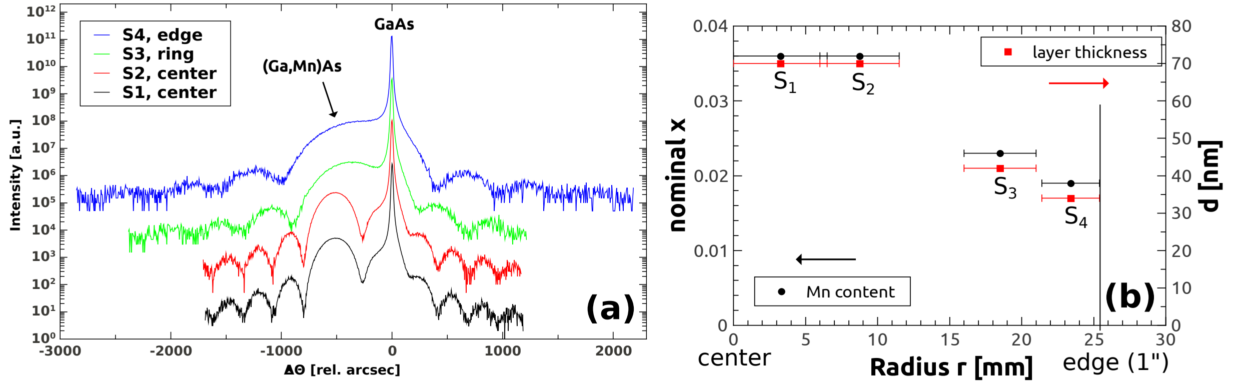

Figure A.5: (a) ω-2Θ scans of the (004) reflection of four sample pieces of a full 2" grown wafer with 70 nm (Ga,Mn)As. S1 and S2 are center pieces, S3 is at least 16.0 mm away from center and S4 directly at the edge of the wafer. (b) Mn content and layer thickness as a function of wafer radius r.

The center pieces S1 and S2 have the same vertical lattice constant ($a_{\perp} = 5.675$ $\mathring{A}$) within the error of the measurement and therefore the same Mn content $x = 0.036$. The determination of the distance between the thickness fringes reveals the same layer thickness d of 70 nm for S1 and S2. Sample S3, which is inside the color-ring region, has a lower vertical lattice constant $a_{\perp} = 5.668$ $\mathring{A}$ with a corresponding lower Mn content of $x = 0.023$ and additionally a lower $d = 42$ nm. A decrease in Mn content of 36 % and a decrease in d of 40 % is measured. The edge sample S4 has a vertical lattice constant of $a_{\perp} = 5.664$ $\mathring{A}$ and therefore a decrease of Mn content of about 47 % ($x = 0.019$). Here, the layer thickness d decreases of about 51 % (34 nm).

A plausible explanation for the deviation in layer thickness and Mn content at the outer parts of the full 2" wafer is the N2-shroud, which has an opening of about 6 cm in diameter with a distance of about 20 cm to the cell openings. This condition leads to a (partial) shadowing effect of the molecular beams of the cells. As a result, the growth conditions at the outer parts of the wafer strongly differ from the center part.

As a workaround of these findings, the samples have been grown on quarter wafers. In general, quarter wafers have been glued upon the center of a Molybdenum block, so a homogeneous grown layer structure is expected compared to a full 2" wafer.

A.2.2 Mirror on a Molybdenum Block

Figure A.6: A mirror on a Molybdenum block which can be inserted into the UHV growth chamber. The tool offers a front view at the effusion cells and its cell shutters.

A very useful gimmick for the UHV MBE growth chamber with its special geometry is a concave mirror which is fixed on a Molybdenum block. It can be inserted into the UHV system. The concave form is helpful to have a look at the effusion cell openings and its cell shutters. When the mirror is in growth position and the main shutter is opened, it is possible to see a mirror image of the cell openings and cell shutters through the heated view port. In principle, it is the only in-situ method to have a front view of the cells due to the N2-shroud, which is positioned between substrate and effusion cells. Figure A.6 shows the molybdenum block with fixed concave mirror. This tool has been used to determine the time delay of the Mn shutter movement, presented in Chapter 5.1.1.

Bibliography

[Abo01] M. Abolfath, T. Jungwirth, J. Brum, and A. MacDonald, Phys. Rev. B **63**, 054418 (2001).

[Ade11] J. Adell, I. Ulfat, L. Ilver, J. Sadowski, K. Karlsson and J Kanski, J. Phys. Cond. Matt. **23**, 085003 (2011).

[Alb08] K. Alberi, K. M. Yu, P. R. Stone, O. D. Dubon, W. Walukiewicz, T. Wojtowicz, X. Liu, and J. K. Furdyna, Phys. Rev. B **78**, 075201 (2008).

[Avr05] V. Avrutin, D. Humienik, S. Frank, A. Koeder, W. Schoch, W. Limmer, R. Sauer, and A. Waag, J. Appl. Phys. **98**, 023909 (2005).

[Bax02] D. V. Baxter, D. Ruzmetov, J. Scherschligt, Y. Sasaki, X. Liu, J. K. Furdyna, and C. H. Mielke. Phys. Rev. B, **65**, 212407 (2002).

[Ber70] L. Berger, Phys. Rev. B, **2**, 4559 (1970).

[Bir74] G. L. Bir and G. E. Pikus, *Symmetry and Strain-Induced Effects in Semiconductors*, Wiley, New York (1974).

[Bli03] J. Blinowski, P. Kacman, Phys. Rev. B **67**, 121204 (2003).

[Bow98] D. K. Bowen, B. K. Tanner, *High resolution x-ray diffractometry and topography*, Taylor & Francis (1998).

[Bro00] I. N. Bronstein, K. A. Semendjajew, G. Musiol, H. Mühlig, Harri Deutsch Verlag, 5. überarbeitete und erweiterte Auflage (2000).

[Bur08] K. S. Burch, D. D. Awschalom, and D. N. Basov, J. Magn. Magn. Mater. **320**, 3207 (2008).

[Cal66] H. B. Callen and E. Callen, J. Phys. Chem. Solids **27**, 1271 (1966).

[Cam03] R. P. Campion, K. W. Edmonds, L. X. Zhao, K. Y. Wang, C. T. Foxon, B. L. Gallagher, C. R. Staddon, Journal of Crystal Growth **247**, 42-48 (2003).

[Che93] W. Q. Chen, S. M. Wang, T. G. Andersson, and J. Thordson, Phys. Rev. B **48**, No. 19, 14264 (1993).

[Che09] L. Chen, S. Yan, P. F. Xu, J. Lu, W. Z. Wang, J. J. Deng, X. Qian, Y. Ji, and J. H. Zhao, Appl. Phys. Lett **95**, 182505 (2009).

[Cun86] J. E. Cunningham, T. H. Chiu, A. Ourmazd, J. Shah, and W. T. Tsang, J. Appl. Phys. **60**, 4165 (1986).

[Dae06] J. Daeubler, M. Glunk, W. Schoch, W. Limmer, and R. Sauer, Appl. Phys. Lett. **88**, 051904 (2006).

[Dae90] L. Däweritz, R. Hey, Surface Science, **236**, 15-22 (1990).

[Del78] J. A. Del Cueto and N. J. Shevchik, J. Phys. C **11**, 829 (1978).

[Die00] T. Dietl, H. Ohno, F. Matsukura, J. Cibert, and D. Ferrand, Science, **287**, 1019 (2000).

[Die01] T. Dietl, H. Ohno, and F. Matsukura, Phys. Rev. B **63**, 195205, (2001).

[Ebe06] L. Ebel, *Molekularstrahlepitaxie und Charakterisierung von (Ga,Mn)As-Schichtstrukturen und InAs Quantenpunkten*, Diploma thesis, Universität Würzburg (2006).

[Edm03] K. W. Edmonds, R. P. Campion, K. -Y. Wang, A. C. Neumann, B. L. Gallagher, C. T. Foxon, and P. C. Main, J. Appl. Phys. Lett. **93**, 6787 (2003).

[Edm04] K. W. Edmonds, P. Bogusławski, K. Y. Wang, R. P. Campion, S. N. Novikov, N. R. S. Farley, B. L. Gallagher, C. T. Foxon, M. Sawicki, T. Dietl, M. Buongiorno Nardelli, and J. Bernholc, Phys. Rev. Lett. **92** 3, 037201 (2004).

[Edm05] K. W. Edmonds, N. R. S. Farley, T. K. Johal, G. van der Laan, R. P. Campion, B. L. Gallagher, and C. T. Foxon, Phys. Rev. B **71**, 064418 (2005).

[Erw02] , S. C. Erwin, and A. G. Petukhov, Phys. Rev. Lett. **89**, 227201 (2002).

[Fee93] , R. M. Feenstra, J. M. Woodall, and G. D. Pettit, Phys. Rev. Lett. **71**, 1176-1179 (1993).

[Fox75] C. T. Foxon, and B. A. Joyce, Surface Science **50**, 434-450 (1975).

[Fre09] M. Freitag, *Methoden zur Kontrolle der magnetischen Eigenschaften von (Ga,Mn)As durch Gating*, Diploma thesis, Universität Würzburg (2009).

[Fur88] J. K. Furdyna, J. Appl. Phys. **64**, R29 (1988).

[Gei99] W. Geißelbrecht, U. Pfeiffer, A. Thränhardt, U. Klütz, A. C. Gossard, G. H. Döhler, J. Chrystal Growth **201/202**, 163-165 (1999).

[Goe05] S. T. B. Goennenwein, S. Russo, A. F. Morpurgo, T. M. Klapwijk, W. Van Roy, and J. De Boeck, Phys. Rev. B **71**, 193306 (2005).

[Gou04] C. Gould, C. Rüster, T. Jungwirth, E. Girgis, G. M. Schott, R. Giraud, K. Brunner, G. Schmidt, and L. W. Molenkamp. Phys. Rev. Lett. **93**, No. 11, 117203, (2004).

[Gou08] C. Gould, S. Mark, K. Pappert, R. G. Dengel, J. Wenisch, R. P. Campion, A. W. Rushforth, D. Chiba, Z. Li, X. Liu, W. van Roy, H. Ohno, J. K. Furdyna, B. L. Gallagher, K. Brunner, G. Schmidt, and L. W. Molenkamp, New J. Phys. **10**, 055007 (2008).

[Gra00] B. Grandidier, J. P. Nys, C. Delerue, D. Stiévenard, Y. Higo, and M. Tanaka, Appl. Phys. Lett. **77**, 4001 (2000).

[Gre11] F. Greullet, L. Ebel, F. Münzhuber, S. Mark, G. V. Astakhov, T. Kießling, C. Schumacher, C. Gould, K. Brunner, W. Ossau, and L.W. Molenkamp, Appl. Phys. Lett. **98**, 231903 (2011).

[Gro04] R. Gross and A. Marx, *Grundlagen der Magnetoelektronik*, Vorlesungsskript, Technische Universität München (2004).

[Har04] Th. Hartmann, S. Ye, P. J. Klar, W. Heimbrodt, M. Lampalzer, W. Stolz, T. Kurz, A. Loidl, H.-A. Krug von Nidda, D. Wolverson, J. J. Davies, and H. Overhof, Phys. Rev. B **70**, 233201 (2004).

[Iof98] Electronic archive of Ioffe Physico-Technical Institute, http://http://www.ioffe.ru/SVA/NSM/Semicond/index.html, (1998-2001).

[Jan57] J. P. Jan, Solid State Physics, Academic Press Inc., New York (1957).

[Jun05] T. Jungwirth, K. Y. Wang, J. Mašek, K. W. Edmonds, J. König, J. Sinova, M. Polini, N. A. Goncharuk, A. H. MacDonald, M. Sawicki, A. W. Rushforth, R. P. Campion, L. X. Zhao, C. T. Foxon, and B. L. Gallagher, Phys. Rev. B **72**, 165204 (2005).

[Jun06] T. Jungwirth, J. Sinova, J. Mašek, J. Kučera, A. H. MacDonald, Rev. Mod. Phys. **78**, 809 (2006).

[Jun07] T. Jungwirth, J. Sinova, A. H. MacDonald, B. L. Gallagher, V. Novák, K. W. Edmonds, A. W. Rushforth, R. P. Campion, C. T. Foxon, L. Eaves, E. Olejník, J. Mašek, S.-R. Eric Yang, J. Wunderlich, C. Gould, L. W. Molenkamp, T. Dietl, and H. Ohno, Phys. Rev. B **76**, 125206 (2007).

[Kur04] I. Kuryliszyn-Kudelska, J. Z. Domagała, T. Wojtowicz, X. Liu, E. Łusakowska, W. Dobrowolski, and J. K. Furdyna, J. Appl. Phys. **95**, 603 (2004).

[Les92] M. Leszczynski, M. Micovic, C. A. C. Mendonca, A. Ciepielewska, P. Ciepielewski, Cryst. Res. Technol. **27**, 97-100 (1992).

[Lin97] M. Linnarsson, E. Janzén, B. Monemar, M. Kleverman, and A. Thilderkvist, Phys. Rev. B **55**, No. 11, 6938-6944 (1997).

[Liu95] X. Liu, A. Prasad, J. Nishio, E. R. Weber, Z. Liliental-Weber and W. Walukiewicz, Appl. Phys. Lett **67** (2), 279 (1995).

[Lod03] S. Lodha, D. B. Janes and N.-P. Chen, J. Appl. Phys. **93**, 2772 (2003).

[Luy97] M. Luysberg, H. Sohn, A. Prasad, P. Specht, Z. Liliental-Weber, E. R. Weber, J. Gebauer and R. Krause-Rehberg, J. Appl. Phys. **83**, 561 (1997).

[Mac02] F. Máca, and J. Mašek, Phys. Rev. B. **65**, 235209 (2002).

[Mac08] S. Mack, R. C. Myers, J. T. Heron, A. C. Gossard, and D. D. Awschalom, Appl. Phys. Lett. **92**, 192502 (2008).

[Mar11] S. Mark, P. Dürrenfeld, K. Pappert, L. Ebel, K. Brunner, C. Gould, L.W. Molenkamp, Phys. Rev. Lett. **106**, 057204 (2011).

[Mar11a] S. Mark, *A Magnetic Semiconductor based Non-Volatile Memory and Logic Element*, PhD thesis, Universität Würzburg (2011).

[Maš03] J. Mašek, J. Kudrnovský, and F. Máca, Phys. Rev. B. **67**, 153203 (2003).

[Maš04] J. Mašek, and F. Máca, Phys. Rev. B. **69**, 165212 (2004).

[Maš05] J. Mašek, and F. Máca, arXiv: cond-mat 0508760 (2005).

[McD00] A. H. MacDonald, P. Schiffer, and N. Samarth, Nature Materials, **4**, 195-202 (2005).

[McG75] T. R. McGuire and R. I. Potter. IEEE Trans. Magn. **11**, 1018, (1975).

[Mik04] A. Mikkelsen, L. Ouattara, H. Davidsson, E. Lundgren, J. Sadowski, and O. Pacherova, Appl. Phys. Lett. **85**, 4660 (2004).

[Mil84] R. C. Miller, A. C. Gossard, D. A. Kleinman, and O. Munteanu, Phys. Rev. B, **29**, No. 6, 3740 (1984).

[Moo65] G. E. Moore, Electronics Magazine **38**, No.8, (1965).

[Mor03] R. Moriya and H. Munekata, J. Appl. Phys. **93**, 4603 (2003).

[Mot64] N. F. Mott, Advances in Physics **13**, 325 (1964).

[Mye06] R. C. Myers, B. L. Sheu, A. W. Jackson, A. C. Gossard, P. Schiffer, N. Samarth, and D. D. Awschalom, Phys. Rev. B **74**, 155203 (2006).

[Nex11] http://www.nextnano.de, software for the simulation of electronic and optoelectronic semiconductor nanodevices and materials (2011).

[OHa94] S. O'Hagen and M. Missous, J. Appl. Phys. **75**, 7835 (1994).

[Ohb93] I. Ohbu, M. Takahama, and H. Mizuta, Appl. Phys. Lett. **62**, 3279 (1993).

[Ohn96] H. Ohno, A. Shen, F. Matsukura, A. Oiwa, A. Endo, S. Katsumoto, and Y. Iye, Appl. Phys. Lett. **36**, 363 (1996).

[Ohn98] H. Ohno, Science, **281**, 951 (1998).

[Ohn99] H. Ohno, Journal of Magnetism and Magnetic Materials **200**, 110-129 (1999).

[Ole08] K. Olejník, M. H. S. Owen, V. Novák, J. Mašek, A. C. Irvine, J. Wunderlich, and T. Jungwirth, Phys. Rev. B **78**, 054403 (2008).

[Ort01] K. Ortner, *p-Dotierung von quecksilberhaltigen II-VI-Heterostrukturen mit Arsen und Plasma-aktiviertem Stickstoff*, PhD thesis, Universität Würzburg (2001).

[Owe09] M. H. S. Owen, J. Wunderlich, V. Novák, K. Olejník, J. Zemen, K. Výborný, S. Ogawa, A. C. Irvine, A. J. Ferguson, H. Sirringhaus and T. Jungwirth, New J. Phys. **11**, 023008 (2009).

[Pap07] K. Pappert, C. Gould, M. Sawicki, J. Wenisch, K. Brunner, G. Schmidt, and L. W. Molenkamp, New Journ. Phys. **9**, 354 (2007).

[Pap07a] K. Pappert, S. Hümpfner, J. Wenisch, K. Brunner, C. Gould, G. Schmidt, and L. W. Molenkamp. Appl. Phys. Lett. **90**, 062109 (2007).

[Pap07b] K. Pappert, S. Hümpfner, C. Gould, J. Wenisch, K. Brunner, G. Schmidt, and L. W. Molenkamp, Nature Physics **3**, 573-578 (2007).

[Res98] H. R. Ress, *Neue Methoden der hochauflösenden Röntgendiffraktometrie*, PhD thesis, Universität Würzburg (1998).

[Rie09] S. W. E. Riester, I. Stolichnov, H. J. Trodahl, N. Setter, A. W. Rushforth, K. W. Edmonds, R. P. Campion, C. T. Foxon, B. L. Gallagher, and T. Jungwirth, Appl. Phys. Lett. **94**, 063504 (2009).

[Ruz04] D. Ruzmetov, J. Scherschligt, D. V. Baxter, T. Wojtowitcz, X. Liu, Y. Sasaki, J. K. Furdyna, K. M. Yu, and W. Walukiewicz, Phys. Rev. B **69**, 155207 (2004).

[Sad00] J. Sadowski, J. Z. Domagala, J. Bak-Misiuk, S. Kolesnik, M. Sawicki, and K. Swiatek, J. Vac. Sci. Technol. B **18**, 1697-1700 (2000).

[Sad02] J. Sadowski, R. Mathieu, P. Svedlindh, M. Karlsteen, J. Kanski, Y. Fu, J. Z. Domagala, W. Szuszkiewicz, B. Hennion, D. K. Maude, R. Airey, G. Hill, Thin Solid Films **412**, 122-128 (2002).

[Sad04] J. Sadowski, and J. Z. Domagala, Phys. Rev. B **69**, 075206 (2004).

[Saw04] M. Sawicki, F. Matsukura, A. Idziaszek, T. Dietl, G. M. Schott, C. Ruester, C. Gould, G. Karczewski, G. Schmidt, and L. W. Molenkamp, Phys. Rev. B **70**, 245325 (2004).

[Saw05] M. Sawicki, K. Y. Wang, K. W. Edmonds, R. P. Campion, C. R. Staddon, N. R. S. Farley, C. T. Foxon, E. Papis, E. Kamiňska, A. Piotrowska, T. Dietl, and B. L. Gallagher, Phys. Rev. B **71**, 121302(R) (2005).

[She97] A. Shen, H. Ohno, F. Matsukura, Y. Sugawara, N. Akiba, T. Kuroiwa, A. Oiwa, A. Endo, S. Katsumoto, Y. Iye, Journal of Crystal Growth **175/176**, 1069-1074 (1997).

[Shi99] H. Shimizu, T. Hayashi, T. Nishinaga, and M. Tanaka, Appl. Phys. Lett. **74** No.3, 398 (1999).

[Sch03] G. M. Schott, G. Schmidt, L. W. Molenkamp, R. Jakiela, A. Barcz, and G. Karczewski, Appl. Phys. Lett. **82**, 4678 (2003).

[Sch04] G. M. Schott, *Molekularstrahlepitaxie und Charakterisierung von (Ga,Mn)As Halbleiterschichten*, PhD thesis, Universität Würzburg (2004).

[Sch06] M. Schmidt, *Electronic and magnetic properties of bound hole states in (Ga,Mn)As*, Diploma thesis, Universität Würzburg (2006).

[Spr87] A. J. SpringThorpe, S. J. Ingrey, B. Emmerstorfer, P. Mandeville, and W. T. Moore, Appl. Phys. Lett. **50**, 77 (1987).

[Sto03] M. B. Stone, K. C. Ku, S. J. Potashnik, B. L. Sheu, N. Samarth, and P. Schiffer, Appl. Phys. Lett **83**, 4568 (2003).

[Sto08] I. Stolichnov, S. W. E. Riester, H. J. Trodahl, N. Setter, A. W. Rushforth, K. W. Edmonds, R. P. Campion, C. T. Foxon, B. L. Gallagher, and T. Jungwirth, Nat. Mat. **7**, 464-467 (2008).

[Sto08b] P. R. Stone, K. Alberi, S. K. Z. Tardif, J. W. Beeman, K. M. Yu, W. Walukiewicz, and O. D. Dubon, Phys. Rev. Lett. **101**, 087203 (2008).

[Sze07] S. M. Sze, Kwok K. NG, Wiley, Hoboken, New Jersey (2007).

[Tuo04] F. Tuomisto, K. Pennanen, K. Saarinen, J. Sadowski, Phys. Rev. Lett. **93** 055505 (2004).

[Var67] Y. Varshni, Physica **34**, 149-154 (1967).

[Vur01] I. Vurgaftman, J. R. Meyer, and L. R. Ram-Mohan, J. Appl. Phys **89**, 5815 (2001).

[Wan92] S. M. Wang, G. Treideris, W. Q. Chen, and T. G. Andersson, Appl. Phys. Lett. **62**, 61 (1992).

[Wan08] M. Wang, R. P. Campion, A. W. Rushforth, K. W. Edmonds, C. T. Foxon, and B. L. Gallagher, Appl. Phys. Lett. **93**, 132103 (2008).

[Wel02] U. Welp, V. K. Vlasko-Vlasov, X. Liu, J. K. Furdyna, and T. Wojtowicz, Phys. Rev. Lett. **90**, 167206 (2003).

[Wen07] J. Wenisch, C. Gould, L. Ebel, J. Storz, K. Pappert, M.J. Schmidt, C. Kumpf, G. Schmidt, K. Brunner, and L.W. Molenkamp, Phys. Rev. Lett. **99**, 077201 (2007).

[Wen07a] J. Wenisch, L. Ebel, C. Gould, G. Schmidt, L. W. Molenkamp, and K. Brunner, J. Cryst. Growth **301-302**, 638-641 (2007).

[Wen08] J. Wenisch, *Ferromagnetic (Ga,Mn)As Layers and Nanostructures: Control of Magnetic Anisotropy by Strain Engineering*, PhD thesis, Universität Würzburg (2008).

[Wur08] U. Wurstbauer, *Herstellung und Charakterisierung von Mangan dotierten III-V Halbleiterheterostrukturen*, PhD thesis, Universität Regensburg (2008).

[Yu02] K. M. Yu, W. Walukiewicz, T. Wojtowicz, I. Kuryliszyn, X. Liu, Y. Sasaki, J. K. Furdyna, Phys. Rev. B **65**, 201303 (2002).

[Zim07] M. Zimmermann, *Wege zur Kontrolle der magnetischen Eigenschaften von (Ga,Mn)As*, Diploma thesis, Universität Würzburg (2007).

Acknowledgements

At this point, I would like to express my gratefulness to the following people, who have contributed in any form or by any means to the results of my thesis.

- My special thank goes to my supervisor Prof. Karl Brunner, who has supported me to continue the research in this interesting field long after my membership in the MBE group as a diploma student. His patience and our fruitful discussions were a key to the progress of my work.

I also want to thank:

- Prof. Laurens W. Molenkamp, Prof. Georg Schmidt and PD Dr. Charles Gould for a very interesting and successful collaboration in the spintronics group.
- Tsvetelina Naydenova, Dr. Fanny Greullet and Jennifer Constantino for uncountless measurements of my samples. Stefan Mark gets my gratitude for explanations of transport results of my samples and for our weekly discussions about soccer news.
- Dr. Claus Schumacher for his great support relating to the MBE technique, HRXRD measurements and IT solutions.
- My colleagues of room E095 for the great and harmonious atmosphere during my time as a PhD student. From Volkmar Hock, I have learned a lot about clean room matters and the UHV technique. Additionally, he is my fellow sufferor in case of the Eintracht. Anita Gebhard and Petra Wolf-Müller receive my thankfulness for the sample preparation of hundreds of substrates.
- Alfred Schönteich, Martin Zipf, Florian Stimmler and Roland Ebert for the excellent technical support and mechanical maintenance of the UHV system and in cryogenic matters.
- Franz Krause, Heinz Rüb, Hans-Peter Lindenberger, Carsten Bergmann, Rainer Brauner and all other members of the electronic and mechanical workshop to fix numerous Eurotherms and other small problems of the growth chamber.

- Christopher Ames, Christoph Brühne, Felicitas Gerhard, Florian Lochner, Rebecca Pfeuffer, Christoph Pohl and Steffen Schreyeck for a respectful and harmonious time in the MBE group. Special thanks go to Alex Frey for a bunch of physical and non-physical discussions as well as joint participations at various conferences.
- Dr. Jan Wenisch as my antecessor who has handed a well-maintained MBE growth chamber over to me. The cooperation during the time as his diploma student and later on as his succesor was really good.
- Dr. Tanja Borzenko, Dr. Tobias Kießling and everyone else from EP3, who is not explicitly mentioned.
- Richard Campion from Nottingham University for the invitation to his lab and very interesting discussions from the point of view of a (Ga,Mn)As grower.
- Martin Schwab for proofreading and helpful suggestions in the final stages of my thesis.
- my parents, my brother, my sister and her husband for their endless support during my physics study and later on as a PhD student. It feels good to know that you have been highly interested in my work although it is quite difficult to grasp for someone who is not familiar with such topics. Thank you Gundula, Walter, Matthias, Nicole and Michael!

Annie, a simple 'thank you' is far too little to express my gratitude. Your endless support and patience during my time at the university and especially in the last year, when you and Lotta have backed me up at the weekends, were essential to finish my thesis. I do not exaggerate by saying that your portion of this thesis is at least the same size as my portion. Thank you so much!!!